Université de Québec
Institut National de la Recherche Scientifique
Énergie Matériaux Télécommunications

Synthesis and Functional Properties of $BiFeO_3$ and Bi_2FeCrO_6 based Nanostructures and Thin Films

Shun Li

Thèse présentée pour l'obtention
du grade de Philosophiæ Doctor (Ph.D.)
en Sciences de l'énergie et des matériaux

Jury d'évalauation

Président du jury et examinateur interne	Andreas Ruediger INRS ÉMT
Examinateur externe	Nazir Kherani Université de Toronto
Examinateur externe	Pablo Bianucci Université Concordia
Directeur de recherche	Federico Rosei INRS ÉMT

Contents

Abstract

There is an increasing interest in developing and characterizing multiferroic materials, in which both ferromagnetic and ferroelectric orders coexist, as they exhibit rich physical properties and offer exciting opportunities for data storage, spintronics, sensors, electromagnets and photovoltaic (PV) applications. Among all multiferroic materials studied so far, $BiFeO_3$ (BFO) has attracted considerable attention because it shows intrinsic ferroelectric (T_C ~ 1103 K) and G-type antiferromagnetic (T_N ~ 643 K) orders simultaneously well above room temperature. In addition, multiferroic $BiFeO_3$, with band gap energy of 2.2-2.8 eV, has been recently identified as a promising candidate for PV devices and photocatalysts in the visible range. Moreover, the coupling between ferroic orders in $BiFeO_3$ materials offers new modes for investigating and controlling the PV effect, which may endow next generation solar and photoelectrochemical (PEC) cells with multiple functionalities. On the other hand, considerable interest has been attributed to multiferroic $BiFeO_3$ nanostructures in the quest of miniaturizing devices and discovering interesting fundamental physics at nanoscale. $BiFeO_3$ nanomaterials with various sizes and shapes such as nanoparticles, nanotubes, nanowires, and nano-/micro cubes have been reported so far and exhibit quite different physical and chemical properties compared to the bulk form of $BiFeO_3$ crystals due to the nanosize effect. Therefore, the synthesis of multiferroic $BiFeO_3$ nanostructures and investigation of their functional properties are considered important

for both fundamental research as well as designing new multifunctional materials combining magnetic, ferroelectric and optoelectronic properties.

Meanwhile, recent emergence of a novel double perovskites multiferroic material Bi_2FeCrO_6 (BFCO), with functional properties well above room temperature, opens new opportunities for practical applications of multiferroics. Bi_2FeCrO_6 has a similar crystal structure as $BiFeO_3$ and exhibits a particularly Fe/Cr cationic ordering along the [111] pseudocubic direction. Recent works demonstrated that an ordered Bi_2FeCrO_6 phase can be obtained in both thin film and nanostructured form using pulsed laser deposition (PLD) technique. The reported Bi_2FeCrO_6 thin films possess a remnant polarization of about 55 $\mu C/cm^2$ along the [001] pseudocubic direction, and are ferrimagnetic with a magnetic moment depending on Fe/Cr cationic ordering, about 1.8 μ_B per formula unit, far exceeding the properties of parent $BiFeO_3$. In addition, theoretical studies showed that Fe and Cr mixed *d* orbital transition allow a small band gap around 2.3 eV. Therefore, Bi_2FeCrO_6 is expected to be a promising candidate for efficient PV devices and PEC cells using sun light.

The work performed in this thesis was therefore driven by two main objectives: (1) synthesis and understanding the fundamental physical properties (i.e. ferroelectric and magnetic) of various low-dimensional $BiFeO_3$ nanostructures; (2) design and investigate $BiFeO_3$ and Bi_2FeCrO_6 based nanomaterials and thin film devices for high efficiency solar energy conversion (solar to chemical/electrical energy) applications. The results obtained in this work are resumed in two sections as follows:

In the first section, we have synthesized and investigated the ferroelectric, magnetic and photocatalytic properties of $BiFeO_3$ nanomaterials (1D nanowires and 2D nanoplates). We

studied the ferroelectric properties of 1D single-crystalline $BiFeO_3$ nanowires using piezoresponse force microscopy (PFM). PFM measurements demonstrated that the as-synthesized $BiFeO_3$ nanowires, down to 40 nm in diameter, have components of spontaneous polarization along both in plane and out of plane directions, thereby confirming the ferroelectric nature of the wires. We explained our results by estimating the shape of the piezoelectric tensor for the rhombohedral symmetry. We have also studied the photocatalytic solar water splitting properties of the $BiFeO_3$ nanowires and discovered that the nanowires exhibit better visible-light-driven photocatalytic activity for generation of O_2 from water than other $BiFeO_3$ materials (e.g. nanocubes) reported previously, which could be attributed to the unique morphology of the nanowires. To further enhance the photocatalytic activity, we designed and synthesized a hybrid $Au/BiFeO_3$ nanocomposite photocatalyst consisting of single crystalline $BiFeO_3$ nanowires and laser ablated Au nanoparticles by a functionalization-step-free solution process. We found that 1.0 wt% Au nanoparticle decorated $BiFeO_3$ nanowires exhibit significantly higher photocatalytic activity (~30 times) of water oxidation for O_2 than that of the parent wires during the first 4 h of the reaction. Their superior catalytic activity can be attributed to the role of the Au as electron trapping centers as well as the unique surface-chemistry features of the laser ablated Au nanoparticles that can strengthen the interaction and promote charge transfer. Meanwhile, we observed that the localized surface plasmonic resonance (LSPR) effect of Au nanoparticles could also contribute to the enhancement of the photoactivity. In addition, we developed a novel approach to synthesize (100) pseudocubic facets exposed 2D single crystalline $BiFeO_3$ nanoplates, with thickness ranging from 20 to 120 nm and lateral size of sub-micrometers, via a rapid (1-2 min) microwave-assisted hydrothermal method. The $BiFeO_3$ nanoplates exhibited

weak ferromagnetic properties at room temperature, which we attribute to the size-confinement effect on magnetic ordering.

The second section is focused on solar energy conversion (i.e. PV and PEC) applications of Bi_2FeCrO_6 thin film based cells. First, we presented the optical and PV properties of Bi_2FeCrO_6 epitaxial thin films grown on (100)-oriented $SrTiO_3$ substrate buffered with $SrRuO_3$ electrode deposited via PLD. In this part of work, we have achieved a wide band gap tunability from 1.4 to 2.5 eV in the epitaxial Bi_2FeCrO_6 films with significant polarization by tuning the ordering of transition-metal element Fe and Cr cations, which is remarkably large as compared with reported values from other doped ferroelectrics, opening up the possibility of discovering new narrow band gap multiferroic materials and designing high efficient oxide solar cells. With optimized PLD deposition conditions, we got a record power conversion efficiency of 3.3% under AM1.5G illumination (100 mW/cm^2) in the Bi_2FeCrO_6 thin film based solar cells. Additionally, we demonstrated the use Bi_2FeCrO_6 epitaxial thin film as a new photocathode material for the visible-light-driven reduction of water to hydrogen. PEC measurements showed that the highest photocurrent up to −1.0 mA/cm^2 at a potential of −1.0 V versus reversible hydrogen electrode (RHE) was obtained in *p*-type Bi_2FeCrO_6 thin film grown on $CaRuO_3/SrTiO_3$ substrate. For the positively poled Bi_2FeCrO_6 thin film, the photocurrent density was further enhanced by a factor of ~2, as a result of the modulation of the internal electric field gradient resulting from the ferroelectric polarization.

Acknowledgements

First I would like to thank my advisor, Prof. Federico Rosei, for continual guidance and assistance throughout the duration of my Ph.D., and without whom this work would not have been possible. Professionally, Dr. Rosei launches my scientific career, to which I am determined to dedicate the rest of my life. And personally, he has always been a strong supporter when I need help. Being able to study under his supervision is one of the most important achievements in my life.

I would also wish to give special thanks to the contributions to this work made by Dr. Riad Nechache. He made vital contributions to most of the work and gave me invaluable help and comments on my research and thesis writing. I am also grateful to all the group members from NFL for their help throughout the work. These people include: Wei Huang, Joyprokash Chakrabartty, Daniel Obi, Driss Soubane, Catalin Harnagea, Liliya Nikolova, Jonathan Laverdiere, Kadiatou Thérèse Dembélé, as well as other collaborators including Jianming Zhang, Md Golam Kibria, Bandar AlOtaibi, Menouer Saidani and Ivan Alejandro Velasco Davalos.

I would like to acknowledge Prof. Andreas Ruediger and Prof. Dongling Ma at INRS-EMT, and Prof. Zetian Mi from McGill University for their kind help and important comments on my project research.

A massive thanks to all my friends who have made the last four years so enjoyable: Guozhu Chen, Yue Huang, and Belete Atomsa, etc., without you I cannot have such wonderful memories these years.

I thank to the departmental and technical staff at INRS-EMT. They are very helpful, particularly Christophe Chabanier. I also would like to acknowledge Jean-Philippe Masse at Ecole Polytechnique for TEM measurements.

I am indebted to my dearest parents, for their constant support and encouragement throughout all of my studies. I wish to thank to my wife, Heping Fan, who loves me deeply and supports me selflessly. I thank my family and my friends for their continuing love and heartily support.

Finally, I wish to acknowledge the following organizations for their financial support to my research: the Natural Sciences and Engineering Research Council of Canada and Canada Foundation for Innovation. I also highly appreciate the support from the China Scholarship Council (CSC) and Fonds québécois de la recherche sur la nature et les technologies (FQRNT) for graduate fellowships.

List of Figures

List of Tables

Chapter 1

Introduction

1.1 Basics

1.1.1 Perovskite Oxides

Transition metal (TM) oxides are one of the most widely studied group of inorganic solid materials, which provide remarkably versatile chemical and physical properties, making them very attractive from both fundamental and applied perspectives [1]. The exceptional characteristics of the materials are because of the unique nature of TM's outer *d* orbital electrons, which give cations with several oxidation states and vary the metal-oxygen bonding from nearly ionic to metallic. Their properties are highly dependent on the crystal structure of TM oxides, which can adopt a wide diversity such as perovskite, spinel, pyrochlore, scheelite and so on.

Among all types of structures, perovskite arrangements that constitute amazingly robust matrices offer affluent options for structural and compositional variations. Perovskite materials exhibit a plethora of interesting and intriguing physical properties including superconductivity, colossal magnetoresistance, ionic conductivity, ferroelectricity and dielectric properties, which are of major importance in electronics and telecommunication. Because of the great flexibility inherent in the perovskite structure there are many different types of distortions which can occur from the ideal structure and reduce the symmetry. These include tilting of the octahedra,

displacements of the cations out of the centers of their coordination polyhedra, and distortions of the octahedra driven by electronic factors (i.e. Jahn-Teller distortions). Many of the physical properties of perovskites depend crucially on the details of these distortions, particularly the electronic, magnetic and dielectric properties which are very important for many of the applications of perovskite materials.

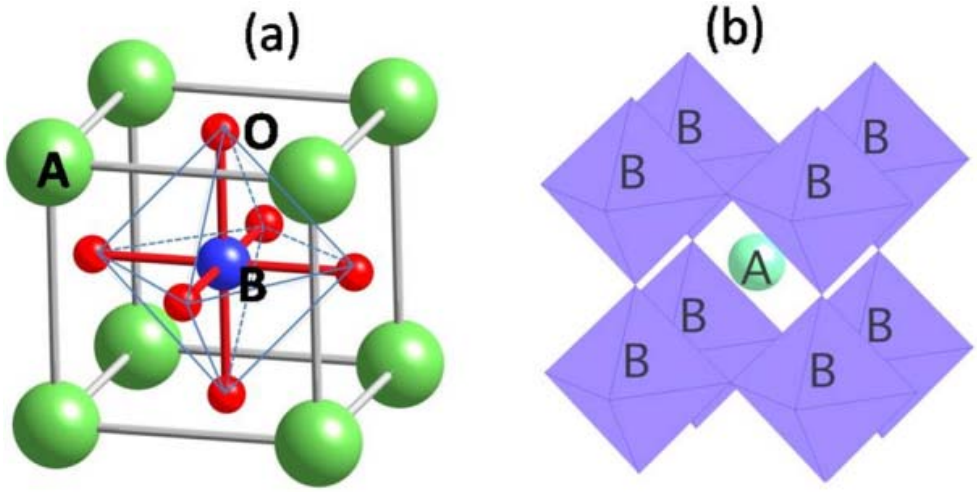

Figure 1. Two typical views of ideal cubic ABO_3 perovskite structure unit cell, where the green, the blue and red spheres represent *A*, *B* cations and oxygen, respectively. The structure of an ABO_3 perovskite with the origin centered at (a) the *B*-site ion and (b) the *A*-site ion [2].

Schematic diagrams of the perovskites structure are shown in Figure 1. The ideal structure of perovskite is a primitive cubic structure of the general stoichiometry ABO_3 (space group $Pm\bar{3}m$) with the lattice parameter $a \approx 4$ Å, containing two cations and one anion. One of the cation sublattices is built-up by "*A*" cations with a coordination number of twelve, surrounded by eight corner-sharing BO_6 octahedra. The second sublattice is formed by the "*B*" cations; usually this is a transition metal, with a coordination number of six, occupying appropriate sites inside the octahedra. The relationship between the ionic radii r_A, r_B and r_O (representative of *A*, *B* and O ions, respectively) is generally defined as:

$$r_A + r_O = t\sqrt{2}(r_B + r_O) \quad \text{(Eq. 1.1)}$$

where the tolerance factor, *t*, was introduced by Goldschmidt [3]. A change in *A* and *B* atomic species which can make the framework of octahedra twisted or distorted will result in the change of the *t* value, hence the crystallographic symmetry will be lowered and can be changed to orthorhombic, rhombohedral, tetragonal or trigonal in many perovskites. As a result, a broad range of properties will be brought by tuning the molecular formula and crystal structures symmetry.

The perovskite structures can be also distorted by *A* and/or *B*-cation substitutions, which are widely investigated to tune the properties of such materials. The substitution may alter the structure due to different sizes of the cations, while the substitution with non-isovalent cations gives rise to mixed-valence in the materials. Therefore, different properties from the parent compounds may take place with the substitution, as an example, the colossal magnetoresistance effects in $La_{1-x}Sr_xMnO_3$ [4]. As for multiferroic materials, for instance, trivalent, divalent or tetravalent cations (e.g. La, Ca, Sr and Ti) substitution or doping for *A* and *B*-sublattice in $BiFeO_3$ have been extensively investigated in order to improve the multiferroic properties [5-7].

An expanded unit cell, in addition to the simple perovskite structure ABO_3, may occur when more than two types of cations are present in one phase [8, 9]. It should be noted that when multiple cations are substituted into either the *A* or *B*-sites, these cations may be either randomly distributed or adopt an ordered configuration, where the ordering of the cations strongly depends on the differences of their charges and sizes. Double perovskites with the general formula $AA'B_2O_6$, for example, 1:1 *A*-site ordering can be represented by $CaFeTi_2O_6$ [10]. On the other hand, in $A_2BB'O_6$ double perovskites, 1:1 *B*-site ordering were observed in various materials

systems such as Sr_2FeMoO_6 [11], Bi_2FeCrO_6 [12], and Ba_2CrWO_6 [13]. Moreover, the combination of *A*- and *B*-site ordering give rise to unusual double perovskites materials in the form of $AA'BB'O_6$, which can be shown by $NaLaMgWO_6$ [14] and $KLaMnWO_6$ [15] as examples.

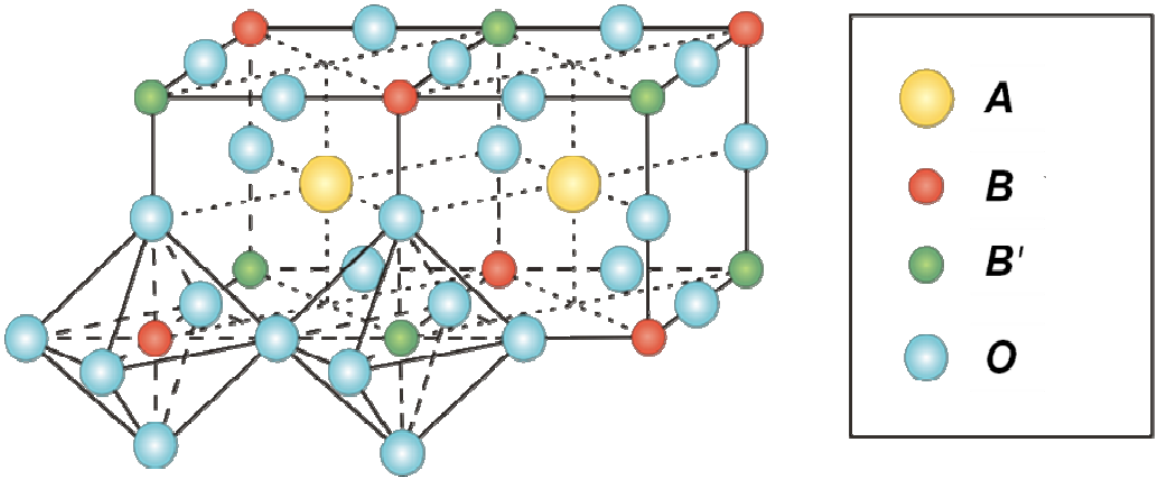

Figure 2. The schematic diagram of double perovskites structure of the general formula $A_2BB'O_6$ [16].

Among the most well-known realizations of multiple-perovskite structure is the double perovskites $A_2BB'O_6$ type by *B*-site aliovalent substitutions. $A_2BB'O_6$ possess a modified perovskite structure where the BO_6 and $B'O_6$ octahedra are alternatively arranged in two interleaving FCC sublattices. As shown in Figure 2, the *A* sites are occupied by alkaline or rare earth ions, while the *B* sites correspond to transition metal ions. Double perovskites $A_2BB'O_6$ materials have been shown intriguing novel physical characteristics (e.g. magnetic properties) resulting from the strong superexchange couplings between various combinations of 3*d*, 4*d* and 5*d* elements [9], making them as promising candidates for electronic devices such as spintronics.

1.1.2 Ferroelectricity

Since the discovery of ferroelectricity in single-crystal materials (Rochelle salt) in 1921 and its subsequent extension into the realm of polycrystalline ceramics (barium titanate, $BaTiO_3$) during

the early to mid-1940s, there has been a continuous succession of new materials and technology developments that have led to a significant number of industrial and commercial applications that can be directly credited to this most unusual phenomenon. Ferroelectrics are a class of materials with a permanent polar axis, and the polarization direction can be switched by applying an electric field. At temperatures above Curie temperature (T_C), the crystals are non-polar and no longer ferroelectric and behave like normal dielectrics. They are widely used for designing sensors, tunable capacitors, as well as ferroelectric random access memories (Fe-RAM) in which the information is stored by the remnant polarization [17, 18].

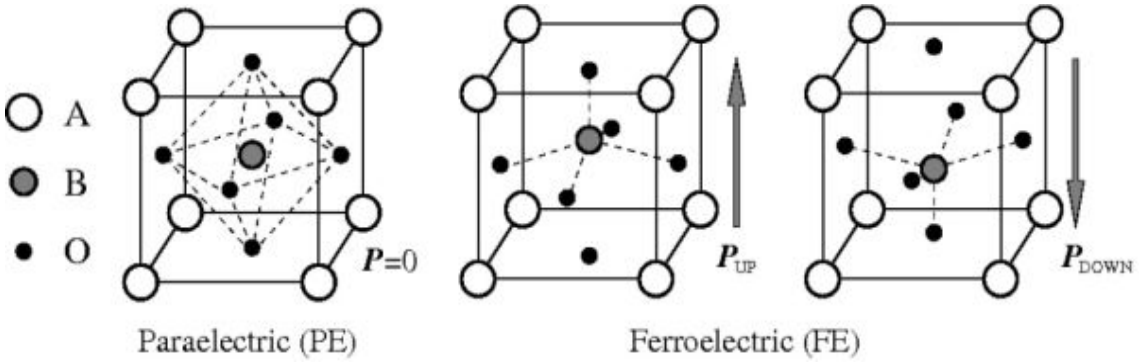

Figure 3. Atomic structures of perovskite oxides ABO_3 in the paraelectric phase and ferroelectric phase with upward and downward polarization [19].

Consider the typical perovskite with formula ABO_3 as an example, in which a central positive *B*-ion is surrounded by an octahedron of negatively charged oxygen ions (Figure 3). A shift in the position of the *B*-site ion would break the inversion symmetry and cause the induction of a dipole moment, giving rise to ferroelectric order. Such shifts can occur during structural phase transitions, in which the system moves from a high to low symmetry state (e.g. cubic to tetragonal). One of the best known examples of ferroelectric is $BaTiO_3$. In the majority of ferroelectric perovskites, the *B*-site atom has an empty *d* electron shell, which allows covalent bonding with the full *p* orbitals of the oxygen atoms. Ferroelectricity can also occur owing to the

existence of lone pairs of electrons on the outer shell of the *A*-site atom, which are highly susceptible to polarization. This is the cause of ferroelectricity in $BiFeO_3$, for example.

1.1.3 Magnetism

Ferromagnetism can be described as a collection of atomic spins that are all aligned with their magnetic moments in the same direction, causing a macroscopic net magnetic moment. The earliest magnetic material known to man is magnetite, a naturally occurring magnetic ceramic (ferrite). Pieces of this mineral were found to exert attractive or repulsive forces when brought close to another piece of the same material. Later, when iron objects became available, they were attracted to these earlier magnetic materials. The functional use of magnetic materials has a long history. The first description of the magnetic compass dates back to 1088 when Shen Kuo wrote about this navigational instrument in his Dream Pool Essay. Some recent examples are used for recording and storing data such as hard drive [20]. Apart from diamagnetism which arises in all substances with the application of an external magnetic field, the magnetic behavior of a material is caused by the presence of unpaired electrons. Magnetic properties are mainly exhibited by materials containing transition metals or lanthanides resulting from their partially filled *d* and *f* orbitals, respectively. When the moments in the material are oriented randomly, it is known as a paramagnet, in which the alignment of the moments can be achieved through the application of a magnetic field. A spontaneous magnetic ordering can be observed, however, when the interaction between unpaired electrons leads to alignments of electron spins.

Three main types of magnetic behaviors are given below and the diagrams of the alignments are schematically illustrated in Figure 4a-c. In ferromagnetic materials, the electron spins are oriented parallel to each other and giving an overall magnetic moment, as shown in Figure 4a.

When the moments on the neighboring atoms are aligned antiparallel and the magnetic moments are cancelled by each other, the ordering is antiferromagnetic (Figure 4b). A ferrimagnet possesses multiple types of magnetic ions and their magnetic moments may be aligned antiparallel, but a net magnetic moment occurs due to the unequal magnitudes (Figure 4c). Similar to simple ferrimagnetism, a residual magnetic moment exists in a canted antiferromagnet, which shows the almost antiparallel arrangement of the spins but with a canting angle (Figure 4d). The material is also known as a weak ferromagnet owing to the net magnetic components.

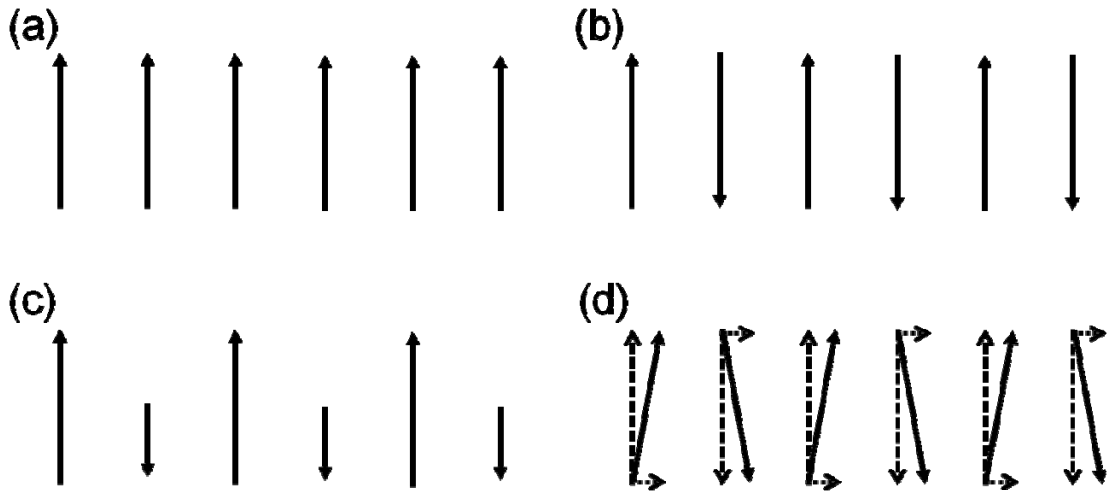

Figure 4. Schematic diagrams showing the spins of (a) ferromagnet, (b) antiferromagnet, (c) ferrimagnet and (d) canted antiferromagnetic, where the magnetic components in different directions are represented by dashed arrows.

1.1.4 Multiferroic Materials

Following a trend towards device miniaturization, modern technology has led to increasing interest in the integration of electronic and magnetic properties in a multifunctional device. The attempts to integrate ferromagnetic and ferroelectric properties into single materials can be traced back to 1960s. In the past few decades, multiferroics materials which exhibit more than one type of ferroic order (e.g. ferromagnetism and ferroelectricity) behaviors simultaneously became

significant for a basic understanding of the interaction between magnetic and electric coupling and immense potential for multifunctional applications [21-26]. In addition to the fascinating physical properties resulting from the independent existence of two or more ferroic order parameters in one material, the coupling between magnetic and electric properties named as magnetoelectric effect (as illustrated in Figure 5), gives rise to the possibility of manipulating electrical polarization and magnetization by applying a magnetic and electric field, respectively [27, 28]. This effect is very attractive for novel spintronic devices such as tunnelling magnetoresistance (TMR) sensors, spin valves with functionality that is tunable by an electric field, and multi-state memories in which data are written electrically and read magnetically.

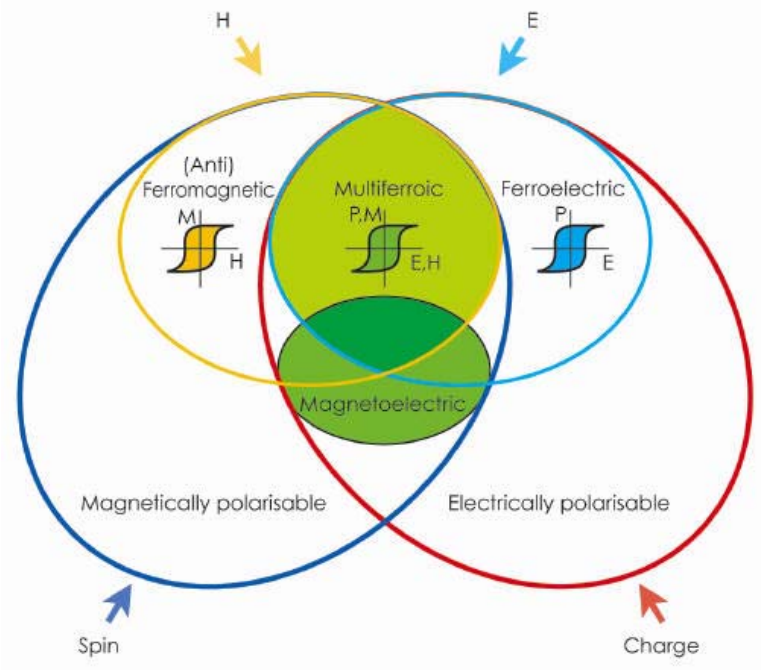

Figure 5. Portrayal of multiferroics possessing magnetic and ferroelectric properties [29].

Although ferromagnetism or ferroelectricity can be found in numerous systems, it is difficult to have intrinsic multiferroic materials, since the conditions for co-existence of magnetic and ferroelectric order are very stringent [29, 30]. This is because in most ferroelectrics, such as

$BaTiO_3$, the ferroelectricity is driven by a hybridization of empty *d* orbitals with occupied *p* orbitals of the octahedrally coordinated oxygen ions. This mechanism requires empty *d* orbitals and thus cannot lead to multiferroic behavior. There are consequently very few ferroelectrics that exhibit long range magnetic order, and rarer still are materials where these two disparate order parameters exist and exhibit significant coupling. Most of the actively studied multiferroics (shown in Figure 6) fall into a class of materials known as complex oxides [27]. Typical materials showing such properties are perovskite transition metal compounds including $TbMnO_3$ [31] and $HoMn_2O_5$ [32], as well as bismuth compounds like $BiFeO_3$ [24, 33, 34], $BiMnO_3$ [35, 36] and so on.

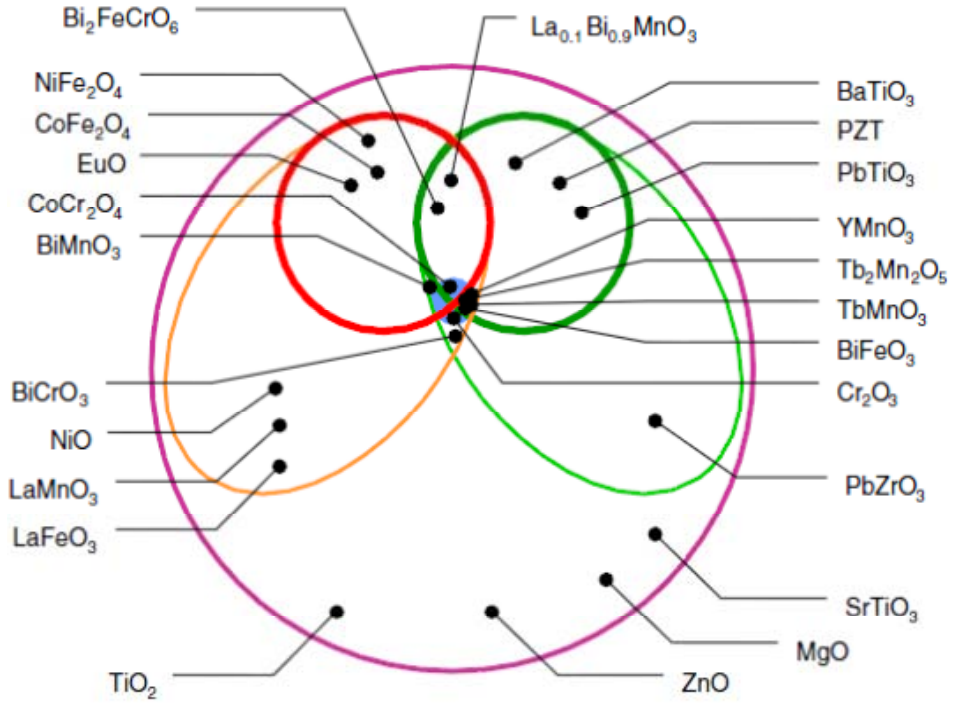

Figure 6. Classification of insulating oxides. The largest circle represents all insulating oxides among which one finds electrically polarizable materials (green ellipse) and magnetically polarizable materials (orange ellipse). Within each ellipse, the circle represents materials with a finite polarization (ferroelectrics) and/or a finite magnetization (ferro- and ferrimagnets). Depending on the definition, multiferroics correspond to the intersection between the ellipses or the circles. The small circle in the middle denotes systems exhibiting a magnetoelectric coupling [37]. PZT represents $PbZr_xTi_{1-x}O_3$.

Generally, single phase multiferroic materials can be categorized into two main groups depending on the origin of the ferroelectricity. The first class is proper (or type I) multiferroics where the ferroelectricity and the magnetic ordering occur for different reasons while are coupled together, and their critical temperatures of the magnetic and ferroelectric transitions can be well above room temperature. Unfortunately, generally in this class of materials, the coupling between magnetism and ferroelectricity is rather weak. This is because of the different origins of anti/ferromagnetic and ferroelectric orderings whereby ferromagnetism desires transition metals with unpaired *d* electrons and unfilled *d* orbital, whereas ferroelectric polarization requires transition metals with empty *d* orbitals. The well-known type-I multiferroic perovskites is exemplified by $BiFeO_3$ [24, 33, 34], $BiMnO_3$ [35, 36], and $PbVO_3$ [38]. The polarization in these materials is because of the *A*-cation lone pairs of Bi^{3+} or Pb^{2+} cations rather than transition metal cations. In these ions, there are two outer 6*s* electrons (lone pairs) that do not participate in chemical bonds. One more mechanism that can lead to ferroelectricity to type-I multiferroics can be charge ordering, often observed in transition metal compounds, especially those formally containing transition metal ions with different valence such as $Pr_{0.5}Ca_{0.5}MnO_3$ [39]. Another mechanism is derived from "geometric" ferroelectricity, which can be observed in $YMnO_3$ [40].

On the other hand, in improper (or type II) multiferroic materials, ferroelectricity can only exist in a magnetically ordered state and is caused by a particular type of magnetism. Usually type-II multiferroics can be divided into two groups in terms of the origin of ferroelectricity. For the first group, the ferroelectricity occurs with particular type of magnetic spiral or helicoidal structures that results from spin frustration, and both orders are deeply coupled. This is the case in $TbMnO_3$ [31], $TbMn_2O_5$ [32] and $Ni_3V_2O_8$ [41]. As for the second group, the ferroelectricity appears in collinear magnetic structures, in which all magnetic moments aligned along a

particular axis without the necessary involvement of the spin-orbit interaction. Polarization can appear in these materials as a consequence of exchange striction because the magnetic coupling varies with the atomic positions. This can be found in Ca_3CoMnO_6 [42], for example. Type II multiferroics are of fundamental interest but not of practical use nowadays due to their low critical parameters while the type-I represent the main area for future applications because of their relatively high Currie temperature.

1.2 $BiFeO_3$

As one of the most promising single-phase multiferroic materials, $BiFeO_3$ has been a focal point of research for the development of multifunctional devices because of its distinctive properties including high Currie temperature of ferroelectricity ($T_C \sim 1103$ K), high Néel temperature of antiferromagnetism ($T_N \sim 643$ K), lead-free piezoelectricity, and noteworthy photoelectric response in the visible range [24, 43, 44]. These features make $BiFeO_3$ particularly applicable in the fields of ferroelectrics, magnetics, piezoelectrics, and photovoltaic devices. In addition, the coupling of these properties may endow next generation electronic devices with multiple functionalities. The study of $BiFeO_3$ was started as early as 1950s. In 2003, the discovery of large remnant polarization, 15 times larger than that of previously obtained for the bulk samples (6.1 $\mu C/cm^2$), together with strong ferromagnetism measured in $BiFeO_3$ thin films by Ramesh' group [24], has led to the revival of research in this area and numerous other studies have been carried out on the bulk, thin film and nanostructured forms of $BiFeO_3$ materials since then.

1.2.1 Crystal Structure and Physical Properties of $BiFeO_3$

The atomic structure of $BiFeO_3$ was first determined by Michel *et al*. in 1969 [46]. Then in 1990 Kubel and Schmid carried out precise X-ray diffraction study on monodomain single crystals of

$BiFeO_3$ [47]. The structure of $BiFeO_3$ can be characterized by two distorted perovskite blocks connected along their body diagonal or the pseudocubic [111] direction, to build a rhombohedral unit cell (Figure 7). In this structure, the two oxygen octahedra of the cells connected along the [111] direction are rotated clockwise and counterclockwise around the [111] direction by ± 13.8(3)° and the Fe-ion is shifted by 0.135 Å along the same axis away from the oxygen octahedron center position. In $BiFeO_3$, the mismatched ion sizes result in tilted metal-oxygen octahedra. By using the Goldschmid tolerance formula (Eq. 1.1), the tolerance factor t = 0.88 was obtained. This results in a distorted Fe-O-Fe angle which is the most important factor to control both the magnetic exchange and the orbital overlap between Fe and O in $BiFeO_3$ crystals. The lattice parameters of its unit cell have been reported as a = 3.965 Å and a rhombohedral angel α = 89.3° at room temperature [24]. On the other hand, the unit cell can also be described as a hexagonal structure with the c-axis parallel to the diagonals of the perovskite cube, namely $[001]_{hex}//[111]_{pseudocubic}$. In this case, the lattice parameters have been reported as a_{hex} = 5.58 Å and c_{hex} = 13.89 Å.

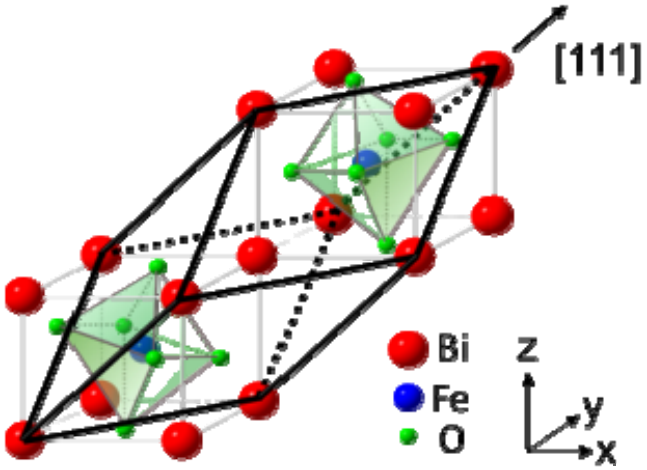

Figure 7. Schematic drawing of the crystal structure of perovskite $BiFeO_3$ (space group: $R3c$) [24]. Two unit cells along the [111] direction are shown in the figure.

$BiFeO_3$ exhibits excellent ferroelectric performance which is comparable to that of conventional ferroelectric materials such as $PrZr_xTi_{1-x}O_3$ at room temperature. The ferroelectricity of $BiFeO_3$ is ascribed to the lone pair $6s^2$ electrons of the Bi ions, which is similar to the case of $PbTiO_3$ [48]. Theoretically, the rhombohedral and tetragonal $BiFeO_3$ structures are expected to show spontaneous polarizations of ~100 $\mu C/cm^2$ in the [111] direction and ~150 $\mu C/cm^2$ in the [001] direction, respectively [49].

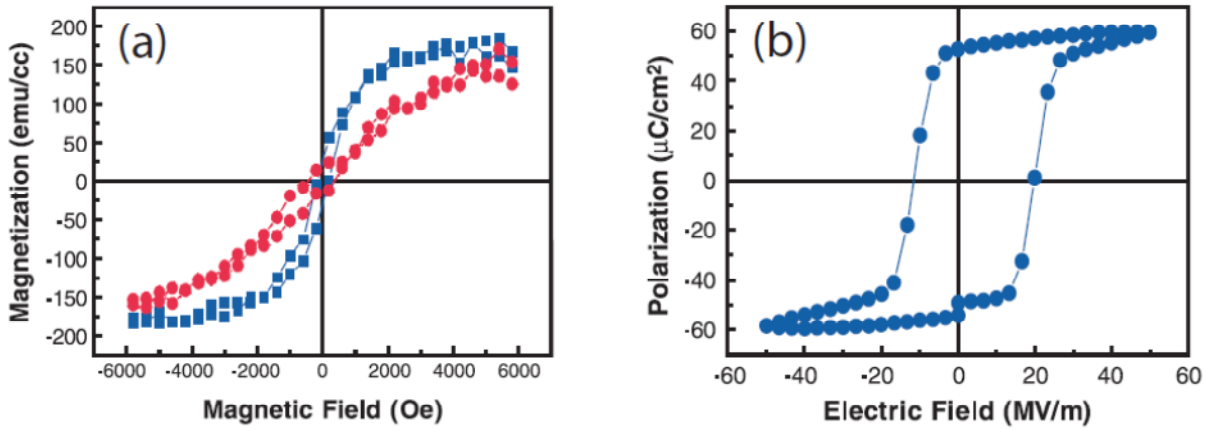

Figure 8. (a) Magnetic hysteresis loop for a $BiFeO_3$ film of 70 nm thickness (blue data is in plane, red data is out of plane of the film), and (b) electric hysteresis loop for a $BiFeO_3$ film of 200 nm thickness, measured at a frequency of 15 kHz. All data was measured at room temperature. Adapted from [24].

Measurement of the ferroelectricity of bulk $BiFeO_3$ can be traced back to the 1960s and 1970s [50, 51]. Only small values of the remnant polarization (P_r) can be obtained, even for a single crystal sample (6 $\mu C/cm^2$), and the current leakage which results in lack of saturation is likely to be the reason for this small P_r, as reported by Teague [51]. It took several decades for their prediction to be proven right by measurement on high-quality thin films, single crystals and ceramics of $BiFeO_3$. In 2003, Ramesh's group reported an unexpectedly large P_r in a $BiFeO_3$ thin film sample (Figure 8b) that was 15 times larger than previously seen in a bulk sample, on par with that of conventional ferroelectric materials such as $PbZr_xTi_{1-x}O_3$, which has enormously

stimulated the research on this material [24]. Subsequently, large spontaneous polarization has been confirmed in both high quality bulk and thin film samples [52-54], demonstrating that $BiFeO_3$ is favorable for use in Fe-RAM applications.

Magnetism in $BiFeO_3$ can be attributed to both short- and long-range orderings. In terms of local short-range ordering, $BiFeO_3$ is antiferromagnetic with a G-type spin configuration (Néel temperature of 643 K) [43, 55]; that is, one Fe^{3+} spin is surrounded by six antiparallel spins on the nearest neighboring Fe^{3+} ions (Figure 9). Due to the structural distortion, the arrangement of the neighboring spins is in fact not perfectly antiparallel. It was noted that if the moments were oriented perpendicular to the [111] polarization direction, the symmetry also permits a small canting of the antiferromagnetic sublattices of the Dzyaloshinskii-Moriya (DM) interaction, resulting in a local weak spontaneous magnetization.

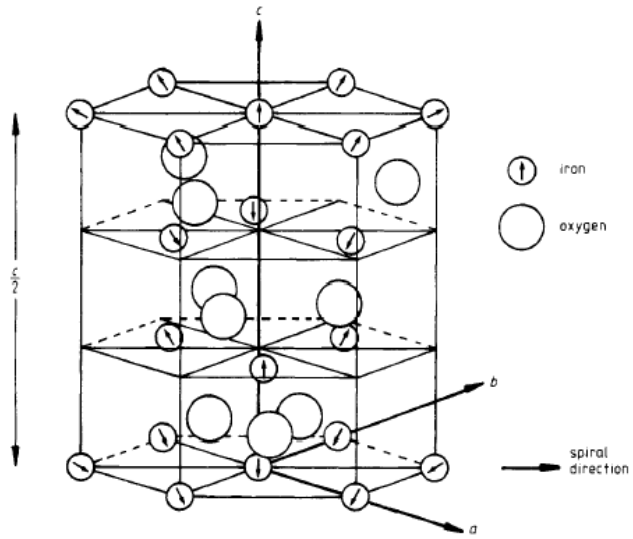

Figure 9. Portion of hexagonal $BiFeO_3$ lattice. The arrows indicate the Fe^{3+} moment direction [56].

This magnetization is macroscopically canceled by a spiral spin structure caused by the rotation of the antiferromagnetic axis through the crystal with an incommensurately long-wavelength period of 62-64 nm (Figure 10). This spiral spin structure might be suppressed in the

film form of $BiFeO_3$ and the resulting magnetic moment is caused by a weak ferromagnetism of 0.1 μ_B/Fe atom. The direction of the spin cycloid is along the [110] axis. The cycloidal model of spin ordering in $BiFeO_3$ was first proposed by Sosnowska in 1982 [56], and it was verified by various experimental data soon afterwards. Zalesskii and his co-workers proposed that the cycloid could become distorted at low temperature and the possible origin for these transitions is considered to be spin reorientation [57].

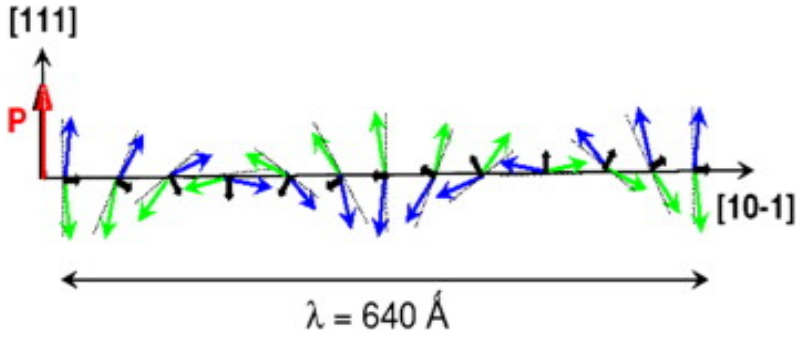

Figure 10. Schematic representation of the spin cycloid of $BiFeO_3$. The canted antiferromagnetic spins (blue and green arrows) give rise to a net magnetic moment (purple arrows) that is spatially averaged out to zero due to the cycloidal rotation. The spins are contained within the plane defined by the polarization vector (red) and the cycloidal propagation vector (black) [58].

Besides multiferroic properties of $BiFeO_3$ material that have been intensively studied previously, it also shows distinctive optical-related properties, which is expected to cross-correlate with the other physical properties. The details of the optical, photovoltaic and photocatalytic properties of $BiFeO_3$ materials have been relegated to a subsequent section 1.4.

1.2.2 $BiFeO_3$ Nanomaterials

In recent years, considerable interest has been attributed to multiferroic nanostructures in the quest of miniaturizing devices and discovering interesting fundamental physics at nanoscale. Moreover, for multiferroic nanostructures, the manners in which the properties scale with the

structure size as well as how the coupling behaves when size is decreased are critical for their potential application at the macroscopic scale. Realization of micro- and nanostructures of such multiferroic materials and their local characterization is desirable to answer fundamental questions about possible size effects of their functional properties (ferroelectric, ferromagnetic, optical and catalytic). The recent rapid development in the synthesis of $BiFeO_3$ nanomaterials provides great opportunities to study the fundamental physical properties at nanoscale. $BiFeO_3$ materials, including zero dimensional (0D, such as nanoparticles), one dimensional (1D, including nanowires, nanofibers, nanorods and nanotubes) and two dimensional (2D, such as nanoplates and thin films) nanostructures can be synthesized. We will introduce by two subsections: (1) the current deposition techniques of $BiFeO_3$ thin film and the synthesis methods of low-dimensional $BiFeO_3$ nanostructures; (2) size effects on the physical properties of $BiFeO_3$ nanostructures.

1.2.2.1 Synthesis of $BiFeO_3$ Thin Films and Nanostructures

Great strides have been made in the production of nanostructures and thin films form of $BiFeO_3$ materials in the last few decades. Most of the efforts have been made in understanding the structure, properties, and growth of thin films of $BiFeO_3$. High quality epitaxial $BiFeO_3$ films have been grown via various methods including pulsed laser deposition (PLD) [59, 60], radio-frequency (RF) sputtering [61], metal organic chemical vapor deposition (MOCVD) [62], and chemical solution deposition (CSD) [63] on a wide range of substrates including traditional oxide substrates as well as Si and GaN.

More recently, numerous reports have described the synthesis of $BiFeO_3$ nanomaterials by various routes that involve hydrothermal/solvothermal method [64, 65], rapid molten salt

sintering [66], mechanochemical synthesis [67], sol-gel method [68, 69], wet chemistry [70], and electrospinning [71]. Meanwhile, the reported synthesis approaches have been proposed to develop low-dimensional substrate-free $BiFeO_3$ nanostructures with various sizes and shapes such as nanoparticles [69], nanotubes [72, 73], nanowires [74, 75], nanorods [76], nanofibers [77, 78], nanospindles [79], nano-/micro cubes [80, 81] and hollow spheres [82], offering great possibilities to study their ferroelectric, magnetic and optical behaviors at nanoscale.

1.2.2.2 Size Effects in $BiFeO_3$ Nanostructures

Nanomaterials are known to exhibit significant property differences as compared to their bulk counterparts. In recent years, interesting properties that are quite different compared to the bulk form of $BiFeO_3$ have been found in nanostructured $BiFeO_3$ materials due to the nanosize effects. In terms of crystal structure, a deviation of the lattice parameters from their bulk values has been observed as the size of $BiFeO_3$ nanoparticle decreases. It was found that the rhombohedral distortion of the unit cell of $BiFeO_3$ decreases and the structure approaches cubic perovskite [83]. Meanwhile, some distinct phenomena in $BiFeO_3$ are associated with size effect [84, 85]. For example, the Néel temperature of $BiFeO_3$ has been shown to decrease with decreasing particle size, namely T_N drops from 643 K in bulk samples to approximately 550 K in particles of ~5 nm in size [83]. Curie temperature has been also shown to decrease with decreasing particle size [84].

As for ferroelectric properties, structural parameters have been used to evaluate the size dependence of the spontaneous polarization (P_s). For example, Selbach *et al*. estimated P_s from the relative displacement of Bi and Fe cations and found a decrease of polarization with decreasing particle size down to approximately 75% of the bulk value for 13 nm particles, and a critical size for ferroelectricity of about 9 nm was estimated from the size dependence of the

pseudotetragonality (c/a) [83]. On the other hand, Goswami *et al*. [86] reported that the net unit cell polarization decreases with a reduction of particle size from 28 to 19 nm, but it attained much higher values than what has been observed in bulk samples or even in thin films. Theoretical calculations also predicted an enhancement of the polarization in nanoparticles in comparison to the bulk case [87].

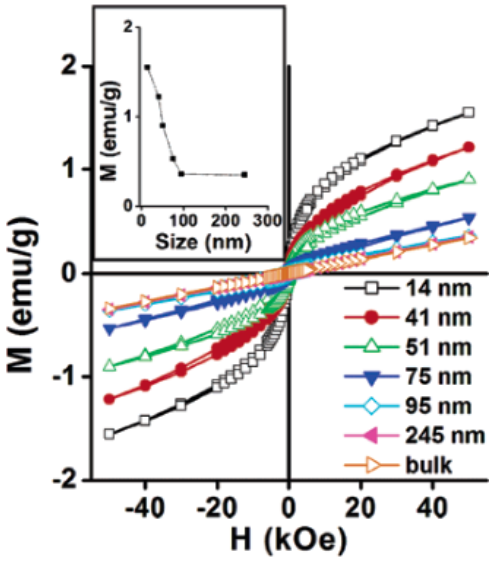

Figure 11. *M-H* hysteresis loops of $BiFeO_3$ nanoparticles with various sizes at room temperature [69].

The magnetic structure of $BiFeO_3$ is G-type antiferromagnetic, and the combined action of exchange and spin-orbit interactions produces spin canting away from perfect antiferromagnetic ordering, resulting in a spiral spin arrangement with a wavelength of about 62 nm, and thereby producing a helimagnetic order and a vanishing magnetization in the bulk [55, 88]. However, weak ferromagnetism was observed in thin films, which has been related to the destruction of the spiral modulated structure by epitaxial strain [24, 89]. The nanostructures of $BiFeO_3$ including nanoparticles [69, 90], nanotubes [72] and nanowires [75] also showed enhanced magnetization correlated with the decreasing of the size. The magnetic response was found to increase as the size of $BiFeO_3$ nanoparticles decreases [69] (Figure 11). This could be attributed to surface-

induced magnetization due to the uncompensated surface spins, an increase in spin canting due to lattice strain in the nanocrystals, ferromagnetism caused by an apparent oxygen deficiency, or an incomplete spiral of magnetic order in particles of size less than 62 nm [84].

1.3 Bi_2FeCrO_6

In most simple perovskite (ABO_3) materials, the antiferromagnetic superexchange interaction is induced between the same TM ion orbitals (t_{2g} or e_g) via their overlapping with oxygen ion orbitals (pπ or pσ) in a *B*-O-*B* (almost) linear arrangement according to the Kanamori-Goodenough (KG) rules [91, 92]. Therefore, double perovskites oxides with general formula $A_2BB'O_6$ are needed, where there are two different 3*d* TM ions (*B* and *B*') giving rise to an intrinsic strong ferromagnetic interaction. According to the KG rules, ferromagnetism appears when one TM ion with e_g electrons (*B*) and another without e_g electrons (*B*') are ordered (*B*-O-*B*') in a rock-salt manner at the *B*-sites of the perovskite structure.

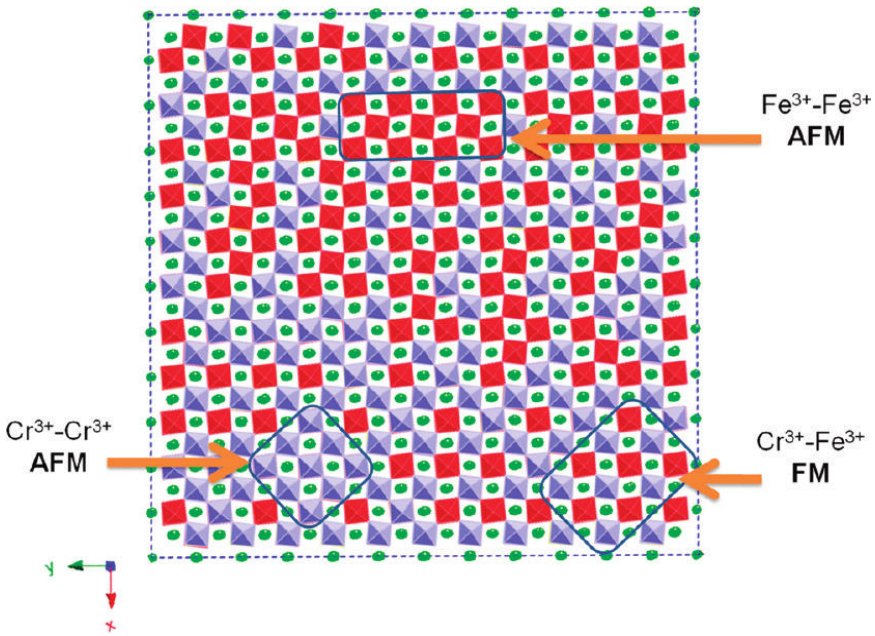

Figure 12. Magnetic microdomains in double perovskites $A_2BB'O_6$ materials, where Fe^{3+} and Cr^{3+} are located in the *B* and *B*' sites [93].

As an example, when the *B and B′* sites are occupied by Fe^{3+} and Cr^{3+} respectively and ordered in an adequate way (Figure 12), a nonconducting ferromagnetic material would be produced because of the superexchange interactions between these cations, with following electronic configurations, $t_{2g}^3e_g^2$ (Fe^{3+}) and $t_{2g}^3e_g^0$ (Cr^{3+}), respectively. This strategy has also resulted in other double perovskites oxides such as La_2MMnO_6 (M = Co, Ni) [94, 95] and Bi_2MMnO_6 (M = Ni, Fe, Co) [96-98].

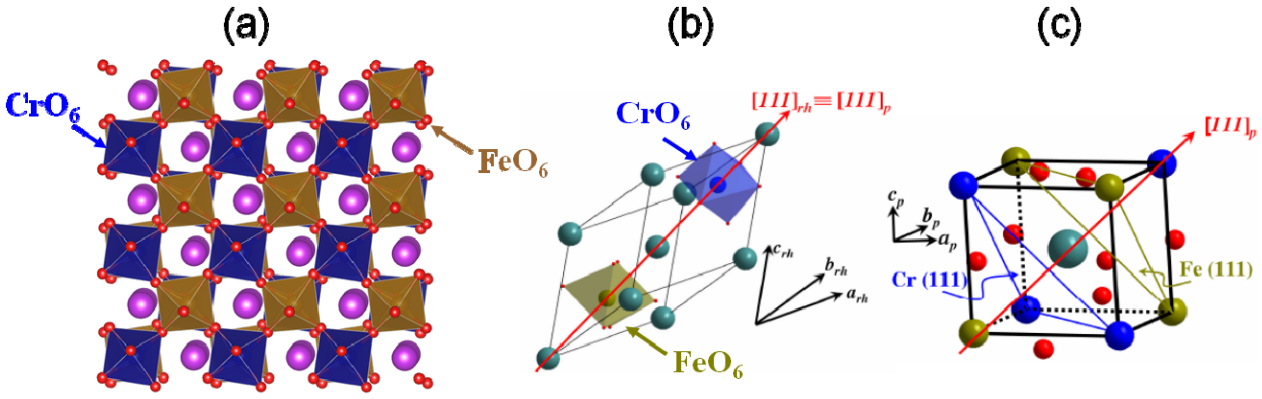

Figure 13. (a, b) Sketch of the double-perovskite crystal structure and (c) corresponding pseudo-cubic unit cell of Bi_2FeCrO_6. Adapted from [101].

It is well understood now that for ferroelectricity and magnetism to coexist in a single phase, the atoms that move off centre to form the electric dipole moment (i.e., ferroelectric polarization) should be different from those that carry the magnetic moment (i.e., magnetization). As predicted by first-principles calculations [99, 100], the particular double perovskites structure of Bi_2FeCrO_6 was introduced to circumvent the typical difficulties associated with the fabrication of robustly insulating ferromagnets, which are at the origin of the scarcity of multiferroic materials. In the predicted Bi_2FeCrO_6 material, ferroelectricity is due to the $6s^2$ lone pair on Bi^{3+} ions, a well-established mechanism in other multiferroics, such as $BiMnO_3$ and $BiFeO_3$, while magnetism is introduced via ferrimagnetic behaviour. The coupling between neighboring Cr and

Fe magnetic moments is robustly antiferromagnetic, and the difference between their magnetizations yields a net magnetization for Bi_2FeCrO_6. According to the authors, the hypothetical double perovskites Bi_2FeCrO_6, where Fe^{3+}/Cr^{3+} should be long-range-ordered (Figure 13), would have a magnetic moment of ~2 μ_B per formula unit (~160 emu/cm^3) at 110 K resulting from the antiferromagnetic exchange interaction between 5*d* Fe^{3+} and 3*d* Cr^{3+} with 5 μ_B per Fe^{3+} and 3 μ_B per Cr^{3+} in opposite directions and a ferroelectric polarization of ~80 $\mu C/cm^2$.

1.3.1 Synthesis and Characterizations of Bi_2FeCrO_6

Bi_2FeCrO_6 double perovskites compound with long range *B*-site cation order is not likely to form since Fe^{3+} (r = 0.645 Å) and Cr^{3+} (r = 0.615 Å) have the same valence state and closer ionic radii. Thus, Bi_2FeCrO_6 is expected to adopt a simple perovskite structure with random occupancy of Fe^{3+} and Cr^{3+} on the *B*-site. Nevertheless, a number of attempts have been undertaken to synthesize Bi_2FeCrO_6 with an ordered double perovskites structure. Experimental results confirmed that $Bi(Fe,Cr)O_3$ in ceramic form as well as epitaxial thin films are isostructural to $BiFeO_3$ with a rhombohedral distortion [102, 103]. They reported excellent ferroelectric properties for Bi_2FeCrO_6 with a polarization of ~55 $\mu C/cm^2$, while a small magnetization at room temperature was observed. This is due to the lack of Fe/Cr cation ordering along the [111] cubic direction in the samples. Nechache *et al*. [104] first reported the successful synthesis of ferrimagnetic-ferroelectric epitaxial Bi_2FeCrO_6 thin film using PLD, and the experimental measurements revealed strong ferroelectric polarization with Curie temperature well above room temperature and ferrimagnetic properties, in agreement with the theoretical predictions. Subsequently, both thin film and nanostructured form of $Bi(Fe,Cr)O_3$ materials have attracted considerable attention by several groups [105-108].

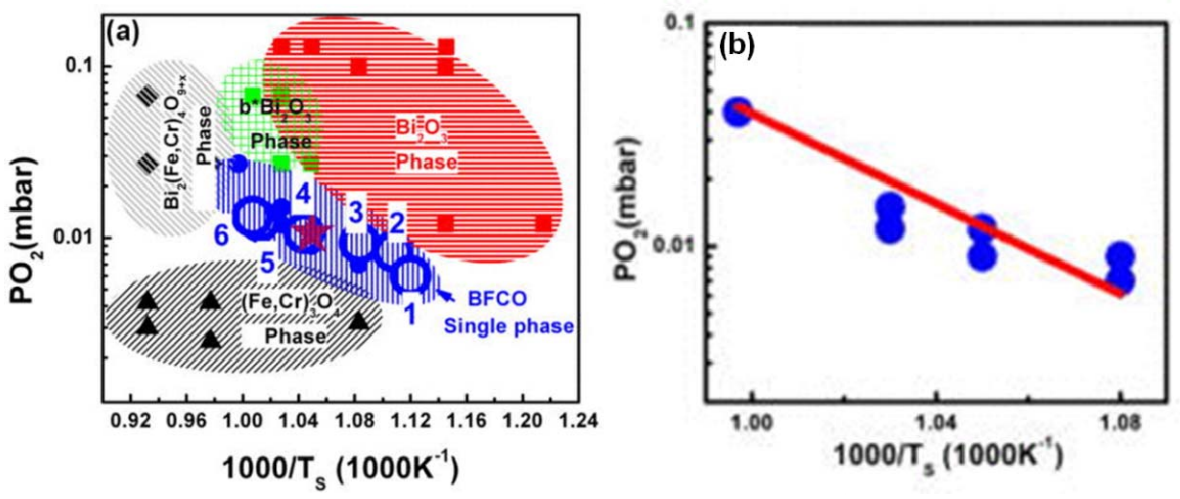

Figure 14. (a) Pressure-temperature phase diagram for thin films of the Bi-Fe-Cr-O system with a nominal thickness of 90 nm. (b) Oxygen pressure-substrate temperature data points in the phase diagram for which pure phase Bi_2FeCrO_6 films are obtained together with the vapour pressure curve of metallic Bi drawn in the same diagram [109].

Among all methods reported until now, PLD is one of the most suitable techniques to grow complex oxides such as Bi_2FeCrO_6, allowing the modification of their properties by strain engineering. Bi_2FeCrO_6 films with different thicknesses were deposited by PLD on various substrates including (100) and (111)-oriented $SrTiO_3$ (STO), MgO (100) and SiO_2 coated Si (100). The films can be synthesized under oxygen atmospheres in the pressure range of 5 to 20 mTorr at substrate temperatures ranging from 575 to 675°C [12, 101, 109]. As usual with the deposition of Bi-based compounds [110], the high volatility of Bi brings complexity to the pressure-temperature phase diagram and makes the optimization process of growing Bi_2FeCrO_6 single crystal film a difficult task. The Bi_2FeCrO_6 single phase can be obtained only in a narrow window, around 1.2×10^{-2} mbar and 680°C. Several elements point toward a relationship between nonstoichiometry (i.e., defects oxygen and cation vacancies) and the destabilization of the Bi_2FeCrO_6 single phase. The analysis of the various phase formation under different growth conditions is graphically summarized in the phase diagram presented in Figure 14.

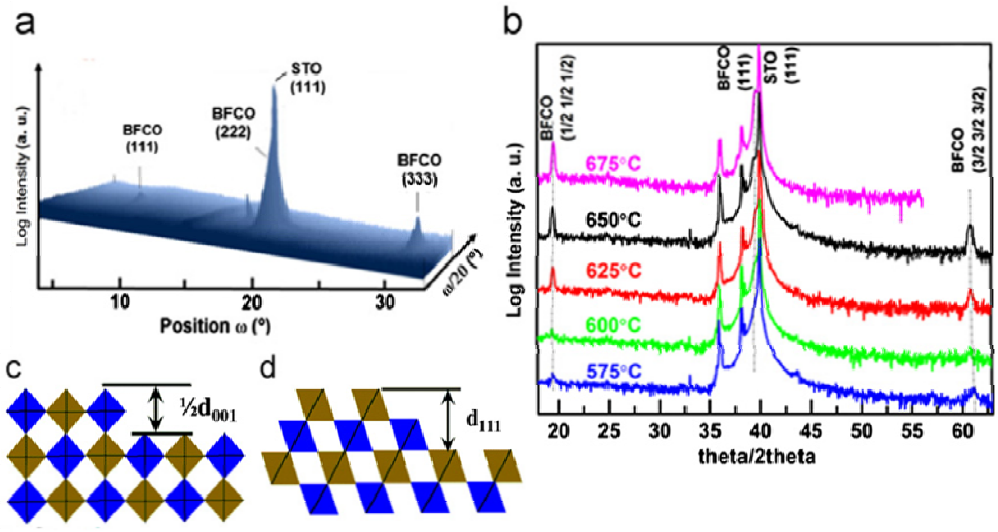

Figure 15. (a) RSM scan around (111) reflection recorded for (001) oriented Bi_2FeCrO_6 films. (b) $\theta/2\theta$ XRD scans of Bi_2FeCrO_6 thin films on $SrTiO_3$ (111) at different growth temperatures. Different types of Fe and Cr octahedral stacking in Bi_2FeCrO_6 along (c) the [001] and (d) the [111] cubic directions. Adapted from [101].

Since the Fe/Cr cation ordering plays an important role in establishing a strong magnetism in Bi_2FeCrO_6, the evidence of its existence in the films is a crucial step to understand the functional properties of this material. Several experimental approaches were used to demonstrate the presence of the Fe/Cr ordering and to quantify it in the films. As seen from different types of stacking in Figure 15c and d, the alternation of FeO_6 and CrO_6 planes is achieved only in the [111] cubic direction. Following the extinction rules in the double perovskites structure, the superstructure reflections (00*l*) where *l* is an even integer number are not visible in the (001)-oriented Bi_2FeCrO_6 thin films.

To observe the superstructure peaks in the (001)-oriented films, Nechache *et al.* [12] performed a large scan of the reciprocal space mapping (RSM) around the (111) cubic reflection of the $SrTiO_3$. The RSM map in Figure 15a reveals the existence of two extra spots in addition to the (111) main reflection of $SrTiO_3$ and Bi_2FeCrO_6. The periodicity of the superstructure

reflections is about 4.58 Å, which is double of the (111) perovskite cubic distance Bi_2FeCrO_6 $d_{½ ½ ½}/2 \approx SrTiO_3$ d_{111} (2.28 Å). This doubling of the perovskite unit cell suggests the existence of the Fe/Cr ordering in the films along [111] crystal structure (Figure 15d), in agreement with the predicted rhombohedral Bi_2FeCrO_6 structure.

1.3.2 Multiferroic Properties of Bi_2FeCrO_6

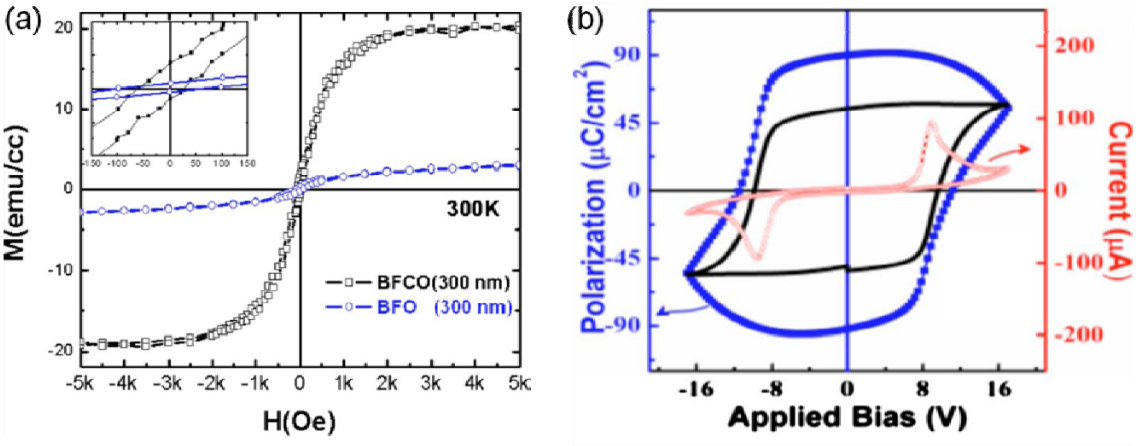

Figure 16. (a) Magnetization hysteresis of Bi_2FeCrO_6 film compared to that of $BiFeO_3$ film at room temperature. The direction of applied magnetic field *H* was in the plane of the films. (b) Current *vs*. applied voltage curve and the corresponding ferroelectric hysteresis loop and obtained at room temperature for a 200 nm thick Bi_2FeCrO_6 thin film. The solid line corresponds to the polarization hysteresis loop after subtracting the leakage contribution. Adapted from [104, 109].

The most striking characteristic of epitaxial Bi_2FeCrO_6 films is their good magnetic properties at room temperature. The observed hysteresis loop clearly indicates the presence of an ordered magnetic phase (Figure 16a). The very different magnetic properties of Bi_2FeCrO_6 with respect to $BiFeO_3$, despite a similar structure, can be explained by antiferromagnetic exchange interaction between 5*d* Fe^{3+} and 3*d* Cr^{3+} with 5 μ_B per Fe^{3+} and 3 μ_B per Cr^{3+} in opposite directions, as we discussed above. Epitaxial Bi_2FeCrO_6 films have a measured maximum magnetization of 1.9 μ_B per Fe-Cr pair, which partially confirmed the prediction by Baettig's

predictions [99, 100]. The reported Bi_2FeCrO_6 thin films possess a remnant polarization of about 55 $\mu C/cm^2$ (Figure 16b) along the [001] pseudocubic direction, similar with that of $BiFeO_3$, resulting from the $6s^2$ lone pair on Bi^{3+} ions.

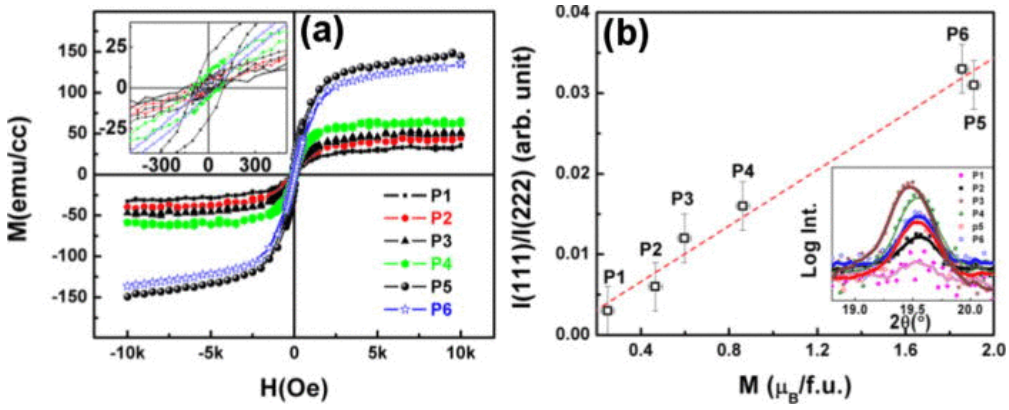

Figure 17. (a) Magnetic hysteresis loops of various Bi_2FeCrO_6 thin films prepared with different deposition conditions but all prepared with deposition conditions within the phase diagram region where single phase Bi_2FeCrO_6 is obtained, as indicated by the open circles labelled P1 to P6 in the phase diagram (Fig. 14a). The inset shows an enlarged figure. (b) Relationship between the degree of ordering in Fe/Cr estimated from the I_{111}/I_{222} ratio and the saturated magnetization measured at room temperature (Applied magnetic field is in-plane). The inset shows RSM-extracted profile lines around the (111) superstructure reflection obtained for the different films [109].

The relationship between the degree of Fe/Cr cationic ordering and the magnetization of the Bi_2FeCrO_6 films has been also investigated. As shown in Figure 17, it was found that even though all the films are pure phase Bi_2FeCrO_6, their magnetic hysteresis and saturation magnetization (M_s) varied significantly. For all the films, the RSM study around the (111) $SrTiO_3$ cubic reflection revealed the presence of the superlattice reflections (111) and (333), indicating a clear *B*-site ordering in the doubled perovskite unit cell. It is clearly seen that the increase of M_s is very strongly correlated with the increase in the degree of *B*-site cation ordering. This relationship between the magnetization and the degree of *B*-site ordering observed in Bi_2FeCrO_6 films can be explained by a ferro/ferrimagnetic coupling within Fe-O-Cr structure [109].

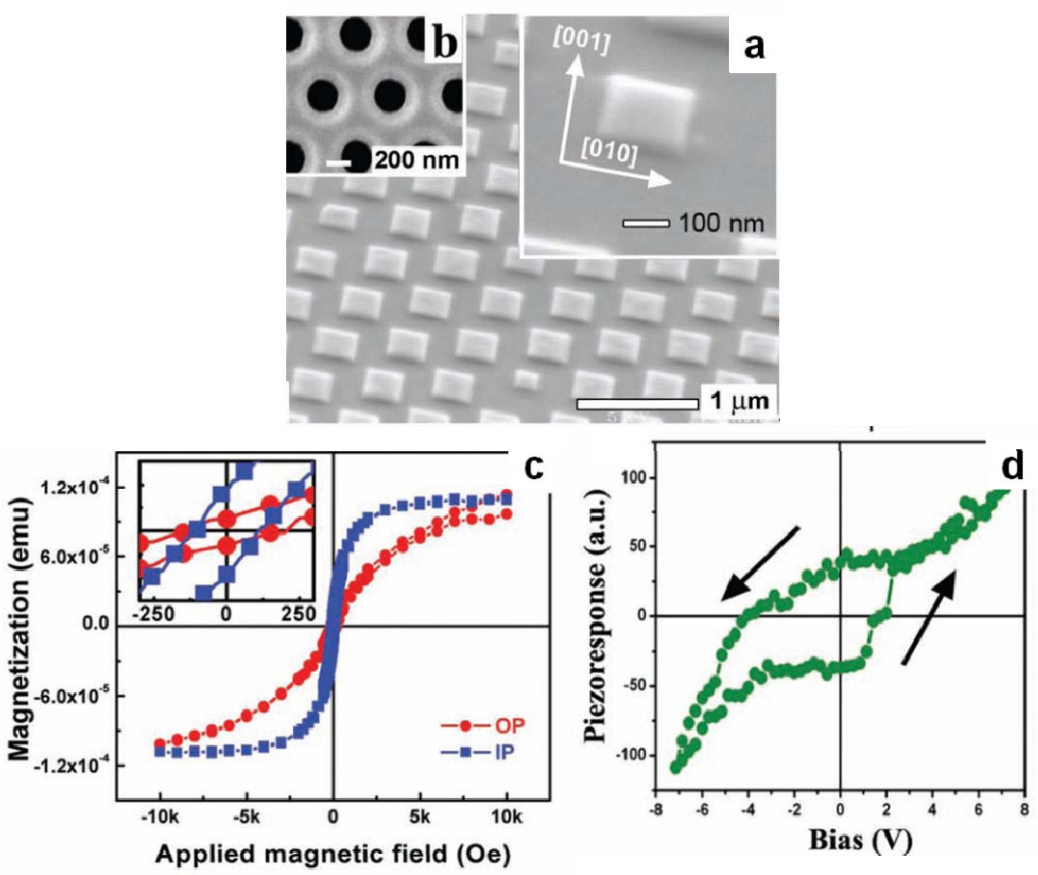

Figure 18. (a) SEM image showing a well-defined array of square Bi_2FeCrO_6 nanostructures. (b) SEM image of a typical Si_3N_4 membrane nanostencil. (c) In plane (IP) and out of plane (OP) magnetic hysteresis loops for the whole patterned area of Bi_2FeCrO_6 structures at room temperature. (d) Piezoresponse hysteresis loop recorded from an individual Bi_2FeCrO_6 island in OP-PFM mode. Adapted from [111].

More recently, ordered arrays of sub-micrometer Bi_2FeCrO_6 multiferroic structures have been deposited on Nb-doped $SrTiO_3$ substrates by PLD through a nanostencil [111]. It is reported that the as grown Bi_2FeCrO_6 patterns retain room temperature multiferroic (ferroelectric and magnetic) characters even at submicrometer dimensions, as shown in Figure 18c and d. In addition, nanoscale ultrathin Bi_2FeCrO_6 films have been reported by controlling the growth mode by either tuning PLD deposition parameters or using a buffer layer [106]. The local piezoelectric measurements showed that the ferroelectric character of Bi_2FeCrO_6 persists even at

nanoscale size (thickness of the film is ~2.5 nm). The coexistence of these properties in the ultrathin films and sub-micrometer patterns of low dimensional Bi_2FeCrO_6 materials pave the way to design novel device concepts for spintronic and electronic applications, such as ferroelectric tunnel junctions or magnetic tunnel junctions with ferroelectric barriers.

Moreover, Nechache *et al*. [112] later reported the direct observation of local electronic and magnetic properties of those Bi_2FeCrO_6 nanostructures by element-specific polarized x-ray techniques. Sizable magnetic ordering in the remanent state is observed at room temperature for both Fe and Cr ions. These results suggest a coexistence of antiferromagnetic and ferromagnetic superexchange interaction between Fe and Cr spins in the nanostructures at room temperature.

1.4 Multiferroic Materials for Solar Energy Conversion

The rapid increase in energy supply demands of the modern society, combined with the negative environmental impacts of fossil fuel combustion and quick depletion of natural resources in a foreseeable future, have urged us to explore alternative clean energy sources and energy efficiency technologies. Among the renewable sources of energy available on earth such as mechanical, heat and solar energies, the solar flux is the most fascinating one as it can provide by far the largest source with an average incident energy flux which is on the order of 10^4 times larger than the total global power consumption. Although the harvesting and storage techniques of solar energy are attractive and promising to tackle the energy shortage and corresponding environmental pollution problems, the implementation of solar energy technologies has been limited by high costs, low efficiency and resource intermittency issues. Accordingly, tremendous researches have been focused on conversion and storage of solar energy, with an emphasis on increasing efficiency and reducing manufacturing costs.

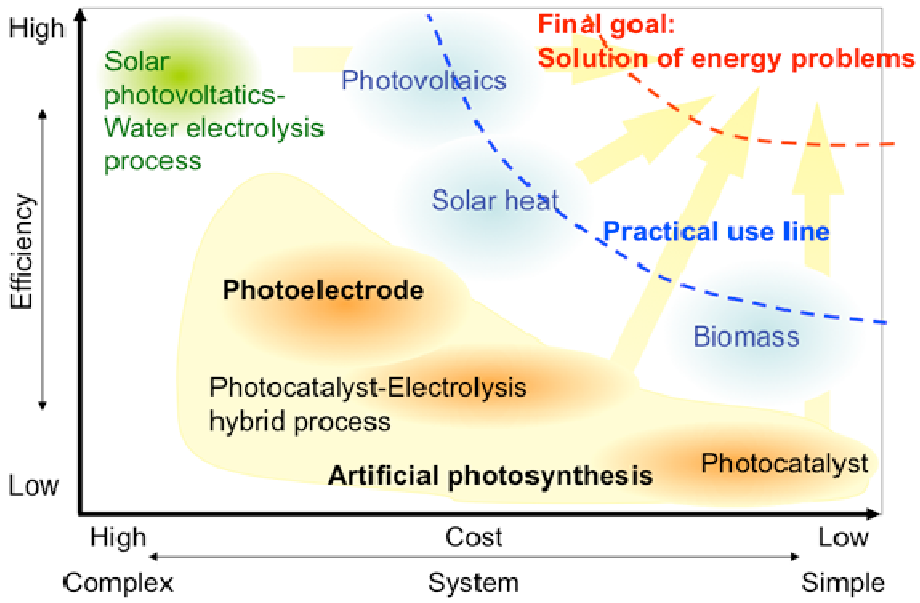

Figure 19. Comparison of various solar energy conversion technologies [113].

Basically, solar energy can be harvested in the form of biomass, heat, chemical energy and electricity, as shown in Figure 19. Compared with the energy conversion efficiencies into biomass and heat (commonly ~0.3% and 20%), conversion of sunlight directly into electricity has the highest theoretical efficiency and flexibility [114]. Therefore, there is a great potential for us to explore techniques to convert solar energy in the form of electricity such as PVs. On the other hand, photocatalytic water splitting with semiconductor materials has been investigated as a clean and renewable process for directly converting sunlight into chemical energy. In this way, the solar energy is harvested and stored in the form of molecular bonds. Compared to solar electricity, the use of chemical bonds to store solar energy promises significantly reduced device fabrication cost, as well as the cost associated with energy storage. We will discuss these two ways of converting solar energy with particularly focus on multiferroic materials in the following parts.

1.4.1 Multiferroic Materials for Photovoltaic Applications

1.4.1.1 Basics of Photovoltaics

Photovoltaic (PV) cells, also known as solar cells, are used to directly harvest the solar energy by converting the incident photons from solar radiation into flowing free charge carriers and thus producing electricity. However, after decades of development, the commercialized crystalline silicon solar panels are still expensive to compete with fossil energy. While silicon wafer devices have been the dominant solar cell type, novel PV materials are being explored in pursuit of improved efficiency and low cost. For examples, polycrystalline-Si (p-Si), amorphous-Si (a-Si) [115], Cu(In,Ga)Se_2 (CIGS) [116] and CdTe/CdS [117] thin film cells have been studied as the second generation solar devices. Solar cells made of III-V semiconductor compounds have the potential for high efficiency. Meanwhile, PV cells based on new concept have been designed and investigated such as dye-sensitized solar cells (DSSC) and polymer-based cells (including organic/inorganic hybrids) [118]. Particularly, tremendous research activity has focused on nanostructures [119], quantum dots [120], and perovskite materials [121, 122] based PV devices recently, which showed promising prospect for enhancing the conversion efficiency of solar cells.

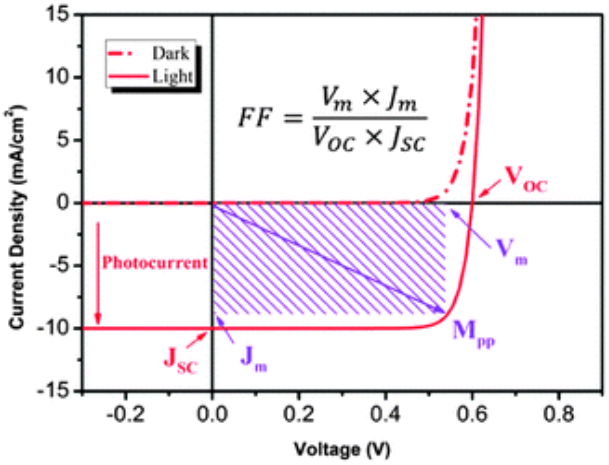

Figure 20. Typical current-voltage (*I-V*) curve of a solar cell with and without illumination [122].

The power conversion efficiency (PCE, η) of a solar cell, defined by the electric energy output divided by the solar energy it absorbs, is expressed as:

$$\eta = \frac{P_{\text{out}}}{P_{\text{in}}} * 100\% = \left(\frac{FF * J_{\text{sc}} * V_{\text{oc}}}{P_{\text{in}}}\right) \qquad \text{(Eq. 1.2)}$$

where J_{sc} is the short circuit current density, V_{oc} is the open circuit voltage, and FF is the fill factor, which is the ratio of maximum obtainable power to the product of the V_{oc} and J_{sc}, as illustrated in Figure 20. In designing efficient solar cell, we have to consider and put effort to make those four parameters J_{sc}, V_{oc}, FF and η as optimum as possible.

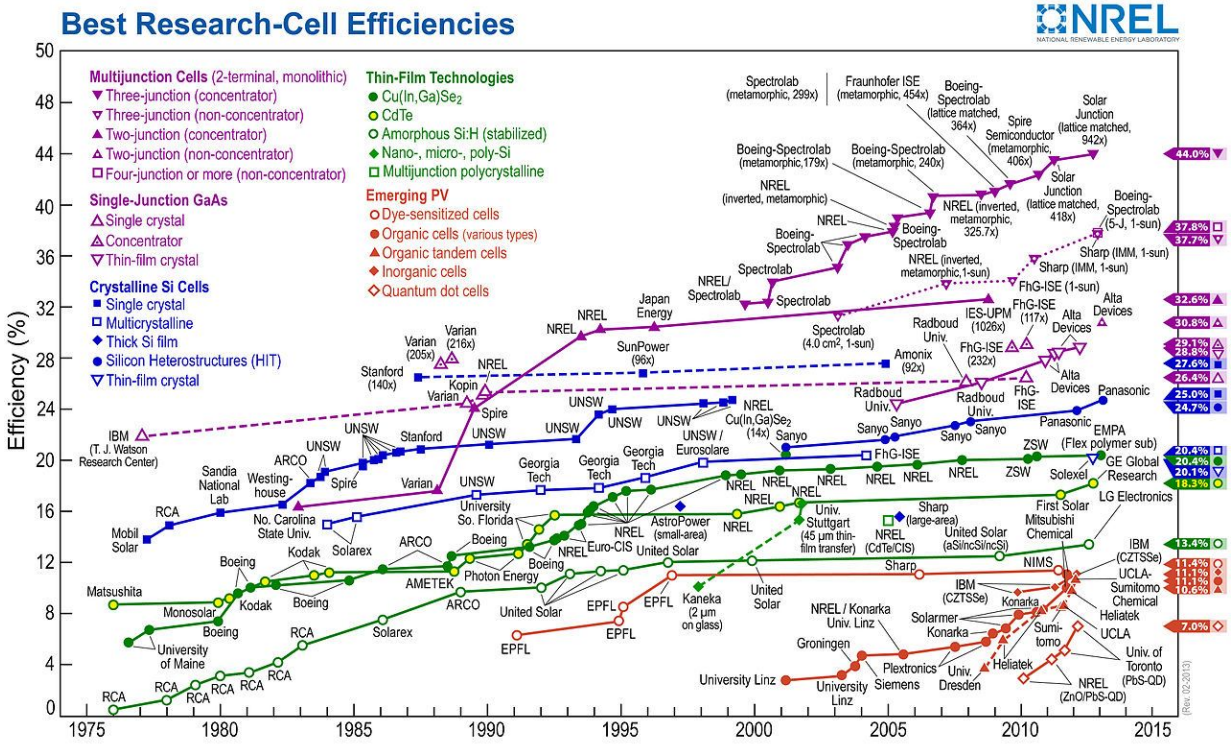

Figure 21. NREL compilation of best research solar cell efficiencies [123].

PV effects typically involve two basic processes: the generation and the separation of e^-/h^+ pairs. In the most commonly used semiconductor-based PV materials, such as silicon solar cells, the electric field at the space charge region of a *p-n* junction or Schottky barrier plays the

function of separating the charge carrier. Solar cell output performance depends on several factors including quantum efficiency of generation of carriers, effectiveness of separation of carriers before recombination, and collection of the separated carriers. In order to improve solar cell efficiencies, many aspects could be considered which can be categorized as follows: high absorption coefficient (> 10^5/cm), narrow band gap (~ 1.5 eV), high electron-hole pair generation rate, high quantum efficiency, long diffusion length of charge carriers, low recombination velocity, and high charge mobility. The chart of current best PCE solar cells is shown in Figure 21.

1.4.1.2 Bulk Photovoltaic Effect in Ferroelectrics

Ferroelectric materials are currently explored as an alternative pathway to achieve light into electricity conversion for PV applications. The bulk photovoltaic effect (BPVE) observed in ferroelectric materials has regained attention due to its potential for optoelectronics, energy conversion, and optical information storage. BPVE was discovered about half a century ago in non-centrosymmetric crystals [124], and was subsequently found in a variety of ferroelectric materials including $BaTO_3$ [125], $LiNbO_3$ [126] and $PbZr_xTi_{1-x}O_3$ [127-129], in which a steady PV response (photovoltage and photocurrent) can be generated along the polarization direction.

Among next generation PV technologies, ferroelectric PV effect is completely different from the traditional *p-n* junction PV effect as shown in Figure 22. In traditional *p-n* junction solar cells (Figure 22a), the absorbed photons can pump the electrons from the valence band of a light absorbing semiconductor material to its conduction band, with holes left in the valence band. The photogenerated electrons and holes are quickly separated by the built-in electric field inside the *p-n* junction and collected by the respective electrodes. Theoretically, the magnitude of

V_{oc} in *p-n* junction solar cells is determined by the quasi-Fermi energy difference of photogenerated electrons and holes which is limited by the band gap of the light absorbing semiconductors. Nevertheless, for the BPVE devices (Figure 22b), photocurrent can flow in a uniform ferroelectric material without forming interface or complex structures (i.e. *p-n* junction) driven by the ferroelectric polarization-induced internal electric field. Under homogeneous illumination of ferroelectric single crystals, a stationary short-circuit photovoltaic current parallel to the direction of the ferroelectric polarization axis is generated. In ferroelectrics the photogenerated electrons and holes are driven toward cathode/anode by the polarization-induced internal electric field that extends over the whole volume. Therefore, in contrast to the junction case, where the field is only present in a thin depletion layer at the interface, charge transport through ferroelectrics is not primarily limited by diffusion and no low-energy barrier affects the output photovoltage. Ferroelectric materials show several advantages compared with traditional semiconductor-based PV materials, such as extremely large photovoltage (not limited by the band gap), a photocurrent proportional to the polarization magnitude, and charge-carrier separation in homogeneous media [130].

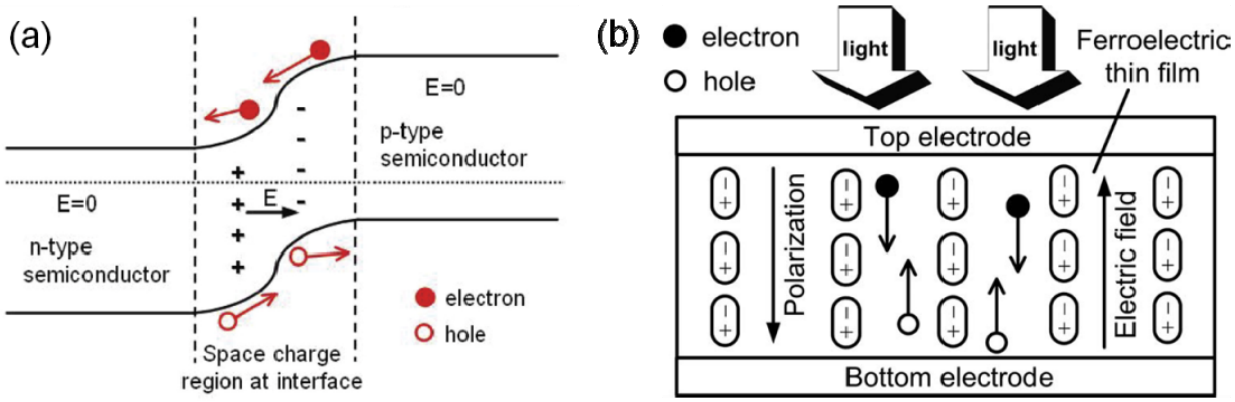

Figure 22. Simplified schematics of PV mechanism in (a) semiconductor *p-n* junction and (b) ferroelectric thin film [131].

Recently BPVE has seen a resurgent interest, especially in ferroelectric thin films. The PV properties of thin-films of prototypical ferroelectrics have been explored, such as $BaTiO_3$ [132], $PbZr_xTi_{1-x}O_3$ [127-129], as well as organic ferroelectrics [133, 134]. Several important theoretical and experimental works on this field have been reported related to the factors influencing the PV properties such as depolarization field, film thickness, electrodes and interfaces, and screening charge effect [131, 135-142]. High PCE up to 19.5% were theoretically predicted in ultrathin ferroelectric films of $(Pb_{0.97}La_{0.03})(Zr_{0.52}Ti_{0.48})O_3$ when the screening effect and the interfacial Schottky barrier could be eliminated [136]. Additionally, a new concept has been demonstrated by Yang *et al*. [143] in which the photocurrent in a ferroelectric $PbZr_xTi_{1-x}O_3$ thin film is enhanced by implanting Ag_2O nanoparticles that possess a narrow energy gap so as to absorb more energy from the visible light spectrum. It is also worth mentioning that Cao *et al*. [144] introduced an *n*-type Cu_2O layer between the $PbZr_xTi_{1-x}O_3$ film and the cathode Pt contact which leads a 120-fold enhancement of the short-circuit photocurrent (4.80 mA/cm^2), and a PCE of 0.57% under AM1.5G (100 mW/cm^2) illumination, since the *n*-type Cu_2O provide a favorable energy level alignment for efficient electron-extraction on the cathode. This work opens up a new method that has the potential for fulfilling cost-effective ferroelectric-film PV devices. Nevertheless, the measured overall PCE of these materials is still very low for practical applications due to the short lifetime of non-thermalized photogenerated charges ($\sim 10^{-12}$ s) and their characteristic large bandgaps (typically 3-4 eV). Although recently considerable efforts have been undertaken to explore new strategies to enhance their PV performance [138, 143-148], the highest PCE ever reported is merely 1.25% in $PbZr_xTi_{1-x}O_3$ based PV devices [148].

Therefore, utilization of narrow band gap ferroelectrics without affecting their ferroelectric properties is becoming a promising route towards their application in novel optoelectronic and

PV devices with high conversion efficiency. More recently, several new ferroelectrics with narrow band gaps have been investigated for PV applications. As an example, a lower band gap of 1.6 eV has been recently demonstrated in weakly ferroelectric non-perovskite material $KBiFe_2O_5$ [149]. Very recently, Grinberg *et al*. discovered a novel ferroelectric perovskite $[KNbO_3]_{1-x}[BaNi_{1/2}Nb_{1/2}O_{3-\delta}]_x$ solid solutions which exhibit both ferroelectricity and a wide variation of direct band gaps in the range 1.1-3.8 eV [146].

1.4.1.3 Advances in Multiferroic Materials for Photovoltaic Applications

Multiferroics possess a magnetic order parameter simultaneously with the ferroelectric one and the electron-electron interaction governing the magnetic ordering leads to a smaller gap than for the other ferroelectric perovskites [146, 149], therefore offers a unique opportunity to investigate possible PV effects. Among them, multiferroic $BiFeO_3$, with the emergence of a band gap energy ~2.2-2.8 eV, is reported to exhibit appreciable photoconductivity in the visible light region [150-153]. Optical studies by combined absorption and ellipsometry spectroscopies (Figure 23) have shown that $BiFeO_3$ has a direct band gap with high absorption coefficient (10^5 cm^{-1}) [154-156].

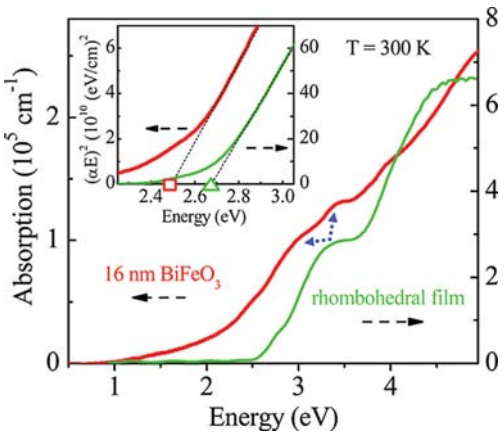

Figure 23. The absorption coefficient $\alpha(E)$ of $BiFeO_3$ nanoparticles (average grain size of ~16 nm) as compared with that of an epitaxially grown rhombohedral thin film. Inset: direct band gap analysis. Blue dashed arrows denote the charge transfer excitation split by 0.5 eV [156].

Unusual and intriguing charge conduction behavior was observed in multiferroic $BiFeO_3$. Among the published works, T. Choi *et al*. [152] first reported the PV effect and a bulk electric polarization induced diode behaviour in a single domain $BiFeO_3$ crystal, associated with a substantial zero-bias PV current induced by visible light. It was found that the direction of photocurrent could be controlled by changing the polarization orientation in the $BiFeO_3$ using a voltage applied across the electrodes. Later on, Yi and co-workers synthesized epitaxial $BiFeO_3$ thin film by sputtering deposition and examined the polarization dependence of the PV performance [150]. PV switch based on lateral single-domain $BiFeO_3$ channels has been also systematically studied by Sung *et al*. [157], and they provide visual evidence for such operations with a series of spatially and spectrally resolved short-circuit photocurrent images.

Importantly, a fundamentally new mechanism occurring at the domains walls has been introduced as a further origin of the observed high photovoltage in the multiferroic $BiFeO_3$ thin films by Yang *et al*. [151]. Potential offsets owing to the presence of domain walls enable a more efficient separation of carriers, and a net potential difference evolves across the entire sample as shown in Figure 24.

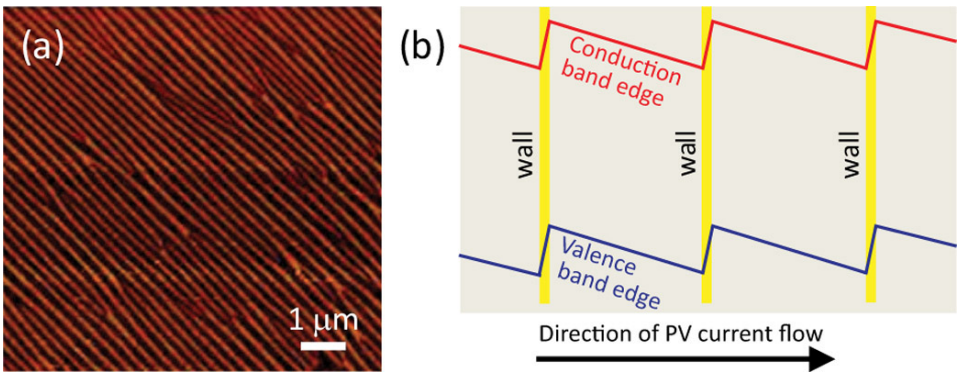

Figure 24. (a) PFM image showing well-aligned arrays of domain walls in an epitaxial $BiFeO_3$ film. The domains of opposite electrical polarization are 150 nm wide, and the walls between them (light contrast) are 2 nm in width. (b) Schematic band structure and PV current flow. Adapted from [151, 158].

Meanwhile, a number of strategies have been applied to improve the performance of $BiFeO_3$ based PV devices. Chen *et al*. presented the effect of the top electrode (ITO and Au) on the PV response of $BiFeO_3$ films [160]. Later on, Zang *et al*. [161] reported enhanced PV properties in polycrystalline $BiFeO_3$ thin films using graphene as top electrodes. Additionally, carbon nanotubes and CdSe quantum dots have been added into $BiFeO_3$ based PV devices to enhance their performance as well [162]. $BiFeO_3$ ultrathin ferroelectric layer was incorporating into $BiVO_4$ semiconductor based PV devices by Dong *et al* [163]. It was found that the $BiFeO_3$ layer with strong self-polarization and high carrier density is desirable to enhance the PV efficiency. Besides that, to understand issues relating to the dynamic processes of charge under illumination in $BiFeO_3$, spatial and temporal evolution of photoinduced charge generation and carrier separation in heteroepitaxial $BiFeO_3$ thin films were studied using Kelvin probe and PFM [164, 165]. Despite the fact that plenty of research in this field has been done, the power conversion efficiency of $BiFeO_3$ based thin film devices is still very low for practical applications.

Double perovskites multiferroic Bi_2FeCrO_6 materials offer opportunities for potential applications in the emerging fields of spintronics, data storage, and more recently in PVs [12]. However, the investigation of the optical properties of Bi_2FeCrO_6 is in its infancy. Some theoretical studies predicted a small band gap for ferrimagnetic-ferroelectric Bi_2FeCrO_6, corresponding to photosensitivity in the near infrared range [167, 168]. Previous study in Rosei's group demonstrated a significant PV response in epitaxial multiferroic ordered Bi_2FeCrO_6 thin-films with a power conversion efficiency of 6.5% under the illumination of red light laser (Figure 25) [166]. In addition, it was found that the cationic ordering of Fe and Cr plays a very important role on the PV performance of Bi_2FeCrO_6 thin films. Thus, multiferroic oxides such as Bi_2FeCrO_6 should lead to higher PV efficiencies.

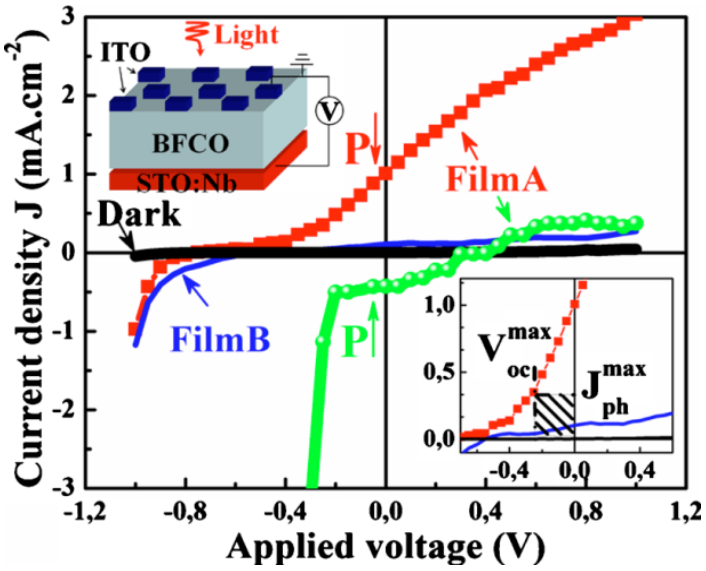

Figure 25. Dark and red light illumination *J-V* measurements curves revealing a PV effect in the Bi_2FeCrO_6 epitaxial films. The top-left inset displays a schematic of the device. The bottom-right inset is a zoom around zero indicating the maximum current density and open circuit voltage used for the calculation of the efficiency [166].

1.4.2 Multiferroic Materials for Photocatalytic Water Splitting Applications

Photocatalytic water splitting with semiconductor materials has been investigated as a clean and renewable process for converting sunlight into chemical energy [169-171], in which the solar energy is harvested and stored in the form of molecular bonds. Compared to solar electricity, the use of chemical bonds to store solar energy significantly reduces device fabrication cost. The photon energy is converted to chemical energy accompanied with a largely positive change in the Gibbs free energy through water splitting [H_2O (l) → H_2 (g) + ½O_2 (g), ΔG_0 = +237.2 kJ/mol]. There are two approaches to achieve water splitting: photocatalytic water splitting by powder semiconductors and photoelectrochemical (PEC) water splitting by semiconductor electrodes.

1.4.2.1 Photocatalytic Water Splitting by Powder Semiconductors

Photocatalytic reactions proceed on powder semiconductor materials are schematically illustrated in Figure 26. When the energy of incident light is larger than the band gap of a semiconductor, electrons and holes are generated in the conduction and valence bands, respectively. The photogenerated charges cause redox reactions by which water molecules are reduced by the electrons to form H_2 and are oxidized by the holes to form O_2 for overall water splitting.

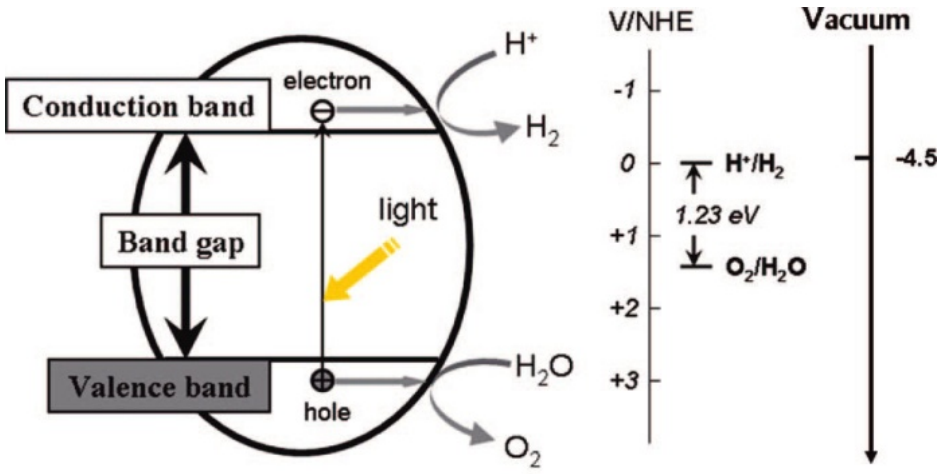

Figure 26. Fundamental principle of semiconductor-based photocatalytic water splitting for hydrogen generation [170]. NHE represents reversible hydrogen electrode.

The processes in the photocatalytic generation of hydrogen are illustrated in Figure 27. They include light absorption of the semiconductor photocatalyst, generation of excited charges (electrons and holes), recombination of the excited charges (bulk and surface), separation of excited charges, migration of the charges, trap of excited charges, and transfer of excited charges to water or other molecules. All of these processes affect the final generation of hydrogen from the semiconductor photocatalyst system.

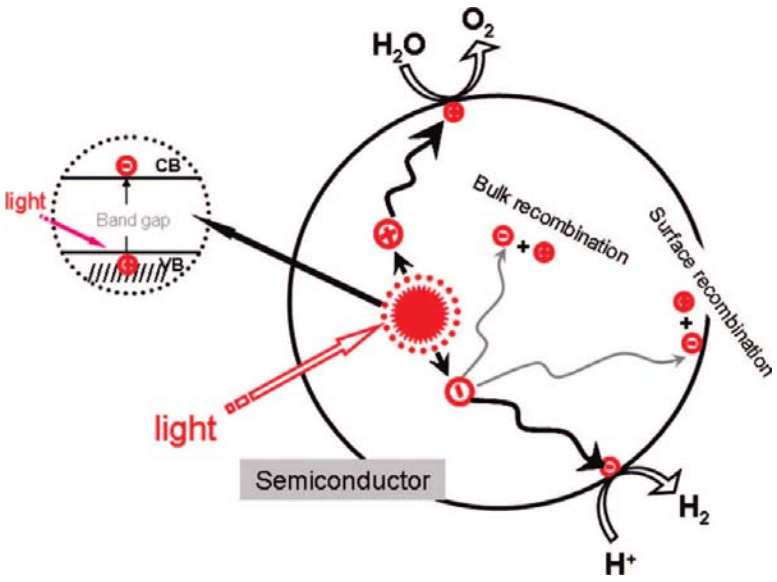

Figure 27. Main processes in photocatalytic water splitting [170].

Taking into consideration the basic mechanism and processes of photocatalytic water splitting, there are two keys to developing a suitable high-efficiency semiconductor for the photocatalytic splitting of water into H_2 and/or O_2: (1) a photocatalyst should have a sufficiently narrow band gap (1.23 eV < E_g < 3.0 eV) to both harvest visible light and possess the proper band structure; (2) photoinduced charges in the photocatalyst should be separated efficiently in order to avoid bulk/surface electron/hole recombination. In addition, they must migrate to the photocatalyst surface for hydrogen and/or oxygen evolution at the respective photocatalytic active sites. In summary, it is generally accepted that the suitable band structure for efficient visible-light harvesting and effective separation of the photoexcited electrons and the holes is essential to improve the photocatalytic properties of the semiconductor. In addition, it is also very important that the photocatalysts needs to be low cost with photostability.

A single material system is unlikely to satisfy all these requirements, and the heterogeneous photocatalysts have been the focus of recent research [171-173]. In general, heterogeneous photocatalysts can offer several potential benefits: (1) enhanced light absorption: for example,

small band gap semiconductors and molecules with high absorption coefficient can be used to functionalize (or sensitize) the semiconductor materials with large band gaps [174, 175]; (2) efficient charge separation and transportation: a *p-n* (semiconductor/semiconductor heterostructures) or the Schottky junction (metal/semiconductor heterostructures) with built-in electrical potential can be created in heterogeneous photocatalysts to effectively direct electron-hole pair separation and transportation [174-180]; (3) cocatalyst effect: the integration with a proper cocatalyst can lower the redox overpotential at the respective active sites [171, 172].

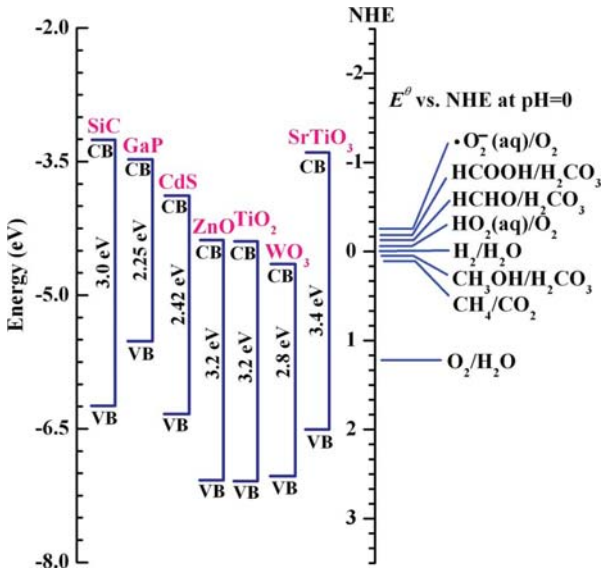

Figure 28. Band-edge positions of semiconductor photocatalysts relative to the energy levels of various redox couples in water [169].

1.4.2.2 Photoelectrochemical Water Splitting by Semiconductor Electrodes

The Honda-Fujishima effect of water splitting using a TiO_2 electrode was reported in the early 1970s [181]. Since then extensive efforts have been made to construct an efficient photoelectrochemical (PEC) water-splitting system and to develop new semiconductor materials for efficient photoelectrodes. PEC water splitting incorporates conversion of solar energy into electrical energy by using semiconductor/electrolyte junction. The PEC cell converts water into

hydrogen and oxygen using sunlight in a two electrode system: semiconductor (possessing either *p* or *n* type conductivity) as working electrode and platinum (Pt) as counter electrode.

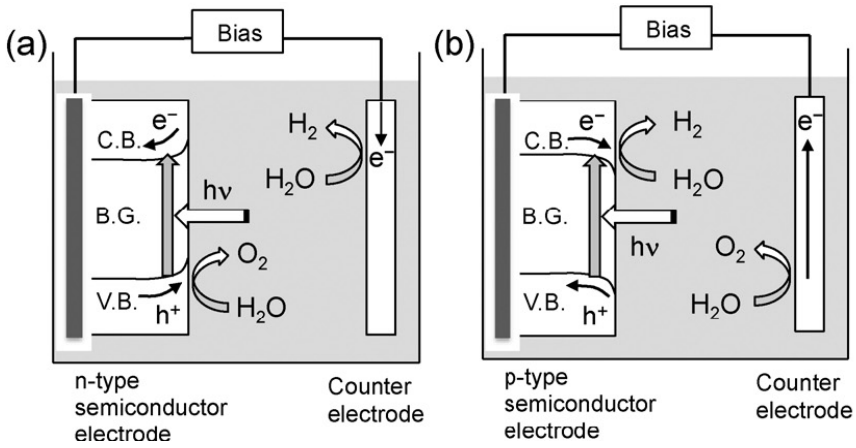

Figure 29. Photoelectrochemical water splitting systems using (a) *n*-type semiconductor photoanode, and (b) *p*-type semiconductor photocathode. Adapted from [182].

Figure 29a shows a PEC water splitting setup based on *n*-type semiconductor (e.g. TiO_2) electrodes. Electrons and holes are generated when an *n*-type semiconductor absorbs photons with higher energies than its band gap. The photoexcited electrons transfer to a counter electrode through the outer circuit and then reduce water to H_2, whereas the holes transfer to the semiconductor surface and then oxidize water to O_2. In most cases, an external bias supply or a pH difference (a chemical bias) between the electrodes is necessary for efficient charge separation, even when the *n*-type semiconductor possesses a suitable conduction band energy level (higher than the potential of H_2/H_2O) for reducing water to H_2, possibly due to the resistance produced between the two electrodes in the solution and to that produced at the interfaces between semiconductor particles within the electrode. In the case of *p*-type semiconductor materials (Figure 29b), water is reduced on the semiconductor surface, while water is oxidized on the counter electrode. The use of a semiconductor electrode as a photoanode

or photocathode overcomes the need to have a material with band edges that straddle both the required oxidation and reduction potentials, as an additional electrical bias can be used to provide an additional energy input to enable the reaction at the counter electrode.

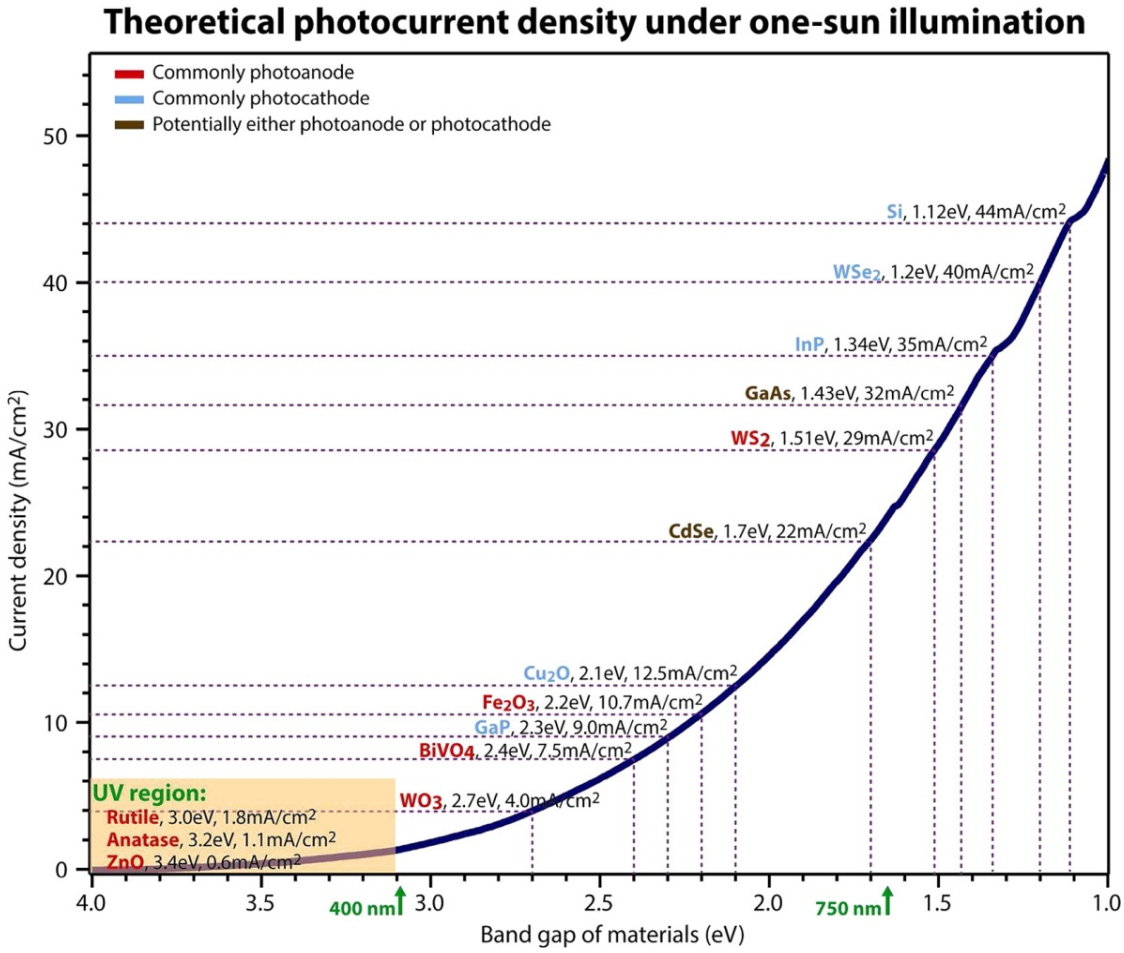

Figure 30. Theoretical photocurrent densities for semiconductors under one-sun illumination. The blue curve is the integrated photon flux at different cutoff energies, based on the AM1.5G solar spectrum [183].

The aim of PEC material fabrication is to design a photoelectrode that has the potential to satisfy most of the requirements [184-186]: (a) sufficient visible light absorption (i.e. band gap) in the range of 1.5 to 2.0 eV, (b) efficient separation and fast transport of photo-generated electron-hole pairs to prevent recombination, (c) favourable alignment of conduction and valence band edge position with respect to redox potential of water and the resultant photovoltage output

to drive the reaction, (d) non-corrosive and high chemical stability in the electrolyte, and (e) low cost. Large band gap semiconducting oxides such as TiO_2, WO_3, $SrTiO_3$, SnO_2 and ZnO etc., are stable in aqueous electrolyte but absorb in the UV region which is only about 4% of the solar spectrum, whereas small band gap semiconductors such as Si, GaAs, InP, CdTe, CdSe and Cu_2O etc., could absorb the visible part of solar spectra but corrode when dipped in electrolyte [187]. Figure 30 lists band gap and theoretical photocurrent density of the current photoelectrode materials of research focus. Upon examining several typical semiconductors for PEC applications, the choice of available materials with band gaps ranging between 1.5 and 2.0 eV is limited and thus new semiconductors with narrow band gap and novel configurations for photoelectrode are needed for practical applications.

1.4.2.3 $BiFeO_3$ for Photocatalysts and Photoelectrodes

Recent discovery of photocatalytic activity of $BiFeO_3$ brought light to new opportunities for the application of $BiFeO_3$ in solar water splitting and water purification. Multiferroic material $BiFeO_3$ was found to possess relatively narrow band gaps (2.2-2.8 eV) which allow it to harvest parts of the visible light of solar spectrum, as well as good chemical stability [80, 82, 188-190].

Several important works on the investigation of photocatalytic properties of $BiFeO_3$ materials have been published. Lou *et al*. [191] first reported that $SrTiO_3$-coated $BiFeO_3$ core/shell nanostructures can produce H_2 under visible-light irradiation. Subsequently, Gao *et al*. [188] utilized $BiFeO_3$ in the form of bulk and nanoparticles as photocatalyst to degrade methyl orange under sunlight irradiations. Later on, they found that $BiFeO_3$ nanowires synthesized by a sol-gel method showed photoinduced oxidization ability to produce O_2 in $AgNO_3/H_2O$ system with considerable initial efficiency of 1876.28 $mol \cdot h^{-1}g^{-1}$, indicating that $BiFeO_3$ would be a

promising candidate as photocatalyst [75]. Meanwhile, Joshi *et al*. [81] synthesized $BiFeO_3$ nanocubes with sizes in the range of 50-200 nm via a microwave procedure and studied their photocatalytic and PEC performance (Figure 31). In 2010, Li and co-workers [80] synthesized various $BiFeO_3$ uniform microcrystals (microspheres and micro/submicrocubes), and demonstrated that the optical and photocatalytic properties of the microsized $BiFeO_3$ crystals are strongly related to their shape and size. Then, Huo *et al*. [82] developed a facile and rapid aerosolspraying approach to prepare mesoporous $BiFeO_3$ hollow spheres with high surface area. The unique hollow chamber could promote the light absorbance via multiple light reflections, leading to high activity in photocatalytic degradation of Rhodamine B (RhB) under visible-light irradiation.

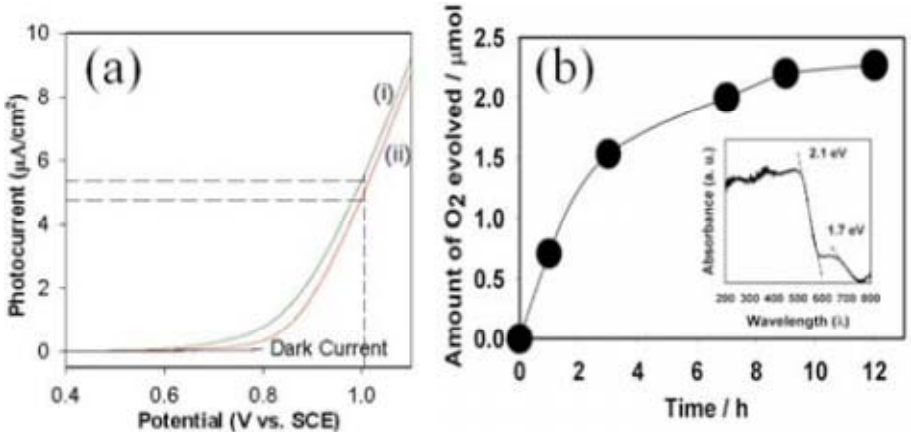

Figure 31. (a) Photocurrent density-potential curves of (i) $BiFeO_3$ nanocubes and (ii) $BiFeO_3$ bulk thin film electrodes under visible illumination. (b) Photocatalytic oxygen evolution under visible light irradiation over $BiFeO_3$ nanocubes. Inset shows photoabsorption spectrum of the $BiFeO_3$ nanocubes. Light source is a 500 W Hg lamp with a cutoff filter of 420 nm [81].

$BiFeO_3$ based nanocomposites have been also investigated to enhance the photocatalytic performance [192, 193]. For example, $BiFeO_3/\gamma$-Fe_2O_3 nanocomposite exhibited significantly increased visible-light photocatalytic ability towards degradation of RhB compared with pure $BiFeO_3$ nanoparticles [192]. Another work by Li *et al*. on nanohybrids of $BiFeO_3$

nanocrystallites and graphene nanosheets have shown a significant enhancement in the visible light photocatalytic activity due to the combined effects of modulated band gap (1.78 eV) and covalent bonding between $BiFeO_3$ and graphene [193]. In addition, Zhang *et al*. [194] discovered that TiO_2 films supported on $BiFeO_3$ substrates can reduce silver cations from aqueous solutions when excited by visible light with energy less than TiO_2's band gap, indicating that electrons generated in the substrate are influenced by the electric fields in the ferroelectric domains and transported through the TiO_2 film to reduce silver on the surface, providing new insight into the impact of ferroelectric polarization on the photocatalytic behavior. Another work was focused on Ag nanoparticles decorated $BiFeO_3$ particles prepared by a chemical reduction method [195], and exhibited an enhanced photoactivity compared with bare $BiFeO_3$ particles due to the effective transfer of photogenerated electrons from $BiFeO_3$ to Ag nanoparticles.

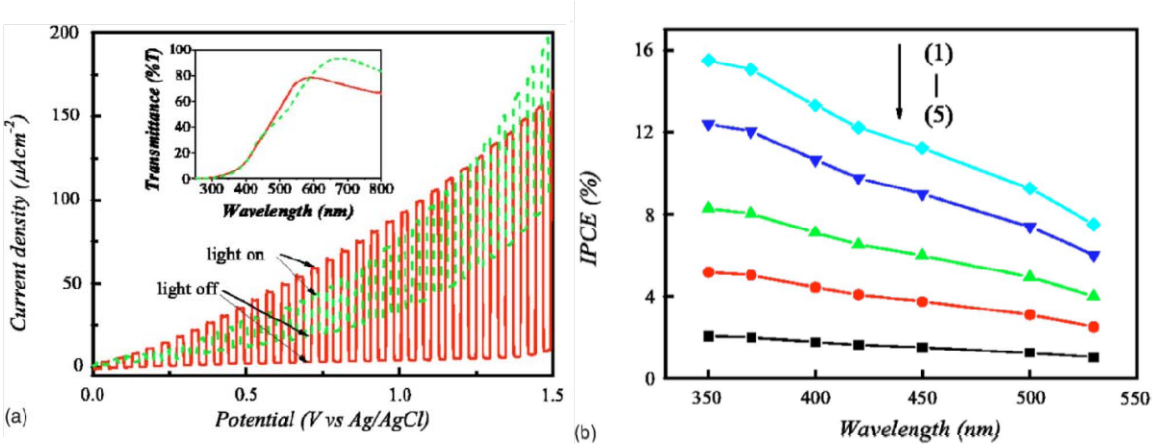

Figure 32. (a) Current-potential dependence of the $BiFeO_3$ film electrode under visible-light irradiation (λ > 420 nm, light intensity: 60 mW/cm^2). Solid line for the polycrystalline film and dashed line for the amorphous film. (b) IPCE (incident photon to charge carrier efficiency) of the polycrystalline $BiFeO_3$ film electrode measured at different potentials: (1) 1.5 V, (2) 1.2 V, (3) 0.8 V, (4) 0.5 V, and (5) 0.2 V. Adapted from [196].

Besides research on powdered nanostructures, $BiFeO_3$ in thin film form has been investigated for PEC applications as well. $BiFeO_3$ films deposited on $Pt/TiO_2/SiO_2/Si$ substrate

by PLD were studied as photoelectrode for water splitting for the first time by Chen *et al* [196]. They found that the incident photon to current conversion efficiency (IPCE) for the polycrystalline $BiFeO_3$ electrode was approximately 16% at 350 nm and 7% at 530 nm at 1.5 V (Figure 32).

Very recently, PEC properties of epitaxial $BiFeO_3$ thin films grown on $SrRuO_3$ coated $SrTiO_3$ substrates have been studied under anodic bias by Ji *et al* [197]. It was noted that both thinner films and negative polarization charges on the film surface result in a cathodic shift of the photocurrent onset (Figure 33). In addition, large switchable polarization can modify the surface properties to promote the hydrogen and oxygen evolutions on the surfaces with positive and negative polarization charges, respectively. This study shed light on the utilization of epitaxial ferroelectric thin film for PEC water splitting applications.

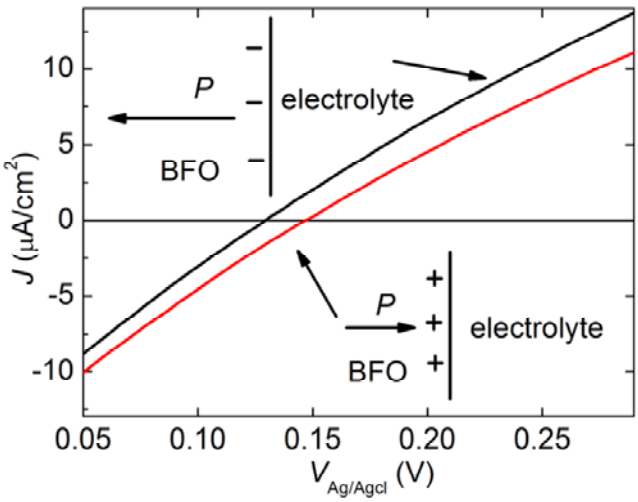

Figure 33. Linear sweep voltametry curves of $BiFeO_3/SrRuO_3/SrTiO_3$ (001) with different ferroelectric polarizations. Black: negative polarization charges on the surface; red: positive polarization charges on the surface [197].

In spite of a number of investigations, the PEC conversion efficiencies of reported ferroelectrics and multiferroic $BiFeO_3$ materials were observed to be limited by the generated

small photocurrent density (order of nA or μA cm^{-2}), as well as the wide band gaps (typically 2.7-4 eV) of these materials, which only allow to use about 8-20% intensity of the solar spectrum. Hence, the real potential of using semiconducting ferroelectric oxides for PEC water splitting applications is yet to be demonstrated.

Chapter 2

Research Objectives and Thesis Organization

2.1 Research Objectives

This thesis is divided into two sections with two corresponding objectives:

The first section is mainly devoted to the synthesis and functional properties (ferroelectric, magnetic and photocatalytic) of low dimensional $BiFeO_3$ based nanostructures.

So far, various $BiFeO_3$ nanomaterials have been reported and exhibit different properties compared to the bulk form of $BiFeO_3$ crystals. Therefore, the investigation of the functional properties of multiferroic $BiFeO_3$ nanostructures is important for fundamental research and designing new multifunctional materials combining magnetic, ferroelectric and optoelectronic properties. Although exhaustive research on the synthesis of low dimensional $BiFeO_3$ materials has been well reported in literature, synthesizing single-crystalline $BiFeO_3$ nanostructures with controllable morphologies and crystallographic facets by template- or surfactant free solution routes is still a major challenge, and the investigation of their physical (e.g. ferroelectric and magnetic) properties at nanoscale is still lacking. Additionally, multiferroic $BiFeO_3$ materials have recently been recognized as a potential system for applications in photocatalysis due to their relatively narrow band gaps (2.2-2.8 eV), which allow them to be used in the visible range, as

well as good chemical stability. Whereas, investigations of $BiFeO_3$ nanomaterials for photocatalytic water splitting are still limited. $BiFeO_3$ nanowires (NWs) in single-crystalline form which are expected to be highly active photocatalysts for solar water splitting have not been explored yet. Therefore, the objectives for this thesis are as following:

(1) Synthesize 1D $BiFeO_3$ nanowires and study their ferroelectric properties; (2) Investigate the photocatalytic water splitting properties of $BiFeO_3$ nanowires and explore strategies to enhance their photocatalytic activity; (3) Develop a surfactant free approach for synthesizing 2D $BiFeO_3$ nanostructures and understand their magnetic behavior.

The second section is mainly focused on the investigation of solar energy conversion (i.e. PV and PEC) performance of Bi_2FeCrO_6 based thin film devices.

With the increasing needs for clean and renewable solar energy, researchers are continuously exploring novel materials and fundamentally investigating photoelectric conversion mechanisms for achieving higher performance of photovoltaic devices. The unique bulk photovoltaic effect (BPVE) working mechanism in non-centrosymmetric crystals, especially ferroelectric materials provides an alternative viable route to convert sunlight into electric energy. The ferroelectric PV device, in which homogeneous ferroelectric material is used as a light absorbing layer, has been investigated during the past several decades with numerous ferroelectric oxides. However, over half a century, BPVE effect has remained to be an academic curiosity rather than any real applications because of the very low energy conversion efficiency (< 1%) achieved in regular ferroelectric materials based devices, mainly due to small photocurrent densities on the order of ~nA/cm^2 and large band gap in most bulk ferroelectrics (3-4 eV). Therefore, utilization of narrow band gap ferroelectrics is becoming a promising route

towards their application in novel optoelectronic and solar energy devices. Although the investigations of electronic transport, magnetic and electronic structure, and other aspects of Bi_2FeCrO_6 materials are emerging, the optical properties have not been studied yet. Moreover, effects of cationic ordering of Fe/Cr on the PV properties of double perovskites Bi_2FeCrO_6 thin films remain unknown. In addition, the integration of Bi_2FeCrO_6 thin film in PEC cells has not been reported yet. These issues have motivated our present study. Therefore, the objectives of this section are:

(1) Investigate the impact of Fe/Cr ordering on the optical properties of Bi_2FeCrO_6 thin films; (2) Study the PV properties of Bi_2FeCrO_6 thin film based devices and gain a deeper fundamental understanding of the effect ferroelectricity on their PV performance; (3) Test the possibilities of using Bi_2FeCrO_6 thin films as photoelectrode for solar water splitting.

2.2 Thesis Organization

This thesis is divided into nine parts and organized as follows:

Chapter 1 introduces the background;

Chapter 2 presents the motivation and main goals of this thesis;

Chapter 3 describes experimental details of the synthesis process for $BiFeO_3$ and Bi_2FeCrO_6 based nanostructures and thin films. The main characterization techniques are also described in this chapter;

SECTION (I) Synthesis and Functional Properties of $BiFeO_3$ based Nanostructures

Chapter 4 presents the investigation of ferroelectric properties of single crystalline $BiFeO_3$ nanowires, and the publication related to this chapter is:

[198] **S. Li**, R. Nechache, C. Harnagea, L. Nikolova and F. Rosei, *Single-crystalline $BiFeO_3$ Nanowires and Their Ferroelectric Behavior*, Applied Physics Letters, **101**, 102903, 2012.

Chapter 5 demonstrates a highly active visible-light-driven photocatalyst consisting of single crystalline $BiFeO_3$ nanowires and laser ablated Au nanoparticles synthesized via a functionalization-step-free solution process. The publication related to this chapter is:

[199] **S. Li**, J. Zhang, M. G. Kibria, Z. Mi, M. Chaker, D. Ma, R. Nechache and F. Rosei, *Remarkably Enhanced Photocatalytic Activity of Laser Ablated Au Nanoparticle Decorated $BiFeO_3$ Nanowires under Visible-light*, Chemical Communications, **49**, 5856, 2013.

Chapter 6 develops a novel route to fabricate single crystal $BiFeO_3$ nanoplates without surfactant, which show weak ferromagnetic properties resulting from the size effect on the magnetic ordering. The publication related to this chapter is:

[200] **S. Li**, R. Nechache, I. A. V. Davalos, G. Goupil, L. Nikolova, M. Nicklaus, J. Laverdiere, A. Ruediger, F. Rosei, *Ultrafast Microwave Hydrothermal Synthesis of $BiFeO_3$ Nanoplates*, Journal of American Ceramic Society, **96**, 3155, 2013.

SECTION (II) Bi_2FeCrO_6 Thin Films for Solar Energy Conversion Applications

Chapter 7 presents a new approach to effectively tune the band gap and PV performance of double perovskites multiferroic oxides by engineering the cationic ordering of Fe/Cr in the case of Bi_2FeCrO_6. The highest power conversion efficiency of 3.3% was obtained under optimized conditions in Bi_2FeCrO_6 thin film based PV devices. The publication related to this chapter is:

[201] R. Nechache, C. Harnagea, **S. Li**, L. Cardenas, W. Huang, J. Chakrabartty and F. Rosei, *Bandgap tuning of multiferroic oxide solar cells*, Nature Photonics, doi:10.1038/nphoton.2014.255.

Chapter 8 investigates epitaxial Bi_2FeCrO_6 thin film as a photocathode material, with a suitable conduction band position to photoreduce water to H_2 while possessing a relatively narrow band gap (1.9-2.1 eV) that utilizes the visible light. A significant photocurrent density (ca. −1.0 mA/cm^2) was obtained at a bias of ca. −1.0 V, which could be further enhanced by about two times through the modulation of the ferroelectric polarization in the Bi_2FeCrO_6 films. The publication related to this chapter is:

[202] **S. Li**, B. AlOtaibi, W. Huang, Z. Mi, R. Nechache, N. Serpone and F. Rosei, *Multiferroic Bi_2FeCrO_6 Epitaxial Thin Film as a New Visible Light Absorbing Photocathode Material*, submitted to Small.

Chapter 9 briefly summarizes the most important contributions of this work and states prospect of $BiFeO_3$ and Bi_2FeCrO_6 based nanomaterials and thin films in the field of solar energy conversion.

Following the main body of this thesis is an appendix containing a summary of this thesis in French according to INRS policy.

Chapter 3

Experimental Methods

3.1 Materials

Bismuth nitrate pentahydrate, ($Bi(NO_3)_3 \cdot 5H_2O$, > 99.99%), iron(III) chloride hexahydrate ($FeCl_3 \cdot 6H_2O$, > 98%), ethylene glycol ($C_2H_6O_2$), Gold (Au) plate target (99.99%), sodium citrate ($Na_3C_6H_5O_7 \cdot 2H_2O$), hydrogen tetrachloroaurate hydrate (auric acid, $HAuCl_4 \cdot 3H_2O$), ammonia ($NH_3 \cdot H_2O$), sodium hydroxide (NaOH), Potassium hydroxide (KOH), sodium borohydride ($NaBH_4$), sodium sulfate (Na_2SO_4), ethanol (denatured), acetone (99.8%), and 1-methylaminopyrene (MAP) were purchased from Sigma-Aldrich Inc. Hydrochloric acid (HCl, 37.1%), nitric acid (HNO_3, 68.0-70.0%), pressure syringe filter (Millipore Inc.) composed of celluloid membrane filters (0.2 μm), pressure filter-holder celluloid filter, and Amicon Ultra-4 Ultracel-50K centrifuge filters (Millipore Inc.) for all the centrifugation/separation were obtained from Fisher Scientific Inc. All the chemicals were used without further purification. Distilled (D.I.) water was purified by a Millipore Ultrapure water system and has a resistivity of 18.2 MΩ·cm at 25°C for aqueous solution preparation.

3.2 Synthesis Techniques

3.2.1 Conventional Hydrothermal Synthesis

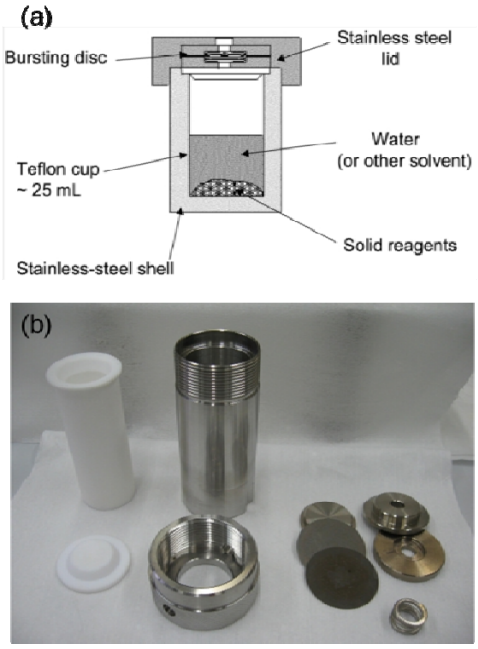

Figure 34. (a) A schematic cross section view of a Teflon-lined, stainless autoclave [203]. (b) A photograph showing the components of a typical autoclave for hydrothermal synthesis.

Hydrothermal/solvothermal synthesis, which involves lower-temperature solution-based chemical reactions carried out in a sealed heated aqueous solution above ambient temperature and pressure, is widely applied to generate different kinds of nanomaterials [204]. Performing a chemical reaction under such conditions using organic solvent is referred to as solvothermal processing. In the specific but more common case where water is used as the solvent, this technique is defined as hydrothermal processing [203]. When a solvent is heated in a sealed vessel (such as an autoclave or a bomb calorimeter-type apparatus) so that the autogenous pressure far exceeds the ambient pressure, this technique allows for solvents to be brought to temperatures well above their boiling points. A temperature gradient is maintained between the opposite ends of the growth chamber. At the hotter end the nutrient solute dissolves, while at the

cooler end it is deposited on a seed crystal, growing the desired crystal. A typical Teflon-lined stainless autoclave and a schematic cross section view are given in Figure 34.

Precise control over hydrothermal/solvothermal synthetic conditions is essential for the success of the preparation of inorganic semiconducting nanostructures. The controllable conditions can be classified as the interior reaction system conditions (e.g. concentration, pH value, time, pressure, organic additives or templates) and the exterior reaction environment conditions (e.g. the modes of input energy). Among all developed synthetic methods, the hydrothermal/solvothermal method has attracted more and more attention because of its outstanding advantages such as simple manipulation, easy control, and uniform products.

3.2.2 Microwave-assistant Hydrothermal Synthesis

Microwave-assisted hydrothermal (M-H) methods using dielectric heating as a non-classical energy source are becoming widespread for the synthesis of nanomaterials [205, 206]. In many cases, it has been shown to dramatically reduce processing time, increase product yields, and enhance product purity or material properties compared to conventionally processed experiments. The traditional form of heating (Figure 35a) is a rather slow and inefficient process for transferring energy to a reaction mixture, since it depends on convective currents and the thermal conductivity of various compounds or materials that have to be penetrated, and often results in the temperature of the reaction vessel being higher than that of the reaction solution. In contrast, microwave heating provides energy to the water by means of molecular interaction with high-frequency electromagnetic radiation, which is essentially different from that of conventional thermal treatment by convection current.

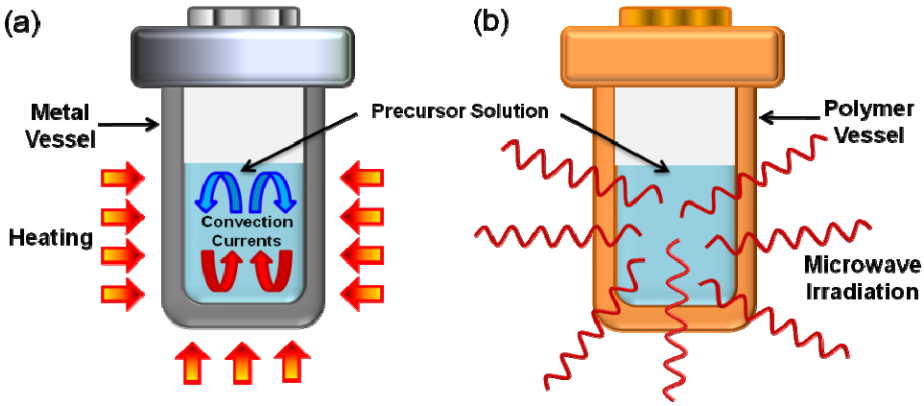

Figure 35. Schematic illustration of the two modes of hydrothermal synthesis technique: (a) conventional hydrothermal (C-H) and (b) microwave-assisted hydrothermal (M-H).

Microwave irradiation triggers heating by two main mechanisms, namely dipolar polarization and ionic conduction. Whereas the dipoles in the reaction mixture (for example, polar solvent molecules or reagents) are involved in the dipolar polarization effect, the charged particles in a sample (usually ions) contribute to ionic conduction. When irradiated at microwave frequencies, the dipoles in the sample align in the direction of the applied electric field. As the electric field oscillates, the molecular dipoles accordingly attempt to re-align themselves along the alternating electric-field, and the energy is lost in the form of heat through molecular friction and dielectric loss (dielectric heating) in such process. Figure 35 illustrates the mechanisms of conventional hydrothermal and M-H synthesis techniques. In M-H processing, the precipitate can be rapidly dissolved in aqueous solution, resulting in enhancement of the reaction kinetics by one to two orders of magnitude by high-frequency electromagnetic radiation (2.45 GHz).

3.2.3 Pulsed Laser Deposition

To deposit various complex oxide materials in thin film form, we used pulsed laser deposition (PLD), a versatile deposition technique widely used in research environments [207]. PLD is a thin film deposition technique in which the thin film is prepared by the ablation of one or more

targets illuminated by a focused pulsed-laser beam. In this method, as illustrated in Figure 36, a high power pulsed laser beam is focused inside a vacuum chamber to melt, evaporate and ionize material from the surface of a target. This "ablation" event produces a transient, highly luminous plasma plume that expands rapidly away from the target surface. The ablated material is collected on an appropriately placed substrate upon which it condenses and the thin film grows. The main advantages of PLD lie in the following aspects. First, high quality thin films with certain crystallographic orientation can be achieved by controlling the growth condition and choosing the substrate properly. Besides, multi-layered films of different materials can be produced by sequential ablation of assorted targets. The most important feature of PLD is that it is able to transfer material from a bulk ceramic target onto the substrate of choice by maintaining the same ratios of the elemental components of the ablated species, even for chemically complex systems, which is resulting from the extremely high heating rate of the target surface (10^8 K/s) due to pulsed laser irradiation.

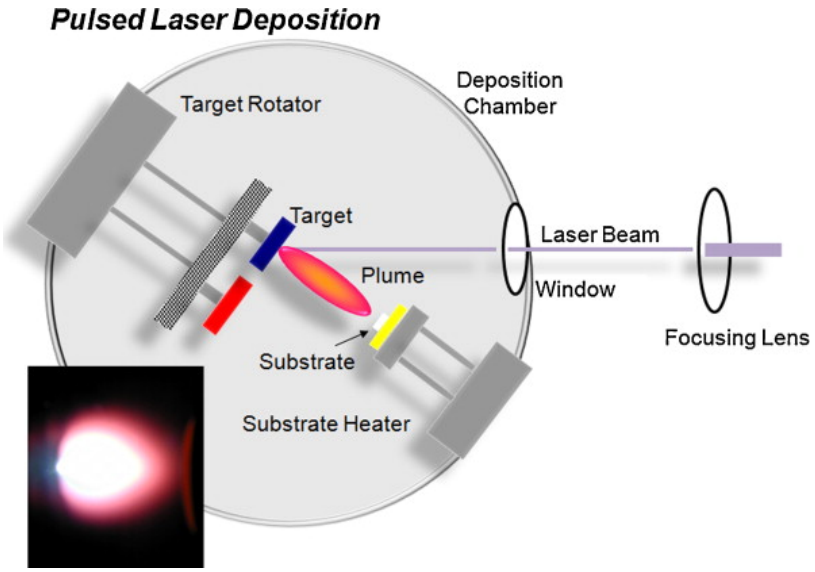

Figure 36. Schematic of a standard pulsed laser deposition system. The inset picture shows an actual photograph of the plume [27].

In our experiment, PLD system using a KrF excimer laser (λ = 248 nm, pulse duration = 14 ns) was employed for ablation with an incidence angle of the laser beam on the target of 45º. The chamber base pressure is 4×10^{-5} Torr. In order to get high quality thin films, four parameters were carefully controlled: substrate temperature, energy of the atom flux, relative and absolute arrival rate of the atoms for compound films, and the partial pressure of oxygen in the chamber. $BiFeO_3$, $BiCrO_3$, and Bi_2FeCrO_6 targets were purchased from MTI Corporation, and $CaRuO_3$ and $SrRuO_3$ targets were purchased from Praxair Surface Technologies. All substrates including $(LaAlO_3)_{0.3}(Sr_2AlTaO_6)_{0.7}$, $LaAlO_3$, $SrTiO_3$ and Nb-$SrTiO_3$ (0.5%) were purchased from CrysTec.

3.3 Characterizations

i) X-ray Diffraction (XRD) and Reciprocal Space Maps (RSM). XRD method is used for determining the crystal structure. Incident X-rays are scattered by a crystalline sample according to Bragg's law:

$$n\lambda = 2dsin\theta \qquad \text{(Eq. 3.1)}$$

where λ is the wavelength of the X-ray beam, θ is the incident angle, and d is the distance between crystal planes. The value for d is dependent on the Miller indices h, k and l. Two different X-ray diffractometers were used to record the diffraction patterns presented in this thesis: the measurements on the film samples were performed using a Panalytical XRD X-pert Pro diffractometer; and D8 Advance (Bruker) using CuK_α radiation (λ = 1.5418 Å) was used to determine the crystal structure of powdered samples. In addition, RSM measurements were carried out around the (204) reflection of the substrate to identify the crystal structure of the obtained films, and to calculate the lattice parameters and the corresponding unit cell volume.

ii) Scanning Electron Microscopy (SEM). In SEM, an electron beam is scanned across a sample's surface. Accelerated electrons in an SEM carry significant amounts of kinetic energy, and this energy is dissipated as a variety of signals produced by electron-sample interactions when the incident electrons are decelerated in the solid sample. The signals which provide the greatest amount of information in SEM are the secondary electrons (that produce SEM images), backscattered electrons (BSE), diffracted backscattered electrons (EBSD that are used to determine crystal structures and orientations of minerals), photons (characteristic X-rays that are used for elemental analysis). Among them, secondary electrons are emitted from the atoms occupying the top surface and produce a readily interpretable image of the surface. The contrast in the image is determined by the sample morphology and charge carrier density. The images of the samples were recorded using a field emission SEM (FESEM, JEOL JSM7401F) at an acceleration voltage of 5 kV.

iii) Transmission Electron Microscopy (TEM) and Selected Area Electron Diffraction (SAED). TEM is an immensely valuable and versatile technique for the characterization of materials. It exploits the very small wavelengths of high-energy electrons to probe solids. Information about local structure (by imaging of defects such as dislocations), average structure (using diffraction to identify crystal class and lattice parameter) and chemical composition can be collected almost simultaneously. In our experiment, TEM is used to directly observe the morphology and size of nanostructures. Crystal structure of samples was identified using SAED. In order to perform these measurements, a small drop of solution containing nanomaterials was deposited onto a Cu grid coated with thin (15-30 nm in thickness) carbon films. The grid was subsequently dried in air and observed with a JEOS-2100F TEM (École Polytechnique de Montréal).

iv) X-ray Photoelectron Spectroscopy (XPS) and Ultraviolet photoelectron spectroscopy (UPS). XPS is a quantitative spectroscopic technique that measures the electronic state of the elements that exist within a material. XPS spectra were taken using ESCA Escalab 220i XL with a monochromated Al K_α X-ray source (1486.6 eV). Curve fitting of the XPS data was performed with Gaussian functions after Shirley background subtraction using casa-XPS version 2.2.107. The binding energies were calibrated by referencing them to the designated hydrocarbon C1*s* binding energy of 284.6 eV. UPS allows the determination of the absolute value of the work function (Fermi level, E_f) and ionization potential (equivalent to valence band edge, E_v) of semiconductor materials. UPS measurements were carried out using He I (21.22 eV) photon lines from a discharge lamp.

v) Zeta-potential Measurement. Zeta potential analysis is a technique for determining the surface charge of nanoparticles in solution. Generally, nanoparticles have a surface charge that attracts a thin layer of ions with opposite charge to their surface. This double layer of ions travels with the nanoparticle as it diffuses throughout the solution. The electric potential at the boundary of the double layer is known as the Zeta potential of the particles and has values that typically range from +100 mV to −100 mV. Zeta-potential measurements were performed with a Brookhaven ZETAPALS Analyzer for colloidal samples (1.5 mL) at different pH values in standard all-side transparent PMMA cuvettes (length: 10 mm; width: 10 mm).

vi) UV-visible (UV-vis) Spectroscopy. Ultraviolet and visible radiation interacts with matter which causes electronic transitions (promotion of electrons from the ground state to a high energy state). The ultraviolet region falls in the range between 190-380 nm, and the visible region is between 380-750 nm. The UV-vis absorption spectrum was carried out for investigating the optical energy gap of the materials based on their optically induced transition. A UV-vis

spectrophotometer (Varian 5000) was used with a scan speed of 600 nm/min. All experimental data were corrected for background absorption by water or ethanol.

vii) Photoluminescence (PL) Spectroscopy. PL is the spontaneous emission of light from a material under optical excitation. The excitation energy and intensity can be chosen to probe different excitation types and also different parts of the sample. PL investigations can be used to characterize a variety of materials parameters. Features of the emission spectrum can be used to identify surface, interface and impurity levels. Under pulsed excitation, PL intensity transients yield lifetimes of excited states. In addition, thermally activated processes of non-radiative recombination can be investigated in this way as well. The PL intensity and its dependence on the level of photo-excitation and temperature are directly related to the dominant recombination process. Analysis of PL helps to understand the underlying physics of the recombination mechanism. In our experiment, steady state PL spectroscopy of samples was measured using an excitation wavelength of 400 nm on a Fluorolog-3 spectrofluorometer (Horiba Jobin Yvon). All spectra were collected over the range of 450-600 nm from powder samples dispersed in ethanol (1 mL of solution in quartz micro cuvettes, 0.5 mg/mL).

viii) Spectroscopic Ellipsometry. Spectroscopic ellipsometry is an optical technique, which measures the changes of the polarization state of a polarized light beam after reflection from the sample under study. These changes are measured as the ellipsometric parameters ψ and Δ. These values depend on the thickness, roughness, refractive index n, and extinction coefficient k of the layers and the substrate. The absorption coefficient α of the films is deduced from the extinction coefficient k by using the following formula: $\alpha = 4\pi k/\lambda$, where λ is the wavelength of incident light. To investigate the absorption properties of the obtained thin film samples, spectroscopic ellipsometry measurements were performed at an angle of incidence 60° using a VASE

ellipsometer (J.A. Woollam Company). The optical constants of thin film samples were determined by analyzing the ellipsometric spectra with a multilayer model that describes the optical response of a system consisting of air, thin films, bottom electrode and substrate.

ix) Atomic Force Microscopy (AFM) and Piezoresponse Scanning Force Microscopy (PFM). AFM is a microscopic technique imaging a surface topography by using attractive and repulsive interaction forces between a few atoms attached at a tip on a cantilever and a sample. If the AFM is operated in contact mode with a conductive tip, the local polarization state and the electromechanical properties of ferroelectric thin films can be probed via the converse piezoelectric effect. This technique is based on the detection of local vibrations of a ferroelectric sample (ferroelectrics are always piezoelectric) induced by a testing AC signal applied between the conductive tip of the AFM and the bottom electrode of the sample. The mechanical oscillations of the sample underneath the tip are transmitted to the cantilever, provided that the contact between tip and sample is firm. This condition is fulfilled when the contact force dominates over the electrostatic and adhesion force, i.e. the AFM is in the contact mode of operation with stiff cantilevers, thus the electrostatic signal could be minimized. The oscillations of the cantilever are then detected from the global cantilever deflection using a lock-in (Figure 37). Since the first harmonic of the oscillations represents the piezoelectric constant, these vibrations converted into an electrical AC signal are further referred to as piezoresponse signal.

An Enviroscope atomic force microscope (Veeco) was used equipped with NSC36 cantilevers and tips coated with Co/Cr from Mikromasch. We used medium-stiffness cantilevers ($k \sim 1$ N/m) to achieve a low contact force. The resulting piezoelectric deformations transmitted to the cantilever and both out-of-plane and in-plane components were detected from the global deflection signal using two Lock-in amplifiers (Signal Recovery, model 7265). The large bias

required for hysteresis measurements was applied using a DC source (Keithley 2400 Sourcemeter) in series with the AC driving voltage.

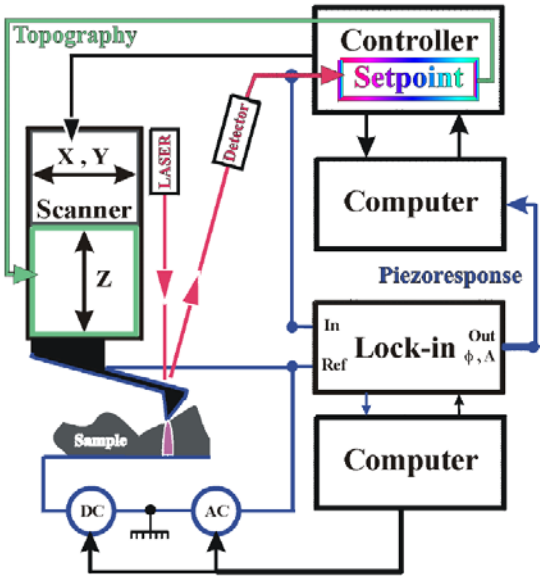

Figure 37. Experimental setup of PFM measurement [208].

x) Magnetization Measurement. The Superconducting Quantum Interference Device (SQUID) magnetometer is an instrument which is very sensitive to magnetic fields, making it ideal for measuring subtle changes in the magnetic behavior of a sample when it is subjected to different temperatures, magnetic fields or pressures. The samples were placed in a plastic capsule with inverse capsule configuration to prevent sample movement within the capsule which would consequently disturb the measurement. The magnetization as a function of the magnetic field (hysteresis loops) was investigated using a SQUID (MPMS-XL7, San Diego, CA) with an applied magnetic field of 1 T at room temperature.

SECTION (I) Synthesis and Functional Properties of $BiFeO_3$ based Nanostructures

Chapter 4

Ferroelectric Properties of Single Crystalline $BiFeO_3$ Nanowires (NWs)

1D ferroelectric perovskites have recently been studied extensively in the quest to miniaturize devices for nonvolatile random access memory applications and discovering novel physics phenomena at nanoscale [209]. The recent rapid development in the synthesis of a wide variety of piezoelectric/ferroelectric 1D nanomaterials such as $BaTiO_3$ [210, 211], $SrTiO_3$ [210, 211], and $KNbO_3$ [212], as well as 1D heterostructures such as $NaNbO_3/Nb_2O_5$ [213] and $MgO/PbZr_{0.58}Ti_{0.42}O_3$ [214], provides great opportunity to study the ferroelectricity of 1D nanostructures of such well-defined crystalline oxides. Scanning probe microscopy (SPM), and in particular its derivative piezoresponse force microscopy (PFM), is a powerful technique and widely used to study ferroelectricity and piezoelectricity at nanoscale. For example, Suyal *et al*. confirmed the ferroelectric nature of $K(Nb_{0.8}Ta_{0.2})O_3$ nanorods by PFM [215]. Using an ultrahigh vacuum SPM, Yun *et al*. [216] demonstrated that individual single-crystalline $BaTiO_3$ nanowires with 10 nm in diameter retain ferroelectricity at nanoscale. Nevertheless, whether ferroelectric behavior maintained at nanoscale in $BiFeO_3$ materials is still unknown.

Recent synthesis approaches have been proposed to develop low-dimensional substrate-free $BiFeO_3$ nanostructures, which offer the possibility to study their ferroelectric, magnetic, and

optical behavior at nanoscale. However, to date, little effort has been expended in research related to the ferroelectric performance of substrate-free $BiFeO_3$ nanostructures. Recently, Xie *et al*. [77, 217] investigated the ferroelectric domains and piezoresponse of $BiFeO_3$ nanocrystalline fibers using both traditional and a dual frequency resonance tracking PFM. However, the issue about the size effect on ferroelectric properties in 1D single-crystal $BiFeO_3$ nanowires has not been clarified yet. Their piezoelectric/ferroelectric behaviors are still unknown. In this chapter, we are trying to understand the ferroelectric properties of individual single-crystalline $BiFeO_3$ nanowires.

4.1 Experimental Section

$BiFeO_3$ nanowires were synthesized according to a published work [74]. 2.425 g $Bi(NO_3)_3 \cdot 5H_2O$ and 1.352 g $FeCl_3 \cdot 6H_2O$ were mixed in 50 mL of acetone for 30 min under sonification. Then 200 mL of D.I. H_2O and concentrated ammonia were added under vigorous stirring until the pH value of the solution reached 10-11. After filtering and rinsing with distilled water, the red co-precipitate was re-dispersed in 40 mL D.I. water. Under vigorous stirring, 8 g NaOH was added into the suspension. Next, the hydrothermal solution was put inside a stainless steel autoclave with a Teflon liner (Parr Instrument Company) and heated at 140°C for 48 hours. The final product was dried at 80°C for 2 h.

For PFM measurements, the samples were prepared as follows: a small amount of the nanowires powder was dispersed in ethanol by ultrasonication, and few droplets of the resulting suspension were deposited on a platinum-coated silicon substrate and dried at 80°C in a lab oven.

4.2 Structural and Morphological Characterizations

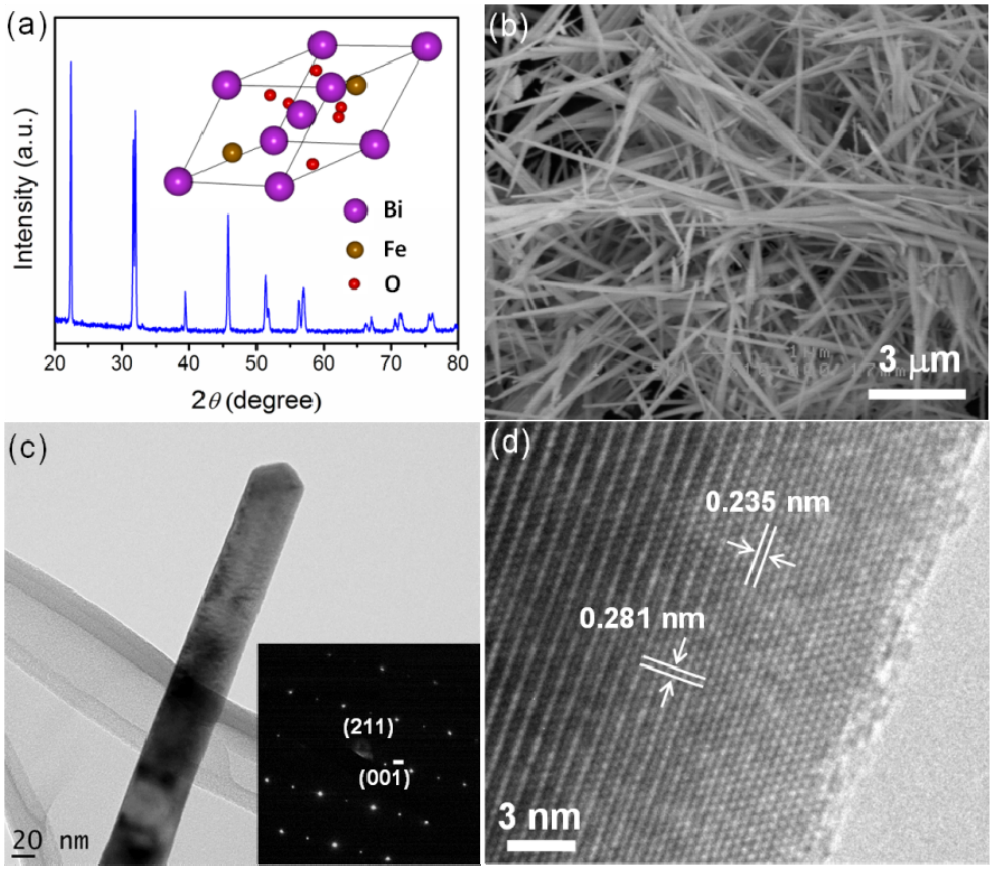

Figure 38. (a) XRD pattern of as-synthesized $BiFeO_3$ nanowires powders. Inset shows the crystal structure of $BiFeO_3$. (b) A typical SEM image of the nanowires [198]. (c) Representative TEM image of an individual nanowire. Inset: electron diffraction patterns taken from the nanowire. (d) HRTEM image taken from the edge of the nanowire in (c).

The XRD patterns of as-synthesized powders are shown in Figure 38a. All the diffraction peaks can be indexed with respect to the rhombohedrally distorted perovskite phase of single crystalline $BiFeO_3$ with *R*3*c* space group, and match the diffraction data of JCPDS No. 20-0169 well, in good agreement with the previous reports [69, 74]. The sharp peaks demonstrate good crystallinity of the nanowires. The SEM image is presented in Figure 38b and shows the ensemble of randomly aligned $BiFeO_3$ nanowires with diameters from 40 to 200 nm and lengths

up to several micrometers. The crystal structure of the $BiFeO_3$ nanowires was further confirmed by TEM (Figure 38c). The single-crystalline nature of the nanowires is clearly seen in the SAED pattern obtained from an individual nanowire (inset of Figure 38c). The indexation of the SAED patterns reveals that the growth direction of the nanowires is perpendicular to the rhombohedral (211) crystal plane, consistent with the previous report [74]. The spacing of the lattice fringes measured from high-resolution TEM image (Figure 38d) are 0.265 and 0.306 nm, which corresponds to (100) and (211) plane of rhombohedral $BiFeO_3$, respectively.

4.3 Ferroelectric Properties

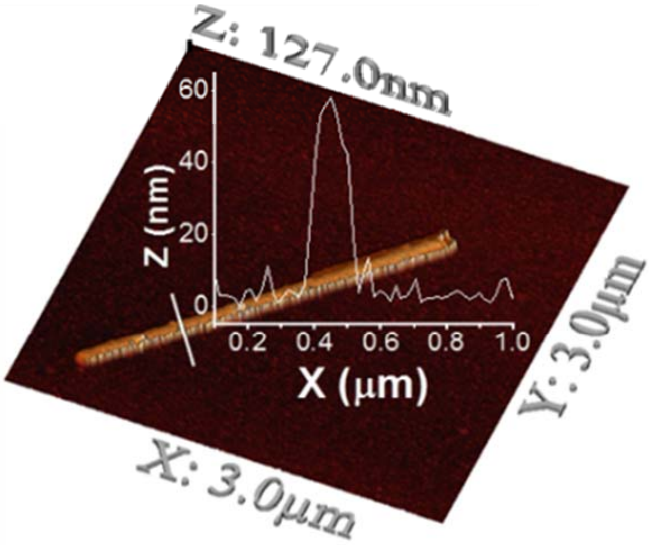

Figure 39. Three-dimensional AFM topographic image representation of an individual nanowire lying on platinum coated silicon substrate surface. The inset shows the corresponding scanline taken along the solid white line crossing the nanowire [198].

A typical measurement was performed as follows: first, after having located a nanowire by AFM operated in tapping mode, the probe tip was positioned on the crest of the nanowire; second, the AFM mode was switched to contact, followed by the application of AC and DC voltage combination for local hysteresis measurements. The loops were acquired by scanning a DC bias

in 200 steps, with the duration of each step being 0.1 s. The applied AC signal has amplitude of 0.5 V and frequency of 25 kHz. During the PFM measurement, extreme care was taken to prevent the movement of nanowire under the force applied by the AFM tip. Figure 39 shows a 3D representation of an individual $BiFeO_3$ nanowire acquired by tapping mode AFM. The nanowire is 2.5 μm long with a diameter of about 60 nm, as measured from the height profile of the nanowire (inset of Figure 39).

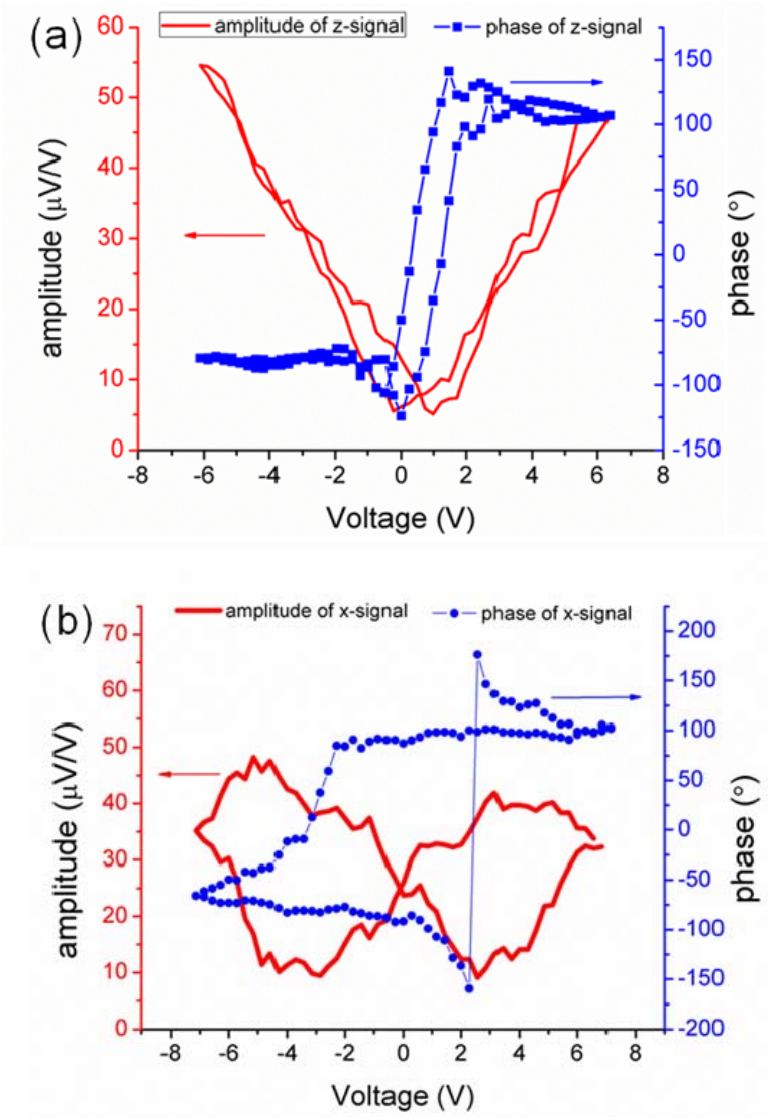

Figure 40. An example of PFM phase-voltage hysteresis and amplitude-voltage "butterfly" loops of an individual $BiFeO_3$ nanowire in (a) *z*- (out of plane) and (b) *x*- (in plane) direction, respectively [198].

The local piezoelectric hysteresis loops of both in plane (x-PFM) and out of plane (z-PFM) signals clearly demonstrate the ferroelectricity of the nanowires. Here we have chosen to present our PFM data in the form of the mixed PFM signal [$Amplitude \times cos\ (\Phi - \Phi_0)$], where Φ and Φ_0 are the phase of the signal and a phase offset with respect to the driving excitation voltage, respectively. Φ_0 was adjusted prior to measurements such that the quadrature signal [$Amplitude \times sin\ (\Phi - \Phi_0)$] is zero within the noise limits of our system rather than in the form of amplitude and phase because it is a more concise mode of showing the results. Otherwise, the amplitude and phase of the hysteresis loops of the mixed PFM signals (both z and x), for example, shown in Figure 41a would need two graphs, as shown in Figure 40. The relationships between the mixed PFM signals and their amplitude/phase representation is obvious: amplitude = $[(lockin\ X)^2 + (lockin\ Y)^2]^{1/2}$, and $(\Phi - \Phi_0) = atan2\ [(lockin\ Y)/(lockin\ X)]$, where "$atan2$" is the arc tangent function expanded to all 4 quadrants of the trigonometric plane.

The hysteresis loops shown in Figure 41a, acquired from the nanowire shown in the inset, exhibit a well-defined hysteretic behavior. The electrostatic (linear) part was subtracted from the z-PFM loop, to emphasize only the ferroelectric contribution as reported in the literature [218]. The hysteresis loops clearly imply the existence of a switchable ferroelectric polarization in the as-synthesized $BiFeO_3$ nanowires. The estimated coercive field is about 400 kV/cm, which is the same order of magnitude of that of epitaxial $BiFeO_3$ thin films [219]. The hysteresis loops suggest a strong asymmetry, which could arise from a built-in field caused either by stoichiometric or crystalline defects or by an asymmetric charge compensation of polarization. Besides shifting the hysteresis loop, the electric field could even cause a non-180° switching of polarization [215].

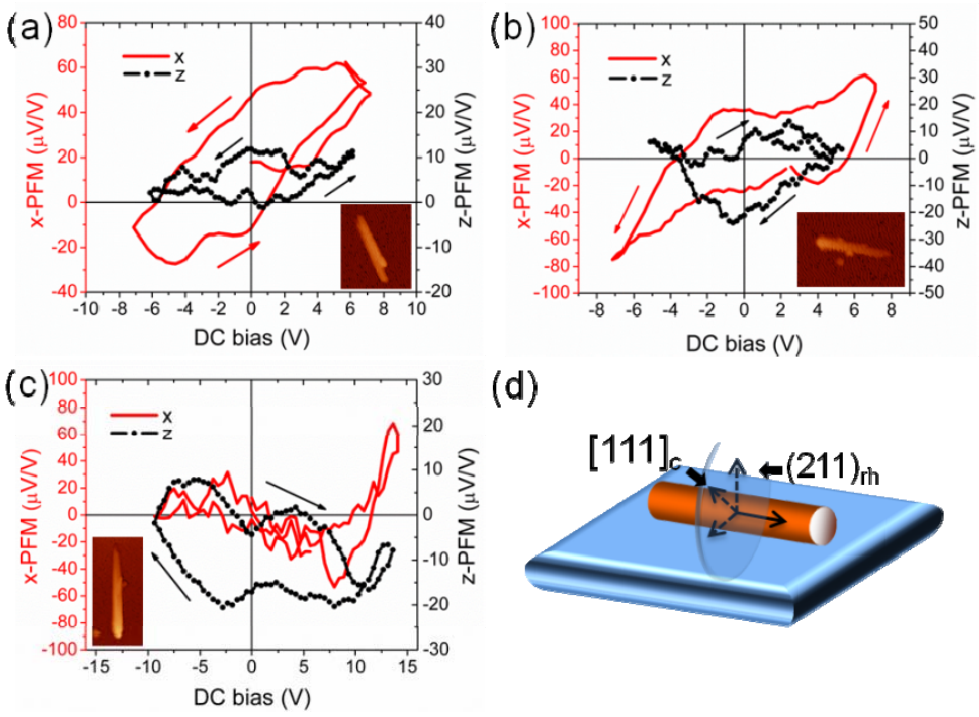

Figure 41. (a-c) PFM hysteresis loops (*x* and *z*-direction) taken from the nanowires shown in each figure, respectively. (d) Schematic diagram showing the relative geometry position between $[111]_c$ direction in the nanowires and the substrate [198].

In addition, we found that the intensity of both the *x*- and *z*-PFM signals have large variations from one nanowire to another, apparently dependent on the relative orientation between the nanowire axis and cantilever (Figure 41b and c). However, most of the nanowires exhibit a prominent and well-defined *x*-PFM hysteresis, while the *z*-PFM component has a lower magnitude and a rather irregular shape. The latter is thought to originate from the fact that the loops are not completely saturated, since we limited our maximum bias applied to relatively low values (8-12 V) to avoid the electrical breakdown of the nanowires.

4.4 Discussion

To explain the results, we first focused on the orientation of the crystalline lattice in the as-synthesized $BiFeO_3$ nanowires. As shown by the SAED pattern and HRTEM image (Figure 38c

and d), the cross section of the $BiFeO_3$ nanowires (radial direction) is parallel with rhombohedral (211) planes, and the (001) planes are almost perpendicular (89°) to the (211) planes. Alternatively, the unit cell can be described in a hexagonal frame of reference with its *c*-axis parallel to the diagonal of the perovskite cube, i.e., $[001]_{hex}||[111]_c$. Hence, the pseudocubic $[111]_c$ direction is perpendicular to the nanowires longitudinal axis.

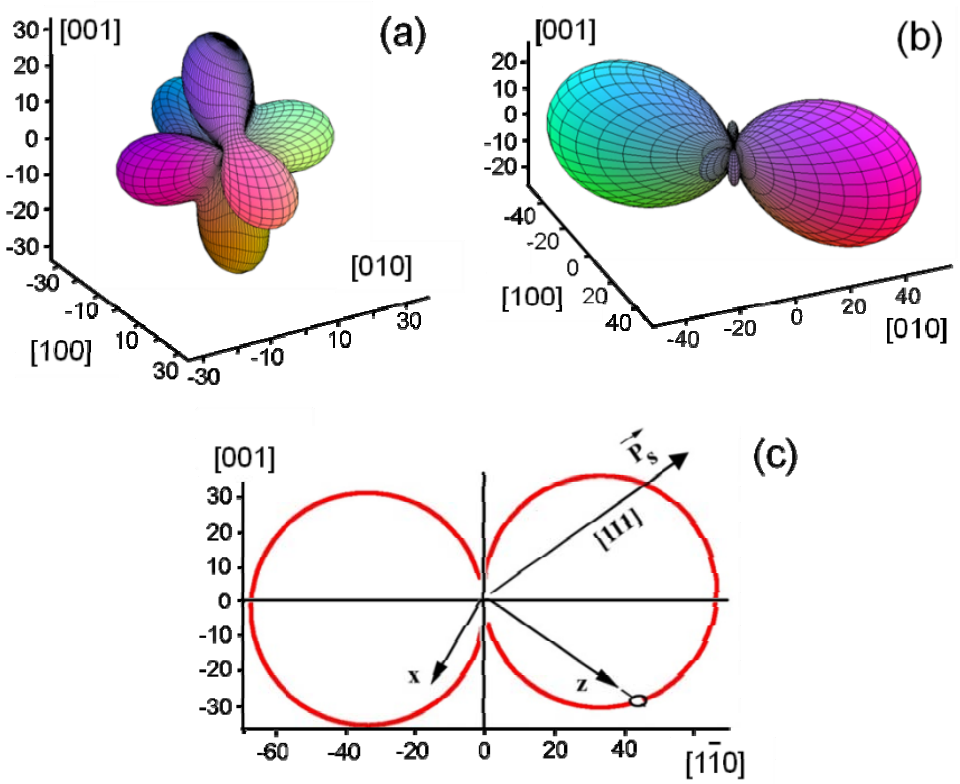

Figure 42. Calculated piezoelectric tensor for the longitudinal piezoresponse d_{zz} (a) and lateral piezoresponse d_{zxz} (b). (c) Cross-section of (b) in the ($\mathbf{1\bar{1}0}$) plane, containing the spontaneous polarization [198].

The spontaneous polarization of bulk $BiFeO_3$ is known to lie along the $[111]_c$ direction [24], and we consider that this is also the case for our unstressed nanowires. However, because piezoelectricity is characterized by a 3rd-order rank tensor, in general case the magnitude of the piezoelectric response is not simply related to the polarization component along the measurement

direction [220-222]. To interpret the PFM hysteresis loops, we estimated the piezoelectric coefficients of rhombohedral $BiFeO_3$ using the electrostriction coefficients Q_{11}, Q_{12} and Q_{44} calculated by Zhang *et al* [223]. For the rhombohedral symmetry, there are four independent piezoelectric coefficients that can be calculated using the phenomenologically-derived equations [224]: the two independent (relative) permittivity coefficients for the rhombohedral phase were estimated using the values measured for epitaxial films of $BiFeO_3$ with different orientations as $\varepsilon_{11} = (1+ \eta_{11}) \sim 80$ and $\varepsilon_{12} = \eta_{12} \sim -21$ for the pseudocubic axes. We calculated the following values for the piezoelectric coefficients in the pseudocubic system: $d_{33} = d_{[001]} = 31$ pm/V, $d_{31} = -15$ pm/V, $d_{14} = -2$ pm/V and $d_{15} = 2.9$ pm/V.

The estimated dependence of the longitudinal piezoelectric coefficient (d_{zz}) on the measurement direction is shown in Figure 42a, and we notice that its shape resembles the piezoelectric surface tensor of rhombohedral lead zirconate titanate, implying that the maximum of d_{zz} is not along the polarization direction (the $[111]_c$), but very close to the principal pseudocubic directions. This could explain why we found a *z*-PFM response almost for every nanowire probed, irrespective of its orientation with respect to the cantilever, since the angular window for which d_{zz} is zero is very small. The dependence of the d_{zxz} coefficient, associated with the *x*-PFM signal, is shown in Figure 42b. To better understand the angular dependence, we also show a cross-section of the surface in the $(1\bar{1}0)$ pseudocubic plane that contains also the direction of spontaneous polarization Figure 42c. Again, the maximum of the d_{zxz} coefficient (intersection of the *z*-axis with the piezoelectric surface) does not occur along the polarization direction, but occurs when the electric field (along the direction *z* in the Fig.) is close to the $[1\bar{1}0]$ crystallographic direction. However, in contrast to d_{zz}, the lobes of the d_{zxz} surface are more concentrated close to the $(1\bar{1}0)$ plane. Since the nanowires are randomly oriented, it means that

the chances to measure a zero *x*-PFM response are higher than that of the *z*-PFM, thus explaining why we could measure an almost zero in-plane response (Figure 41c).

4.5 Summary

In this chapter, the ferroelectric properties of single crystalline $BiFeO_3$ nanowires synthesized by a hydrothermal method were investigated by PFM. We have shown that nonvolatile electric polarization can be switched in both *x*- and *z*-directions of these nanowires, evidencing that they retain ferroelectricity despite their small radial dimension. Furthermore, we observed that the magnitude of both the *x*- and *z*-PFM signals has variations from one nanowire to another, dependent on the relative orientation of the crystalline lattice of the nanowire and cantilever. We described this behavior by estimating the shape of the surface piezoelectric coefficients tensor for the rhombohedral symmetry. These results will improve our understanding of the fundamental ferroelectric properties of 1D single crystal $BiFeO_3$ nanowires and also be helpful for designing low dimensional ferroelectric nonvolatile memory devices using such nanowires as building blocks.

Chapter 5

Highly Active Nanocomposite Photocatalyst Consisting of $BiFeO_3$ Nanowires and Laser Ablated Au Nanoparticles (PLAL-AuNPs)

Semiconductor photocatalysis has received considerable attention as a potential solution to the worldwide energy shortage and for counteracting environmental degradation. The emergence of nanostructured semiconductor materials as photocatalysts has given rise to diverse and flexible ways of promoting photocatalytic efficiency. Among them, the use of 1D semiconductor is one of the most promising routes for solar water splitting. In comparison with bulk materials, photocatalysts in the form of 1D nanostructure such as nanowires [225, 226], nanotubes [227] and nanobelts [228] have demonstrated enhanced efficiencies for photocatalytic water splitting. The reduced radial dimension and the extremely large surface-to-volume ratio promote rapid diffusion of photogenerated electrons/holes to the nanowires' surface before recombination can occur, and thus can increase separation efficiency of charge carriers [119]. Most importantly, single crystalline nanowires are deemed to be more active since ballistic charge transport along the wire axis is significantly more efficient than the diffusive transport in powdered or polycrystalline materials. Multiferroic materials $BiFeO_3$ have recently been recognized as a potential system for applications in photocatalysis due to their relatively narrow band gaps (2.2-

2.8 eV), which allow them to harvest part of visible light of solar radiation, as well as good chemical stability [80, 82, 188, 189]. However, investigations of $BiFeO_3$ nanomaterials for photocatalytic water splitting are still limited [75, 81, 191]. $BiFeO_3$ nanowires in single-crystalline form which are expected to be highly active photocatalysts for solar water splitting have not been explored yet.

On the other hand, semiconductor-noble metal hybrid nanocrystals that integrate multiple functional components into one system represent a promising novel class of materials with multifunctional characters and the possibility of effectively coupling different properties that are different from the original components. They have potential applications in various significant fields including solar cells, photocatalysis, light emission and electronic devices. It is reported that the photocatalytic performance of semiconductor materials can be enhanced by the combination with noble metal (e.g. Ag, Au, Pt, etc.) nanostructures [171, 178, 229]. Among them, gold nanoparticles (AuNPs) are very promising because they exhibit excellent chemical stability and a characteristic absorption peak in the visible wavelength range [230]. The enhanced photoactivity is attributed to the roles of the AuNPs as electron-trapping centers [171, 231] and/or the localized surface plasmon resonance (LSPR) effect [178, 232, 233]. In addition, it has also been discovered that AuNPs exhibit a dual role as light harvesters injecting electrons into the semiconductor and also as catalytic sites for gas generation [234-236]. Pulsed laser ablation in liquid phase (PLAL) on an Au bulk target produces relatively ‘‘bare and clean’’ AuNPs [237, 238], which have been proven to facilitate catalytic reactions as the reactive sites on the nanoparticles’ surface are mostly exposed and readily accessible to reactants. It is recently reported that the PLAL-AuNPs/CeO_2 nanocomposites exhibit improved catalytic activity

compared to other catalysts for the reduction of 4-nitrophenol [239], prompting us to expand the applications of PLAL-AuNPs in solar water splitting field.

5.1 Experimental Section

5.1.1 Materials Synthesis

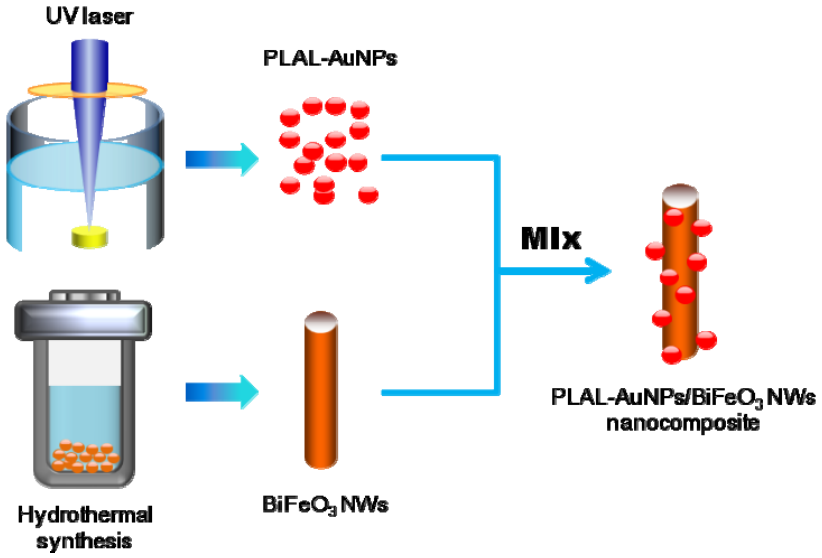

Figure 43. Schematic diagram for synthesizing PLAL-AuNPs/$BiFeO_3$ nanowires hybrid nanostructures [199].

5.1.1.1 Synthesis of AuNPs by Laser Ablation in Liquid (PLAL-AuNPs)

Laser ablation was carried out with a KrF excimer laser (GSI Lumonics PM-846, wavelength: 248 nm, repetition rate 20 Hz). The beam was focused by an objective lens with a focal length of 7.5 cm onto a gold plate target with a diameter of 8 mm and 1.5 mm in thickness. The gold target was placed at the bottom of a glass vessel (6 mL) filled with D.I. H_2O (pH ≈ 6.0). The depth of the water layer above the target was 10 mm. The laser fluence on the target was set at ~40.0 J/cm^2 during all ablation processes.

5.1.1.2 Synthesis and Purification of AuNPs by Chemical Method (Chem-AuNPs)

The chemically synthesized AuNPs were prepared as a previous publication [240]. First, 1 mL $HAuCl_4 \cdot 3H_2O$ aqueous solution (1 wt%) was added into 90 mL of distilled water, followed by injection of 2 mL of sodium citrate solution (38.8 mM). The reaction mixture was then stirred for 1 min. Subsequently, 1 mL of 0.075 wt% freshly prepared $NaBH_4$ solution (in 38.8 mM sodium citrate solution) was added and the reaction mixture was stirred for 12 h at room temperature. Then, all as-synthesized Au colloidal solution was purified to remove un-attached or un-reacted chemical species, and 93 mL of 1.25 mM sodium citrate solution was loaded and sonicated to re-disperse the AuNPs. A delicate purification process was performed to the as-prepared Chem-AuNPs solution by using ultra-centrifuge filters. In a typical experiment, 12 mL of as-prepared Au colloidal solution was centrifuged at 4500 rpm with ultra-centrifuge filters into 4 mL concentrated solution (8 mL of the filtrate was discarded). And then 8 mL of distilled water was introduced to re-disperse the 4 mL highly concentrated AuNPs. After the pre-purification process, additional washing was repeated twice. Finally, AuNPs were re-dispersed in pure D.I. water and used immediately for hybridization and characterization.

5.1.1.3 Preparation of Hybrid AuNPs/$BiFeO_3$ Nanowires Nanocomposites

50 mg of $BiFeO_3$ nanowires powder (see details in the experimental section of chapter 4) was added to freshly prepared PLAL-AuNPs (or purified Chem-AuNPs) solution and mixed by shaking. The mixture solution was incubated at room temperature for 30 min. Then the precipitate was recovered by centrifugation, followed by washing with distilled water. Then the nanocomposites were heated at 200°C for 10 h to enhance the bonding between the Au NPs and $BiFeO_3$ nanowires.

5.1.2 Photocatalytic Water Splitting Measurements

In the photocatalytic reactions, the photocatalyst powder (50 mg) was dispersed in $FeCl_3$ solution (4 mmol/L, 50 mL). The photocatalytic reactions were performed by adopting a 300 W xenon lamp (optical filter, $\lambda > 380$ nm) as an outer irradiation source. The quartz cover allowed ample transmission from the xenon lamp into the chamber. The Pyrex chamber was cooled by partially submerging it in cold water during photocatalytic reactions. The gas in the chamber was sampled by vacuum-tight syringes and then immediately analyzed by a gas chromatograph (Shimadzu GC-8A) using a thermal conductivity detector (TCD). For wavelength dependence photocatalytic measurement, optical filters (530 ± 25 nm, and 630 ± 25 nm) from Edmund Optics were used.

5.2 Characterizations

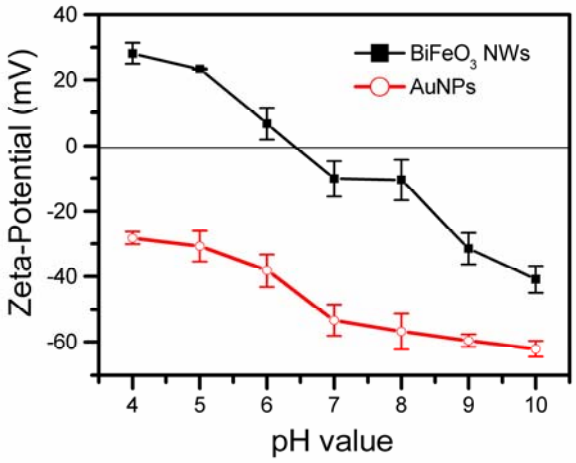

Figure 44. Zeta-potential of $BiFeO_3$ nanowires and PLAL-AuNPs aqueous solution at different pH values [199]. The solid line is to guide the trend of the measured points.

The formation process of the PLAL-AuNPs/$BiFeO_3$ nanowires nanocomposites is conceptually displayed in Figure 43. Our synthesis approach of the hybrid PLAL-AuNPs/$BiFeO_3$ nanowires differs from conventional methods for synthesizing metal-semiconductor nanocomposites, where the support semiconductor materials and/or metal nanoparticles need to be first functionalized

with functional groups to promote their coupling. Indeed, it does not require pre-functionalization of either the $BiFeO_3$ nanowires or the AuNPs. The effective immobilizing process is associated with the surface chemistry of the PLAL-AuNPs and $BiFeO_3$ nanowires.

Zeta-potential measurement (Figure 44) reveals that the Isoelectric Point (IEP) of $BiFeO_3$ nanowires is about 6.5. As the pH value of the incubation solution (D.I. water) is less than 6.0, the surface of $BiFeO_3$ is slightly positively charged. On the other hand, the PLAL-AuNPs are negatively charged at this pH value, which is caused by the adsorption of -OH groups [238]. As a result, the electrostatic interaction between them is expected to result in the formation of a hybrid $Au/BiFeO_3$ structure.

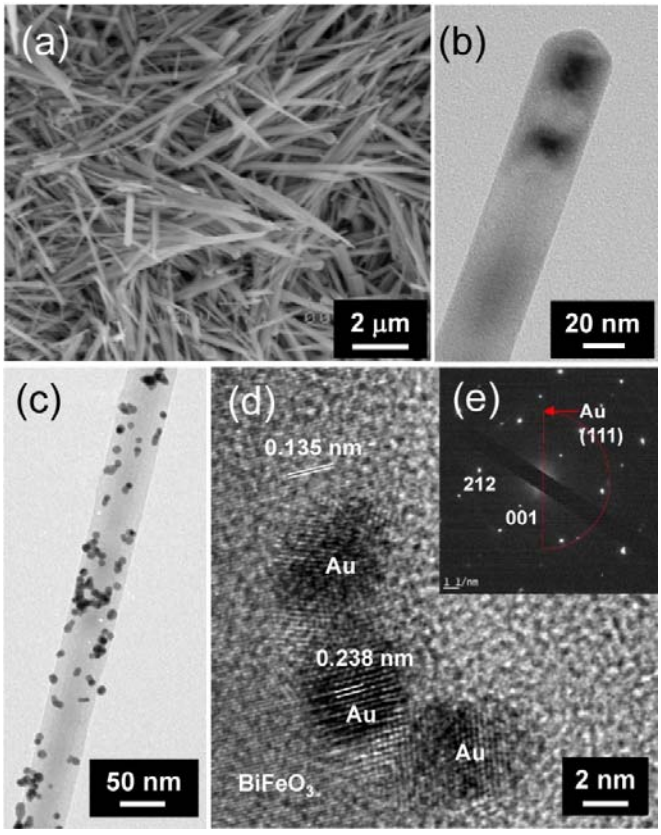

Figure 45. (a) SEM and (b) TEM images of the $BiFeO_3$ nanowires. (c) TEM and (d) HRTEM images of the PLAL-AuNPs (1.0 wt%) decorated $BiFeO_3$ nanowires, respectively. (e) SAED pattern taken from (c) [199].

SEM image of the as-synthesized $BiFeO_3$ nanowires is shown in Figure 45a. Figure 45b and c show TEM images of the $BiFeO_3$ nanowires and PLAL-AuNPs(1.0 wt%)/$BiFeO_3$ nanowires nanocomposite, respectively. Uniform AuNPs with an average diameter of about 5 nm were distributed evenly on the surface of the $BiFeO_3$ nanowires. The Au/$BiFeO_3$ hybrid nanostructures were further characterized using HRTEM, as shown in Figure 45d. The lattice fringes of attached AuNPs and the $BiFeO_3$ NW surface were clearly observed, with a spacing of 2.38 Å corresponding to that of the (111) plane of face-centered cubic Au, and a lattice spacing of 1.35 Å matching that of the (422) crystal planes of perovskite structured $BiFeO_3$. These results regarding crystalline structures are in good agreement with those obtained from the SAED patterns (Figure 45e).

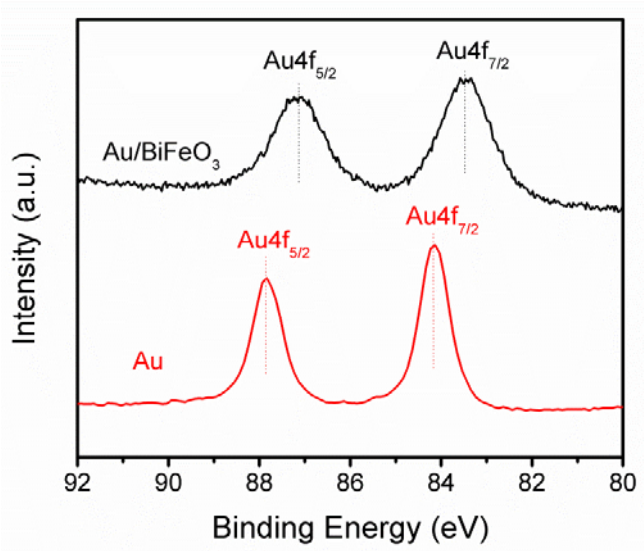

Figure 46. XPS spectra of Au4*f* in pristine PLAL-AuNPs and PLAL-AuNPs (1.0 wt%)/$BiFeO_3$ nanowires nanocomposite [199].

To gain more detailed insight into the interaction between the AuNPs and $BiFeO_3$ nanowires support, the valence states of Au4*f* in the PLAL-AuNPs/$BiFeO_3$ nanowires nanocomposite and pristine AuNPs were investigated using XPS. As shown in Figure 46, the XPS peaks observed for PLAL-Au (1.0 wt%)/$BiFeO_3$ nanowires confirm the presence of Au(0) with binding energies

of 87.1 and 83.5 eV that are somewhat shifted towards lower values than binding energies of pristine AuNPs (87.8 and 84.2 eV). This suggests the occurrence of charge transfer between the $BiFeO_3$ nanowires support and AuNPs, as reported in other counterpart noble metal nanoparticle-semiconductor systems [234, 241]. It should be noted that the peak intensity of pristine Au is higher than that of the nanocomposite. This is due to the minute amount (1.0 wt%) of Au in the Au/$BiFeO_3$ nanocomposite, making the Au element difficult to detect by XPS measurements.

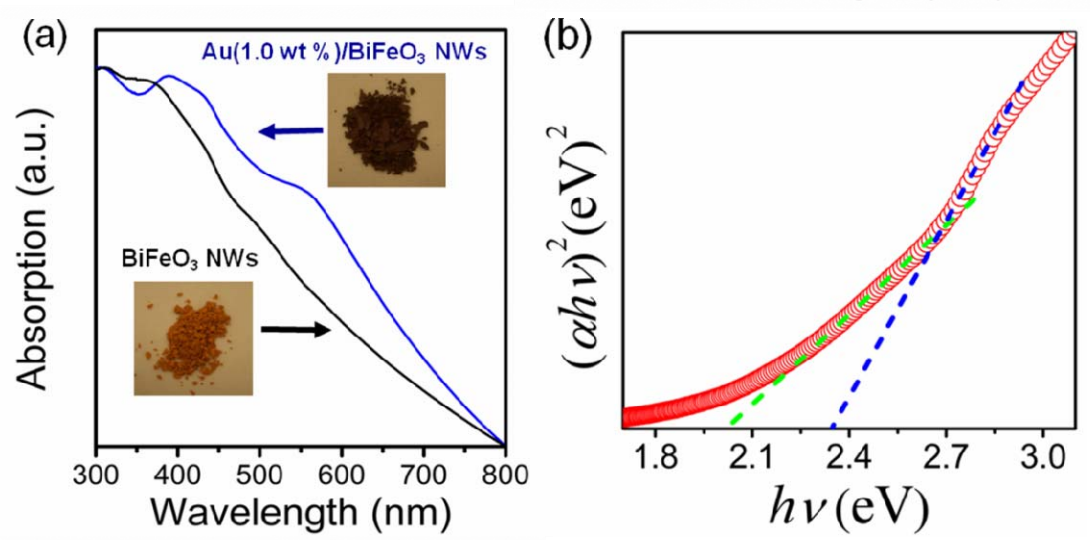

Figure 47. (a) Normalized UV-vis absorption spectra of $BiFeO_3$ nanowires and PLAL-Au(1.0 wt%)/$BiFeO_3$ nanowires nanocomposite dispersed in ethanol. (b) Calculation diagram of the band gap of $BiFeO_3$ nanowires [199].

It is well-known that the optical absorption property of semiconductors is a key factor in determining their band gaps and photocatalytic performance. Figure 47a shows the UV-vis absorption spectra of $BiFeO_3$ nanowires with and without AuNPs. The optical spectroscopy of $BiFeO_3$ nanowires shows an absorption edge which is due to the band gap transition. The optical absorption coefficient near the band edge follows the equation [242]:

$$\alpha h\nu = A(h\nu - E_g)^{n/2} \qquad \text{(Eq. 5.1)}$$

where α, h, ν, E_g, and A are absorption coefficient, Planck constant, light frequency, band gap and a constant, respectively. The optical band gap of $BiFeO_3$ photocatalyst can thus be obtained from the plots of $(\alpha h\nu)^2$ versus photon energy $h\nu$. This relationship gives the band gap (E_g) by extrapolating the straight portion of $(\alpha h\nu)^2$ against $h\nu$ plot to the point $\alpha = 0$ (Figure 47b). Because of the plots of linear nature, the value of n for $BiFeO_3$ is 1, indicating that it has a direct band gap. After calculations, the values were determined to be 2.35 eV from the absorption onsets, which is quite comparable with previous results [80, 81, 188]. In addition, a secondary edge that can be assigned to crystal field transition or defect (e.g. oxygen vacancy) was observed at higher wavelengths. As expected, the UV-vis spectrum of the $Au/BiFeO_3$ samples exhibits a typical Au surface plasmon band in the visible region between 500 and 600 nm.

5.3 Photocatalytic Water Splitting Performance

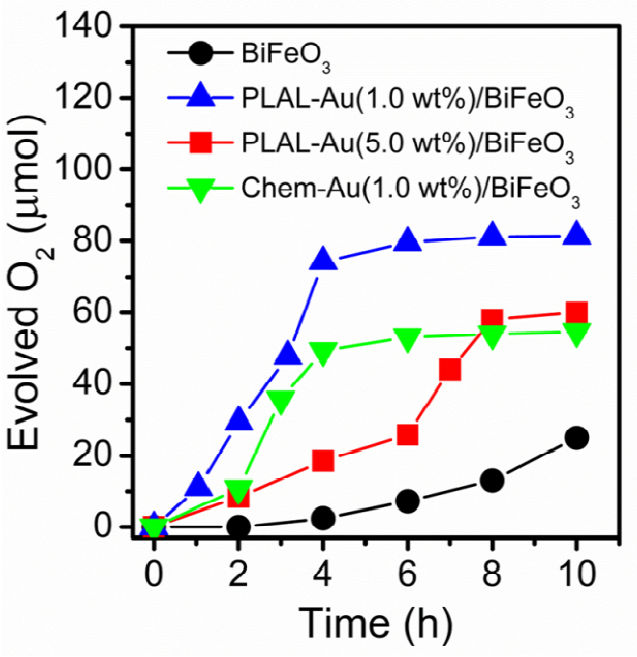

Figure 48. Oxygen evolved upon visible light (λ > 380 nm) illumination of $FeCl_3$ suspension (4 mmol/L, 50 mL) containing the photocatalysts (50 mg) [199].

The capability of the $BiFeO_3$ nanowires to drive oxygen evolution from water oxidation under visible light ($\lambda > 380$ nm) illumination was analyzed using $FeCl_3$ as a sacrificial electron acceptor. Figure 48 shows oxygen evolution over time for the pristine $BiFeO_3$ nanowires and a series of Au/$BiFeO_3$ samples. Table 1 lists parameters for photocatalytic activity of all samples under study. The $BiFeO_3$ nanowires exhibit much better photocatalytic activity than previously reported $BiFeO_3$ nanocubes under similar conditions and the same loading amount of catalysts [81], which can be attributed to high surface area and unique morphology of the nanowires. Interestingly, the amount of oxygen produced using the PLAL-AuNPs/$BiFeO_3$ photocatalyst with 1 wt% Au loading is ~30 times higher than that produced using the parent wires during the first 4 h, indicating remarkable influence of AuNPs on water oxidation activity under visible light. Such an enhancement of photocatalytic activity is much more significant than that (~2-10 times) of other reported Au-semiconductor systems [230, 231, 243-245].

Table 1. Initial reaction rate (r_0) and amount of oxygen evolved after 4 h under visible light irradiation with different photocatalysts.

Catalyst	r_0 (μmol/min)	Evolved O_2, 4 h (μmol)
$BiFeO_3$ nanowires	0.010	2.0
PLAL-AuNPs (1.0 wt %)/$BiFeO_3$ nanowires	0.309	73.7
PLAL-AuNPs (5.0 wt %)/$BiFeO_3$ nanowires	0.077	18.8
Chem-AuNPs (1.0 wt %)/$BiFeO_3$ nanowires	0.171	49.5

For a fair comparison, a nanocomposite photocatalyst consisting of $BiFeO_3$ nanowires and 1.0 wt% of chemically synthesized, citrate ligand-capped AuNPs (Chem-AuNPs) with an average diameter similar to that of the PLAL-AuNPs was prepared and its photocatalytic activity was tested under the same conditions. Figure 49a and b show the TEM images of PLAL-AuNPs and Chem-AuNPs, respectively. As we can see that the average size of the Chem-AuNPs (4.43

nm) and PLAL-AuNPs (4.78 nm) is quite similar. The photoabsorption spectra shown in Figure 49c confirm that these two types of AuNPs process quite similar optical characteristics as well.

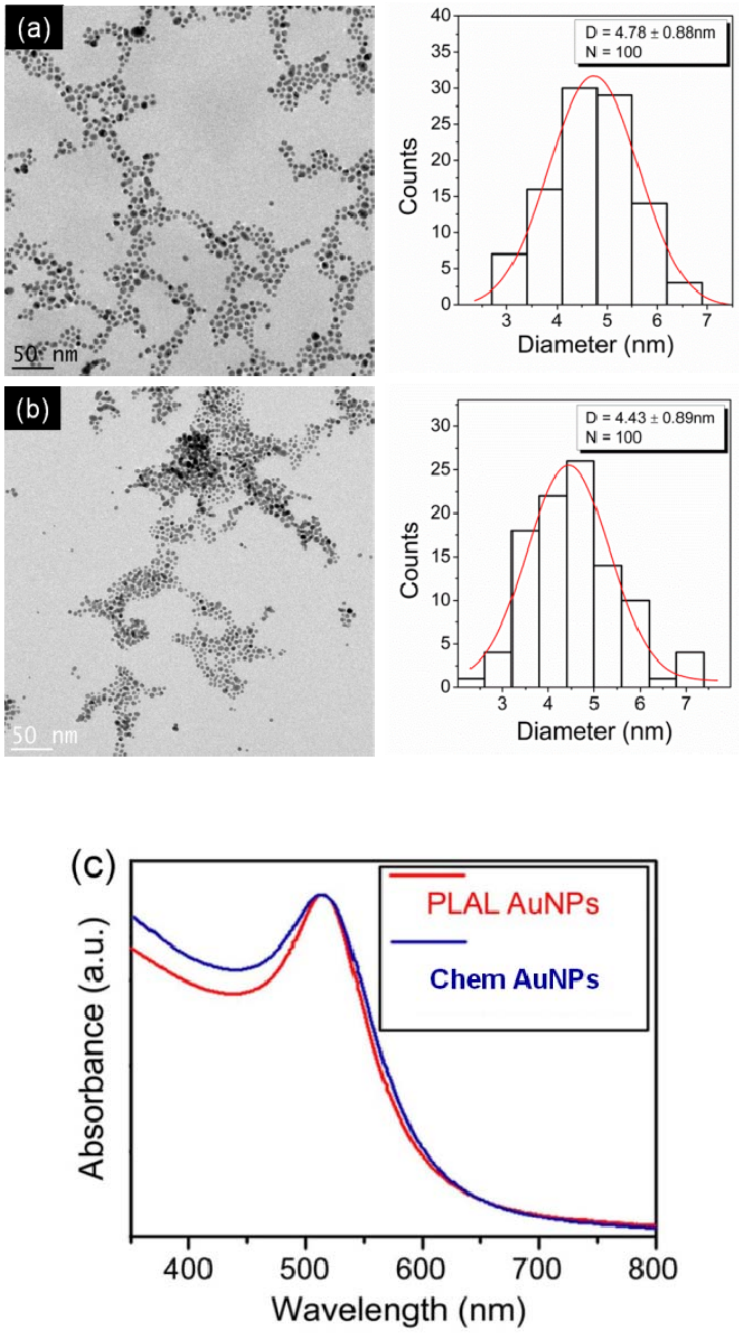

Figure 49. TEM images of (a) PLAL-AuNPs and (b) Chem-AuNPs. On the right of each figure the histograms of size distribution is displayed, respectively. (c) UV-vis absorption spectra of PLAL- and Chem-AuNPs [199].

As listed in Table 1, the initial reaction rate (r_0) of the Chem-AuNPs (1.0 wt%)/$BiFeO_3$ nanocomposite is 0.171 mmol/min, about 1.5 times smaller than that (0.309 mmol/min) of the PLAL-AuNPs (1.0 wt%)/$BiFeO_3$ nanowires sample. The PLAL-AuNPs and Chem-AuNPs have similar average size, size distribution, optical absorption (Figure 49) and the Au-support ratio, therefore the distinct difference in photoactivity should be related to their inherent difference in surface-chemistry features.

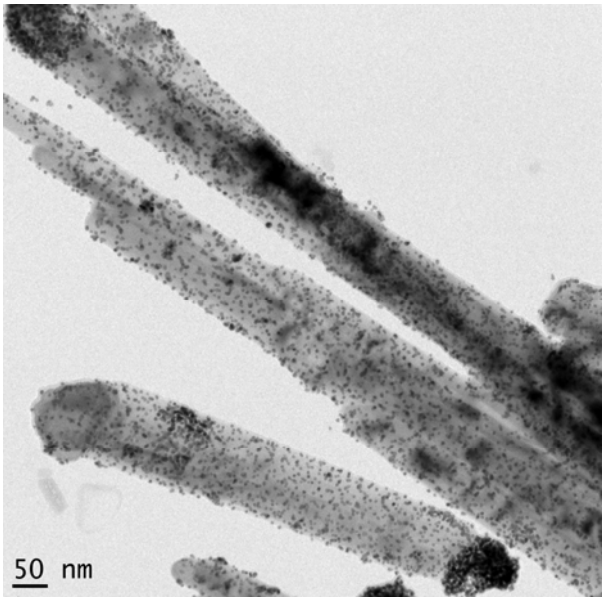

Figure 50. TEM image of PLAL-AuNPs (5.0 wt%)/$BiFeO_3$ nanowires nanocomposite [199].

The photoactivity decreases upon increasing the Au loading to 5.0 wt%. As we can see from the TEM image shown in Figure 50, the surface of the $BiFeO_3$ nanowires are largely covered by AuNPs and some of them are attached with each other. It was reported that AuNPs by themselves do not exhibit any photoactivity [246]. Therefore, the cooperative effect of the AuNPs and the support surface on the reaction can be used to describe our results. The balanced combination of several factors (e.g. surface coverage of the support semiconductor, population of residual hydroxyl groups, and metal dispersion, etc.) that are influenced by the Au loading amount determines the maximum photocatalytic efficiency. AuNPs would also serve as electron-

hole recombination centers when the support surface is largely covered by AuNPs, and thereby reduce the photoactivity [247].

5.4 Proposed Mechanism

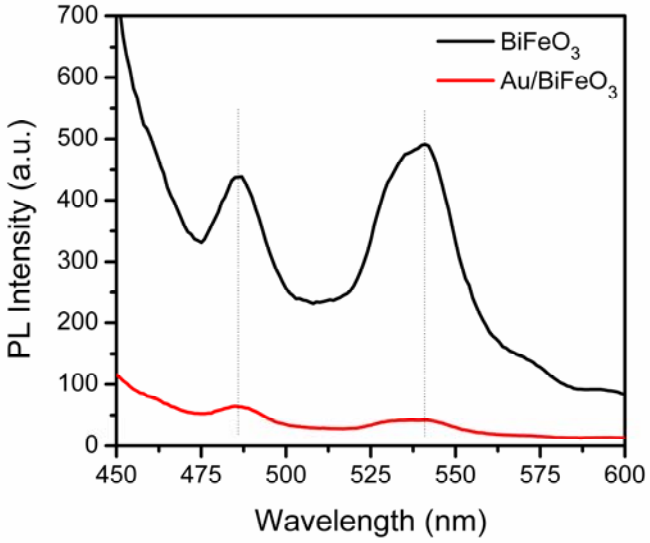

Figure 51. Photoluminescence spectra of $BiFeO_3$ nanowires and PLAL-AuNPs (1.0 wt%)/$BiFeO_3$ nanowires nanocomposite [199].

To understand the mechanism of the enhanced photocatalytic activity, we investigated the photoluminescence (PL) spectra of the $BiFeO_3$ nanowires and PLAL-AuNPs (1.0 wt%)/$BiFeO_3$ nanowires nanocomposite (Figure 51). Two emission peaks were detected at around 485 and 540 nm in the case of $BiFeO_3$ nanowires, consistent with those reported in the literature [248]. The PL emission of $BiFeO_3$ is drastically quenched in the presence of PLAL-AuNPs, suggesting the occurrence of efficient charge and/or energy transfer from $BiFeO_3$ nanowires to AuNPs. Energy transfer may also occur since the absorption spectrum of Au overlaps with the emission spectrum of $BiFeO_3$. The charge/energy transfer process is closely related to the distance between the two materials involved. It is known that when both transfer processes are present, charge transfer usually dominates at short distance [249, 250]. In our case, the AuNPs and $BiFeO_3$ nanowires are

tightly attached to each other. Therefore, the observed quenching of the PL peak is most probably due to the electron transfer instead of energy transfer. In addition, this charge transfer mechanism is also consistent with the improved photocatalytic performance.

Figure 52a illustrates the proposed dominating mechanism in the present photocatalyst system. The Fermi level of Au is more positive (+0.5 V versus NHE), compared to the conduction band energy of $BiFeO_3$ (+0.1 V versus NHE) [194], as shown in Figure 52b. Thus, the charge transfer from the excited $BiFeO_3$ to AuNPs would be thermodynamically favorable. After combining them together, the photogenerated electrons will transfer from the conduction band of $BiFeO_3$ to Au to reach a new common Fermi level E_f due to electron accumulation around their interface. This charge transfer process can reduce the recombination rate of e^-/h^+ pairs, thus enhancing the photocatalytic activity.

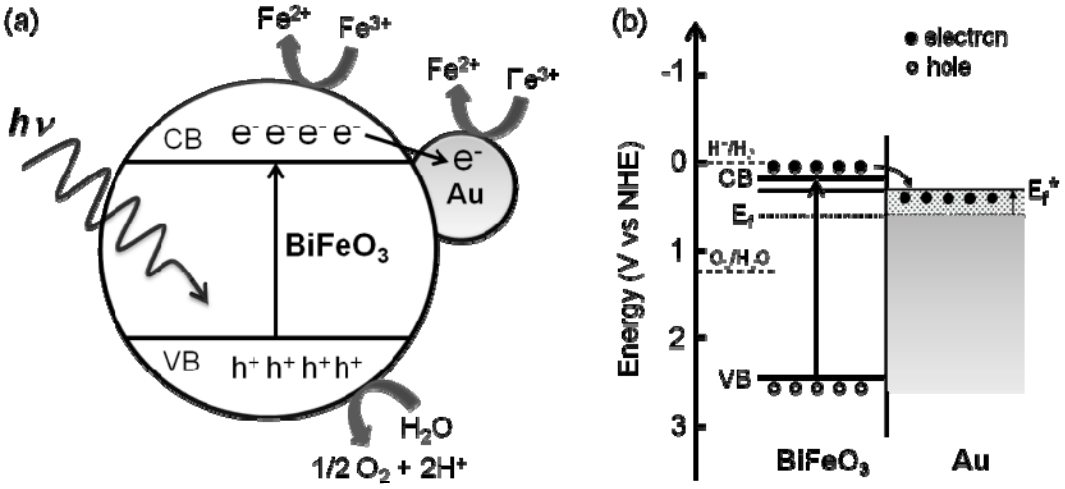

Figure 52. (a) Elementary step the photocatalytic oxygen evolution by Au/$BiFeO_3$ nanocomposite under visible light. (b) Proposed mechanism of charge transfer with energy levels on the NHE scale [199].

To further verify the contribution of the LSPR effect of AuNPs to the photoactivity, we tested the dependence of the photocatalytic reaction rate on radiation wavelength (Figure 53). The enhancement of photoactivity at a wavelength of 530 ± 25 nm (in the range of plasmonic

absorption peak) is more significant (~3 times) than that at 630 ± 25 nm compared with pristine $BiFeO_3$ nanowires, suggesting that the LSPR effect of the AuNPs also plays an important role in the remarkably enhanced efficiency of PLAL-Au/$BiFeO_3$ nanowires samples.

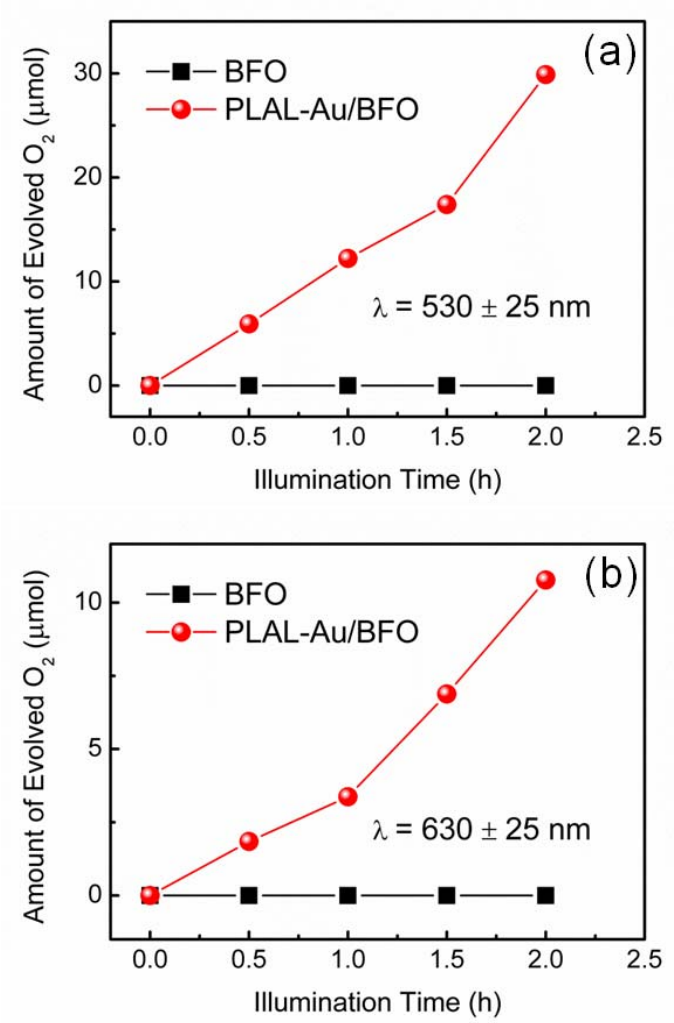

Figure 53. Oxygen evolved upon visible light illumination at different wavelengths (a) 530 ± 25 nm and (b) 630 ± 25 nm of $BiFeO_3$ nanowires and PLAL-AuNPs (1.0 wt%)/$BiFeO_3$ nanowires nanocomposite in $FeCl_3$ suspension (4 mmol/L, 30 mL) containing the photocatalysts (30 mg) [199].

The enhancement of the photocatalytic activity can be attributed to several reasons. First, the light absorption can be enhanced due to the LSPR effect in a certain wavelength range. In addition, it is known that the surface plasmon can heat up the local environment, increasing the

mass transfer of the molecules and enhancing the reaction rates [178, 229]. Another possibility is that the LSPR-exited electrons in AuNPs which have sufficient energy can across the space-charge region and transfer to the conduction band of $BiFeO_3$. Until now, there are only very limited studies photocatalytic properties on the Au NPs and visible-light-active semiconductor hybrid systems such as Au/N-doped TiO_2 [251] and Au/$BiVO_4$ nanocomposite [252]. These reports have also confirmed that LSPR is a critical factor in enhancing the photoactivity under visible light. Further studies are still needed to better understand the charge transfer mechanism during the photocatalytic process of such systems.

5.5 Summary

In this chapter, we have demonstrated the potential of a hybrid PLAL-AuNPs/$BiFeO_3$ nanowires nanocomposite synthesized by a functionalization step-free solution process for solar water splitting applications. An enhancement of ~30 times in photocatalytic activity for oxygen generation under visible light was observed when minute amount of AuNPs (1.0 wt%) prepared by laser ablation was added on the surface of $BiFeO_3$ nanowires. In addition, the photoactivity of PLAL-AuNPs/$BiFeO_3$ nanowires nanocomposite was found to be much better than that of Chem-AuNPs/$BiFeO_3$ nanowires nanocomposite. Their superior catalytic activity is likely due to the role of the AuNPs as electron trapping centers as well as the unique surface-chemistry features of the PLAL-AuNPs that can strengthen the interaction and promote charge transfer from $BiFeO_3$ to AuNPs. Also, the LSPR effect of the AuNPs plays an important role in remarkably enhanced photocatalytic efficiency of PLAL-AuNPs/$BiFeO_3$ nanowires samples.

Chapter 6

Microwave-assistant Hydrothermal Synthesis and Magnetic Properties of $BiFeO_3$ Nanoplates

$BiFeO_3$ nanomaterials with various sizes and shapes such as nanowires [74], nanotubes [72], nanocubes [80], nanospindles [79], nanorods [76], and hollow spheres [82] have been reported and possess a variety of interesting functional properties compared to their bulk form. Therefore, synthesis of multiferroic $BiFeO_3$ nanostructures with novel and well-defined morphology is important for both fundamental research and relevant for designing new multifunctional materials combining magnetic, ferroelectric and optoelectronic characteristics. 2D nanomaterials such as nanosheets and nanoplates have been explored extensively because their anisotropic shape is advantageous with respect to irregular-shaped nanocrystals for constructing nanodevices [253-255]. Design and morphological control of crystal facets is a commonly employed strategy to optimize the physical and chemical properties of various crystalline semiconductors. Recent developments in the synthesis of 2D crystalline nanosheets/plates show promising properties for developing new generation of optoelectronic devices and high-performance catalysts [256-260]. Lu *et al*. reported the synthesis of 2D $BiFeO_3$ plates using surfactant of cetyltrimethylammonium bromide (CTAB) [261]. However, synthesizing single-crystalline planar $BiFeO_3$ nanosheets or

nanoplates with controllable crystallographic facets by template- or surfactant free solution routes is still a major challenge.

Numerous reports have described the synthesis of $BiFeO_3$ materials by various routes that involve solid-state reactions [262], rapid molten salt sintering [66], mechanochemical synthesis [67], sol-gel method [68], or wet chemistry [70]. The majority of these processes require long reaction times and high temperatures, therefore involving high-energy consumption and cost. The most commonly used conventional solid-state synthesis of $BiFeO_3$ crystals requires a prolonged treatment at considerably high calcination temperatures (800°C or higher), causing a loss of bismuth and severe impurity contaminations [262, 263]. The hydrothermal technique is becoming one of the most important tools for advanced materials processing, as it is a simple and low-cost route with low reaction temperature, and also because it is very useful for producing various new types of nanohybrid and nanocomposite materials [264]. Recently, hydrothermal processing methods have been shown to yield highly crystalline $BiFeO_3$ products at low temperatures (100-250°C) [64, 80, 265]. Although this method can be efficient in the synthesis of materials using relatively low temperature, its main disadvantage is related to the long processing time due to slow reaction kinetics at the relevant temperature.

Microwave-assisted hydrothermal (M-H) methods are becoming widespread for the synthesis of nanomaterials as they offer a simple and low-cost approach to obtain highly crystalline nanocrystals within a very short reaction time with high yields [203-205]. Microwave heating provides energy to the reactants by means of molecular interaction with high-frequency electromagnetic radiation, which is different from that of conventional thermal treatment by convection current. In M-H processing, the precipitate can be rapidly dissolved in the aqueous solution to provide a saturated solution, resulting in enhancement of the reaction kinetics by one

to two orders of magnitude by high-frequency electromagnetic radiation (2.45 GHz). In addition to the extensively studied $BaTiO_3$ [266], recently the synthesis of several important inorganic materials (e.g. TiO_2 [267] and Fe_2O_3 [268]) was demonstrated in one step under M-H conditions. Up to now, a few reports have also presented the fabrication of $BiFeO_3$ nanostructures by the M-H approach [81, 269, 270], yet the treatment time needed for all these reports are still long (30 min or more) and a systematic study is still lacking.

In this chapter, we demonstrate a solution-based method for the synthesis of $BiFeO_3$ nanoplates under M-H conditions within a very short reaction time (1-2 min). The products were characterized by XRD, SEM, HRTEM and XPS. Various parameters influencing the products such as reaction time, radiation power, and alkali concentration were discussed in detail in this study. We further investigated the magnetic properties of the as-synthesized $BiFeO_3$ nanoplates. All samples obtained in our experiment under various conditions are listed in Table 2.

Table 2. Synthesis parameters, phases and grain sizes of different samples prepared by M-H method. For samples with secondary phases, the mean size was not considered. For mean size calculation, only samples with pure phase were considered.

Sample	Concentration of NaOH (M)	Radiation power (W)	Time (s)	Phase	Mean Size (nm)	Thickness of the nanoplates (nm)
MH-1	0.07	360	150	$BiFeO_3$, $Bi_2Fe_4O_9$	~580	40-100
MH-2	0.07	600	90	$BiFeO_3$	~720	60-150
MH-3	0.07	720	45	Amorphous, $Bi_{25}FeO_{40}$	/	/
MH-4	0.07	720	60	$BiFeO_3$, $Bi_{25}FeO_{40}$	~420	20-40
MH-5	0.07	720	75	$BiFeO_3$	~470	50-80
MH-6	0.03	720	65	$BiFeO_3$, $Bi_{25}FeO_{40}$	/	/
MH-7	0.07	720	65	$BiFeO_3$	~480	40-80
MH-8	0.15	720	65	$BiFeO_3$	~850	60-160
MH-9	0.50	720	65	$BiFeO_3$, $Bi_{25}FeO_{40}$	/	/

6.1 Synthesis of $BiFeO_3$ Nanoplates

0.0025 mol $Bi(NO_3)_3 \cdot 5H_2O$ and 0.0025 mol $FeCl_3 \cdot 6H_2O$ were dissolved in 50 mL of ethylene glycol solution. Secondly, aqueous NH_4OH (0.25 M) solution was slowly introduced into the above solution until the pH value reached 10-11. Subsequently, the aqueous solution was stirred for 30 min. After filtering and rinsing to remove residual Cl^-, NO_3^-, $NH_3 \cdot H_2O$ and $C_2H_6O_2$, the precipitate was re-dispersed in 60 mL of pre-prepared NaOH solution. Then 15 mL of the mixture was transferred into a Microwave Acid Digestion Autoclave (Parr Instrument Company) with capacity of 23 mL. The microwave processing was performed in a Panasonic Inverter Microwave Oven (2.45 GHz). For comparison, a conventional hydrothermal (C-H) experiment was conducted using the same solution with a stainless steel autoclave of the same volume and the filling factor. It was placed in an oven at 170°C for 16 h without moving or shaking (the final sample is listed as CH). After the autoclaves were cooled down to RT, the resulting products were collected, washed for several times using ethanol and distilled water respectively, and dried at 70°C for 4 h.

6.2 Characterizations of $BiFeO_3$ Nanoplates

Table 3. Relevant parameters from Rietveld refinement XRD patterns of $BiFeO_3$ samples prepared by C-H and M-H (MH-5) method; space group *R*3c.

Sample	Lattice parameters (Å)			Atom coordinates			Chi2
				X	y	z	
CH	a = 5.577(1) c = 13.863(4)	Bi	6*a*	0	0	0	1.68
		Fe	6*a*	0	0	0.221(1)	
		O	18*b*	0.453(9)	0.021(6)	0.951(3)	
MH-5	a = 5.584(2) c = 13.876(6)	Bi	6*a*	0	0	0	2.04
		Fe	6*a*	0	0	0.211(1)	
		O	18*b*	0.480(2)	0.040(1)	0.959(5)	

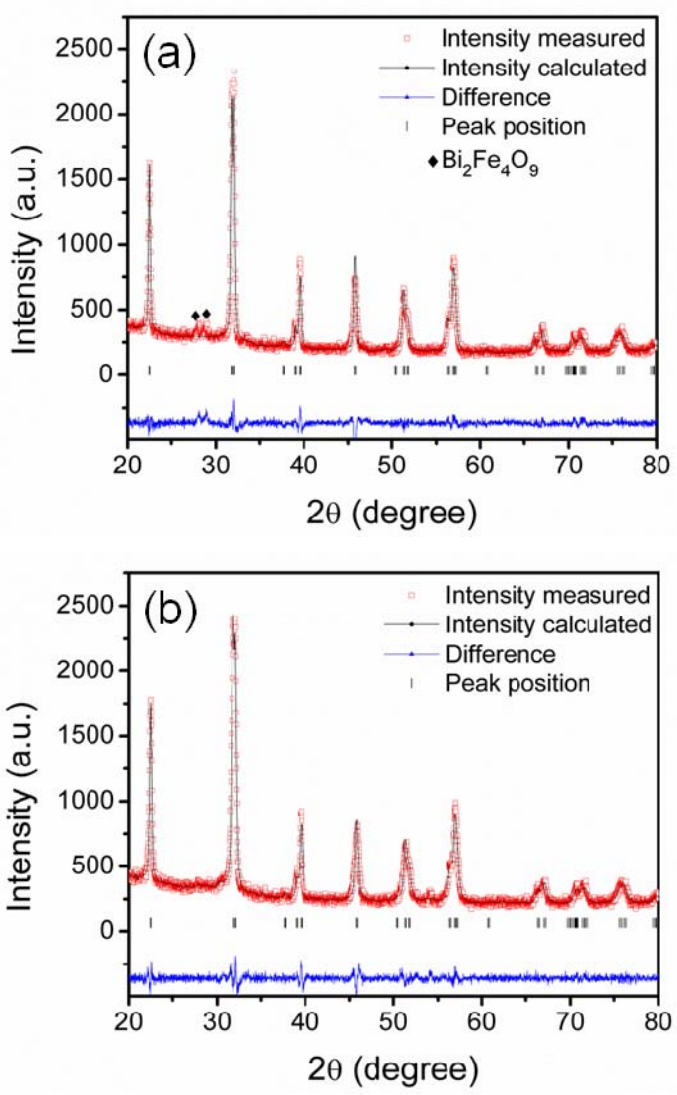

Figure 54. Rietveld refinement profile of the powder XRD patterns obtained for $BiFeO_3$ samples synthesized by (a) C-H and (b) M-H method (MH-5) [200].

Crystal structure characteristics of samples prepared by M-H (choosing sample MH-5) and C-H method were investigated by XRD first, as depicted in Figure 54. For the sample obtained by C-H treatment (Figure 54a), the main phase can be indexed to a rhombohedral lattice of $BiFeO_3$ with the space group *R*3*c* (JCPDS card No. 86-1518). However, a trace amount of secondary phase $Bi_2Fe_4O_9$ (JCPDS card No. 72-1832) is present, in addition to the main phase. On the other hand, for the sample synthesized by M-H treatment (Figure 54b), all the reflection peaks in the

pattern belong to the rhombohedral structure of $BiFeO_3$ without any other secondary phases. In addition, the intensity of the peaks of MH-5 is similar to those of sample CH, indicating that the microwave treatment gives comparable improvement in crystallinity with respect to traditional hydrothermal process while requiring significantly less time. To obtain more detailed information on the crystal structure, the XRD patterns collected for both samples were refined by the Rietveld method using FULLPROF. The space group *R*3*c* in its hexagonal representation was used as the basis, and the starting values for all Rietveld refinements were a_{hex} = 5.63 Å, and c_{hex} = 13.98 Å with atomic position of Bi (0,0,0), Fe (0,0,0.224), O (0.441,0.023,0.949) [271]. The structure parameters have been estimated and are summarized in Table 3.

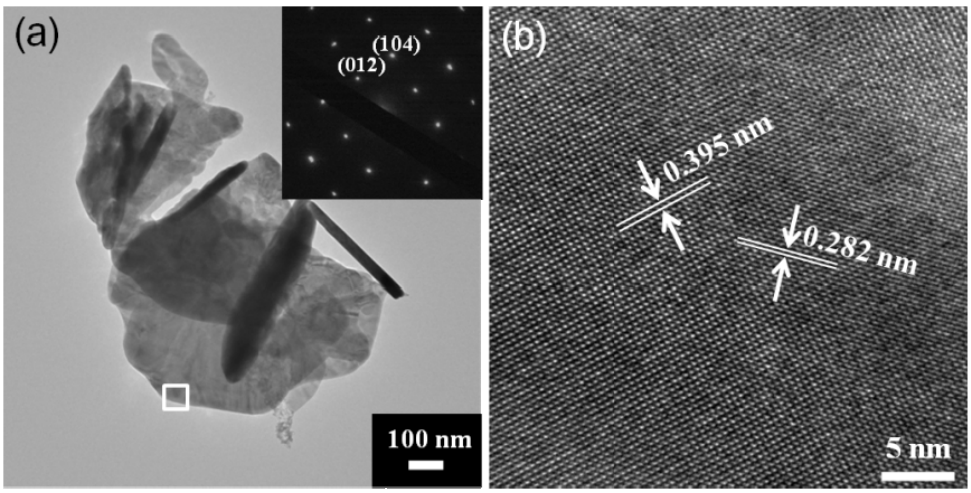

Figure 55. (a) TEM image of the $BiFeO_3$ nanoplates (MH-5), and inset shows typical SAED patterns taken from the nanoplate. (b) HRTEM image taken from the selected area of the nanoplate in (a) [200].

TEM image of the sample prepared by M-H method (MH-5) (Figure 55a) exhibits a 2D plate-like morphology with submicrometer in width and about 50-80 nm in thickness. SAED patterns taken from an individual nanoplate (inset of Figure 55a) show the presence of sharp diffraction spots, which are indicative of the formation of well-defined, single-crystalline $BiFeO_3$ nanoplates. Figure 55b shows the HRTEM image recorded from the selected area of the

nanoplate shown in Figure 55a. The fringe spacing of 0.395 and 0.282 nm matches the spacing of the (012) and (104) lattice planes of $BiFeO_3$, respectively, in agreement with the SAED patterns. The unit cell of $BiFeO_3$ can be described in a hexagonal frame of reference with its *c*-axis parallel to the diagonal of the perovskite cube (i.e., $[001]_{hex}||[111]_c$), so the (012) hex corresponds to $(100)_c$ pseudocubic crystal plane. Therefore, the results demonstrate that the $BiFeO_3$ nanoplates are exposed with $(100)_c$ plane, similar to the $BiFeO_3$ nano/microcubes reported previously [80, 81].

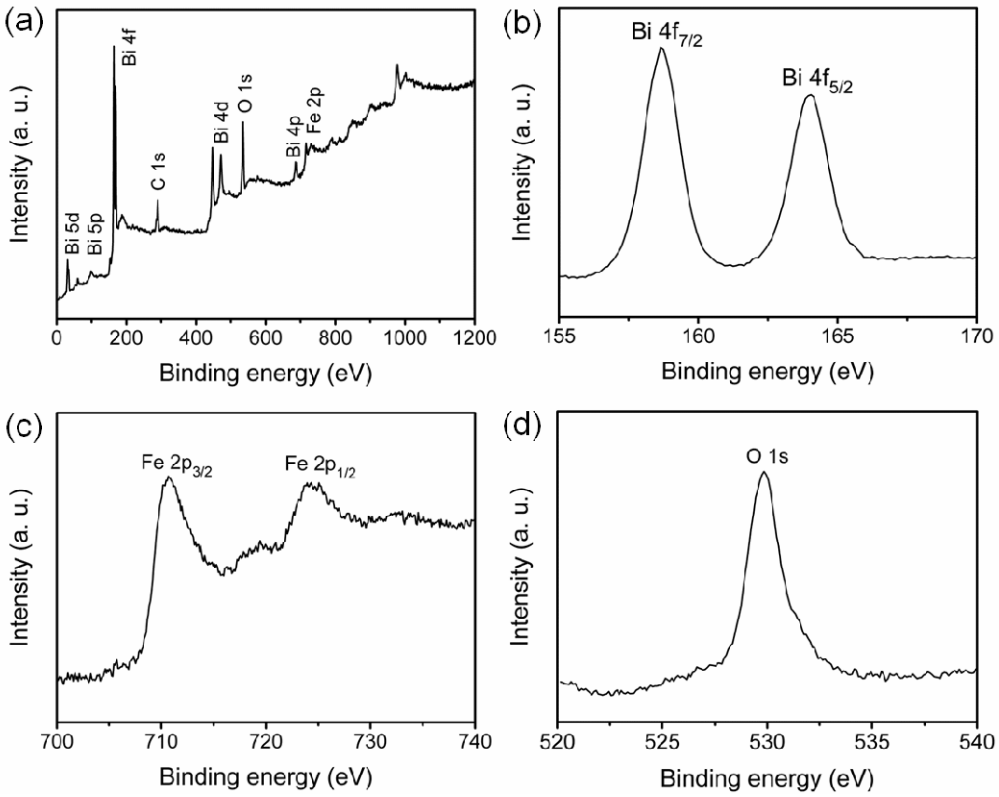

Figure 56. (a) XPS spectrum of the $BiFeO_3$ nanoplates (MH-5). (b-d) High-resolution XPS spectra of the Bi 4*f*, Fe 2*p*, and O 1*s* core level, respectively [200].

XPS measurements were performed to further indentify the chemical composition of the as-obtained $BiFeO_3$ nanoplates (MH-5). The wide-scan XPS spectrum shown in Figure 56a confirms that the $BiFeO_3$ nanoplates consist of Bi, Fe and O. Double Bi 4*f* peaks at binding

energies of 164.0 and 158.6 eV are corresponding to Bi^{3+}, shown in Figure 56b. In addition, peaks at 710.6 and 724.3 eV (Figure 56c) correspond to Fe^{3+} while no peak from Fe^{2+} was detected, which demonstrates that the oxidation state of Fe is only 3+ in the $BiFeO_3$ nanoplates. The XPS peak of O1*s* (Figure 56d) shows only one symmetrical peak at binding energies of 529.8 eV, verifying that the $BiFeO_3$ nanoplates are single phase, which is consistent with reports on $BiFeO_3$ nanoparticles obtained by the rapid molten salt sintering method [66].

Several studies have investigated the role of microwave radiation in the synthesis of inorganic materials [267, 272, 273]. Our results show that through the use of the M-H treatment, the reaction time needed for synthesizing $BiFeO_3$ nanocrystals with comparable crystal quality can be reduced from 16 h when using C-H method to only 1-2 min. Microwave heating is significantly faster due to the high penetration depth of microwave radiation, which enhances the reaction kinetics. As a result, the enhancement of crystallinity of $BiFeO_3$ performed in short periods via microwave treatment could be attributed to very rapid (within minutes) heating of the precursor and fewer thermal gradients compared with C-H treatment. Moreover, in the present case, the use of an inverter microwave oven that provides a higher intensity in the center of the oven, also contributes to the very rapid reaction of obtaining $BiFeO_3$ nanocrystals.

6.3 Effect of Synthesis Parameters on $BiFeO_3$ Nanoplates

6.3.1 Effect of Radiation Power and Energy

To study the influence of microwave power on the crystallization process, we conducted a series of experiments keeping a constant energy under different output power and time combinations (Table 2). The XRD patterns of the as-synthesized powders are presented in Figure 57a. For the samples treated at powers between 360 and 720 W (MH-1, MH-2, and MH-5), all the diffraction

peaks can be indexed to the rhombohedral structure of $BiFeO_3$, except a trace amount of $Bi_2Fe_4O_9$ which appears as a secondary phase in MH-1. The intensities of the peaks increase correspondingly as the radiation power increases from 360 to 600 W. However, the peaks decrease in intensity when 720 W was used. These results indicate that $BiFeO_3$ crystals can be synthesized under different radiation output powers. The morphological and size changes in the as-prepared $BiFeO_3$ samples also strongly depend on the radiation power.

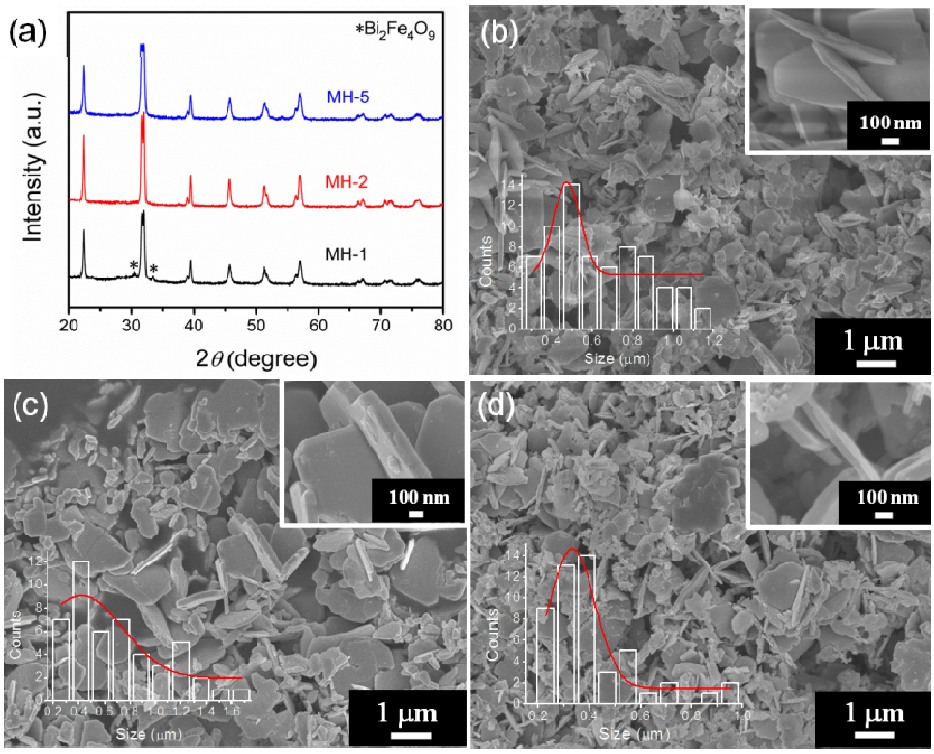

Figure 57. (a) XRD patterns of the as-synthesized products by M-H method at various output power with constant energy. SEM images of the $BiFeO_3$ products: (b) MH-1, (c) MH-2, and (d) MH-5. Inset shows the higher magnification image and lateral size distribution histograms of each sample, respectively [200].

Figure 57b-d present typical SEM images of the obtained $BiFeO_3$ samples synthesized under different radiation output powers. All the resulting products consist predominantly of plate-like nanostructures. At higher magnification, we can clearly see that the thickness of the nanoplates increases while increasing the radiation output power from 360 to 600 W, and decreases when

further increasing the power to 720 W. This is an interesting phenomenon observed in our experiment that the mean crystal size and morphology of the $BiFeO_3$ nanoplates can be tuned by adjusting the irradiation power when keeping the total energy constant. As listed in Table 2, a statistic investigation on crystalline sizes through SEM also confirms that the mean grain size increases with power, to decrease above a threshold of 600 W at a constant energy. The results demonstrate that irradiation power is very important to attain the crystallinity of the final products during the rapid synthesis process of M-H treatment. Further systematic studies are needed to better understand the influence of irradiation power on the crystallization behavior of the final products during the M-H treatment process and the involved mechanism.

6.3.2 Effect of Alkali Concentration

The alkali concentration of the precursor solution also plays a critical role on the formation of the $BiFeO_3$ nanoplates. The XRD patterns (Figure 58a) indicate that the $BiFeO_3$ crystal can be obtained under a range of NaOH concentrations. SEM imaging (Figure 58b-e) shows that when the NaOH concentration is either too low (0.03 M) or too high (0.5 M), the $BiFeO_3$ crystals are composed of irregular-shaped particles. Only the samples prepared at concentrations between 0.07 and 0.15 M were observed to self-organize into 2D nanostructures.

In the hydrothermal process for synthesizing oxide crystals, OH^- ions are found to be one of the dominating anions that affect the nucleation and growth behavior of oxide materials. It has been reported that the OH^- ions can serve as capping agents and adsorb on certain crystallographic faces of oxide crystals, which may create growth anisotropy and direct the crystal growth as well [274-277]. Some cluster facets have a preference to absorb OH^- due to the difference of surface energy associated with certain facets before crystal nuclei are assembled

together, which strongly depends on reaction conditions such as the precursor, concentration of mineralizer or surfactant, temperature and so on. As a consequence, the shielding effect of OH^- ions on the interface will control the growth rate of the OH^- absorbed facets.

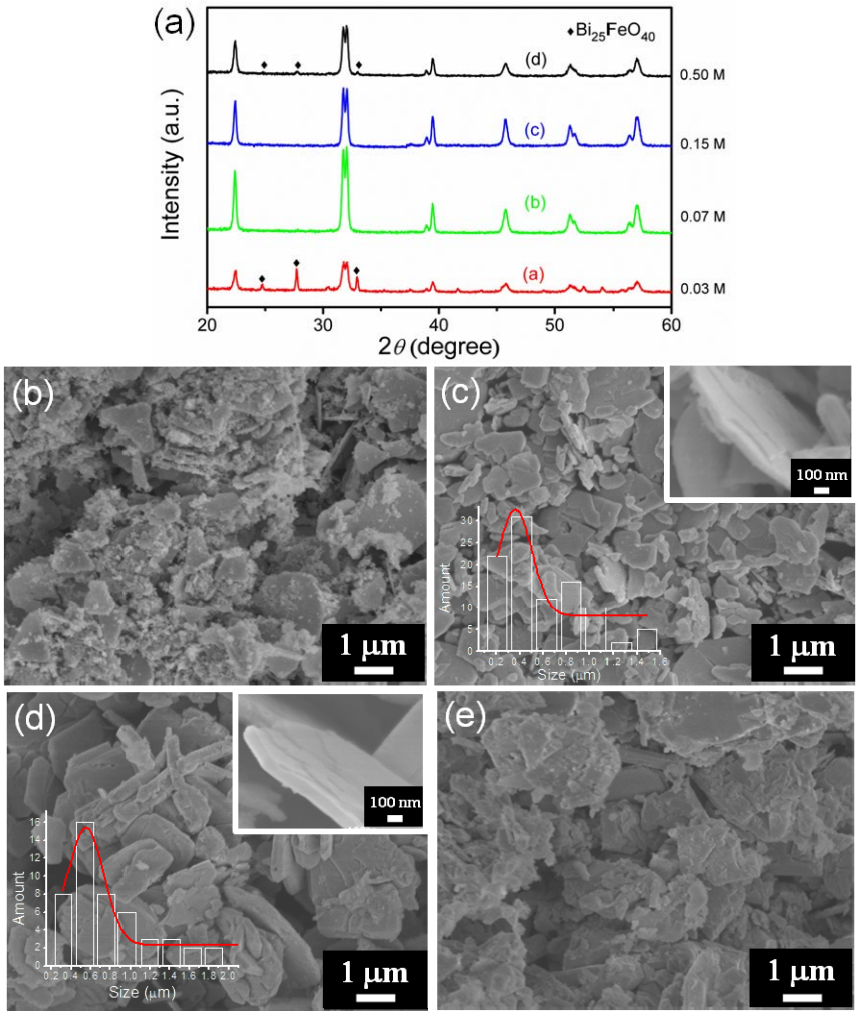

Figure 58. (a) XRD patterns of the as-synthesized products using various concentrations of NaOH. SEM images of the $BiFeO_3$ samples: (b) MH-6, (c) MH-7, (d) MH-8, and (e) MH-9 [200].

A great number of 1D and 2D nanostructures have been fabricated applying such a control approach [258, 274-280]. Previous reports confirmed that uniform $BiFeO_3$ nano-/micro-materials with highly exposed crystal facets such as $(111)_c$ exposed nanorods [76], and $(100)_c$ enclosing nano-/micro-cubes [80, 81] can be obtained by adding alkali under different reaction

environment. In our case, we consider that under the microwave treatment, OH^- may adsorb onto surfaces of the $(100)_c$ crystal facets of nucleating $BiFeO_3$ to regulate the lamellar growth and suppress the aggregation tendency of the growing plates consequently. To obtain $BiFeO_3$ nanoplates with controllable crystallographic facets, nucleation kinetics should be carefully controlled by choosing the favorable alkali concentration of the reaction solution. Further experimental and theoretical work would be helpful for better understanding of the adsorption behaviors of OH^- ions with certain $BiFeO_3$ crystal facet under the M-H condition.

6.3.3 Effect of Reaction Time

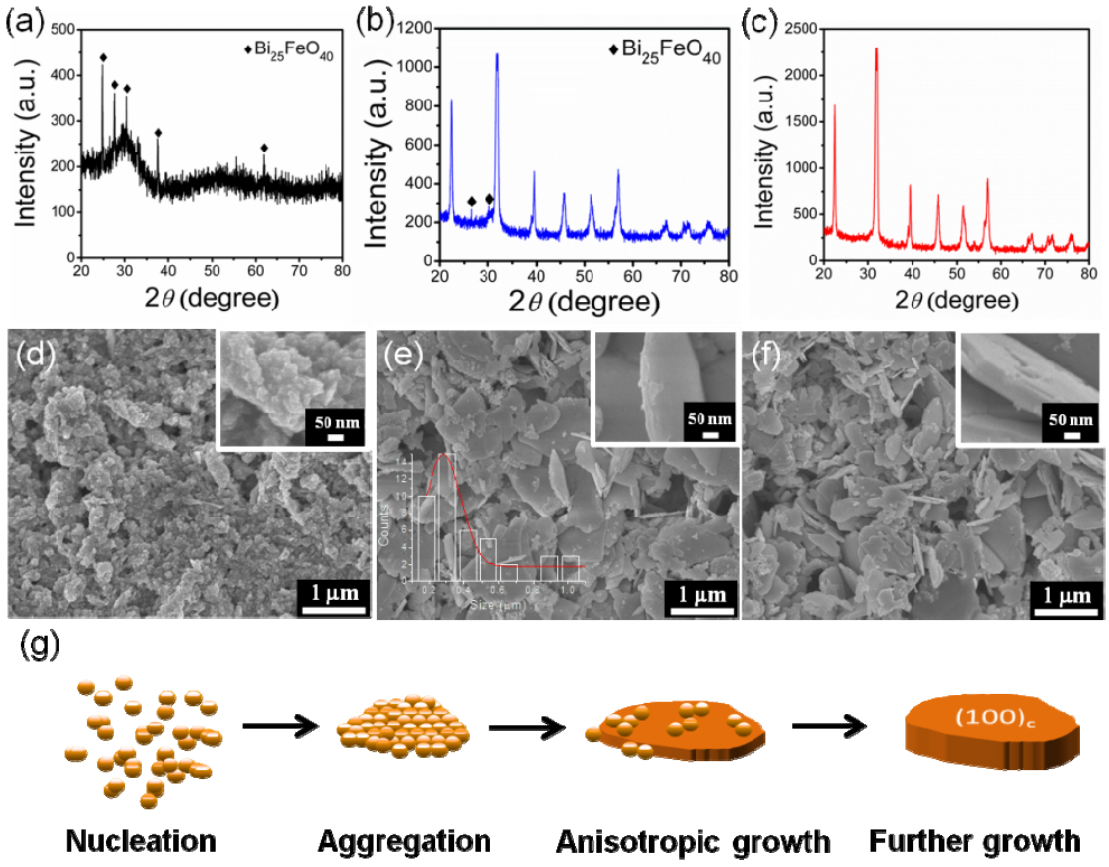

Figure 59. XRD patterns of the as-synthesized products with different reaction time at a fixed output power of 720 W: (a) 45 s, (b) 60 s, and (c) 75 s. SEM images of the as-synthesized products: (d) MH-3, (e) MH-4, and (f) MH-5. (g) Schematic illustration of the formation process of $BiFeO_3$ nanoplate [200].

To develop a better understanding of the evolution process of the $BiFeO_3$ nanoplates, we trapped intermediate states of the product by varying the reaction time at a fixed output power of 720 W. XRD patterns of the samples obtained at different M-H radiation times were recorded (Figure 59a-c). The sample MH-3 treated for 45 s does not show a crystallized $BiFeO_3$ phase (Figure 59a). The 60 s irradiated sample (MH-4), on the other hand, gives peaks corresponding to perovskite $BiFeO_3$ phase (Figure 59b). The peaks show a consistent yet remarkable rise in intensity compared to that of MH-4 upon increasing the radiation time up to 75 s (Figure 59c).

The time-dependent morphological evolution process was followed by SEM at various stages of the M-H process, providing valuable information regarding the formation of $BiFeO_3$ nanoplates. Figure 59d-f present SEM images of samples prepared by radiating the solutions between 45 and 75 s. A large amount of small crystallites nucleate without any particular orientation when the reaction time was 45 s (Figure 59d). The sample prepared with 60 s of radiation (Figure 59e), however, shows the presence of $BiFeO_3$ nanoplates, and a similar morphology is retained up to 75 s (Figure 59f) of radiation. The crystalline size slightly increases when the treatment time increased from 60 to 75 s (Table 2), as analyzed from SEM characterizations. This means that extended periods of microwave hydrothermal treatment greatly enhance the crystallinity, yet have little influence on the lateral crystalline size.

6.4 Proposed Formation Mechanism

The theory of dissolution/recrystallization can be applied to interpret the present M-H reaction process. Bismuth oxide nitrate ($BiONO_3$) [76, 281, 282] and iron hydroxides ($Fe(OH)_3$) are readily formed as thermodynamically stable materials at an initial stage during the synthesis process. The involved reactions during this process are as follows:

$$Bi^{3+} + NO_3^- + 2NH_3(aq) + H_2O \longrightarrow BiONO_3 + 2NH_4^+ \quad \text{(Eq. 6.1)}$$

$$Fe^{3+} + 3NH_3(aq) + 3H_2O \longrightarrow Fe(OH)_3 + 3NH_4^+ \quad \text{(Eq. 6.2)}$$

After running the microwave treatment, the precursor compounds experience a dissolution process. Next, the precursor recrystallize to $BiFeO_3$ nanocrystal gradually through a slow aggregation and crystallization of primary colloids, depending on the degree of supersaturation and the chemical potential of OH^-, by the following reactions [76]:

$$BiONO_3 + H_2O \longrightarrow Bi^{3+} + 2OH^- + NO_3^- \quad \text{(Eq. 6.3)}$$

$$Fe(OH)_3 \longrightarrow FeO_3^{3-} + 3H^+ \quad \text{(Eq. 6.4)}$$

$$Bi^{3+} + FeO_3^{3-} \longrightarrow BiFeO_3 \quad \text{(Eq. 6.5)}$$

On the basis of the above time-dependent transformation process, the formation of $BiFeO_3$ nanoplates can be achieved by the following procedure (Figure 59g): i) the precursor nucleate to form a large amount of tiny crystal nuclei in the initial reaction process; ii) with prolonged time, the newly formed $BiFeO_3$ crystal nuclei aggregate with the formerly formed ones, and begin to grow into two-dimensionally thin plate-like structures due to the adsorption of OH^- ions on $(001)_c$ faces; iii) the primary $BiFeO_3$ particles continue to adsorb onto these growing plates and then gradually ripen into single-crystal nanoplates. In addition, we observed that fine particles adhered to the large ones from SEM imaging (Figure 59e), indicating that the growth of $BiFeO_3$ nanoplates follows the Ostwald ripening mechanism.

6.5 Magnetic Properties of $BiFeO_3$ Nanoplates

The magnetization hysteresis loops of the as-synthesized $BiFeO_3$ nanoplates (MH-1, MH-2 and MH-5) are shown in Figure 60. From the enlarged figure inset of Figure 60, we can clearly see

that all the samples exhibit weak ferromagnetic behavior at room temperature. It is well known that bulk $BiFeO_3$ exhibits a linear magnetic response when a magnetic field is applied at RT because of the antiferromagnetic arrangement of Fe^{3+} magnetic moments [283]. From the XPS analysis we know that the oxidation state of elemental Fe in the $BiFeO_3$ nanoplates is 3+ (Figure 56c). In addition, these $BiFeO_3$ samples consist of 2D plate-like morphologies with thickness ranging from 20 to 150 nm, which are comparable with the wavelength period of the spiral spin arrangement of 62 nm of bulk $BiFeO_3$ [55, 88]. Therefore, we infer that the cycloid structure of bulk $BiFeO_3$ is partially destroyed in the $BiFeO_3$ nanoplates, which leads to the weak ferromagnetic behavior observed at room temperature. Similar observations have been reported in $BiFeO_3$ nanoparticles [69], one-dimensional nanowires [75] and nanotubes [72]. In addition, the saturation magnetization of the nanoplates decreases with increasing crystal size, which is also consistent with previous reports on $BiFeO_3$ nanoparticles [69, 90].

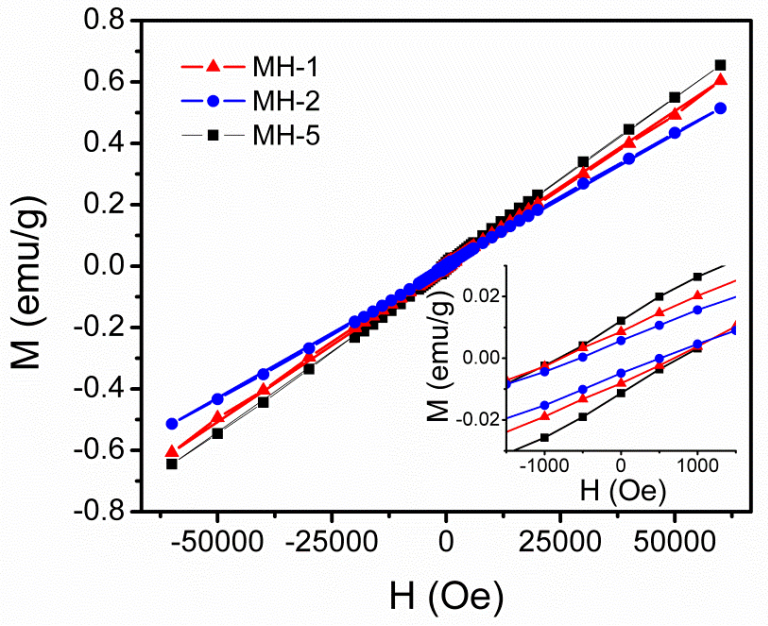

Figure 60. Magnetization hysteresis loops of the $BiFeO_3$ nanoplates. Inset shows the enlarged views [200].

6.6 Summary

In this chapter, we developed a novel method to synthesize 2D $BiFeO_3$ nanocrystals with exposed $(100)_c$ facets by microwave hydrothermal (M-H) reaction without any surfactant. We found that plate-shape $BiFeO_3$ single crystal can be obtained within a very short time of 60-150 s, much less than that of conventional and other M-H process reported before. Moreover, we demonstrated that the radiation power, reaction time, and concentration of alkali are important parameters for the crystallization process of $BiFeO_3$ during the M-H treatment. In addition, weak ferromagnetism of the $BiFeO_3$ nanoplates was observed at room temperature due to the nanoscale size effect, which is different from that of bulk $BiFeO_3$ crystal. The rapid reaction involved with this M-H process of obtaining $BiFeO_3$ nanostructures has the potential to lower the manufacturing cost with significant time and energy savings.

SECTION (II) Bi_2FeCrO_6 Thin Films for Solar Energy Conversion Applications

Chapter 7

Photovoltaic Effect in Epitaxial Bi_2FeCrO_6 Thin Films

Nowadays ferroelectric materials have drawn significant attention for PV applications owing to their efficient ferroelectric polarization-driven carrier separation based on a bulk photovoltaic effect (BPVE), as compared with traditional silicon based bipolar junction solar cell [130]. The phenomenon of BPVE in which charge carriers are transported without the existence of a gradient in the electrochemical potential, was historically observed in non-centrosymmetric crystals especially ferroelectric crystals and ceramics such as $BaTiO_3$, $PrZr_xTi_{1-x}O_3$ and $LiNbO_3$ [126, 284-286]. Theoretically, high PV efficiency up to 70% could be attained in ferroelectric films [131]. Nevertheless, the measured overall energy conversion efficiency of these materials is still very low for practical applications due to the short lifetime of non-thermalized photogenerated charges and the characteristic large band gaps of these materials (typically 3-4 eV) which promote high charge recombination rate. Although recently considerable efforts have been made to explore new ferroelectric materials and ameliorate their performance [138, 143-148], the highest PV efficiency ever reported is merely 1.25% in $PrZr_xTi_{1-x}O_3$ based PV devices [148].

Consequently, utilization of narrow band gap ferroelectrics is becoming a promising route towards their application in novel optoelectronic and PV devices with high conversion efficiency. Among all ferroelectric materials studied so far, multiferroics $BiFeO_3$, with a relatively narrow band gap energy (2.2 to 2.8 eV), has been identified as a promising candidate for PV devices in the visible light region recently [150-153, 157, 160, 162, 287-289]. However, the power conversion efficiency (PCE) of $BiFeO_3$ based thin film devices is still very low for practical applications. Meanwhile, several new ferroelectrics with narrow band gaps have been investigated for PV applications. As an example, a lower band gap of 1.6 eV has been recently demonstrated in weakly ferroelectric non-perovskite $KBiFe_2O_5$ [149]. Very recently, Grinberg *et al*. discovered a novel ferroelectric perovskite $[KNbO_3]_{1-x}[BaNi_{1/2}Nb_{1/2}O_{3-\delta}]_x$ solid solutions which exhibit both ferroelectricity and a wide variation of direct band gaps in the range 1.1-3.8 eV [146].

Theoretical studies showed that Fe and Cr mixed *d* orbital transition allow a small band gap around 2.3 eV in double perovskites La_2FeCrO_6 [292], which has a similar crystal structure with that of Bi_2FeCrO_6. [167]. In addition, previously study reported that epitaxial Bi_2FeCrO_6 thin films demonstrated a high PCE up to 6% under red light laser illumination [166]. These results suggest the great potential of utilizing it as PV devices. Moreover, it was found that the cationic ordering of Fe/Cr plays a very important role on the PV effects in Bi_2FeCrO_6. In this chapter we demonstrated significant band gap tunability in epitaxial Bi_2FeCrO_6 films by tuning the cationic ordering of Cr and Fe, and the PV properties of Bi_2FeCrO_6 thin films based devices have been systematically investigated.

7.1 Experimental Section

7.1.1 Deposition of Bi_2FeCrO_6 Thin Films

Bi_2FeCrO_6 thin films with thickness of ~100 nm were grown onto (100)-oriented $SrTiO_3$ substrates using PLD technique. The substrate holder was heated up to a temperature of 520 to 720°C. The distance between the target and substrate was 5.5 cm. Under these conditions, the film growth rate, estimated from thicknesses measured by X-ray reflectometry, was from 1.5 to 2.1 Å/s. The growth time of Bi_2FeCrO_6 thin films was modified by adjusting the laser repetition rate in the range of 2 to 14 Hz. The oxygen partial pressure was kept around 10 mTorr. After deposition, the samples were cooled to room temperature under the same oxygen pressure as the one used for deposition.

7.1.2 Device Fabrication and PV Measurements

After optimization of the deposition parameters, we used $SrRuO_3$ buffer layer as bottom electrode to promote the epitaxial growth of Bi_2FeCrO_6 films and perform electrical measurements. A 30 nm-thick $SrRuO_3$ film was deposited by PLD with substrate temperature and oxygen partial pressure of 600°C and 100 mTorr, respectively. 2D arrays of ITO transparent conducting top electrodes (120 nm thick) were deposited by PLD through a shadow mask with circular apertures of ~150 μm diameter. The current-voltage characteristics of the electric devices were recorded using a Keithley source meter. One Sun illumination was accomplished by an AAA class Sun simulator equipped with 1.5 AM filter with an irradiation intensity of 100 mW/cm^2. Device characterization was carried out in ambient environment. The ferroelectric properties of Bi_2FeCrO_6 films were measured using a thin film analyzer system at 1 kHz.

7.2 Characterizations of Bi_2FeCrO_6 Thin Films

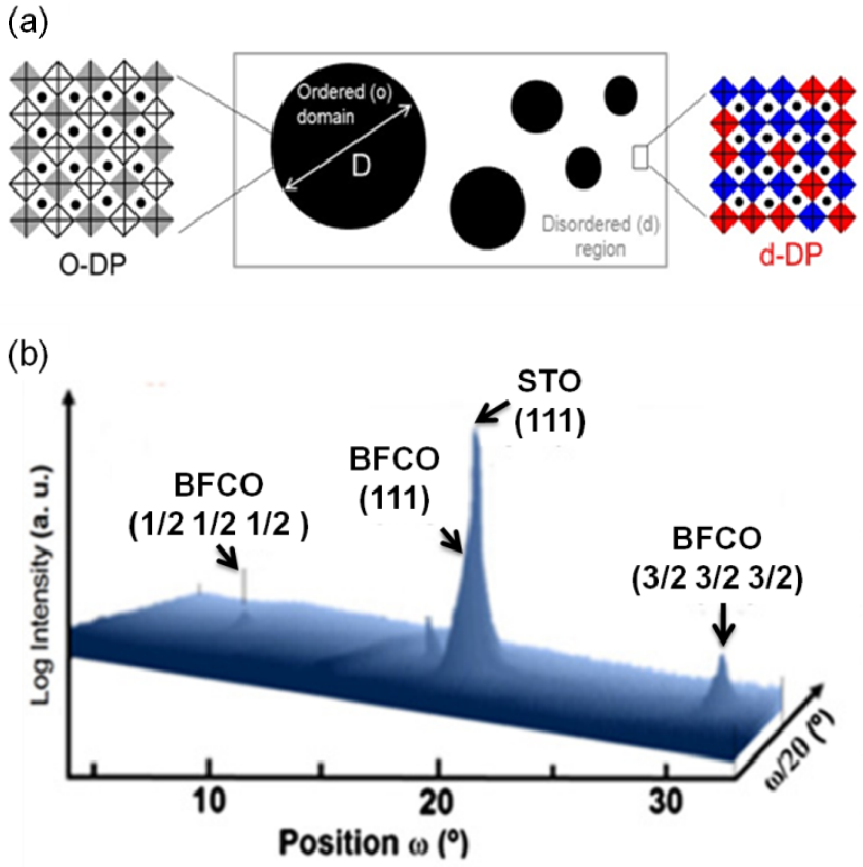

Figure 61. (a) Schematic representation of the distribution of the ordered domain with D size in the disordered region of Bi_2FeCrO_6. Corresponding FeO_6/CrO_6 arrangements in ordered (o-DP) and disordered (d-DP) double perovskites are also illustrated. (b) Asymmetrical XRD RSM ω-2θ scan around (111) reflection recorded for (001) oriented Bi_2FeCrO_6 films showing the superstructure reflections [12].

Two critical parameters that describe the Fe/Cr cationic long range ordering in Bi_2FeCrO_6 thin films are defined at first. The first one is R, represented by the ratio between the superstructure reflection (½ ½ ½) and the main (111) perovskite peak of Bi_2FeCrO_6 ($I_{½½½}/I_{111}$), is measured from the asymmetrical XRD θ-2θ scans of the films around the $SrTiO_3$ (111) reflection, as shown in Figure 61b. The R value is determined by the percentage of long range ordering in the all double perovskites Bi_2FeCrO_6 crystal. The other one is the average size of the ordered domain (denoted as D, illustrated in Figure 61a), which is calculated using the Debye-Scherrer formula

applied to the full width at half maximum (FWHM) of normalized superlattice (½ ½ ½) reflection peaks. The degree of long range ordering in the Bi_2FeCrO_6 thin films (R and D value) can be controlled by either kinetics or thermal equilibrium depending on the temperature range of film growth.

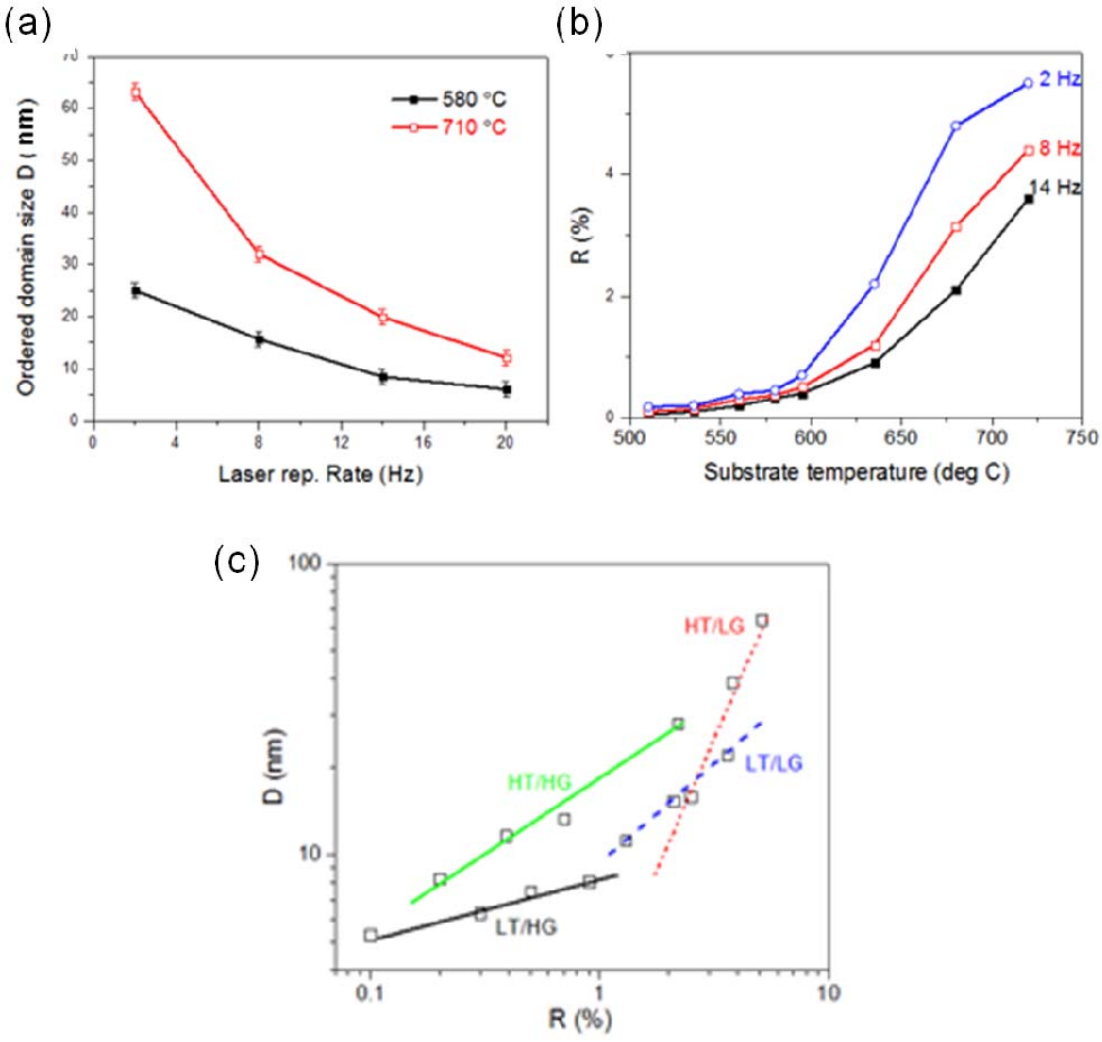

Figure 62. (a) Variation of ordered domain size (D) with the laser repetition rate (f) in the Bi_2FeCrO_6 thin films. (b) Substrate temperature dependence on R ratio. (c) R-D relationship in Bi_2FeCrO_6 films grown at different PLD conditions [201]. (HT: high temperature, LG: low growth rate, LT: low temperature, HG: high growth rate.)

First, we have systematically investigated the influence of experimental parameters on R and D values. Figure 62a shows that small ordered domains were obtained at high laser repetition rate and low growth temperature. From Figure 62b, we can conclude that the effect of the laser repetition rate (f) or the time of growth on ordering is more significant at high deposition temperatures (630-710°C). Highly ordered Bi_2FeCrO_6 phase (R = 5.1%) with large domain size D was obtained when the films were grown at 710°C and at f = 2 Hz. The relationship between D and R [i.e. D(R)] of the ordered domains in Bi_2FeCrO_6 films is shown in Figure 62c. We note that at low temperature and a high growth rate (LT/HG), the D(R) relationship is less significant than that at low temperature and low growth rate (LT/LG).

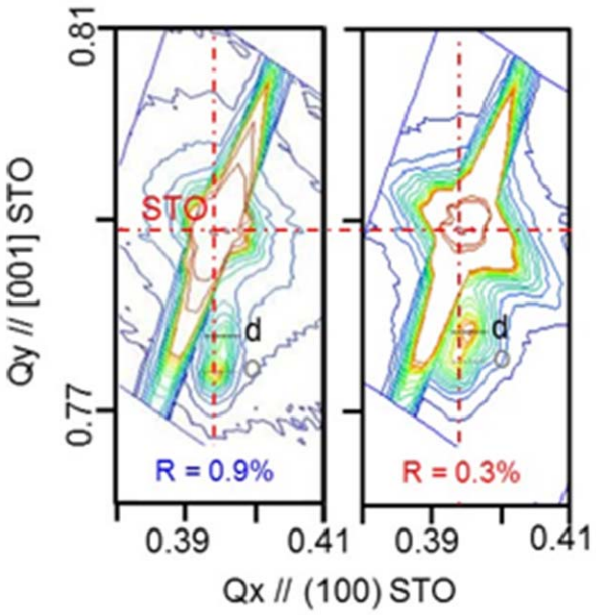

Figure 63. RSM image of Bi_2FeCrO_6 films around the (204) $SrTiO_3$ reflection [201].

Figure 63 shows RSM images around the $SrTiO_3$ (204) reflection for two Bi_2FeCrO_6 thin films with different R value (0.3 and 0.9). In both cases, Bi_2FeCrO_6 films exhibit a tetragonal distorted perovskite structure since the out-of-plane pseudo-cubic lattice *c* is larger than the in-plane parameter *a*. The reciprocal lattice point of each layer (the position of the center of the

peak) is located close to that of $SrTiO_3$ along the Q_x axis for each map, indicating that the in-plane lattice parameter of the heterostructure is very close to that of the substrate. Importantly, the presence of two Bi_2FeCrO_6 phases (i.e. o-Bi_2FeCrO_6 and d-Bi_2FeCrO_6) in the films is confirmed by RSM around the $SrTiO_3$ (204) reflection which clearly shows two distinct spot reflections. As we can see from Figure 63, in more ordered Bi_2FeCrO_6 thin film with an R ratio of 0.9, the spot from the ordered domain is more prominent than that in less ordered sample (R ratio of 0.3). On the other hand, the spot from the disordered domain from Bi_2FeCrO_6 thin film with R ratio of 0.9 is weaker than that in the other sample with R ratio of 0.3.

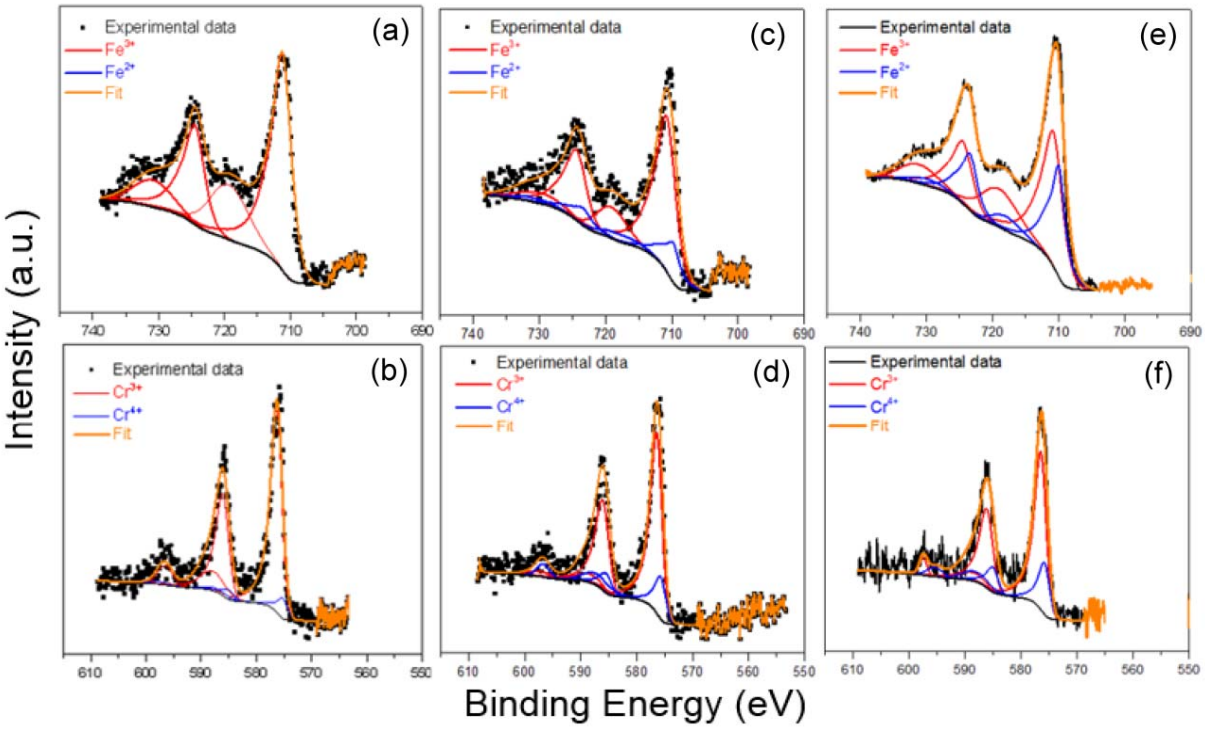

Figure 64. XPS Fe (a) and Cr (b) 2*p* lines spectra of Bi_2FeCrO_6 (R = 0.3%), and Fe (c) and Cr (d) 2*p* lines spectra of Bi_2FeCrO_6 (R = 0.9%). (e) $BiFeO_3$ and (f) $BiCrO_3$ thin films epitaxially grown on $SrTiO_3$ (100) substrates at the same PLD depositions conditions (i.e. oxygen partial pressure and substrate temperature) [201].

XPS has been used to investigate the oxidation states of Fe and Cr elements present in the different Bi_2FeCrO_6 layers. For comparison we also performed measurements on epitaxial $BiFeO_3$ and $BiCrO_3$ thin films grown under the same conditions. The observed XPS Fe and Cr 2*p* core-level spectra are illustrated in

Figure 64. For transition metal ions, the 2*p* core level splits into $2p_{1/2}$ and $2p_{3/2}$ components. The binding energy of Fe $2p_{3/2}$ is expected to be 710.7 eV for Fe^{3+} and 709 eV for Fe^{2+}. In the case of Cr, the expected $2p_{3/2}$ values are around 576.3 and 575.2 eV for Cr^{3+} and Cr^{4+}, respectively.

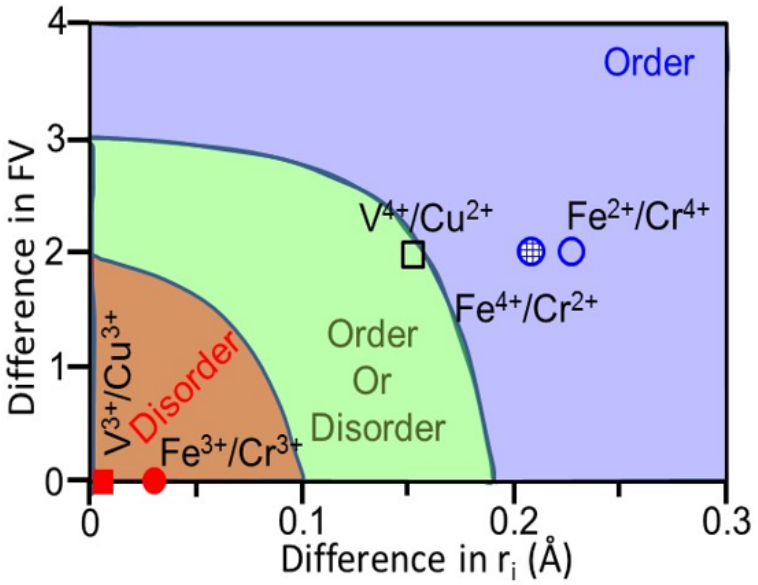

Figure 65. Bulk phase diagram as a function of differences in formal valance (FV) and ionic radii (r_i) [290].

Since cationic ordering is a crucial factor for determining the physical properties of Bi_2FeCrO_6 material, it is important to obtain Bi_2FeCrO_6 with high degree of ordering. According to previous study, highly ordered Bi_2FeCrO_6 crystals are likely to form with Fe^{2+} and Cr^{4+} ions since they have larger difference of ionic radius and formal valance, compared with Fe^{3+} and

Cr^{3+}. To quantify the fraction of Fe and Cr in each chemical state using XPS, we used the method described by Aronniemi *et al*. [109, 290]. Using the traditional Shirley background subtraction, we deconvoluted the 2*p* core levels for the different samples. The line shape used to represent the 2*p* mains peaks was a Gaussian-Lorentzian (GL) product with a constant exponential tail. We imposed the fitting parameters such that the tail parameters and the GL ratio of the $2p_{1/2}$ main peak are equal to those of $2p_{3/2}$ and the satellites are purely Gaussian and without any tail.

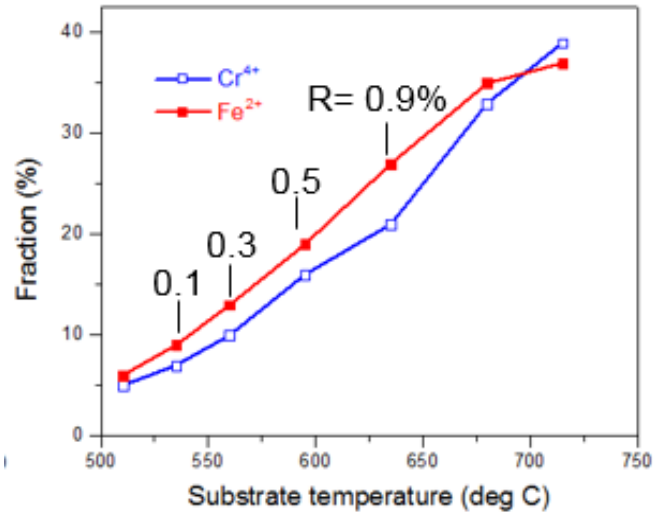

Figure 66. Fe^{2+} and Cr^{4+} fractions versus growth temperature of Bi_2FeCrO_6 thin films in various samples with different R ratios [201].

Analysis of the ratio of different valence state of Fe and Cr suggests that the 3+ state is predominant in all films. However, we observed that the fraction of Cr^{4+} and Fe^{2+} components is higher when the cationic ordering of Bi_2FeCrO_6 films is important. This direct relationship between the cationic ordering and the Cr and Fe components is further evidenced in Figure 66. The fractions of Cr^{4+} and Fe^{2+} linearly increase with the substrate temperature during the Bi_2FeCrO_6 growth. This indicates that the ordering between Fe and Cr in Bi_2FeCrO_6 is mainly achieved by the Fe^{2+} and Cr^{4+}. In contrast to the 3+ valence state, the larger difference in the

valence state between Fe^{2+} and Cr^{4+} promotes the cationic ordering in Bi_2FeCrO_6. Since oxygen vacancy is a very important factor that determines the photocurrent, we studied the O1*s* state of Bi_2FeCrO_6 thin films with and without O^{2-} vacancies by XPS. We observed a small number of oxygen vacancies in our films, as evidenced by XPS measurements (Figure 67). From the ratios of the peak intensities, we estimate that the oxygen vacancies in our films are present at a level of less than 5%. This will not significantly affect the unit cell volume.

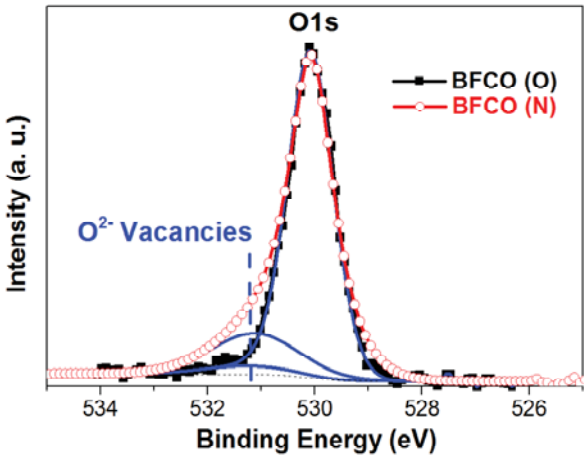

Figure 67. XPS spectra of the O1*s* signal of Bi_2FeCrO_6 thin films with and without O^{2-} vacancies, respectively. The deconvolution of the O1*s* line results in peaks around 530 eV and 531.5 eV, corresponding to oxygen in the Bi_2FeCrO_6 lattice and presence of oxygen vacancies. The Bi_2FeCrO_6 films [labeled as BFCO (N)] with high concentration of O^{2-} vacancies were obtained when the films were deposited under N_2 atmosphere [201].

7.3 Optical Properties of Bi_2FeCrO_6 Thin Films

To better understand the optical properties of Bi_2FeCrO_6 thin films, two series of sample were studied in our work. (1) N-series Bi_2FeCrO_6 samples. To investigate the effect of R on the properties of Bi_2FeCrO_6 films, we studied films grown at low temperature and a high growth rate (LT/HG) conditions, where D is almost constant. The high growth rate limits the kinetic effect on long range ordering which results in smaller D size, typically between 6-10 nm (Figure 62a).

The obtained Bi_2FeCrO_6 films (denoted as N1 to N4) have R values ranging from 0.1 to 0.9% (Figure 62b); (2) L-series Bi_2FeCrO_6 samples. It is known that typically with annealing time, the *B*-site cations (Fe/Cr in our case) gain sufficient kinetic energy to migrate to their specific sites to minimize the configurational entropy, which results in the growth of ordered domains. This modification of spatial ordering distribution obtained through heat treatment is common in many complex perovskite ceramics [291]. To investigate the effect of D on the absorption properties of Bi_2FeCrO_6 films, we varied the growth time from 5 to 60 min by adjusting the laser repetition rate in the range of 2, 6, 10 and 14 Hz (denoted as L1, L2, L3 and L4), respectively.

7.3.1 Effect of Cationic Ordering on Optical Properties

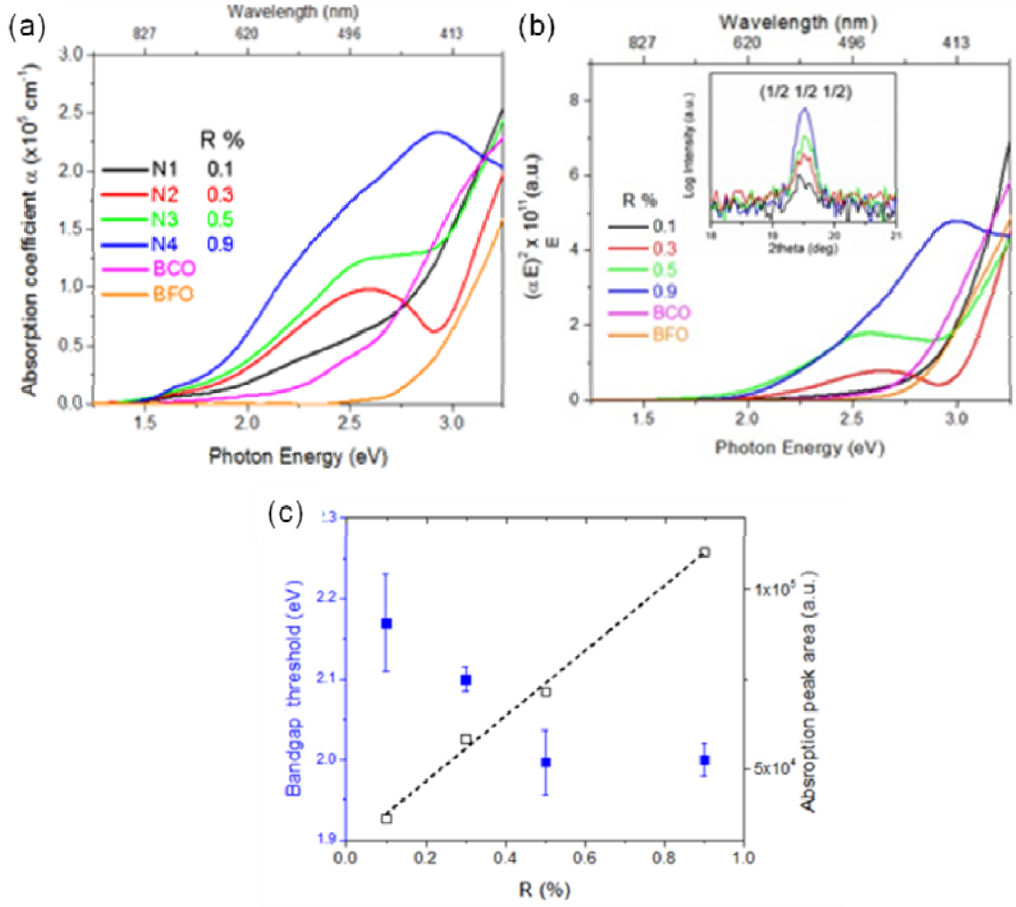

Figure 68. Spectroscopic ellipsometry of Bi_2FeCrO_6 thin films showing the tunability from 2-3.1 eV of the optical band gap, as a function of R ratio (i.e. Fe/Cr cationic ordering): (a) absorption coefficients and (b) direct optical transitions. Inset of (b), normalized XRD intensity of the superstructure peaks. (c) Band gap threshold and corresponding absorption area versus R in Bi_2FeCrO_6 films [201].

Figure 68a displays the absorption coefficient α of the Bi_2FeCrO_6 films measured by ellipsometry, together with that obtained for epitaxial $BiFeO_3$ and $BiCrO_3$ films for comparison. In contrast to the $BiFeO_3$ and $BiCrO_3$ absorption spectra, peak structures appear between 1.5 and 2.7 eV in the optical absorption spectra of the Bi_2FeCrO_6 films, and their height increases monotonically with R. In addition, the direct optical transitions illustrated by the $(\alpha E)^2$ vs. E plots (Figure 68b) are characterized by two linear portions, suggesting the presence of two threshold gaps in Bi_2FeCrO_6 films. Following electronic structure calculations confirmed by absorption spectra of the similar double perovskites La_2FeCrO_6 [292], we attribute the band in the visible range of ~1.99 eV to charge transfer excitations between Cr to Fe mixed *d* orbitals Hubbard transitions that occur in ordered regions (o-Bi_2FeCrO_6).

The peak area of this band strongly depends on R and thus on Fe/Cr cationic ordering, which is clearly visible in Figure 68c showing the variation of E_g and corresponding areas of ordered region in Bi_2FeCrO_6 films with R. While only a small variation of E_g (0.2 eV) is observed with R, we measured a strong dependence (increase by a factor of ~5) of the absorption peak area on R. This demonstrates that R is a key parameter that can be used to tailor the amount of absorbed light in Bi_2FeCrO_6 films. The second threshold gap observed at UV energies ranging from 2.8 to 3.1 eV is close to those of $BiFeO_3$ and $BiCrO_3$ films, and decreases strongly when Fe/Cr ordering increases (R = 0.9%) in the film. These results suggest that in this energy range (2.8 to 3.1 eV), absorptions in Bi_2FeCrO_6, $BiFeO_3$ and $BiCrO_3$ have the same origins namely, O to Fe, O to Cr, and Cr to Cr charge transfers which take place in the disordered Bi_2FeCrO_6 domains.

7.3.2 Effect of Ordered Domain Size on Optical Properties

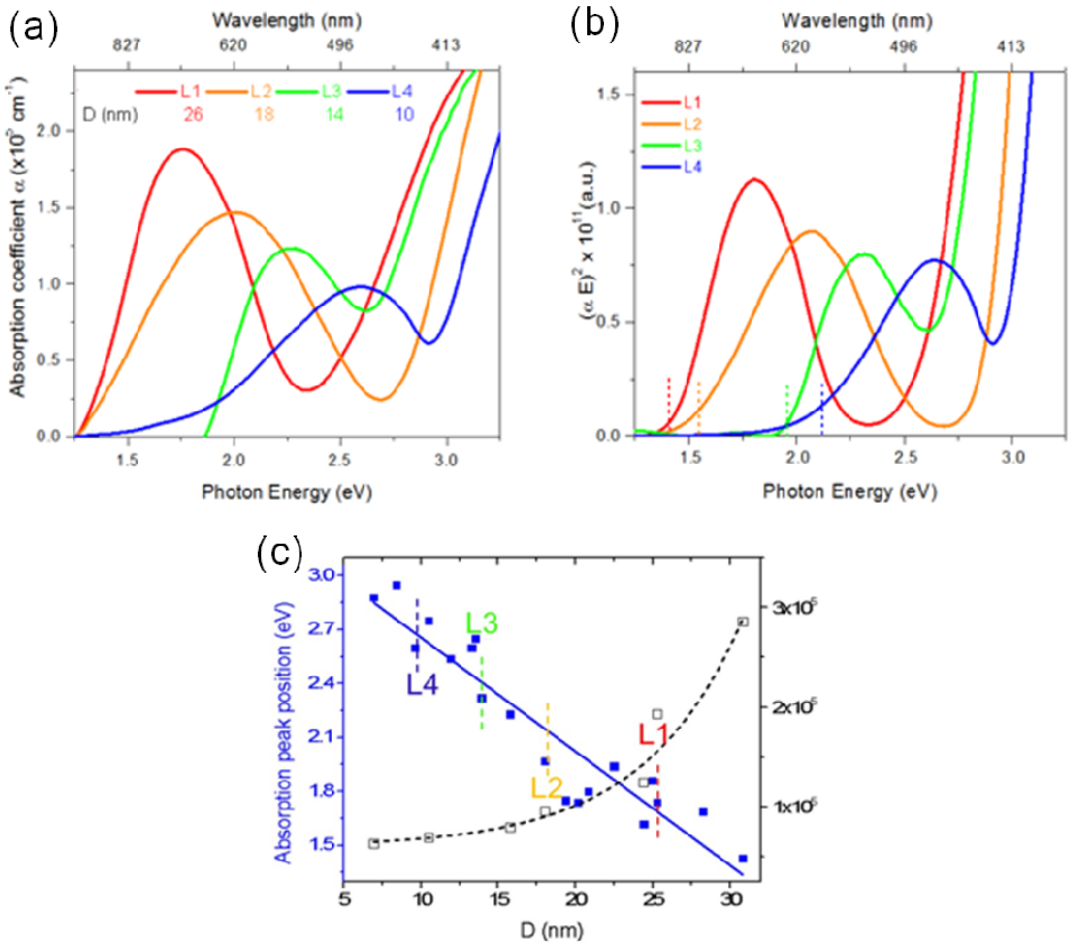

Figure 69. (a) UV-Vis absorption spectra and (b) corresponding direct optical transitions of Bi_2FeCrO_6 thin films. (c) Absorption peak position versus ordered Bi_2FeCrO_6 domain size (D) in films grown with different deposition times or frequencies [201].

For this set of samples (L-series), we obtained a variation of D between 10 nm (film L4 grown at f = 14 Hz) and 26 nm (film L1 deposited at f = 2Hz). The ratio R for these films does not vary considerably, ranging from 0.45% (Film L1) to 0.35% (Film L4), and thus the effect of R on light absorption is minimal. The center of the absorption bands from the visible range varies within large limits, ranging from ~1.75 eV (film L1) to ~2.59 eV (film L4). Films L2 (6 Hz) and L3 (10 Hz) exhibit absorption bands centered at ~1.97 and ~2.25 eV, respectively.

The effect of how R fraction is spatially organized (i.e. D size) on light absorption is shown in Figure 69c. By representing the absorption band positions as a function of D for all obtained films we observed a linear dependence with a negative slope. This red shift behavior of absorption with the increase of D in Bi_2FeCrO_6 films is somehow similar with quantum dot systems where the characteristic absorption position can be controlled by varying the size of the semiconducting nanostructures [293]. As for the mechanism, we consider that the small ordered domains (low D) are more sensitive to the epitaxial strain than the disordered matrix in which they are distributed. We found that the pseudo-cubic unit cell volume of the ordered domain (estimated from asymmetrical RSM measurements) is heavily reduced from 0.0615 nm^3 for films with large D, to reach the value of 0.0602 nm^3 in films with small D. The shrinking of Bi_2FeCrO_6 lattice cell and the decrease of the Cr-O and Fe-O bond distances, which modifies the band gap.

The region given by the ordered domains exhibits a band gap varying from 1.43 to 2.51 eV (Figure 69b). The second threshold gaps observed in Figure 68 originating from the disordered Bi_2FeCrO_6 regions (between 2.75 and 3.12 eV) are also visible in Figure 69b. Hence, we achieved a very low band gap energy in our films, well below the previously reported values of ~2.7 eV obtained from a more complex, doped-ferroelectric thin film system $LaCoO_3$-$Bi_4Ti_3O_{12}$ [294], and relatively close to 1.39 eV obtained very recently by Grinberg *et al.* [146] in weakly ferroelectric films ($P_S \sim 1$ μC/cm^2).

For the $(Fe^{3+})d^5$-$(Cr^{3+})d^3$ system, the oxygen octahedra surrounding the TM cations are rigid and will be less sensitive to strain, due to the homogeneous distribution of the spins in Fe and Cr degenerated *d*-orbitals. On the other hand, for the $(Fe^{2+})d^6$-$(Cr^{4+})d^2$ system, a Jahn Teller CrO_6/FeO_6 octahedra distortion will occur. In this case, the oxygen octahedra surrounding the

TM cations are flexible and will be more sensitive to strain. Therefore, the modification of Jahn Teller CrO_6/FeO_6 octahedra volumes modifies the band gap of ordered Bi_2FeCrO_6.

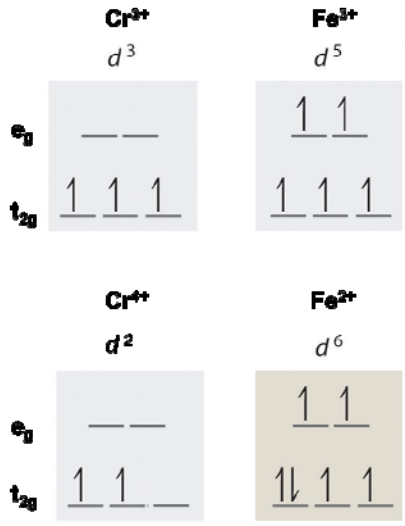

Figure 70. Ground-state electron configuration in octahedral environment of Cr^{3+}, Fe^{3+}, Cr^{4+} and Fe^{2+}.

7.4 Ferroelectric Properties of Bi_2FeCrO_6 Thin Films

We performed PFM measurements on Bi_2FeCrO_6 film surfaces to better understand the surface topography and the ferroelectric properties of the film locally. Figure 71 shows typical out of plane PFM images for Bi_2FeCrO_6 films with different R ratios (L-series). As we can see, all the films have smooth surface with roughness of few nanometers. The as-grown films show no clear preferential orientation of their ferroelectric polarization. We decide to only focus on the out of plane component polarization due to the vertical PV device architecture used here. Ferroelectric domains are visible after applying a DC voltage (± 8V). A comparison of topology with the out-of-plane PFM images shows no direct relationship between grain microstructure and ferroelectric domains in all films. Homogeneous contact distribution is obtained in ordered and disordered-Bi_2FeCrO_6 films. The PFM image indicates that the perpendicular component of polarization can be switched between two stable states.

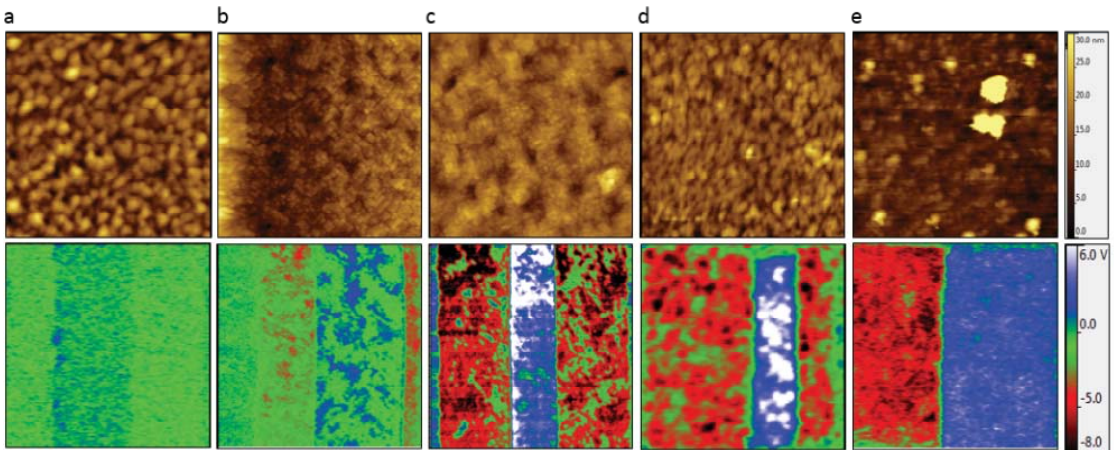

Figure 71. Topography (top) and vertical (bottom) PFM measurements of (a) highly ordered Bi_2FeCrO_6, (b) L1, (c) L2, (d) L3 and (e) highly disordered Bi_2FeCrO_6 films [201].

We also assessed the effect of long range ordering on the ferroelectric properties presented in Figure 72. The ferroelectric measurements were performed at frequencies ranged from 1-2 kHz at room temperature. In the range of low R/small D, the band gap is large (2.3 eV) and no significant effect is observed on polarization, indicating that ferroelectric properties, with $P_r \sim 45$ μC cm^{-2}, persist. At high R/large D the band gap decreases (E_g ~1.4 eV). However, there is also a significant reduction of the ferroelectric polarization, which is detrimental for PV performance. The results show unsaturated hysteresis loop of the highly Fe^{2+}/Cr^{4+} ordered Bi_2FeCrO_6 films (i.e. R = 5.1%) with low ferroelectric polarization value (Figure 72b).

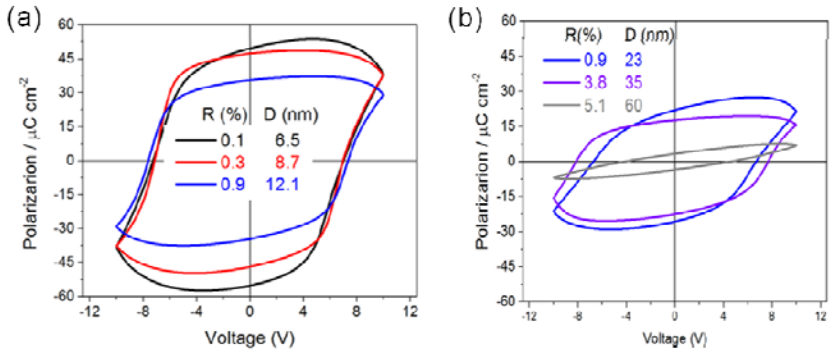

Figure 72. Typical ferroelectric hysteresis loops recorded for Bi_2FeCrO_6 films with cationic ordering in the range of (a) low R/small D and (b) high R/large D [201].

7.5 PV Properties of Bi_2FeCrO_6 Thin Films

To achieve highly efficient Bi_2FeCrO_6-based PV devices, three parameters have to be considered. The Bi_2FeCrO_6 films with suitable semiconducting band gaps, good optical absorption and significant ferroelectric polarizations are needed to promote the generation and separation of the photocharge carriers. Based on the results, we have established the mappings of these three parameters with ordering characteristics R and D values in Bi_2FeCrO_6 films, as shown in Figure 73. The optimal ranges of parameters are illustrated by the rectangle shown in the maps.

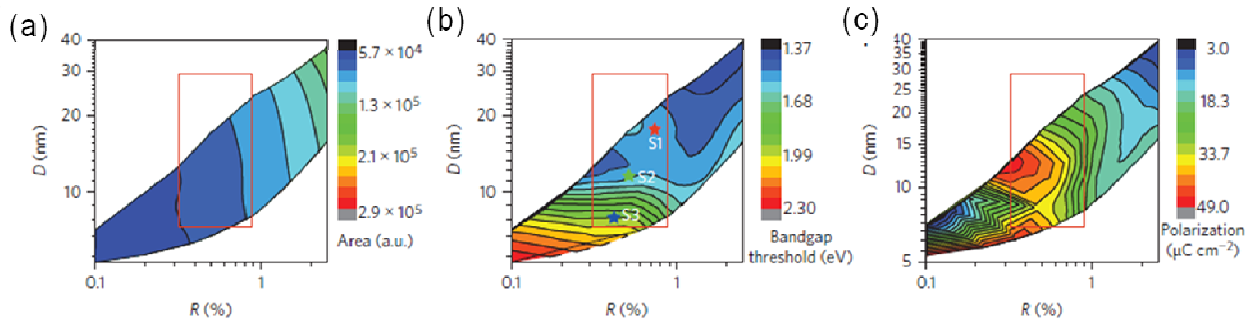

Figure 73. Mappings of absorption peak area (a), band gap threshold (b) and ferroelectric polarization (c) with ordering characteristics R and D in Bi_2FeCrO_6 films.

We subsequently assessed the PV performance of three samples in this area. The device architecture is illustrated in Figure 74a. $SrRuO_3$ conducting perovskite and 2D arrays of ITO transparent conducting layer was used as bottom and top electrode, respectively. The Bi_2FeCrO_6 thin film active layers were deposited at 580°C and at different PLD repetition rates f of 2, 8, 14 Hz (denoted as S1, S2 and S3, similar to the L-series films discussed above) respectively. The performance of these single layer-based PV devices is presented in Figure 74b, and summarized in Table 4.

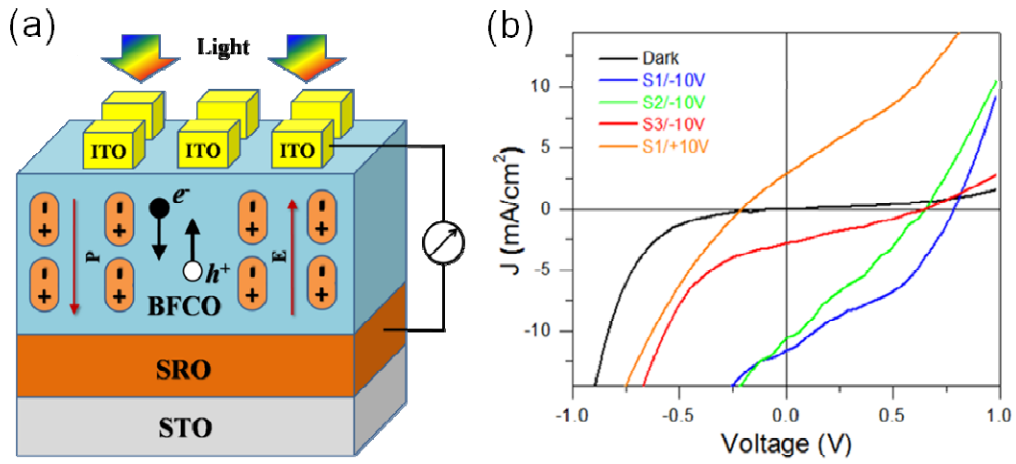

Figure 74. (a) Device geometry of Bi_2FeCrO_6 thin film based PV cells. (b) *J-V* characteristics of Bi_2FeCrO_6 thin film devices under AM1.5G illumination from a calibrated solar simulator with an irradiation intensity of 100 mW/cm^2 [201].

Table 4. Summary of device performance for various Bi_2FeCrO_6 based thin films solar cells.

Samples	J_{sc} (mA/cm^2)	V_{oc} (V)	FF (%)	PCE (%)
S1	11.7	0.79	36	3.3
S2	10.8	0.65	29	2.1
S3	2.8	0.66	27	0.5

The power conversion efficiency (PCE) increases when decreasing the growth rate, reaching a value of 3.3% for device S1, which exhibits a J_{sc} = 11.7 mA/cm^2, a V_{oc} = 0.79 V, and a fill factor (FF) of 0.36. The lowest efficiency (0.5%, FF = 27%) was obtained for S3. We attribute the increased J_{sc} to the decrease of the photogenerated charges recombination rate and enhanced light absorption promoted by ferroelectric polarization and band gap reduction in ordered Bi_2FeCrO_6 regions, respectively. Switching the ferroelectric polarization by applying a pulse of +10 V to the bottom electrode reverses the sign of V_{oc} and J_{sc} of the device, demonstrating that the ferroelectric contribution dominates the PV effect in our devices, and thus a strong *P* is required to achieve high PCE.

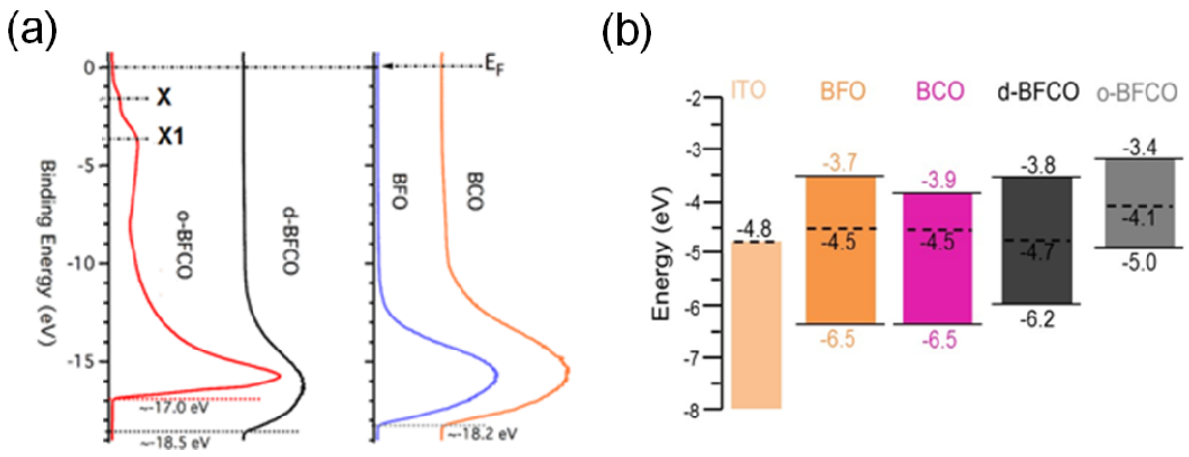

Figure 75. (a) Corresponding UPS valence band structure of o-Bi_2FeCrO_6, d-Bi_2FeCrO_6, $BiFeO_3$ and $BiCrO_3$ samples. (b) Energy level diagram showing the conduction and valence band energies of each film, and the Fermi levels (dashed lines) [201].

To understand PV performance of Bi_2FeCrO_6 based-devices and their dependence on polarization, we analyzed their electronic structure using ultraviolet photoelectron spectroscopy (UPS). The work function E_f is extracted by subtracting the cut-off value of the curve from the kinetic energy of He I (21.22 eV) photon. The ionization potential E_v is extracted from the cut-off value of the curve and it represents the energy below the Fermi level of the material. The UPS spectra were collected using Au as reference for experimental data correction. A significant difference is observed in the highly ordered Bi_2FeCrO_6 case. New states are visible in the 1-3 eV area of the valence band. These correspond to the two highest states, the X at ca. −1.7 eV and X1 at ca. −3.9 eV. The energy of the highest occupied state measured by UPS corresponds to the ionization potential (E_v) of the o-Bi_2FeCrO_6 structure and enables us to distinguish the ordered vs. disordered phases. The ordered phase is characterized by a higher work function (−4.1 eV) and a lower E_v (−5.0 eV). Moreover, d-Bi_2FeCrO_6, $BiFeO_3$ and $BiCrO_3$ are characterized by a higher energy cutoff, resulting in E_f and E_v values of −4.5 and −6.2 eV, respectively.

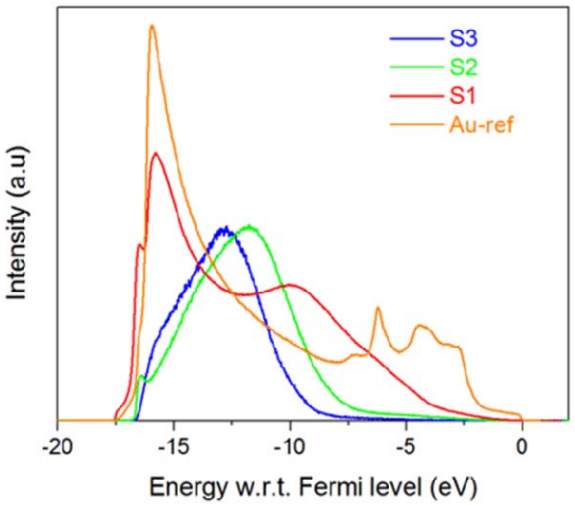

Figure 76. UPS spectra obtained for S-series Bi_2FeCrO_6 films (w.r.t. means with respect to) [201].

For the heterostructures deposited on $SrRuO_3/SrTiO_3$ substrates, since $\phi_{ITO} > \phi_{BFCO}$, when ITO is in contact with Bi_2FeCrO_6 under a condition of thermal equilibrium, electrons pass from the conduction band of Bi_2FeCrO_6 into ITO until the Fermi levels equalize. This leaves behind a depletion region in Bi_2FeCrO_6 with an upward band bending. The region of this contact is highly resistive, called a barrier layer, and this contact is a Schottky contact. In contrast, an ohmic contact with a downward band bending will form at the interface between the Bi_2FeCrO_6 and $SrRuO_3$ interface because of $\phi_{BFCO} > \phi_{SRO}$. The region of this contact is of low resistance, called an anti-barrier layer, and does not affect the conduction behavior under an applied voltage.

For structures of Bi_2FeCrO_6 films (S1-S3), the schematic energy band diagrams are difficult to establish due to the existence of complex ordered/disordered Bi_2FeCrO_6 phases in the films. A qualitative analysis could be performed based on the UPS results obtained from these films (Figure 76). Figure 77a illustrates the energy band distribution of each component materials involved in the structures S1, S2 and S3. In those cases, the Bi_2FeCrO_6 part is represented by empty and filled rectangular shapes related to disordered and ordered regions respectively which coexist in the films.

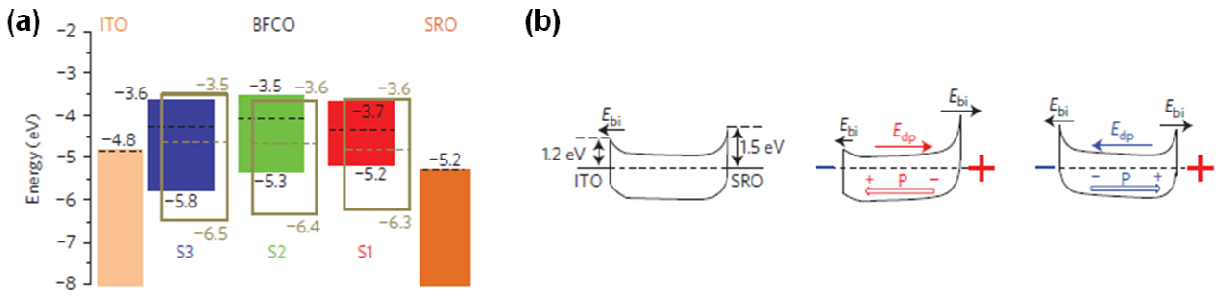

Figure 77. (a) Energy-level diagram based on UPS results showing the valence and conduction energies of each component materials involved in the Bi_2FeCrO_6 device structures. (b) Schematic illustration of simplified energy band diagrams showing the modulation of the Schottky barriers for ITO/ $Bi_2FeCrO_6/SrRuO_3$ heteroepitaxial structures, for an ideal metal-semiconductor interface (left) without polarization and for samples negatively/positively poled at −/+ 10V (middle/right) [201].

A simplified schematic illustration of the energy band diagrams of the heterostructure is shown in Figure 77b. The drawing (left) shows the ideal diagram for ITO/$Bi_2FeCrO_6/SrRuO_3$ junctions, in the absence of a net ferroelectric polarization (*P*). During the *J-V* measurement, a positive voltage is applied to the $SrRuO_3$, resulting in an electric field with opposite direction to the bottom barrier field and along with the top one. The case of Bi_2FeCrO_6 films poled negatively (1 μs, −10 V pulse to the $SrRuO_3$ electrode) the energy band diagram is modified as shown in Figure 77b middle, and this ensures a maximum photo-ferroelectric driving force.

This change is due to the modulation of the energy band induced by *P* flipping [295]. The accumulation of the positive (negative) surface charge at the polarization vector head (tail) side shifts the energy levels in the ferroelectric down (up), resulting in the reduction (increase) of the barrier height (E_{bi}), which becomes large enough to reverse, for positive poling, the original band bending of the ITO/$Bi_2FeCrO_6/SrRuO_3$ structure (Figure 77b). The small V_{oc} and J_{sc} measured after positive poling might be explained by the incomplete *P* switching or/and the presence of recombination sites such as oxygen vacancies that usually exist in such materials. Efficiencies up

to 3.3%, estimated from *J-V* curves obtained after negative poling of the samples, are strongly related to the ferroelectric polarization of Bi_2FeCrO_6.

7.6 Summary

In this chapter, we have systematically investigated the optical and PV properties of Bi_2FeCrO_6 epitaxial thin film grown on (100)-oriented $SrTiO_3$ substrate buffered with $SrRuO_3$ electrode deposited via PLD. We investigated the multiferroic Bi_2FeCrO_6 oxide and established that its electronic band gap can be tuned down to 1.4 eV, by tailoring the Fe/Cr cation ordering and the ordered domain size. In addition, we have shown that the polarization played a very important role on the generated photocurrent. We demonstrated multiferroic Bi_2FeCrO_6 thin film based PV cells with a high efficiency (3.3%) that largely exceeds the highest value (1.25%) of previously reported ferroelectric materials based PV devices.

Chapter 8

Photoelectrochemical (PEC) Properties of Epitaxial Bi_2FeCrO_6 Thin Films

The production of chemical fuels (e.g. hydrogen) by solar energy conversion is being considered as a promising and sustainable approach to overcome the limited supply of fossil fuels [170]. PEC cells, in which energy collection and water electrolysis are combined into a single semiconductor electrode, permit to split water into hydrogen and oxygen by the direct use of sunlight [181, 186, 296, 297]. Of critical importance to the PEC cell is the realization of paired photoanodes (*n*-type) and photocathodes (*p*-type) for oxidation and reduction reactions, respectively. Among various semiconductor photoelectrodes, metal oxides hold the most promise in terms of easy processability and long-term stability [298, 299]. Whereas a plethora of research has been directed at highly efficient *n*-type photoanodes [300-303], research effort in metal-oxide *p*-type semiconducting photocathodes, which are more suitable for the hydrogen generation because their band bending is favorable for the electron transfer to the interface between the electrode and the electrolyte, has been disproportionately scarce with only a few examples such as Cu_2O [304, 305], metal-doped Fe_2O_3 [306], $CaFe_2O_4$ [307], and Rh-doped $SrTiO_3$ [308]. Therefore, there is a an emerging interest in identifying and investigating novel cost-effective *p*-type oxide-based photocathode materials with suitable conduction band

positions, small band gaps (1.6 eV < E_g < 2.2 eV) that absorb visible light, efficient charge transfer to the solid/liquid interface and chemical stability under illumination.

Ferroelectric materials have regained attention as an alternative pathway to achieve solar energy to electricity conversion owing to their efficient ferroelectric polarization-driven carrier separation based on bulk photovoltaic effect [123, 309], in which charge carriers are transported without the existence of a gradient in the electrochemical potential, as compared with traditional silicon based bipolar junction solar cells [126, 131, 134, 150, 285]. In ferroelectric materials, the internal electric field originates from ferroelectric polarization, offering new approaches for exploring and controlling the PV effect which may lead to the development of the next generation solar cells or other optoelectronic devices [130, 151]. By analogy, appropriate control of the polarization induced internal electric fields is also highly expected to enhance the PEC performance of ferroelectric materials based photoelectrodes. PEC behavior has been studied in several material systems with internal electric field [310, 311], mainly focusing on a few ferroelectric oxides that include $BaTiO_3$ [312, 313], $Pb(Zr_xTi_{1-x})O_3$ [314-317], as well as multiferroic $BiFeO_3$ [81, 197]. The conversion efficiencies, however, were observed to be limited by the generated small photocurrent density (on the order of nA or μA cm^{-2}), as well as the wide band gaps (typically 2.7-4 eV), which allow the use of only 8-20% of the solar spectrum. Hence, the real potential of using semiconducting ferroelectric oxides for PEC water splitting applications is yet to be demonstrated. Among all ferroelectrics, double perovskites multiferroic materials possess a magnetic order parameter besides the ferroelectric one and the electron-electron interaction governing the magnetic ordering lead to a smaller gap than for the other ferroelectric perovskites [166, 318], therefore offers a unique opportunity to investigate PEC effects. The recent emergence of a new double perovskites multiferroic material Bi_2FeCrO_6, with

functional properties well above room temperature, opens new opportunities for practical applications of multiferroics [101, 104, 112]. Although a few works have been devoted on the electronic transport, magnetic and ferroelectric behavior, the potential of Bi_2FeCrO_6 material for solar energy conversion applications (e.g. PV) has only begun to be explored [166], and the utility of Bi_2FeCrO_6 in a PEC cell has not been demonstrated yet.

In this chapter, we present *p*-type double perovskites Bi_2FeCrO_6 thin film photocathodes with small band gap energy in the range of 1.9-2.1 eV and suitable conduction band position, exhibiting a relatively high photocathodic current for reducing water. Most importantly, we report an effective tuning of PEC water splitting performance by modulating the ferroelectric polarization in such thin film photoelectrodes. Our studies shed light on the promising potential of utilizing multiferroic materials for the production of H_2 under visible light irradiation, and prove that the manipulation of internal fields within photochemically active ferroelectric materials is a promising strategy for improving their PEC water splitting performance.

8.1 Experimental Section

8.1.1 Deposition of Bi_2FeCrO_6 Epitaxial Thin Films

The Bi_2FeCrO_6 films were deposited onto a series of (100)-oriented substrates including $LaAlO_3$ (LAO), $(LaAlO_3)_{0.3}(Sr_2AlTaO_6)_{0.7}$ (LSAT) and $SrTiO_3$ (STO) single crystalline substrates by PLD at 650 ºC with a laser repetition rate of 8 Hz. The oxygen partial pressure was kept around 10 mTorr. We used $CaRuO_3$ as bottom electrodes in order to promote epitaxial growth and apply the voltage needed to perform the PEC measurements. The $CaRuO_3$ films bottom electrode with thickness around 15 nm was deposited by PLD at 650 ºC under oxygen pressure of 20 mTorr.

After deposition, the samples were cooled down to RT under the same oxygen pressure as the one used for deposition.

8.1.2 PEC Measurements

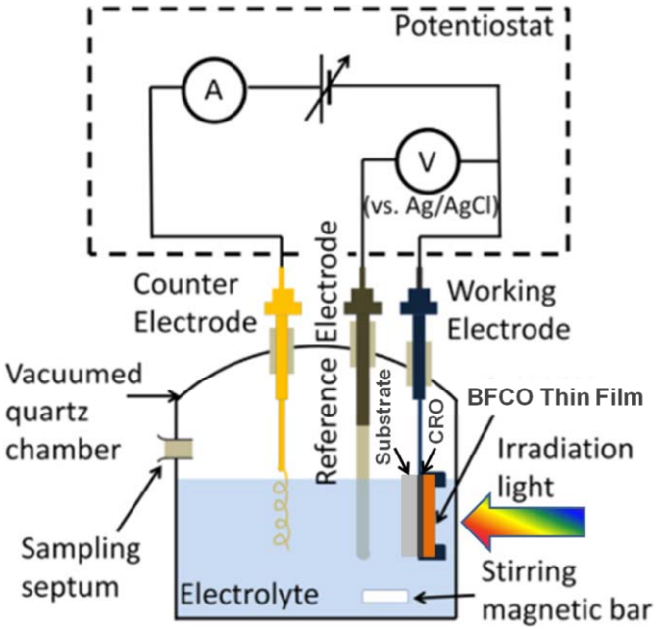

Figure 78. Schematic representation of the photoelectrochemical cell used for the for Current-Voltage (*J-V*) measurements of the epitaxial Bi_2FeCrO_6 thin film based photoelectrodes [319].

The PEC performance of the photoelectrodes was evaluated in a three-electrode configuration (Figure 78), which consists of an Ag/AgCl reference electrode, a Pt counter electrode, and a Bi_2FeCrO_6 thin film working electrode. The $CaRuO_3$ bottom electrode was connected with a Cu wire using silver paste. The entire sample except the thin film surface was then covered by insulating epoxy. All PEC measurements were conducted in 1 mol/L Na_2SO_4 (pH = 6.8) as electrolyte. The photoresponse was measured from a 300 W Xe arc lamp used as the light source with an AM1.5G filter. A 420 nm long-pass filter was used to measure the photoresponse in the visible range. All the current versus potential measurements were carried out at a 20 mV/s sweep rate. Mott-Schottky measurements were obtained using an electrochemical impedance method

with AC amplitude of 10 mV. To pole the Bi_2FeCrO_6 thin film, silver electrodes were deposited on top of the film. After electric poling, the sample was subsequently dipped in HNO_3 solution (8 mol/L) to remove the Ag electrodes prior to the PEC measurement.

8.2 Characterizations

Table 5. Lattice parameters and lattice mismatches between $CaRuO_3$, Bi_2FeCrO_6 and different substrates used in our study [320].

	Layer		Substrate		
			$LaAlO_3$	$(LaAlO_3)_{0.3}(Sr_2AlTaO_6)_{0.7}$	$SrTiO_3$
	Lattice	Pseudo-cubic	Cubic	Cubic	Cubic
	Orthorhombic		a = 3.792 Å	a = 3.868 Å	a = 3.905 Å
$CaRuO_3$	a = 5.36 Å	a' = 3.83 Å	(−)1.00%	(+)0.98%	(+)1.92%
	b = 5.53 Å				
	c = 7.66 Å	c' = 3.85 Å	(−)1.53%	(+)0.46%	(+)1.41%
	Rhombohedral				
Bi_2FeCrO_6	a = 5.56 Å	a' = 3.93 Å	(−)3.64%	(−)1.60%	(−)0.64%

A series of epitaxial Bi_2FeCrO_6 thin films were deposited by PLD on several (100)-oriented substrates, namely, $LaAlO_3$, $(LaAlO_3)_{0.3}(Sr_2AlTaO_6)_{0.7}$, and $SrTiO_3$, having in-plane average parameters ranging from 3.792 Å for $LaAlO_3$ to 3.905 Å for $SrTiO_3$, buffered with $CaRuO_3$ electrodes (~15 nm), respectively. Figure 79c shows XRD patterns of the heteroepitaxial $Bi_2FeCrO_6/CaRuO_3$ thin films deposited on different substrates. Only the 00l (l = 1, 2, 3) pseudocubic reflections of the films composing the $Bi_2FeCrO_6/CaRuO_3$ heterostructure and of the substrates are present, indicating that the oxide layers are highly (001)-oriented, and no impurity is observed.

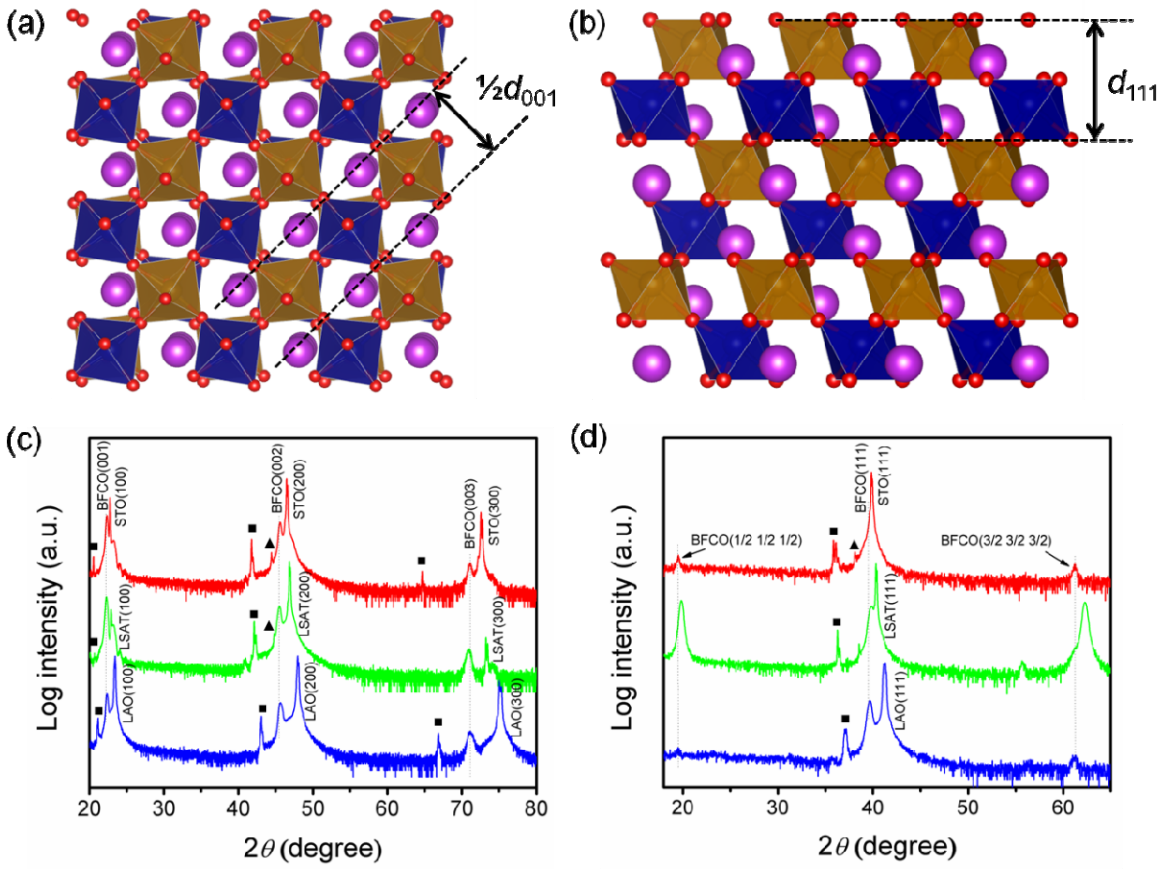

Figure 79. Crystal structure of double perovskites Bi_2FeCrO_6 showing different types of Fe and Cr octahedral stacking along (a) [001] and (b) [111] cubic directions. O and Bi atoms are denoted by the smallest ball with red and the biggest ball with purple, respectively. Fe and Cr octahedral are blue and ochre, respectively. (c) X-ray diffraction patterns of Bi_2FeCrO_6 thin film deposited on (100)-oriented $LaAlO_3$, $(LaAlO_3)_{0.3}(Sr_2AlTaO_6)_{0.7}$ and $SrTiO_3$ substrates buffered wth $CaRuO_3$, respectively. (d) Asymmetrical XRD θ-2θ scan around (111) reflection recorded for all Bi_2FeCrO_6 thin films, showing the superstructure reflections. It should be noted that the superlattice peaks of $Bi_2FeCrO_6/CaRuO_3/(LaAlO_3)_{0.3}(Sr_2AlTaO_6)_{0.7}$ contain contribution from the substrate. In all XRD figures, the squares correspond to K_β peaks while the triangles indicate tungsten contamination from the x-ray tube cathode [202].

RSM around the asymmetrical (204) reflection of Bi_2FeCrO_6 thin films on various substrates are shown in Figure 80. The small condensed reciprocal point of the Bi_2FeCrO_6 in all figures suggests a high quality epitaxial growth of the Bi_2FeCrO_6 thin film on different substrates. The positions of the peaks are located close to the corresponding peaks of the substrates along the Q_x

axis for each map, suggesting that the in-plane lattice parameter of the heterostructure is close to that of the substrate. This reveals highly compressively-strained epitaxial layers throughout the whole heterostructure, originating from the lattice mismatch between the film and the substrate (Table 5). The strain of the $CaRuO_3$ buffered layer leads to fully coherent epitaxial growth of the heterostructure and precludes strain relaxation, especially for Bi_2FeCrO_6 film deposited on $LaAlO_3$ substrate.

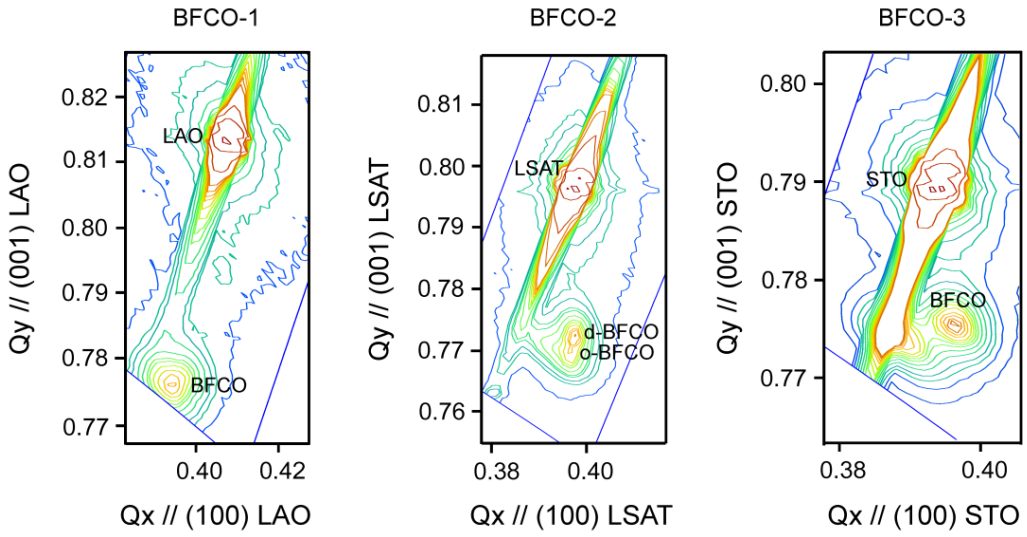

Figure 80. RSM of Bi_2FeCrO_6 films around (204) reflection on different substrates [202].

Table 6. Main structural parameters of different Bi_2FeCrO_6 thin film (o-Bi_2FeCrO_6) based heterostructures calculated from the RSM measurements.

Samples	Ordered domain				
	a (Å)	c (Å)	V (Å)	R (%)	Domain Size (nm)
$Bi_2FeCrO_6/CaRuO_3/LaAlO_3$	3.920	3.971	61.02	0.66	33.5
$Bi_2FeCrO_6/CaRuO_3/(LaAlO_3)_{0.3}(Sr_2AlTaO_6)_{0.7}$	3.861	3.993	59.52	0.72	34.2
$Bi_2FeCrO_6/CaRuO_3/SrTiO_3$	3.860	3.974	59.21	1.20	33.8

Since the *B* site-cationic ordering in double perovskites materials of type $A_2BB'O_6$ plays a crucial role in determining magnetic properties and tuning optical characteristics, evidence of its existence is an important step towards understanding the functional properties of such materials

[101, 292, 321]. As seen from the different types of stacking in Bi_2FeCrO_6 crystals (Figure 79a and b), the alternation of FeO_6 and CrO_6 planes is achieved only in the [111] cubic direction. Hence, we performed asymmetrical θ-2θ scans around the (111) substrate reflections, as shown in Figure 79d. The sample was tilted by 54º (angle between [111] and [001] cubic directions) with respect to the surface normal. Large θ-2θ scans reveal two periodic satellite peaks at 19.5º and 61.2º, corresponding to superstructure reflections of ($^1/_2$ $^1/_2$ $^1/_2$) and ($^3/_2$ $^3/_2$ $^3/_2$), respectively, in addition to main cubic reflections (111) of substrate and Bi_2FeCrO_6. These superstructures reflections suggest a doubling of the crystal structure and the existence of Fe/Cr ordering in the films along the [111] crystal structure, in agreement with the predicted rhombohedral Bi_2FeCrO_6 structure [99]. A careful analysis of normalized intensities of superstructure peaks was carried out to investigate the quality of the degree of Fe/Cr cationic ordering (R) (listed in Table 6), which was estimated from the normalized ratio of the superlattice peaks intensities to the main (111) reflection intensity of Bi_2FeCrO_6 in the pseudo-cubic indexing. It should be noted that for $Bi_2FeCrO_6/CaRuO_3/(LaAlO_3)_{0.3}(Sr_2AlTaO_6)_{0.7}$ an asymmetrical θ-2θ scan was also performed on bare substrate because $(LaAlO_3)_{0.3}(Sr_2AlTaO_6)_{0.7}$ itself shows superstructure along the [111] direction as well, and the R ratio was calculated after subtraction of the contribution from the substrate. These results do not agree with a previous work by Nechache *et al*. [320]. We attribute this discrepancy to the different growth temperature used in this study, which is a crucial parameter that determines the cationic ordering [322].

XPS was performed to identify the chemical composition and oxidation states present in different Bi_2FeCrO_6 thin films (Figure 81). Survey XPS spectra reveal the presence of Bi, Fe, Cr, and O elements with a Bi/Fe/Cr atomic ratio of ≈ 2:1:1 in all films (error < 2%), in agreement with its stoichiometric ratio. For transition metal ions, the 2*p* core level splits into $2p_{1/2}$ and $2p_{3/2}$

components. The binding energy of Fe $2p_{3/2}$ is expected to be 710.7 eV for Fe^{3+} and 709.0 eV for Fe^{2+}. We deduce that the oxidation state of Fe in the Bi_2FeCrO_6 thin films is mainly Fe^{3+} and there is no evidence for Fe^{2+} within the resolution of a few atomic percent. In the case of Cr, the expected $2p_{3/2}$ values are around 576.3 and 575.2 eV for Cr^{3+} and Cr^{4+}, respectively. Analysis of different valence state of Cr suggests that the 3+ state is predominant in all films.

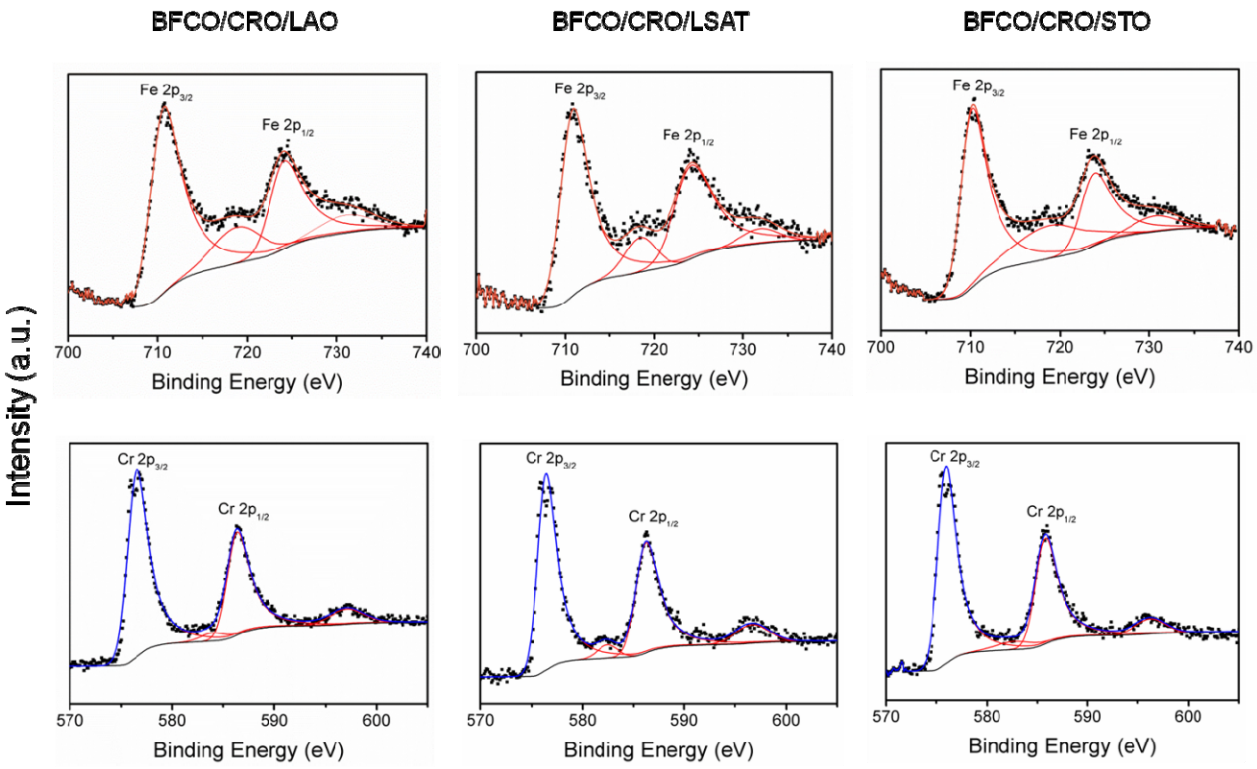

Figure 81. XPS Fe (top) and Cr (bottom) 2*p* lines spectra of different Bi_2FeCrO_6 thin films [202].

We used spectroscopic ellipsometry to elucidate the light absorption properties of the Bi_2FeCrO_6 thin films. Figure 82a displays the absorption coefficient α of different Bi_2FeCrO_6 films, together with that obtained for epitaxial $BiFeO_3$ and $BiCrO_3$ films for comparison. Additional optical transition peaks appear in the range between 500 to 700 nm in the absorption spectra of all the Bi_2FeCrO_6 films, in contrast to that of the $BiFeO_3$ and $BiCrO_3$ films. For all samples, the absorption coefficient α varies between 2.7×10^5 and 6.0×10^5/cm at 550 nm, much

higher than that of widely studied *p*-type Cu_2O which has similar band gap (~2.0 eV) [323]. In addition, we observed a strong dependence (a factor of ~2) of the absorption peak area on R ratio (Figure 83), demonstrating that the Fe/Cr cationic ordering is a crucial parameter that can be used to tailor the amount of absorbed light in double perovskites Bi_2FeCrO_6 films. These results are consistent with the results we got in chapter 7.

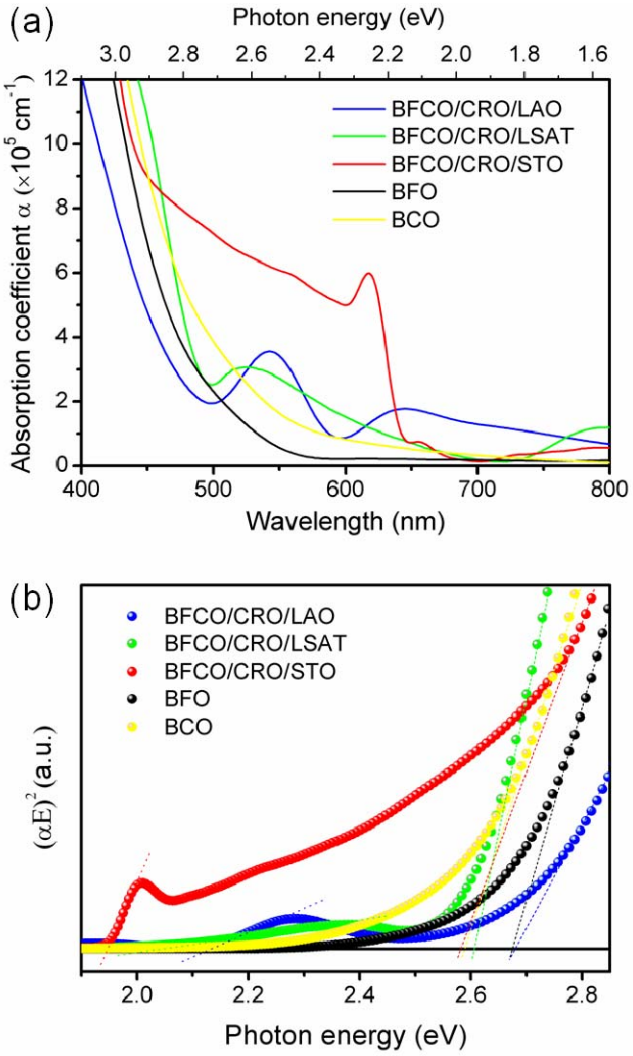

Figure 82. Spectroscopic ellipsometry of Bi_2FeCrO_6 thin films grown on different substrates: (a) absorption coefficients and (b) direct optical transitions [202]. $BiCrO_3$ is denoted by BCO.

As expected, the direct optical transitions presented by the $(\alpha E)^2$ vs. E plots (Figure 82a) feature two linear portions, indicating the presence of two threshold gaps in the Bi_2FeCrO_6 films. The first threshold gap observed in the range of 2.5-2.7 eV is close to that of $BiFeO_3$ and $BiCrO_3$ films, which is attributed to the disordered Bi_2FeCrO_6 regions (d-Bi_2FeCrO_6). As for the second optical transition region, linear extrapolation of $(\alpha E)^2$ to zero versus energy yields band gaps of ~2.12 eV, 2.05 eV, and 1.94 eV in $Bi_2FeCrO_6/CaRuO_3/LaAlO_3$, $Bi_2FeCrO_6/CaRuO_3/(LaAlO_3)_{0.3}(Sr_2AlTaO_6)_{0.7}$, and $Bi_2FeCrO_6/CaRuO_3/SrTiO_3$ thin films, respectively. These band gaps are thought to originate from the ordered domains (o-Bi_2FeCrO_6). According to the electronic structure calculations confirmed by absorption spectra of a similar double perovskites La_2FeCrO_6 [292], we assign these band transitions (~2.0 eV) to charge transfer excitations between Cr to Fe mixed *d* orbitals Hubbard transitions that occur in o-Bi_2FeCrO_6. The E_g of Bi_2FeCrO_6 is theoretically defined by the difference between the Cr 3*d*-O 2*p* hybrids valence band and the empty Fe 3*d* conduction band [99, 167]. Altering E_g requires the modification of transition metal (TM)-O bond lengths and their interaction energies, that is, hybridization energy and Coulomb repulsion [324, 325]. Considering the inverse dependence of E_g with respect to the lattice parameter, i.e., the smaller the lattice parameter the larger the bandgap, we conclude that tuning E_g involves altering the lattice parameters, as examplified by epitaxial $BiFeO_3$ films [326, 327].

In our case, although such a variety of substrates allows a continuous change of the compressive misfit strain (Table 6), the shift in band gap is merely < 0.2 eV, much smaller than both theoretical and experimental values reported for $BiFeO_3$ (> 0.5 eV) [326, 327]. This suggests that tuning of the band gap is insensitive to the compressive strain in the Bi_2FeCrO_6 films. On the other hand, tunability of the band gap is also related to the oxidation states in

perovskite structures [328]. XPS analysis shows that 3+ states are dominant for both Fe and Cr elements (Figure 81). According to previous studies, for the $(Fe^{3+})d^5$-$(Cr^{3+})d^3$ system, the oxygen octahedra surrounding the TM cations are rigid and will be less sensitive to strain, due to the homogeneous distribution of the spins in Fe and Cr degenerated *d*-orbitals [329, 330]. In addition, the size of ordered domains should not affect the band gap since they are quite similar in all Bi_2FeCrO_6 films (Table 6). Thus, the modulation of the band gap can mainly be accommodated by limited octahedral rotations or tilts and will only result in a small change (< 0.2 eV) of E_g.

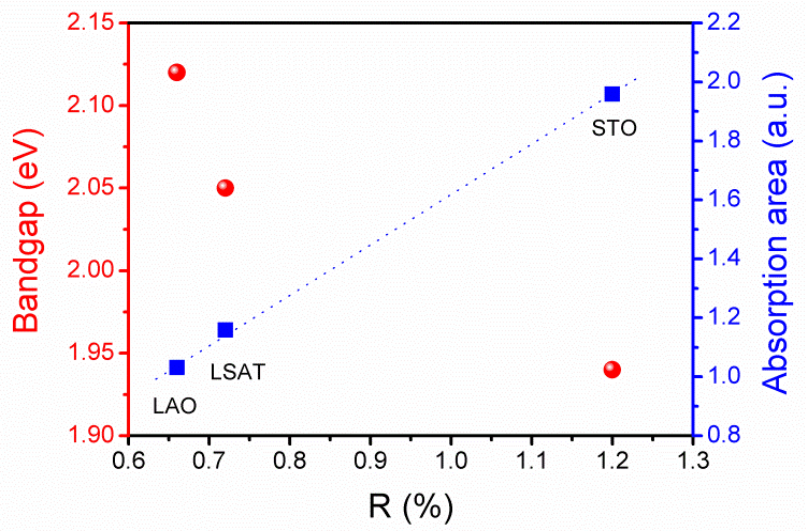

Figure 83. Band gap threshold (o-Bi_2FeCrO_6) and corresponding absorption area versus R in Bi_2FeCrO_6 films grown on different substrates [202]. The dash line is to guide the trend of the measured points.

8.3 PEC Performance

To evaluate the PEC water splitting activity of the epitaxial Bi_2FeCrO_6 thin film photoelectrodes, linear-sweep cyclic voltammogram (*J-V*) were measured under chopped AM1.5G simulated sunlight illumination, so the dark and light current could be monitored simultaneously. As shown in Figure 84b, the Bi_2FeCrO_6 thin film grown on $CaRuO_3/(LaAlO_3)_{0.3}(Sr_2AlTaO_6)_{0.7}$ achieved a

significant cathodic photocurrent density (J_{ph}) of −0.40 mA/cm^2 at −1.0 V applied bias versus RHE after subtraction of the dark current in 1 M Na_2SO_4 at a pH of 6.8, which was the electrolyte used in all PEC experiments in this study.

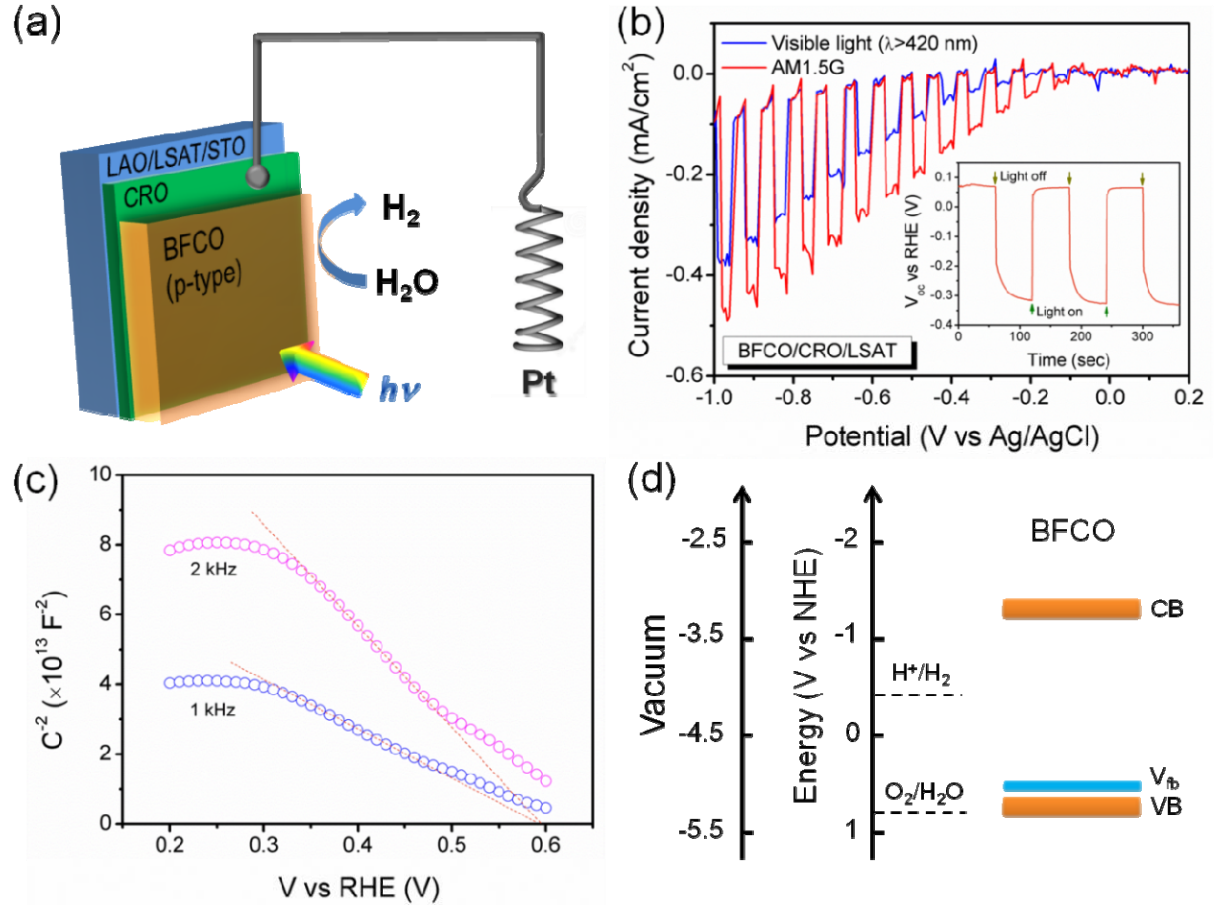

Figure 84. (a) Schematic diagram showing *p*-type Bi_2FeCrO_6 thin film used as photocathode for PEC water splitting. (b) Variations of the current density with applied voltage (vs Ag/AgCl) in 1 mol/L Na_2SO_4 at pH of 6.8 under chopped simulated sunlight illumination of Bi_2FeCrO_6 thin film grown on $CaRuO_3/(LaAlO_3)_{0.3}(Sr_2AlTaO_6)_{0.7}$ substrate. Inset shows the open-circuit potential change of the thin film electrode with and without illumination. (c) Mott-Schottky measurement of the thin film photoelectrode. The intercept of the dashed line can be used to determine the flat-band potential of the Bi_2FeCrO_6 thin film. (d) Calculated energy-level diagram based on Mott-Schottky results showing the flat band potential (V_{fb}), valence band (VB) and conduction band (CB) energies of the Bi_2FeCrO_6 thin film [202].

To confirm the photoresponse of the Bi_2FeCrO_6 thin film electrode in the visible range, a *J-V* measurement was performed with the use of a 420 nm long-pass filter, and a high J_{ph} of −0.30 mA/cm^2 was obtained at −1.0 V. The open-circuit potential increased when the electrode was exposed to AM1.5G illumination (Figure 84b, inset), which is representative of typical *p*-type semiconductor behavior.

Table 7. Summary of structural, physical characteristics and PEC performance of Bi_2FeCrO_6 thin film photoelectrodes.

Device structures	R (%)	Band gap (eV)		J_{ph} (mA cm^{-2})
		Ordered domain	Disordered domain	
$Bi_2FeCrO_6/CaRuO_3/LaAlO_3$	0.66	2.12	2.68	0.2
$Bi_2FeCrO_6/CaRuO_3/(LaAlO_3)_{0.3}(Sr_2AlTaO_6)_{0.7}$	0.72	2.05	2.61	0.4
$Bi_2FeCrO_6/CaRuO_3/SrTiO_3$	1.20	1.94	2.58	1.0

The flat band potential (V_{fb}) of the Bi_2FeCrO_6 thin film was determined via a Mott-Schottky analysis using capacitance impedance measurement on the electrode/electrolyte at 1 and 2 kHz frequencies in the dark, shown in Figure 84c. The negative slope of the Mott-Schottky data is the expected behavior for a *p*-type semiconductor. Thus, the *x*-axis intercept (V_0 = 0.59 V) can be used to determine the V_{fb} from the equation $V_0 = V_{fb} - kT/e$, which yields a V_{fb} of +0.62 V versus RHE (pH = 6.8) for both frequencies (1 and 2 kHz). If the valence band edge is assumed to be located ∼0.1-0.2 V below the flat-band potential, its conduction band edge is determined to therefore occur at ca. ∼−1.33 to −1.23 V vs. RHE, in agreement with our previous results obtained using UPS measurements in chapter 7, suggesting that photoexcited electrons in the conduction band of Bi_2FeCrO_6 can thermodynamically reduce water to H_2. The Bi_2FeCrO_6 thin films for the use as photocathodes are represented by Figure 84a. In addition, an acceptor density (N_A) from the slope of the Mott-Schottky plot was determined by Mott-Schottky relation for *p*-

type semiconductor as follows: $1/C^2 = (2/e\varepsilon_r\varepsilon_0 N_A A^2)[-V + V_{fb} - kT/e]$, where C is the space charge layers capacitance, e is the elementary charge, ε_r is the dielectric constant (80 according to our previous measurement), ε_0 is the permittivity of vacuum, N_A is the acceptor density, V is the applied voltage, V_{fb} is the flat band potential, k is the Boltzmann constant, T is the temperature (300 K) and A is the surface area in contact with electrolyte. This calculation yields a $N_A = 1.6 \times 10^{18}/cm^3$ by using the slope of the line at 2 kHz. This is a similar, but somewhat low, dopant density as that known for other *p*-type semiconductors, such as that found for widely studied Cu_2O [331, 332]. Thus, a promising new *p*-type metal oxide semiconductor is found that can find application in photoelectrode-mediated solar fuel production.

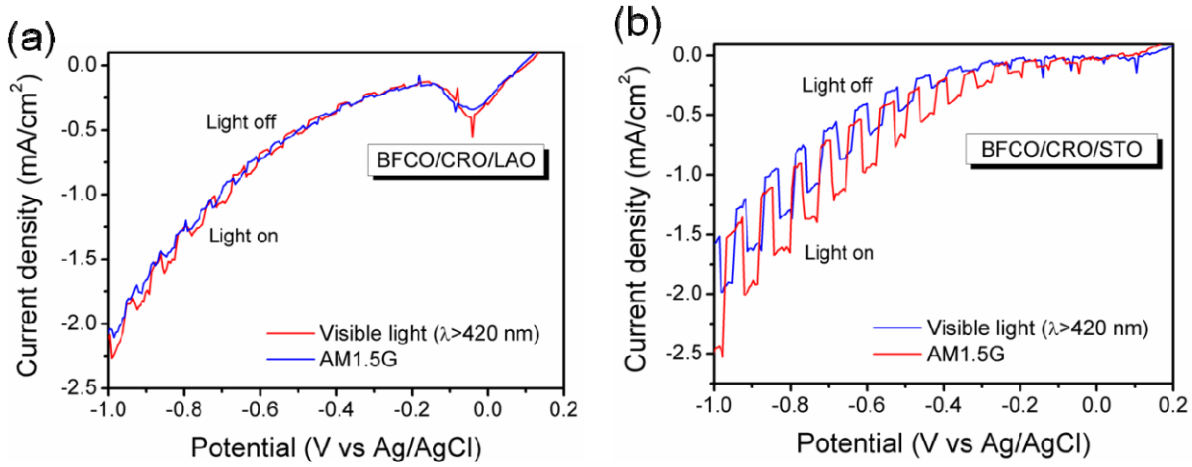

Figure 85. Variations of the current density with applied voltage (vs Ag/AgCl) in 1 mol/L Na_2SO_4 at pH of 6.8 under chopped simulated sunlight and visible light illumination of Bi_2FeCrO_6 thin film grown on (a) $CaRuO_3/LaAlO_3$ and (b) $CaRuO_3/SrTiO_3$ substrate, respectively [202].

To understand the impact of Fe/Cr cationic ordering on the PEC performance, *J-V* measurements of Bi_2FeCrO_6 thin films grown on $LaAlO_3$ and $SrTiO_3$ substrate which have distinct R values (0.66 and 1.20, respectively) were carried out and studied. Figure 85a shows chopped photocurrent densities (AM1.5G simulated sunlight illumination) plotted versus the

RHE. A significant photocurrent density of −1.0 mA/cm^2 at −1.0 V versus RHE was obtained for $Bi_2FeCrO_6/CaRuO_3/SrTiO_3$ while $Bi_2FeCrO_6/CaRuO_3/LaAlO_3$ only reached a current density of −0.2 mA/cm^2 at the same bias. Since $SrTiO_3$ is also active under UV light with a band gap of 3.2 eV, we have performed *J-V* measurement under visible light (λ > 420 nm) to rule out any effects from $SrTiO_3$ substrate (Figure 85b). As for $Bi_2FeCrO_6/CaRuO_3/SrTiO_3$, a high photocurrent of −0.5 mA/cm^2 (−1.0 V) is maintained under visible light irradiation. In contrast, a negligible photoresponse was obtained from $Bi_2FeCrO_6/CaRuO_3/LaAlO_3$ under the same conditions. The J_{ph} values of all samples under study are listed in Table 7. We can see that the photocurrent density of $Bi_2FeCrO_6/CaRuO_3/(LaAlO_3)_{0.3}(Sr_2AlTaO_6)_{0.7}$ sample with R ratio of 0.72 is in between. The substantial differences of photocurrent density of different Bi_2FeCrO_6 thin films can be ascribed to the enhanced light absorption as well as band gap reduction in ordered Bi_2FeCrO_6 regions. Considering that the deposition parameters for Bi_2FeCrO_6 films with higher degree of cationic ordering have not been fully optimized (band gap could be reduced to 1.4 eV in highly ordered Bi_2FeCrO_6 film, according to Chapter 7), these results are very encouraging.

To gain insight into the effects of the ferroelectric polarization on the PEC properties, *J-V* measurements were carried out for the $Bi_2FeCrO_6/CaRuO_3/SrTiO_3$ sample with two different ferroelectric polarization directions, respectively. To pole the Bi_2FeCrO_6 thin film, silver electrodes were deposited on top of the film. An upward poling (P_{up}, 1 μs, −25 V pulse at the $CaRuO_3$ electrode) results in an electric field (opposite to the polarization direction) driving the positive charges accumulated on the film's surface and negative ones to the bottom electrode, as schematically illustrated in Figure 86b (right). Subsequently, the Ag electrodes were removed with HNO_3 solution prior to PEC measurements. The same procedure was repeated for the downward poled (P_{down}, 1 μs, +25 V pulse at the $CaRuO_3$ electrode) Bi_2FeCrO_6 film with

negative charges on the surface and positive charges on the bottom electrode (Figure 86c, right). The negatively poled (P_{up}) Bi_2FeCrO_6 film exhibited a high J_{ph} up to ~−2.0 mA/cm^2 at a potential of ~−1.0 V versus RHE (Figure 86b), approximately two times larger than that of the sample without a net ferroelectric polarization. For the positively poled (P_{down}) Bi_2FeCrO_6 film, on the contrary, the J_{ph} slightly decreased to ~ −0.8 mA/cm^2 (Figure 86c) at the same bias. Thus, Bi_2FeCrO_6 films with positive polar surface (P_{up}) are advantageous for enhancing their PEC water splitting activity, whereas films with negative polar surface (P_{down}) are unfavorable.

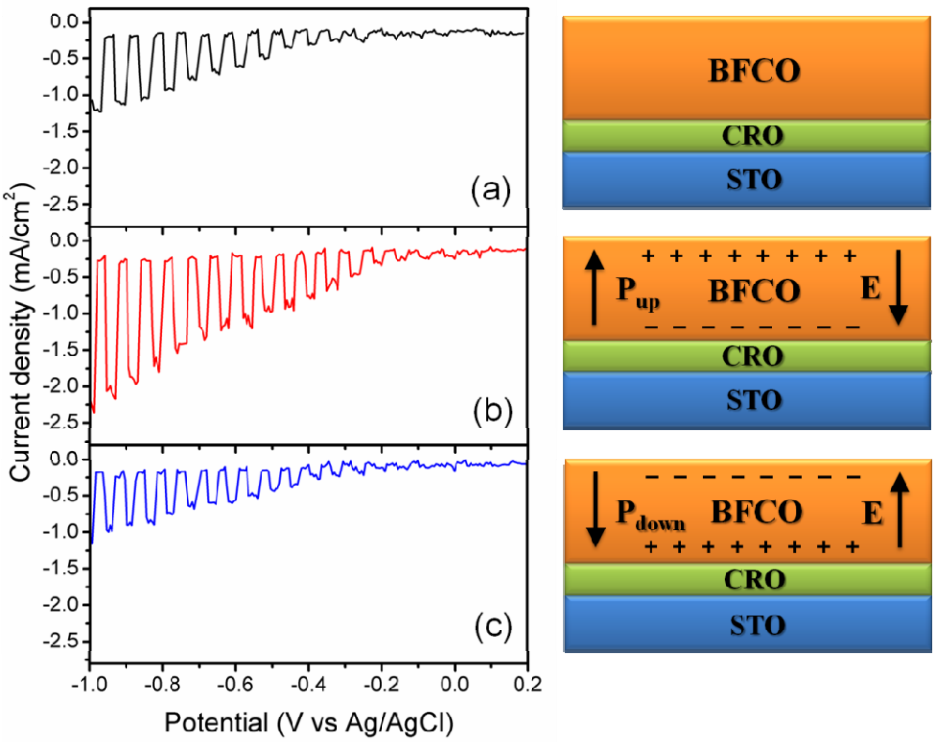

Figure 86. Variations of the current density with applied voltage (vs Ag/AgCl) in 1 mol/L Na_2SO_4 at pH of 6.8 under chopped simulated sunlight illumination (AM1.5G) of $Bi_2FeCrO_6/CaRuO_3/SrTiO_3$ sample: (a) before, (b) after negative (P_{up}, +25V) and (c) positive poling (P_{down}, −25V). Schematic illustration is shown on the right of each figure [202].

These results indicate that for ferroelectric semiconductors possessing the defined direction of polarization vector, the behavior of the photogenerated carriers is strongly influenced by the polarization field, which is consistent with previous results on other ferroelectric perovskites [312,

314, 316]. Additional direct evidence of spontaneous ferroelectric polarization switching under an electric field was examined locally using PFM on the $Bi_2FeCrO_6/CaRuO_3/SrTiO_3$ sample. The observed hysteresis loop confirms the ferroelectric character of the Bi_2FeCrO_6 film (Figure 87).

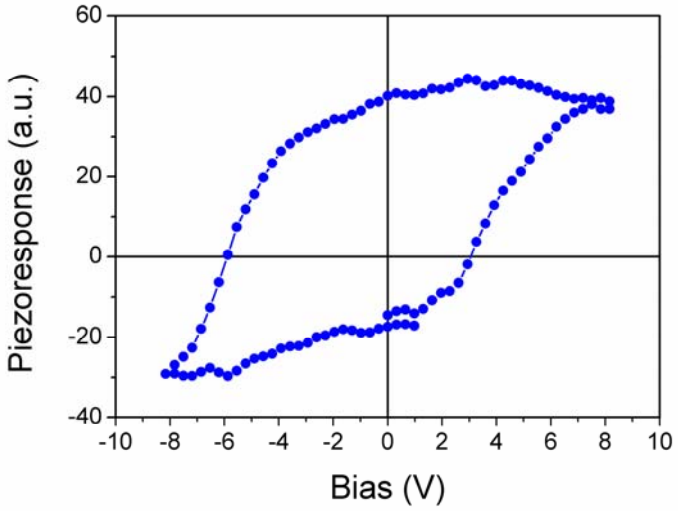

Figure 87. Ferroelectric hysteresis loop (out of plane) recorded from $Bi_2FeCrO_6/CaRuO_3/SrTiO_3$ sample by PFM [202].

On the basis of the above results, a tentative schematic illustration of the energy band diagram of Bi_2FeCrO_6 thin film based photocathode is depicted in Figure 88. The drawing on the left shows the ideal diagram for $CaRuO_3$/*p*-type Bi_2FeCrO_6/electrolyte junctions, in the absence of a net ferroelectric polarization. After poling the ferroelectric Bi_2FeCrO_6 thin film, the surface polarization charge causes band bending within a subsurface region termed the space charge region (SCR), associated with an electric field gradient. The width of the space charge can be estimated from the following expression:

$$W = \sqrt{\frac{2\varepsilon_0\varepsilon_r}{eN_A}(\emptyset_{sc} - \frac{kT}{e})} \qquad \text{(Eq. 8.1)}$$

where $ø_{sc}$ (i.e. $V_{fb} - V$) is the potential drop across the space charge region. Thus, the calculated value of W is in the range of 47 to 94 nm with $ø_{sc}$ from 0.4 to 1.6 V. As the length scale of the films (~120-130 nm) is of the same order as the space charge layer, the influence of band

bending at the interface can no longer be ignored. For the negatively poled Bi_2FeCrO_6 film, the energy band diagram is modified as shown in the middle of Figure 88. Under illumination, the photogenerated e^-/h^+ pairs will be separated by the driving force arising from an internal electric field, and the electrons in Bi_2FeCrO_6 thin films will be driven towards the interface of film surface/electrolyte, while the holes will migrate to the bottom electrode. Consequently, the recombination of the photogenerated e^-/h^+ are effectively hindered, leading to an enhanced PEC activity. When the film is positively poled, on the other hand, the oppositely slanted band causes electrons to drift into the bulk and positive holes to accumulate at the electrolyte (Figure 88, right), which is unfavorable for electron flow, and thus will reduce PEC efficiency.

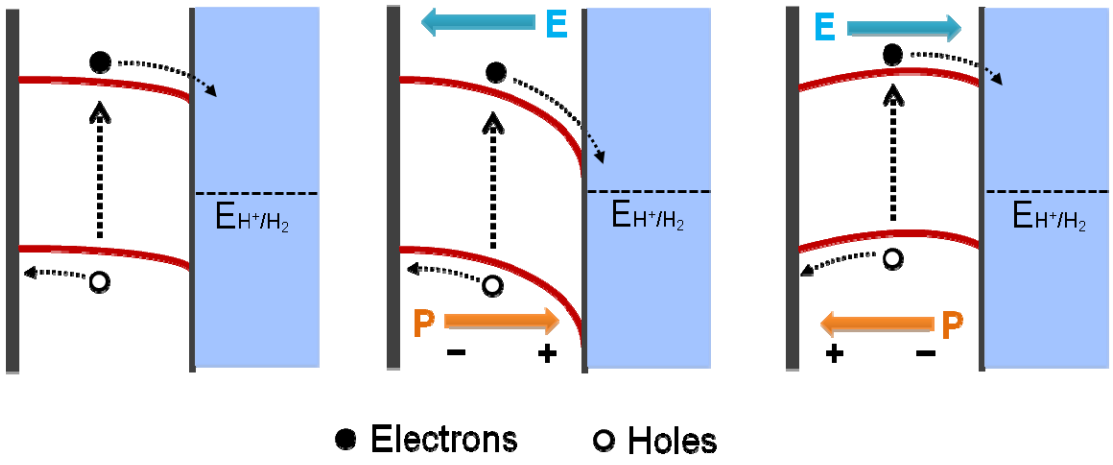

Figure 88. Schematic illustration of simplified energy band diagrams of a PEC cell based on *p*-type Bi_2FeCrO_6 thin film in electrolyte without polarization (left) and negatively/positively poled (middle/right) [202].

8.3 Summary

In conclusion, we demonstrated epitaxial Bi_2FeCrO_6 thin films with a relatively narrow band gap (1.9-2.1 eV) and suitable conduction band position as a novel photocathode material, for the visible-light-driven reduction of water to hydrogen. We found that the band gap energy of Bi_2FeCrO_6 thin film is insensitive to the compressive strain resulting from the misfit of the lattice

parameters between various substrates and the Bi_2FeCrO_6 thin layer, while the amount of absorbed light is tightly related to the degree of Fe/Cr cationic ordering. PEC measurements showed that the highest photocurrent up to −1.0 mA/cm^2 at a potential of −1.0 V versus the RHE was obtained in *p*-type Bi_2FeCrO_6 photocathode with the film grown on $CaRuO_3/SrTiO_3$ substrate. Importantly, after poling the Bi_2FeCrO_6 thin film, the photocurrent density can be further enhanced by ~2 fold due to the modulation of the band structure by controlling the internal electric field. These findings highlight the importance that the manipulation of internal fields through polarization in ferroelectric materials is a promising strategy for the design of improved photoelectrodes.

Chapter 9

Conclusions and Perspectives

9.1 Conclusions

Multiferroic materials in which both ferromagnetic and ferroelectric long range orders coexist are under focus on the search for data storage, spintronics, sensors, electromagnets, and PV applications. Multiferroic nanostructures and thin films have recently been studied extensively in the quest to miniaturize devices such as nonvolatile random access memory applications and discovering novel physics phenomena at nanoscale. Realization of micro- and nanostructures of such multiferroic materials and their local characterization is desirable to answer fundamental questions about possible size effects in their functional properties. Moreover, the coupling between various ferroic orderings in multiferroics offers several modes for investigating and controlling the PV effect, which may endow the next generation solar cells and PEC cells with intriguing multiple functionalities.

To address all these issues and gain more understanding on multiferroic nanomaterials, two materials $BiFeO_3$ and Bi_2FeCrO_6 were involved in the course of this study. On one hand, low dimensional (1D and 2D) $BiFeO_3$ nanostructures were synthesized and their functional properties (ferroelectric, magnetic and photocatalytic) have been investigated. On the other hand, high

quality epitaxial multiferroic Bi_2FeCrO_6 thin films were deposited using PLD onto various substrates, and the optical, PV and PEC properties of the films were characterized with a focus especially on the influence of Fe/Cr cationic ordering. The main conclusions can be summarized as follows:

The ferroelectric properties of single-crystalline $BiFeO_3$ nanowires synthesized by a hydrothermal method were investigated by PFM. We showed that nonvolatile electric polarization can be switched in both *x*- and *z*-directions of these nanowires, evidencing that they retain ferroelectricity despite their small radial dimension. Furthermore, we observed that the strength of both the *x*- and *z*-PFM signals has variations from one nanowire to another, dependent on the relative orientation of the crystalline lattice of the nanowire and cantilever. We explained this behaviour by estimating the shape of the piezoelectric tensor for the rhombohedral symmetry. These results may improve our understanding of the basic ferroelectric properties of 1D single crystal $BiFeO_3$ nanowires and may also be helpful for them to be used as building blocks in various applications such as low-dimensional ferroelectric nonvolatile memory devices.

We demonstrated the potential for solar water splitting with a novel hybrid photocatalyst consisting of $BiFeO_3$ nanowires and Au nanoparticles prepared by laser ablation in liquid. An 30-fold enhancement in photocatalytic activity for oxygen generation under visible light was observed when minute amount of Au (1.0 wt%) nanoparticles was added on the surface of $BiFeO_3$ nanowires. Their superior catalytic activity is attributed to the role of the AuNPs as electron-trapping centers as well as the unique surface-chemistry features of the PLAL-AuNPs. Wavelength-dependent studies on solar water splitting performance of the Au/$BiFeO_3$ nanocomposites confirmed that LSPR effect of Au nanoparticles is also a critical factor in enhancing the photoactivity under visible light.

In addition, we reported on a new way to synthesize 2D $BiFeO_3$ nanocrystals with exposed $(100)_c$ facets by microwave hydrothermal (M-H) reaction without any surfactant. We found that plate-shape $BiFeO_3$ single crystal can be obtained within a very short time of 60-150 sec., much less than that of conventional and other M-H processes reported before. Moreover, we presented that the radiation power, reaction time and concentration of alkali are important parameters for the crystallization process of $BiFeO_3$ during M-H treatment. In addition, a weak ferromagnetism of the $BiFeO_3$ nanoplates was observed at room temperature possibly due to the nanoscale size effect, which is different from that of bulk $BiFeO_3$. The rapid reaction involved with this M-H process of obtaining $BiFeO_3$ nanostructures has the potential to lower the manufacturing cost with significant time and energy savings.

Moreover, we have systematically investigated the optical absorption and PV properties of Bi_2FeCrO_6 epitaxial thin film grown on $SrRuO_3$-coated $SrTiO_3$ substrate. In addition to their built-in electric field originating from spontaneous polarization, which can be exploited to efficiently separate the photogenerated electron-hole pairs, the low band gap enables to increase the energy harvested from the broad solar spectrum. We investigated the multiferroic Bi_2FeCrO_6 oxide and established that its electronic band gap can be tuned down to 1.4 eV, by tailoring the Fe/Cr cation ordering and the ordered domain size. We demonstrated multiferroic Bi_2FeCrO_6 thin film based PV cells with a high efficiency (3.3%) that largely exceeds the highest value (1.25%) of previously reported ferroelectric materials based PV devices.

We also showed the potential of using epitaxial Bi_2FeCrO_6 thin films as photoelectrode for solar water splitting. The Bi_2FeCrO_6 thin films grown on various $CaRuO_3$ coated (100)-oriented substrate including $(LaAlO_3)_{0.3}(Sr_2AlTaO_6)_{0.7}$, $LaAlO_3$ and $SrTiO_3$ were found to be *p*-type. We found that the band gap energy of the Bi_2FeCrO_6 thin film does not exhibit any dependence from

compressive strain. PEC measurements showed that the highest photocurrent in the *p*-type Bi_2FeCrO_6 photocathode is up to ~ −1.0 mA/cm^2 at a potential of ~ −1.0 V versus the RHE, suggesting the promising opportunities of utilizing new double perovskites materials with relatively narrow band gap as photocathode for H_2 generation. Most importantly, we report an effective tuning of the PEC water splitting performance by modulating the internal electric field which stems from the ferroelectric polarization in such visible-light absorbing thin film photoelectrodes. Our study validates the use of multiferroic Bi_2FeCrO_6 thin films with relatively narrow band gap as a photocathode material for PEC water splitting applications. These findings indicate that the manipulation of internal fields through polarization in ferroelectric materials is a promising strategy for the design of improved photoelectrodes.

9.2 Perspectives

The availability of multiferroic $BiFeO_3$ and Bi_2FeCrO_6 materials in both nanostructure and thin film form with multifunctionality involving large spontaneous polarizations with high Currie temperature, high Néel temperature of antiferromagnetism/ferrimagnetism, lead-free piezoelectricity, and large flexibility in the wavelength of visible light region, provides enormous opportunities for their practical applications such as data storage, spintronics and solar energy conversion devices. Further investigations in the following directions could prove fruitful.

(1) *Further understanding of PV properties of Bi_2FeCrO_6 based thin film devices.*

We have studied the optical and photovoltaic effect in Bi_2FeCrO_6 thin films and the highest power conversion efficiency of 3.3% was obtained. However, other factors such as charge mobility, life time as well as quantum efficiency that are very important parameters for

determining the PV performance of solar cells were not investigated in our study. Further works are still needed to better understand the PV properties of Bi_2FeCrO_6 materials.

(2) *Synthesis and investigation on functional properties of multiferroic Bi_2FeCrO_6 nanostructures.*

Generally, a double perovskites Bi_2FeCrO_6 compound with long range *B*-site cation order is not likely to form since Fe^{3+} (r = 0.645 Å) and Cr^{3+} (r = 0.615 Å) have the same charge and very similar ionic radii. Thus, Bi_2FeCrO_6 is expected to adopt a simple perovskite structure with random occupancy of Fe^{3+} and Cr^{3+} on the *B*-site. Although a number of attempts have been undertaken to synthesize an ordered Bi_2FeCrO_6 double perovskites by using PLD technique in thin film form, synthesis of Bi_2FeCrO_6 crystals in powdered nanostructures and bulk form has not been achieved yet. According to previous reports, it remains a big challenge to replace Fe to Cr atom in $BiFeO_3$ crystals, and only small amount of Cr (< 5%) can be doped to the lattice by chemical method. Thus, it is worth exploring alternative ways to synthesize Bi_2FeCrO_6 nanomaterials, thin films and bulk ceramics with long range ordering by other techniques besides PLD for practical applications.

(3) *Multilayer Bi_2FeCrO_6 PV and PEC devices*.

In chapter 7, we demonstrated a new approach to effectively tune the band gap of double perovskites multiferroic oxides by engineering the cationic ordering in the case of Bi_2FeCrO_6. However, the absorption spectrum in single-layer devices is not sufficient for harvesting the whole solar radiation. A natural step to overcome this problem is to combine several layers in a single device, each layer being tuned to absorb in a specific region of the solar spectrum, similar

to multi-junction PV devices. Take into account this, Bi_2FeCrO_6 multilayer films are highly expected to show enhanced PV or PEC performance.

(4) *Theoretically and experimentally realization of band gap tunability in other double perovskites oxides*.

Bi_2FeCrO_6 crystallizes in the double perovskites structure, where ferroelectricity is driven mostly by the Bi^{3+} ions at *A* sites and E_g is controlled by the interaction between Fe and Cr via O alternating at *B* sites. The simultaneous occurrence of these two mechanisms at different double perovskites sites is the key aspect of fabricating semiconducting ferroelectric Bi_2FeCrO_6 oxides with optimal ferroelectricity-optical absorption combinations for efficient PV applications. Based on this mechanism, double perovskites oxide semiconductors with narrow band gaps are worth exploring for novel PV and PEC devices. Besides, theoretically work on the relationship between the band gap and cationic ordering in these materials would prove meaningful for further understanding the mechanism and predicting new materials for solar energy conversion applications.

Bibliography

1. C. Rao, *Transition metal oxides.* Annual Review of Physical Chemistry, 1989, 40, 291.
2. D. Fu and M. Itoh, *Ferroelectricity in Silver Perovskite Oxides*. Ferroelectrics - Material Aspects, 2011.
3. V. M. Goldschmidt, *Die Gesetze der Krystallochemie.* Naturwissenschaften, 1926, 14, 477.
4. A. Millis, B. I. Shraiman, and R. Mueller, *Dynamic Jahn-Teller effect and colossal magnetoresistance in* $La_{1-x}Sr_xMnO_3$. Physical Review Letters, 1996, 77, 175.
5. Y.-H. Lee, J.-M. Wu, and C.-H. Lai, *Influence of La doping in multiferroic properties of* $BiFeO_3$ *thin films.* Applied Physics Letters, 2006, 88, 042903.
6. C.-H. Yang, J. Seidel, S. Kim, P. Rossen, P. Yu, M. Gajek, Y.-H. Chu, L. W. Martin, M. Holcomb, and Q. He, *Electric modulation of conduction in multiferroic Ca-doped* $BiFeO_3$ *films.* Nature Materials, 2009, 8, 485.
7. V. Khomchenko, D. Kiselev, J. Vieira, A. Kholkin, M. Sá, and Y. Pogorelov, *Synthesis and multiferroic properties of* $Bi_{0.8}A_{0.2}FeO_3$ *(A= Ca, Sr, Pb) ceramics.* Applied Physics Letters, 2007, 90, 242901.
8. W.-T. Chen, *Synthesis, structural and property studies of bismuth containing perovskites.* PhD thesis, 2009, University of Edinburgh.
9. D. Serrate, J. M. D. Teresa, and M. R. Ibarra, *Double perovskites with ferromagnetism above room temperature.* Journal of Physics: Condensed Matter, 2007, 19, 023201.
10. K. Leinenweber and J. Parise, *High-pressure synthesis and crystal structure of* $CaFeTi_2O_6$*, a new perovskite structure type.* Journal of Solid State Chemistry, 1995, 114, 277.
11. J. Navarro, L. Balcells, F. Sandiumenge, M. Bibes, A. Roig, B. Martinez, and J. Fontcuberta, *Antisite defects and magnetoresistance in* Sr_2FeMoO_6 *double perovskites.* Journal of Physics: Condensed Matter, 2001, 13, 8481.
12. R. Nechache, C. Harnagea, and A. Pignolet, *Multiferroic properties—structure relationships in epitaxial* Bi_2FeCrO_6 *thin films: recent developments.* Journal of Physics: Condensed Matter, 2012, 24, 096001.
13. J. B. Philipp, P. Majewski, L. Alff, A. Erb, R. Gross, T. Graf, M. S. Brandt, J. Simon, T. Walther, W. Mader, D. Topwal, and D. D. Sarma, *Structural and doping effects in the*

half-metallic double perovskites A_2CrWO_6 (A = Sr, Ba, and Ca). Physical Review B, 2003, 68, 144431.

14. S. García-Martín, E. Urones-Garrote, M. C. Knapp, G. King, and P. M. Woodward, *Transmission Electron Microscopy Studies of $NaLaMgWO_6$: Spontaneous Formation of Compositionally Modulated Stripes.* Journal of the American Chemical Society, 2008, 130, 15028.
15. S. Garcia-Martin, G. King, E. Urones-Garrote, G. Nénert, and P. M. Woodward, *Spontaneous Superlattice Formation in the Doubly Ordered Perovskite $KLaMnWO_6$.* Chemistry of Materials, 2010, 23, 163.
16. http://departments.icmab.es/mulfox/research-topics/latest-results/218-ferromagnetic-and-ferroelectric-bi2nimno6-double-perovskites (01/11/2014)
17. H. Han, Y. Kim, M. Alexe, D. Hesse, and W. Lee, *Nanostructured Ferroelectrics: Fabrication and Structure–Property Relations.* Advanced Materials, 2011, 23, 4599.
18. J. F. Scott, *Applications of Modern Ferroelectrics.* Science, 2007, 315, 954.
19. T. Shimada and T. Kitamura, *Multi-Physics Properties in Ferroelectric Nanowires and Related Structures from First-Principles*. Nanotechnology and Nanomaterials-Nanowires. edited by Paola Prete, 2010.
20. B. D. Cullity and C. D. Graham, *Introduction to magnetic materials*. Wiley, 2011
21. L.W. Martin and R. Ramesh, *Multiferroic and magnetoelectric heterostructures*. Acta Materialia, 2012, 60, 2449.
22. C.-W. Nan, M. I. Bichurin, S. Dong, D. Viehland, and G. Srinivasan, *Multiferroic magnetoelectric composites: Historical perspective, status, and future directions.* Journal of Applied Physics, 2008, 103, 031101.
23. J. F. Scott, *Data storage*: *Multiferroic memories.* Nature Materials, 2007, 6, 256.
24. J. Wang, J. B. Neaton, H. Zheng, V. Nagarajan, S. B. Ogale, B. Liu, D. Viehland, V. Vaithyanathan, D. G. Schlom, U. V. Waghmare, N. A. Spaldin, K. M. Rabe, M. Wuttig, and R. Ramesh, *Epitaxial $BiFeO_3$ Multiferroic Thin Film Heterostructures.* Science, 2003, 299, 1719.
25. H. Schmid, *Multi-ferroic magnetoelectrics.* Ferroelectrics, 1994, 162, 317.

26. L. W. Martin, Y. H. Chu, and R. Ramesh, *Advances in the growth and characterization of magnetic, ferroelectric, and multiferroic oxide thin films.* Materials Science and Engineering: R: Reports, 2010, 68, 89.
27. W. Eerenstein, N. D. Mathur, and J. F. Scott, *Multiferroic and magnetoelectric materials.* Nature, 2006, 442, 759.
28. F. Manfred, *Revival of the magnetoelectric effect.* Journal of Physics D: Applied Physics, 2005, 38, R123.
29. D. Khomskii, *Classifying multiferroics: Mechanisms and effects.* Physics, 2009, 2, 20.
30. N. A. Hill, *Why Are There so Few Magnetic Ferroelectrics?* The Journal of Physical Chemistry B, 2000, 104, 6694.
31. T. Kimura, T. Goto, H. Shintani, K. Ishizaka, T. Arima, and Y. Tokura, *Magnetic control of ferroelectric polarization.* Nature, 2003, 426, 55.
32. N. Hur, S. Park, P. A. Sharma, J. S. Ahn, S. Guha, and S. W. Cheong, *Electric polarization reversal and memory in a multiferroic material induced by magnetic fields.* Nature, 2004, 429, 392.
33. T. Zhao, A. Scholl, F. Zavaliche, K. Lee, M. Barry, A. Doran, M. P. Cruz, Y. H. Chu, C. Ederer, N. A. Spaldin, R. R. Das, D. M. Kim, S. H. Baek, C. B. Eom, and R. Ramesh, *Electrical control of antiferromagnetic domains in multiferroic $BiFeO_3$ films at room temperature.* Nature Materials, 2006, 5, 823.
34. L. W. Martin, *Engineering functionality in the multiferroic $BiFeO_3$-controlling chemistry to enable advanced applications.* Dalton Transactions, 2010, 39, 10813.
35. H. Chiba, T. Atou, and Y. Syono, *Magnetic and Electrical Properties of $Bi_{1-x}Sr_xMnO_3$: Hole-Doping Effect on Ferromagnetic Perovskite $BiMnO_3$.* Journal of Solid State Chemistry, 1997, 132, 139.
36. T. Kimura, S. Kawamoto, I. Yamada, M. Azuma, M. Takano, and Y. Tokura, *Magnetocapacitance effect in multiferroic $BiMnO_3$.* Physical Review B, 2003, 67, 180401.
37. H. Béa, M. Gajek, M. Bibes, and A. Barthélémy, *Spintronics with multiferroics.* Journal of Physics: Condensed Matter, 2008, 20, 434221.
38. A. A. Belik, M. Azuma, T. Saito, Y. Shimakawa, and M. Takano, *Crystallographic features and tetragonal phase stability of $PbVO_3$, a new member of $PbTiO_3$ family.* Chemistry of Materials, 2005, 17, 269.

39. D. V. Efremov, J. Van Den Brink, and D. I. Khomskii, *Bond-versus site-centred ordering and possible ferroelectricity in manganites.* Nature Materials, 2004, 3, 853.

40. T. Choi, Y. Horibe, H. Yi, Y. Choi, W. Wu, and S.-W. Cheong, *Insulating interlocked ferroelectric and structural antiphase domain walls in multiferroic $YMnO_3$.* Nature Materials, 2010, 9, 253.

41. C. Jia, S. Onoda, N. Nagaosa, and J. H. Han, *Microscopic theory of spin-polarization coupling in multiferroic transition metal oxides.* Physical Review B, 2007, 76, 144424.

42. Y. Choi, H. Yi, S. Lee, Q. Huang, V. Kiryukhin, and S.-W. Cheong, *Ferroelectricity in an Ising chain magnet.* Physical Review Letters, 2008, 100, 047601.

43. G. Catalan and J. F. Scott, *Physics and Applications of Bismuth Ferrite.* Advanced Materials, 2009, 21, 2463.

44. F. Zavaliche, S. Yang, T. Zhao, Y. Chu, M. Cruz, C. Eom, and R. Ramesh, *Multiferroic $BiFeO_3$ films: Domain structure and polarization dynamics.* Phase Transitions, 2006, 79, 991.

45. H. Naganuma, *Multifunctional Characteristics of B-site Substituted $BiFeO_3$ Films*. Ferroelectrics - Physical Effects. Edited by Mickaël Lallart, 2011.

46. C. Michel, J.-M. Moreau, G. D. Achenbach, R. Gerson, and W. J. James, *The atomic structure of $BiFeO_3$.* Solid State Communications, 1969, 7, 701.

47. F. Kubel and H. Schmid, *Structure of a ferroelectric and ferroelastic monodomain crystal of the perovskite $BiFeO_3$.* Acta Crystallographica Section B, 1990, 46, 698.

48. R. E. Cohen and H. Krakauer, *Electronic structure studies of the differences in ferroelectric behavior of $BaTiO_3$ and $PbTiO_3$.* Ferroelectrics, 1992, 136, 65.

49. C. Ederer and N. A. Spaldin, *Effect of Epitaxial Strain on the Spontaneous Polarization of Thin Film Ferroelectrics.* Physical Review Letters, 2005, 95, 257601.

50. S. Kiselev, R. Ozerov, and G. Zhdanov. *Detection of magnetic order in ferroelectric $BiFeO_3$ by neutron diffraction*. *Soviet Physics Doklady*. 1963, 7, 742.

51. J. R. Teague, R. Gerson, and W. J. James, *Dielectric hysteresis in single crystal $BiFeO_3$.* Solid State Communications, 1970, 8, 1073.

52. D. Lebeugle, D. Colson, A. Forget, and M. Viret, *Very large spontaneous electric polarization in $BiFeO_3$ single crystals at room temperature and its evolution under cycling fields.* Applied Physics Letters, 2007, 91.

53. J. Dho, X. Qi, H. Kim, J. L. MacManus-Driscoll, and M. G. Blamire, *Large Electric Polarization and Exchange Bias in Multiferroic $BiFeO_3$.* Advanced Materials, 2006, 18, 1445.

54. K. Y. Yun, D. Ricinschi, T. Kanashima, M. Noda, and M. Okuyama, *Giant ferroelectric polarization beyond 150 $\mu C/cm^2$ in $BiFeO_3$ thin film.* Japanese journal of applied physics, 2004, 43, L647.

55. C. Ederer and N. A. Spaldin, *Weak ferromagnetism and magnetoelectric coupling in bismuth ferrite.* Physical Review B, 2005, 71, 060401.

56. I. Sosnowska, T. P. Neumaier, and E. Steichele, *Spiral magnetic ordering in bismuth ferrite.* Journal of Physics C: Solid State Physics, 1982, 15, 4835.

57. A. Zalesskii, A. Zvezdin, A. Frolov, and A. Bush, *57Fe NMR study of a spatially modulated magnetic structure in $BiFeO_3$.* Journal of Experimental and Theoretical Physics Letters, 2000, 71, 465.

58. http://iramis.cea.fr/Phocea/Vie_des_labos/Ast/ast.php?t=fait_marquant&id_ast=1012 (02/11/2014)

59. K. Y. Yun, M. Noda, and M. Okuyama, *Prominent ferroelectricity of $BiFeO_3$ thin films prepared by pulsed-laser deposition.* Applied Physics Letters, 2003, 83, 3981.

60. V. R. Palkar, J. John, and R. Pinto, *Observation of saturated polarization and dielectric anomaly in magnetoelectric $BiFeO_3$ thin films.* Applied Physics Letters, 2002, 80, 1628.

61. Y.-H. Lee, C.-S. Liang, and J.-M. Wu, *Crystal growth and characterizations of highly oriented $BiFeO_3$ thin films.* Electrochemical and Solid-State Letters, 2005, 8, F55.

62. R. Ueno, S. Okaura, H. Funakubo, and K. Saito, *Crystal structure and electrical properties of epitaxial $BiFeO_3$ thin films grown by metal organic chemical vapor deposition.* Japanese journal of applied physics, 2005, 44, L1231.

63. H. Liu, Z. Liu, Q. Liu, and K. Yao, *Ferroelectric properties of $BiFeO_3$ films grown by sol–gel process.* Thin Solid Films, 2006, 500, 105.

64. C. Chen, J. Cheng, S. Yu, L. Che, and Z. Meng, *Hydrothermal synthesis of perovskite bismuth ferrite crystallites.* Journal of Crystal Growth, 2006, 291, 135.

65. Y. N. Huo, Y. Jin, and Y. Zhang, *Citric acid assisted solvothermal synthesis of $BiFeO_3$ microspheres with high visible-light photocatalytic activity.* Journal of Molecular Catalysis a–Chemical, 2010, 331, 15.

66. J. Chen, X. Xing, A. Watson, W. Wang, R. Yu, J. Deng, L. Yan, C. Sun, and X. Chen, *Rapid Synthesis of Multiferroic $BiFeO_3$ Single-Crystalline Nanostructures.* Chemistry of Materials, 2007, 19, 3598.

67. I. Szafraniak, M. Połomska, B. Hilczer, A. Pietraszko, and L. Kępiński, *Characterization of $BiFeO_3$ nanopowder obtained by mechanochemical synthesis.* Journal of the European Ceramic Society, 2007, 27, 4399.

68. J. K. Kim, S. S. Kim, and W.-J. Kim, *Sol–gel synthesis and properties of multiferroic $BiFeO_3$.* Materials Letters, 2005, 59, 4006.

69. T.-J. Park, G. C. Papaefthymiou, A. J. Viescas, A. R. Moodenbaugh, and S. S. Wong, *Size-Dependent Magnetic Properties of Single-Crystalline Multiferroic $BiFeO_3$ Nanoparticles.* Nano Letters, 2007, 7, 766.

70. S. M. Selbach, M.-A. Einarsrud, T. Tybell, and T. Grande, *Synthesis of $BiFeO_3$ by Wet Chemical Methods.* Journal of the American Ceramic Society, 2007, 90, 3430.

71. X. Zhang, H. Liu, B. Zheng, Y. Lin, D. Liu, and C.-W. Nan, *Photocatalytic and Magnetic Behaviors Observed in $BiFeO_3$ Nanofibers by Electrospinning.* Journal of Nanomaterials, 2013, 917948.

72. J. Wei, D. Xue, and Y. Xu, *Photoabsorption characterization and magnetic property of multiferroic $BiFeO_3$ nanotubes synthesized by a facile sol–gel template process.* Scripta Materialia, 2008, 58, 45.

73. X. Zhang, C. Lai, X. Zhao, D. Wang, and J. Y. Dai, *Synthesis and ferroelectric properties of multiferroic $BiFeO_3$ nanotube arrays.* Applied Physics Letters, 2005, 87, 143102.

74. B. Liu, B. Hu, and Z. Du, *Hydrothermal synthesis and magnetic properties of single-crystalline $BiFeO_3$ nanowires.* Chemical Communications, 2011, 47, 8166.

75. F. Gao, Y. Yuan, K. F. Wang, X. Y. Chen, F. Chen, J.-M. Liu, and Z. F. Ren, *Preparation and photoabsorption characterization of $BiFeO_3$ nanowires.* Applied Physics Letters, 2006, 89.

76. L. Fei, J. Yuan, Y. Hu, C. Wu, J. Wang, and Y. Wang, *Visible Light Responsive Perovskite $BiFeO_3$ Pills and Rods with Dominant $\{111\}_c$ Facets.* Crystal Growth & Design, 2011, 11, 1049.

77. S. Xie, A. Gannepalli, Q. N. Chen, Y. Liu, Y. Zhou, R. Proksch, and J. Li, *High resolution quantitative piezoresponse force microscopy of $BiFeO_3$ nanofibers with dramatically enhanced sensitivity.* Nanoscale, 2012, 4, 408.

78. X. Zhang, H. Liu, B. Zheng, Y. Lin, D. Liu, and C.-W. Nan, *Photocatalytic and Magnetic Behaviors Observed in $BiFeO_3$ Nanofibers by Electrospinning.* Journal of Nanomaterials, 2013, 2013, 7.

79. J. T. Han, Y. H. Huang, X. J. Wu, C. L. Wu, W. Wei, B. Peng, W. Huang, and J. B. Goodenough, *Tunable Synthesis of Bismuth Ferrites with Various Morphologies.* Advanced Materials, 2006, 18, 2145.

80. S. Li, Y.-H. Lin, B.-P. Zhang, Y. Wang, and C.-W. Nan, *Controlled Fabrication of $BiFeO_3$ Uniform Microcrystals and Their Magnetic and Photocatalytic Behaviors.* The Journal of Physical Chemistry C, 2010, 114, 2903.

81. U. A. Joshi, J. S. Jang, P. H. Borse, and J. S. Lee, *Microwave synthesis of single-crystalline perovskite $BiFeO_3$ nanocubes for photoelectrode and photocatalytic applications.* Applied Physics Letters, 2008, 92, 242106.

82. Y. Huo, M. Miao, Y. Zhang, J. Zhu, and H. Li, *Aerosol-spraying preparation of a mesoporous hollow spherical $BiFeO_3$ visible photocatalyst with enhanced activity and durability.* Chemical Communications, 2011, 47, 2089.

83. S. M. Selbach, T. Tybell, M.-A. Einarsrud, and T. Grande, *Size-Dependent Properties of Multiferroic $BiFeO_3$ Nanoparticles.* Chemistry of Materials, 2007, 19, 6478.

84. M. E. Castillo, V. V. Shvartsman, D. Gobeljic, Y. Gao, J. Landers, H. Wende, and D. C. Lupascu, *Effect of particle size on ferroelectric and magnetic properties of $BiFeO_3$ nanopowders.* Nanotechnology, 2013, 24, 355701.

85. F. Z. Huang, Z. J. Wang, X. M. Lu, J. T. Zhang, K. L. Min, W. W. Lin, R. X. Ti, T. T. Xu, J. He, C. Yue, and J. S. Zhu, *Peculiar magnetism of $BiFeO_3$ nanoparticles with size approaching the period of the spiral spin structure.* Scientific Reports, 2013, 3, 2907.

86. S. Goswami, D. Bhattacharya, and P. Choudhury, *Particle size dependence of magnetization and noncentrosymmetry in nanoscale $BiFeO_3$.* Journal of Applied Physics, 2011, 109.

87. J. M. Wesselinowa and I. Apostolova, *Theoretical study of multiferroic $BiFeO_3$ nanoparticles.* Journal of Applied Physics, 2008, 104, 084108.

88. C. Ederer and N. A. Spaldin, *Influence of strain and oxygen vacancies on the magnetoelectric properties of multiferroic bismuth ferrite.* Physical Review B, 2005, 71, 224103.

89. F. Bai, J. Wang, M. Wuttig, J. Li, N. Wang, A. P. Pyatakov, A. K. Zvezdin, L. E. Cross, and D. Viehland, *Destruction of spin cycloid in $(111)_c$-oriented $BiFeO_3$ thin films by epitiaxial constraint: Enhanced polarization and release of latent magnetization.* Applied Physics Letters, 2005, 86, 032511.

90. R. Mazumder, P. Sujatha Devi, D. Bhattacharya, P. Choudhury, A. Sen, and M. Raja, *Ferromagnetism in nanoscale $BiFeO_3$.* Applied Physics Letters, 2007, 91, 062510.

91. J. Kanamori, *Superexchange interaction and symmetry properties of electron orbitals*. Journal of Physics and chemistry of Solids, 1959, 10, 87.

92. J. B. Goodenough, *Theory of the role of covalence in the perovskite-type manganites [La, M (II)] MnO_3.* Physical Review, 1955, 100, 564.

93. M. E. Villafuerte-Castrejón, M. García-Guaderrama, L. Fuentes, J. Prado-Gonjal, A. M. González, M. A. de la Rubia, M. García-Hernández, and E. Morán, *New Fe^{3+}/Cr^{3+} Perovskites with Anomalous Transport Properties: The Solid Solution $La_xBi_{1-x}Fe_{0.5}Cr_{0.5}O_3$ $(0.4 \leq x \leq 1)$.* Inorganic Chemistry, 2011, 50, 8340.

94. C. Bull, D. Gleeson, and K. Knight, *Determination of B-site ordering and structural transformations in the mixed transition metal perovskites La_2CoMnO_6 and La_2NiMnO_6.* Journal of Physics: Condensed Matter, 2003, 15, 4927.

95. N. S. Rogado, J. Li, A. W. Sleight, and M. A. Subramanian, *Magnetocapacitance and magnetoresistance near room temperature in a ferromagnetic semiconductor: La_2NiMnO_6.* Advanced Materials, 2005, 17, 2225.

96. M. Azuma, K. Takata, T. Saito, S. Ishiwata, Y. Shimakawa, and M. Takano, *Designed ferromagnetic, ferroelectric Bi_2NiMnO_6.* Journal of the American Chemical Society, 2005, 127, 8889.

97. Y. Du, Z. Cheng, S. Dou, X. Wang, H. Zhao, and H. Kimura, *Magnetic properties of Bi_2FeMnO_6: A multiferroic material with double-perovskite structure.* Applied Physics Letters, 2010, 97, 122502.

98. M. P. Singh, K. D. Truong, P. Fournier, P. Rauwel, E. Rauwel, L. P. Carignan, and D. Ménard, *Anomalously large ferromagnetic Curie temperature of epitaxial Bi_2CoMnO_6 thin films.* Applied Physics Letters, 2008, 92.

99. P. Baettig, C. Ederer, and N. A. Spaldin, *First principles study of the multiferroics $BiFeO_3$, Bi_2FeCrO_6, and $BiCrO_3$: Structure, polarization, and magnetic ordering temperature.* Physical Review B, 2005, 72, 214105.

100. P. Baettig and N. A. Spaldin, *Ab initio prediction of a multiferroic with large polarization and magnetization.* Applied Physics Letters, 2005, 86, 012505.

101. R. Nechache and F. Rosei, *Recent progress in nanostructured multiferroic Bi_2FeCrO_6 thin films.* Journal of Solid State Chemistry, 2012, 189, 13.

102. M. R. Suchomel, C. I. Thomas, M. Allix, M. J. Rosseinsky, A. M. Fogg, and M. F. Thomas, *High pressure bulk synthesis and characterization of the predicted multiferroic $Bi(Fe_{1/2}Cr_{1/2})O_3$.* Applied Physics Letters, 2007, 90, 112909.

103. D. H. Kim, H. N. Lee, M. D. Biegalski, and H. M. Christen, *Large ferroelectric polarization in antiferromagnetic $BiFe_{0.5}Cr_{0.5}O_3$ epitaxial films.* Applied Physics Letters, 2007, 91, 042906.

104. R. Nechache, C. Harnagea, A. Pignolet, F. Normandin, T. Veres, L.-P. Carignan, and D. Ménard, *Growth, structure, and properties of epitaxial thin films of first-principles predicted multiferroic Bi_2FeCrO_6.* Applied Physics Letters, 2006, 89, 102902.

105. S. Ju and G.-Y. Guo, *Colossal nonlinear optical magnetoelectric effects in multiferroic Bi_2FeCrO_6.* Applied Physics Letters, 2008, 92, 202504.

106. R. Nechache, C. Harnagea, and F. Rosei, *Multiferroic nanoscale Bi_2FeCrO_6 material for spintronic-related applications.* Nanoscale, 2012, 4, 5588.

107. J. Zhu, H. Yang, S. Feng, L. Wang, Q. Liu, C. Jin, X. Wang, L. Li, and J. Yu, *The multiferroic properties of $Bi(Fe_{1/2}Cr_{1/2})O_3$ compound.* International Journal of Modern Physics B, 2013, 27, 1362023.

108. S. K. Singh, S. Shanthy, and H. Ishiwara, *Reduced leakage current in $BiFeO_3$–$BiCrO_3$ nanocomposite films formed by chemical solution deposition.* Journal of Applied Physics, 2010, 108, 054102.

109. R. Nechache, C. Harnagea, L.-P. Carignan, O. Gautreau, L. Pintilie, M. P. Singh, D. Ménard, P. Fournier, M. Alexe, and A. Pignolet, *Epitaxial thin films of the multiferroic*

double perovskites Bi_2FeCrO_6 grown on (100)-oriented $SrTiO_3$ substrates: Growth, characterization, and optimization. Journal of Applied Physics, 2009, 105, 061621.

110. H. Béa, M. Bibes, A. Barthélémy, K. Bouzehouane, E. Jacquet, A. Khodan, J.-P. Contour, S. Fusil, F. Wyczisk, A. Forget, D. Lebeugle, D. Colson, and M. Viret, *Influence of parasitic phases on the properties of $BiFeO_3$ epitaxial thin films.* Applied Physics Letters, 2005, 87, 072508.
111. R. Nechache, C. V. Cojocaru, C. Harnagea, C. Nauenheim, M. Nicklaus, A. Ruediger, F. Rosei, and A. Pignolet, *Epitaxial Patterning of Bi_2FeCrO_6 Double perovskites Nanostructures: Multiferroic at Room Temperature.* Advanced Materials, 2011, 23, 1724.
112. R. Nechache, C. Nauenheim, U. Lanke, A. Pignolet, F. Rosei, and A Ruediger, *Coexistence of antiferromagnetic and ferromagnetic orders at remanent state in epitaxial multiferroic Bi_2FeCrO_6 nanostructures.* Journal of Physics: Condensed Matter, 2012, 24, 142202.
113. http://www.aist.go.jp/aist_e/latest_research/2012/20120511/20120511.html (11/03/2014)
114. G. W. Crabtree and N. S. Lewis, *Solar energy conversion.* Physics today, 2007, 60, 37.
115. D. Derkacs, S. Lim, P. Matheu, W. Mar, and E. Yu, *Improved performance of amorphous silicon solar cells via scattering from surface plasmon polaritons in nearby metallic nanoparticles.* Applied Physics Letters, 2006, 89, 093103.
116. M. A. Contreras, B. Egaas, K. Ramanathan, J. Hiltner, A. Swartzlander, F. Hasoon, and R. Noufi, *Progress toward 20% efficiency in Cu (In, Ga) Se_2 polycrystalline thin‐film solar cells.* Progress in Photovoltaics: Research and applications, 1999, 7, 311.
117. J. Britt and C. Ferekides, *Thin‐film CdS/CdTe solar cell with 15.8% efficiency.* Applied Physics Letters, 1993, 62, 2851.
118. G. Conibeer, *Third-generation photovoltaics.* Materials Today, 2007, 10, 42.
119. A. I. Hochbaum and P. Yang, *Semiconductor Nanowires for Energy Conversion.* Chemical Reviews, 2009, 110, 527.
120. P. V. Kamat, *Quantum dot solar cells. Semiconductor nanocrystals as light harvesters.* The Journal of Physical Chemistry C, 2008, 112, 18737.
121. J. Burschka, N. Pellet, S.-J. Moon, R. Humphry-Baker, P. Gao, M. K. Nazeeruddin, and M. Grätzel, *Sequential deposition as a route to high-performance perovskite-sensitized solar cells.* Nature, 2013, 499, 316.

122. Boyuan Qi and Jizheng Wang, *Fill factor in organic solar cells*. Physical Chemistry Chemical Physics, 2013, 15, 8972.
123. http://www.nrel.gov/ncpv/images/efficiency_chart.jpg (2014/11/18)
124. V. M. Fridkin and B. Popov, *Anomalous photovoltaic effect in ferroelectrics.* Soviet Physics Uspekhi, 1978, 21, 981.
125. P. S. Brody, *Large polarization-dependent photovoltages in ceramic $BaTiO_3$+5 wt.% $CaTiO_3$.* Solid State Communications, 1973, 12, 673.
126. A. M. Glass, D. von der Linde, and T. J. Negran, *High‐voltage bulk photovoltaic effect and the photorefractive process in $LiNbO_3$.* Applied Physics Letters, 1974, 25, 233.
127. A. Kholkin, O. Boiarkine, and N. Setter, *Transient photocurrents in lead zirconate titanate thin films.* Applied Physics Letters, 1998, 72, 130.
128. P. Poosanaas, A. Dogan, S. Thakoor, and K. Uchino, *Influence of sample thickness on the performance of photostrictive ceramics.* Journal of Applied Physics, 1998, 84, 1508.
129. V. Yarmarkin, B. Gol'tsman, M. Kazanin, and V. Lemanov, *Barrier photovoltaic effects in PZT ferroelectric thin films.* Physics of the solid state, 2000, 42, 522.
130. Y. Yuan, Z. Xiao, B. Yang, and J. Huang, *Arising Applications of Ferroelectric Materials in Photovoltaic Devices.* Journal of Materials Chemistry A, 2014, 2, 6027.
131. M. Qin, K. Yao, and Y. C. Liang, *High efficient photovoltaics in nanoscaled ferroelectric thin films.* Applied Physics Letters, 2008, 93, 122904.
132. G. Chanussot, V. Fridkin, G. Godefroy, and B. Jannot, *The photoinduced Rayleigh scattering in $BaTiO_3$ crystals showing the bulk photovoltaic effect.* Applied Physics Letters, 1977, 31, 3.
133. K. Asadi, P. de Bruyn, P. W. M. Blom, and D. M. de Leeuw, *Origin of the efficiency enhancement in ferroelectric functionalized organic solar cells.* Applied Physics Letters, 2011, 98.
134. Y. Yuan, T. J. Reece, P. Sharma, S. Poddar, S. Ducharme, A. Gruverman, Y. Yang, and J. Huang, *Efficiency enhancement in organic solar cells with ferroelectric polymers.* Nature Materials, 2011, 10, 296.
135. D. Cao, H. Zhang, L. Fang, W. Dong, F. Zheng, and M. Shen, *Interface layer thickness effect on the photocurrent of Pt sandwiched polycrystalline ferroelectric $Pb(Zr,Ti)O_3$ films.* Applied Physics Letters, 2010, 97, 102104.

136. M. Qin, K. Yao, and Y. C. Liang, *Photovoltaic mechanisms in ferroelectric thin films with the effects of the electrodes and interfaces.* Applied Physics Letters, 2009, 95, 022912.

137. C. Wang, K.-J. Jin, R.-Q. Zhao, H.-B. Lu, H.-Z. Guo, C. Ge, M. He, C. Wang, and G.-Z. Yang, *Ultimate photovoltage in perovskite oxide heterostructures with critical film thickness.* Applied Physics Letters, 2011, 98, 181101.

138. J. Zhang, X. Su, M. Shen, Z. Dai, L. Zhang, X. He, W. Cheng, M. Cao, and G. Zou, *Enlarging photovoltaic effect: combination of classic photoelectric and ferroelectric photovoltaic effects.* Scientific Reports, 2013, 3, 2109.

139. S. M. Young and A. M. Rappe, *First Principles Calculation of the Shift Current Photovoltaic Effect in Ferroelectrics.* Physical Review Letters, 2012, 109, 116601.

140. G.-L. Yuan and J. Wang, *Evidences for the depletion region induced by the polarization of ferroelectric semiconductors.* Applied Physics Letters, 2009, 95, 252904.

141. M. Qin, K. Yao, Y. C. Liang, and S. Shannigrahi, *Thickness effects on photoinduced current in ferroelectric* $(Pb_{0.97}La_{0.03})(Zr_{0.52}Ti_{0.48})O_3$ *thin films.* Journal of Applied Physics, 2007, 101, 014104.

142. Y. Zheng and C. H. Woo, *Hyper-sensitive piezophotovoltaic effects in ferroelectric nanocylinders.* Journal of Applied Physics, 2010, 107, 104120.

143. X. Yang, X. Su, M. Shen, F. Zheng, Y. Xin, L. Zhang, M. Hua, Y. Chen, and V. G. Harris, *Enhancement of Photocurrent in Ferroelectric Films Via the Incorporation of Narrow Bandgap Nanoparticles.* Advanced Materials, 2012, 24, 1202.

144. D. Cao, C. Wang, F. Zheng, W. Dong, L. Fang, and M. Shen, *High-Efficiency Ferroelectric-Film Solar Cells with an n-type* Cu_2O *Cathode Buffer Layer.* Nano Letters, 2012, 12, 2803.

145. B. Chen, Z. Zuo, Y. Liu, Q.-F. Zhan, Y. Xie, H. Yang, G. Dai, Z. Li, G. Xu, and R.-W. Li, *Tunable photovoltaic effects in transparent* $Pb(Zr_{0.53},Ti_{0.47})O_3$ *capacitors.* Applied Physics Letters, 2012, 100.

146. I. Grinberg, D. V. West, M. Torres, G. Gou, D. M. Stein, L. Wu, G. Chen, E. M. Gallo, A. R. Akbashev, and P. K. Davies, *Perovskite oxides for visible-light-absorbing ferroelectric and photovoltaic materials.* Nature, 2013, 503, 509.

147. F. Wu, Y. Guo, B. Guo, Y. Zhang, H. Li, and H. Liu, *Photovoltaic effect of a bilayer thin film with $(Na_{0.5}Bi_{0.5})_{1-x}Ba_xTiO_3/BiFeO_3$ heterostructure.* Journal of Physics D: Applied Physics, 2013, 46, 365304.

148. F. Zheng, Y. Xin, W. Huang, J. Zhang, X. Wang, M. Shen, W. Dong, L. Fang, Y. Bai, X. Shen, and J. Hao, *Above 1% efficiency of a ferroelectric solar cell based on the $Pb(Zr,Ti)O_3$ film.* Journal of Materials Chemistry A, 2014, 2, 1363.

149. G. Zhang, H. Wu, G. Li, Q. Huang, C. Yang, F. Huang, F. Liao, and J. Lin, *New high T_c multiferroics $KBiFe_2O_5$ with narrow band gap and promising photovoltaic effect.* Scientific Reports, 2013, 3, 1265.

150. H. Yi, T. Choi, S. Choi, Y. Oh, and S. W. Cheong, *Mechanism of the Switchable Photovoltaic Effect in Ferroelectric $BiFeO_3$.* Advanced Materials, 2011, 23, 3403.

151. S. Y. Yang, J. Seidel, S. J. Byrnes, P. Shafer, C. H. Yang, M. D. Rossell, P. Yu, Y. H. Chu, J. F. Scott, and J. W. Ager, *Above-bandgap voltages from ferroelectric photovoltaic devices.* Nature nanotechnology, 2010, 5, 143.

152. T. Choi, S. Lee, Y. Choi, V. Kiryukhin, and S.-W. Cheong, *Switchable ferroelectric diode and photovoltaic effect in $BiFeO_3$.* Science, 2009, 324, 63.

153. S. Yang, L. Martin, S. Byrnes, T. Conry, S. Basu, D. Paran, L. Reichertz, J. Ihlefeld, C. Adamo, and A. Melville, *Photovoltaic effects in $BiFeO_3$.* Applied Physics Letters, 2009, 95, 062909.

154. A. J. Hauser, J. Zhang, L. Mier, R. A. Ricciardo, P. M. Woodward, T. L. Gustafson, L. J. Brillson, and F. Y. Yang, *Characterization of electronic structure and defect states of thin epitaxial $BiFeO_3$ films by UV-visible absorption and cathodoluminescence spectroscopies.* Applied Physics Letters, 2008, 92, 222901.

155. P. Chen, N. J. Podraza, X. S. Xu, A. Melville, E. Vlahos, V. Gopalan, R. Ramesh, D. G. Schlom, and J. L. Musfeldt, *Optical properties of quasi-tetragonal $BiFeO_3$ thin films.* Applied Physics Letters, 2010, 96, 131907.

156. P. Chen, X. Xu, C. Koenigsmann, A. C. Santulli, S. S. Wong, and J. L. Musfeldt, *Size-Dependent Infrared Phonon Modes and Ferroelectric Phase Transition in $BiFeO_3$ Nanoparticles.* Nano Letters, 2010, 10, 4526.

157. J. H. Sung, W.-M. Lee, J. H. Lee, K. Chu, D. Lee, X. Moya, N. D. Mathur, C.-H. Yang, J.-H. Park, and M.-H. Jo, *Single ferroelectric-domain photovoltaic switch based on lateral $BiFeO_3$ cells.* NPG Asia Materials, 2013, 5, e38.

158. J. Seidel, D. Fu, S.-Y. Yang, E. Alarcón-Lladó, J. Wu, R. Ramesh, and J. W. Ager, *Efficient Photovoltaic Current Generation at Ferroelectric Domain Walls.* Physical Review Letters, 2011, 107, 126805.

159. M. Alexe and D. Hesse, *Tip-enhanced photovoltaic effects in bismuth ferrite.* Nature communications, 2011, 2, 256.

160. B. Chen, M. Li, Y. Liu, Z. Zuo, F. Zhuge, Q.-F. Zhan, and R.-W. Li, *Effect of top electrodes on photovoltaic properties of polycrystalline $BiFeO_3$ based thin film capacitors.* Nanotechnology, 2011, 22, 195201.

161. Y. Zang, D. Xie, X. Wu, Y. Chen, Y. Lin, M. Li, H. Tian, X. Li, Z. Li, H. Zhu, T. Ren, and D. Plant, *Enhanced photovoltaic properties in graphene/polycrystalline $BiFeO_3$/Pt heterojunction structure.* Applied Physics Letters, 2011, 99, 132904.

162. Y. Zang, D. Xie, Y. Chen, X. Wu, T. Ren, J. Wei, H. Zhu, and D. Plant, *Electrical and thermal properties of a carbon nanotube/polycrystalline $BiFeO_3$/Pt photovoltaic heterojunction with CdSe quantum dots sensitization.* Nanoscale, 2012, 4, 2926.

163. W. Dong, Y. Guo, B. Guo, H. Li, H. Liu, and T. W. Joel, *Enhanced Photovoltaic Effect in $BiVO_4$ Semiconductor by Incorporation with an Ultrathin $BiFeO_3$ Ferroelectric Layer.* ACS Applied Materials & Interfaces, 2013, 5, 6925.

164. W. M. Lee, J. H. Sung, K. Chu, X. Moya, D. Lee, C. J. Kim, N. D. Mathur, S. W. Cheong, C. H. Yang, and M. H. Jo, *Spatially resolved photodetection in leaky ferroelectric $BiFeO_3$.* Advanced Materials, 2012, 24, OP49.

165. F. Yan, G. Chen, L. Lu, and J. E. Spanier, *Dynamics of Photogenerated Surface Charge on $BiFeO_3$ Films.* ACS nano, 2012, 6, 2353.

166. R. Nechache, C. Harnagea, S. Licoccia, E. Traversa, A. Ruediger, A. Pignolet, and F. Rosei, *Photovoltaic properties of Bi_2FeCrO_6 epitaxial thin films.* Applied Physics Letters, 2011, 98, 202902.

167. Z.-W. Song and B.-G. Liu, *Electronic structure and magnetic and optical properties of double perovskites Bi_2FeCrO_6 from first-principles investigation.* Chinese Physics B, 2013, 22, 047506.

168. Q.-X. Zhao, M.-X. Wen, S.-B. Wang, L. Guan, and B.-T. Liu, *Electronic Structures and Optical Properties of $BiFeO_3$ and Bi_2FeCrO_6.* Journal of Synthetic Crystals, 2008, 6, 018.

169. H. Tong, S. Ouyang, Y. Bi, N. Umezawa, M. Oshikiri, and J. Ye, *Nano-photocatalytic Materials: Possibilities and Challenges.* Advanced Materials, 2012, 24, 229.

170. X. Chen, S. Shen, L. Guo, and S. S. Mao, *Semiconductor-based Photocatalytic Hydrogen Generation.* Chemical Reviews, 2010, 110, 6503.

171. M. A. Fox and M. T. Dulay, *Heterogeneous photocatalysis.* Chemical Reviews, 1993, 93, 341.

172. Y. Qu and X. Duan, *Progress, challenge and perspective of heterogeneous photocatalysts.* Chemical Society Reviews, 2013, 42, 2568.

173. S. Rawalekar and T. Mokari, *Rational Design of Hybrid Nanostructures for Advanced Photocatalysis.* Advanced Energy Materials, 2013, 3, 12.

174. W. Ho and J. C. Yu, *Sonochemical synthesis and visible light photocatalytic behavior of CdSe and CdSe/TiO_2 nanoparticles.* Journal of Molecular Catalysis A: Chemical, 2006, 247, 268.

175. J. Yang, D. Wang, H. Han, and C. Li, *Roles of Cocatalysts in Photocatalysis and Photoelectrocatalysis.* Accounts of Chemical Research, 2013, 46, 1900.

176. M. Ni, M. K. Leung, D. Y. Leung, and K. Sumathy, *A review and recent developments in photocatalytic water-splitting using TiO_2 for hydrogen production.* Renewable and Sustainable Energy Reviews, 2007, 11, 401.

177. S. Tabata, H. Nishida, Y. Masaki, and K. Tabata, *Stoichiometric photocatalytic decomposition of pure water in Pt/TiO_2 aqueous suspension system.* Catalysis Letters, 1995, 34, 245.

178. S. Linic, P. Christopher, and D. B. Ingram, *Plasmonic-metal nanostructures for efficient conversion of solar to chemical energy.* Nature Materials, 2011, 10, 911.

179. Q. Xiang, J. Yu, and M. Jaroniec, *Graphene-based semiconductor photocatalysts.* Chemical Society Reviews, 2012, 41, 782.

180. I. V. Lightcap, T. H. Kosel, and P. V. Kamat, *Anchoring Semiconductor and Metal Nanoparticles on a Two-Dimensional Catalyst Mat. Storing and Shuttling Electrons with Reduced Graphene Oxide.* Nano Letters, 2010, 10, 577.

181. A. Fujishima, *Electrochemical photolysis of water at a semiconductor electrode.* Nature, 1972, 238, 37.

182. L. J. Minggu, W. R. Wan Daud, and M. B. Kassim, *An overview of photocells and photoreactors for photoelectrochemical water splitting.* International Journal of Hydrogen Energy, 2010, 35, 5233.

183. C. Liu, N. P. Dasgupta, and P. Yang, *Semiconductor Nanowires for Artificial Photosynthesis.* Chemistry of Materials, 2013, 26, 415.

184. E. Miller, A. DeAngelis, and S. Mallory, *Multijunction Approaches to Photoelectrochemical Water Splitting*, in *Photoelectrochemical Hydrogen Production*. Edited by R. van de Krol and M. Grätzel, 2012, Springer US.

185. A. J. Cowan and J. R. Durrant, *Long-lived charge separated states in nanostructured semiconductor photoelectrodes for the production of solar fuels.* Chemical Society Reviews, 2013, 42, 2281.

186. S. Choudhary, S. Upadhyay, P. Kumar, N. Singh, V. R. Satsangi, R. Shrivastav, and S. Dass, *Nanostructured bilayered thin films in photoelectrochemical water splitting – A review.* International Journal of Hydrogen Energy, 2012, 37, 18713.

187. M. G. Walter, E. L. Warren, J. R. McKone, S. W. Boettcher, Q. Mi, E. A. Santori, and N. S. Lewis, *Solar water splitting cells.* Chemical Reviews, 2010, 110, 6446.

188. F. Gao, X. Y. Chen, K. B. Yin, S. Dong, Z. F. Ren, F. Yuan, T. Yu, Z. G. Zou, and J. M. Liu, *Visible-Light Photocatalytic Properties of Weak Magnetic $BiFeO_3$ Nanoparticles.* Advanced Materials, 2007, 19, 2889.

189. Y. Huo, Y. Jin, and Y. Zhang, *Citric acid assisted solvothermal synthesis of $BiFeO_3$ microspheres with high visible-light photocatalytic activity.* Journal of Molecular Catalysis A: Chemical, 2010, 331, 15.

190. C. Reitz, C. Suchomski, C. Weidmann, and T. Brezesinski, *Block copolymer-templated $BiFeO_3$ nanoarchitectures composed of phase-pure crystallites intermingled with a continuous mesoporosity: Effective visible-light photocatalysts?* Nano Research, 2011, 4, 414.

191. J. Luo and P. A. Maggard, *Hydrothermal Synthesis and Photocatalytic Activities of $SrTiO_3$-Coated Fe_2O_3 and $BiFeO_3$.* Advanced Materials, 2006, 18, 514.

192. R. Guo, L. Fang, W. Dong, F. Zheng, and M. Shen, *Magnetically separable $BiFeO_3$ nanoparticles with a γ-Fe_2O_3 parasitic phase: controlled fabrication and enhanced visible-light photocatalytic activity.* Journal of Materials Chemistry, 2011, 21, 18645.

193. Z. Li, Y. Shen, C. Yang, Y. Lei, Y. Guan, Y. Lin, D. Liu, and C.-W. Nan, *Significant enhancement in the visible light photocatalytic properties of $BiFeO_3$-graphene nanohybrids.* Journal of Materials Chemistry A, 2013, 1, 823.

194. Y. Zhang, A. M. Schultz, P. A. Salvador, and G. S. Rohrer, *Spatially selective visible light photocatalytic activity of TiO_2/$BiFeO_3$ heterostructures.* Journal of Materials Chemistry, 2011, 21, 4168.

195. L. J. Di, H. Yang, G. Hu, T. Xian, J. Y. Ma, J. L. Jiang, R. S. Li, and Z. Q. Wei, *Enhanced photocatalytic activity of $BiFeO_3$ particles by surface decoration with Ag nanoparticles.* Journal of Materials Science: Materials in Electronics, 2014, 25, 2463.

196. X. Y. Chen, T. Yu, F. Gao, H. T. Zhang, L. F. Liu, Y. M. Wang, Z. S. Li, Z. G. Zou, and J.-M. Liu, *Application of weak ferromagnetic $BiFeO_3$ films as the photoelectrode material under visible-light irradiation.* Applied Physics Letters, 2007, 91, 022114.

197. W. Ji, K. Yao, Y.-F. Lim, Y. C. Liang, and A. Suwardi, *Epitaxial ferroelectric $BiFeO_3$ thin films for unassisted photocatalytic water splitting.* Applied Physics Letters, 2013, 103, 062901.

198. S. Li, R. Nechache, C. Harnagea, L. Nikolova, and F. Rosei, *Single-crystalline $BiFeO_3$ nanowires and their ferroelectric behavior.* Applied Physics Letters, 2012, 101, 192903.

199. S. Li, J. Zhang, M. G. Kibria, Z. Mi, M. Chaker, D. Ma, R. Nechache, and F. Rosei, *Remarkably enhanced photocatalytic activity of laser ablated Au nanoparticle decorated $BiFeO_3$ nanowires under visible-light.* Chemical Communications, 2013, 49, 5856.

200. S. Li, R. Nechache, I. A. V. Davalos, G. Goupil, L. Nikolova, M. Nicklaus, J. Laverdiere, A. Ruediger, and F. Rosei, *Ultrafast Microwave Hydrothermal Synthesis of $BiFeO_3$ Nanoplates.* Journal of the American Ceramic Society, 2013, 96, 3155.

201. R. Nechache, C. Harnagea, S. Li, L. Cardenas, W. Huang, J. Chakrabartty and F. Rosei, *Bandgap tuning of multiferroic oxide solar cells,* Nature Photonics, in press.

202. S. Li, B. AlOtaibi, W. Huang, Z. Mi, R. Nechache, N. Serpone and F. Rosei, *Multiferroic Bi_2FeCrO_6 Epitaxial Thin Film as a New Visible Light Absorbing Photocathode Material*, submited to Small.

203. R. I. Walton, *Subcritical solvothermal synthesis of condensed inorganic materials.* Chemical Society Reviews, 2002, 31, 230.

204. S. Feng and R. Xu, *New Materials in Hydrothermal Synthesis.* Accounts of Chemical Research, 2000, 34, 239.

205. S. Komarneni, R. Roy, and Q. H. Li, *Microwave-hydrothermal synthesis of ceramic powders.* Materials Research Bulletin, 1992, 27, 1393.

206. M. Baghbanzadeh, L. Carbone, P. D. Cozzoli, and C. O. Kappe, *Microwave-Assisted Synthesis of Colloidal Inorganic Nanocrystals.* Angewandte Chemie International Edition, 2011, 50, 11312.

207. D. B. Chrisey and G. K. Hubler, *Pulsed laser deposition of thin films.* Pulsed Laser Deposition of Thin Films, by Douglas B. Chrisey (Editor), Graham K. Hubler (Editor), Wiley-VCH, May 2003.

208. C. Harnagea, C. Cojocaru, R. Nechache, O. Gautreau, F. Rosei, and A. Pignolet, *Towards ferroelectric and multiferroic nanostructures and their characterisation.* International Journal of Nanotechnology, 2008, 5, 930.

209. P. M. Rørvik, T. Grande, and M.-A. Einarsrud, *One-Dimensional Nanostructures of Ferroelectric Perovskites.* Advanced Materials, 2011, 23, 4007.

210. J. J. Urban, W. S. Yun, Q. Gu, and H. Park, *Synthesis of Single-Crystalline Perovskite Nanorods Composed of Barium Titanate and Strontium Titanate.* Journal of the American Chemical Society, 2002, 124, 1186.

211. Y. Mao, S. Banerjee, and S. S. Wong, *Large-Scale Synthesis of Single-Crystalline Perovskite Nanostructures.* Journal of the American Chemical Society, 2003, 125, 15718.

212. J.-F. Liu, X.-L. Li, and Y.-D. Li, *Novel Synthesis of Polymorphous Nanocrystalline $KNbO_3$ by a Low Temperature Solution Method.* Journal of Nanoscience and Nanotechnology, 2002, 2, 617.

213. C. Yan, L. Nikolova, A. Dadvand, C. Harnagea, A. Sarkissian, D. F. Perepichka, D. Xue, and F. Rosei, *Multiple $NaNbO_3/Nb_2O_5$ Heterostructure Nanotubes: A New Class of Ferroelectric/Semiconductor Nanomaterials.* Advanced Materials, 2010, 22, 1741.

214. S. Han, C. Li, Z. Liu, B. Lei, D. Zhang, W. Jin, X. Liu, T. Tang, and C. Zhou, *Transition Metal Oxide Core−Shell Nanowires: Generic Synthesis and Transport Studies.* Nano Letters, 2004, 4, 1241.

215. G. Suyal, E. Colla, R. Gysel, M. Cantoni, and N. Setter, *Piezoelectric Response and Polarization Switching in Small Anisotropic Perovskite Particles.* Nano Letters, 2004, 4, 1339.

216. W. S. Yun, J. J. Urban, Q. Gu, and H. Park, *Ferroelectric Properties of Individual Barium Titanate Nanowires Investigated by Scanned Probe Microscopy.* Nano Letters, 2002, 2, 447.

217. S. H. Xie, J. Y. Li, R. Proksch, Y. M. Liu, Y. C. Zhou, Y. Y. Liu, Y. Ou, L. N. Lan, and Y. Qiao, *Nanocrystalline multiferroic $BiFeO_3$ ultrafine fibers by sol-gel based electrospinning.* Applied Physics Letters, 2008, 93, 222904.

218. C. Harnagea, M. Alexe, D. Hesse, and A. Pignolet, *Contact resonances in voltage-modulated force microscopy.* Applied Physics Letters, 2003, 83, 338.

219. V. Shelke, D. Mazumdar, G. Srinivasan, A. Kumar, S. Jesse, S. Kalinin, A. Baddorf, and A. Gupta, *Reduced Coercive Field in $BiFeO_3$ Thin Films Through Domain Engineering.* Advanced Materials, 2011, 23, 669.

220. X. H. Du, U. Belegundu, and K. Uchino, *Crystal orientation dependence of piezoelectric properties in lead zirconate titanate: Theoretical expectation for thin films.* Japanese Journal of Applied Physics Part 1-Regular Papers Short Notes & Review Papers, 1997, 36, 5580.

221. C. Harnagea, A. Pignolet, M. Alexe, and D. Hesse, *Piezoresponse Scanning Force Microscopy: What Quantitative Information Can We Really Get Out of Piezoresponse Measurements on Ferroelectric Thin Films.* Integrated Ferroelectrics, 2002, 44, 113.

222. S. V. Kalinin, B. J. Rodriguez, S. Jesse, J. Shin, A. P. Baddorf, P. Gupta, H. Jain, D. B. Williams, and A. Gruverman, *Vector piezoresponse force microscopy.* Microscopy and Microanalysis, 2006, 12, 206.

223. J. X. Zhang, Y. L. Li, Y. Wang, Z. K. Liu, L. Q. Chen, Y. H. Chu, F. Zavaliche, and R. Ramesh, *Effect of substrate-induced strains on the spontaneous polarization of epitaxial $BiFeO_3$ thin films.* Journal of Applied Physics, 2007, 101, 114105.

224. A. F. Devonshire, *CIX. Theory of barium titanate—Part II.* Philosophical Magazine Series 7, 1951, 42, 1065.

225. J. Jitputti, Y. Suzuki, and S. Yoshikawa, *Synthesis of TiO_2 nanowires and their photocatalytic activity for hydrogen evolution.* Catalysis Communications, 2008, 9, 1265.

226. Y. Li, T. Takata, D. Cha, K. Takanabe, T. Minegishi, J. Kubota, and K. Domen, *Vertically Aligned Ta_3N_5 Nanorod Arrays for Solar-Driven Photoelectrochemical Water Splitting.* Advanced Materials, 2013, 25, 125.

227. J. M. Macak, M. Zlamal, J. Krysa, and P. Schmuki, *Self‐Organized TiO_2 Nanotube Layers as Highly Efficient Photocatalysts.* Small, 2007, 3, 300.

228. Q. Liu, Y. Zhou, J. Kou, X. Chen, Z. Tian, J. Gao, S. Yan, and Z. Zou, *High-Yield Synthesis of Ultralong and Ultrathin Zn_2GeO_4 Nanoribbons toward Improved Photocatalytic Reduction of CO_2 into Renewable Hydrocarbon Fuel.* Journal of the American Chemical Society, 2010, 132, 14385.

229. Z. Xuming, C. Yu Lim, L. Ru-Shi, and T. Din Ping, *Plasmonic photocatalysis.* Reports on Progress in Physics, 2013, 76, 046401.

230. A. Primo, A. Corma, and H. Garcia, *Titania supported gold nanoparticles as photocatalyst.* Physical Chemistry Chemical Physics, 2011, 13, 886.

231. R. Costi, A. E. Saunders, E. Elmalem, A. Salant, and U. Banin, *Visible Light-Induced Charge Retention and Photocatalysis with Hybrid CdSe−Au Nanodumbbells.* Nano Letters, 2008, 8, 637.

232. D. B. Ingram and S. Linic, *Water Splitting on Composite Plasmonic-Metal/Semiconductor Photoelectrodes: Evidence for Selective Plasmon-Induced Formation of Charge Carriers near the Semiconductor Surface.* Journal of the American Chemical Society, 2011, 133, 5202.

233. Y. Qu, R. Cheng, Q. Su, and X. Duan, *Plasmonic Enhancements of Photocatalytic Activity of Pt/n-Si/Ag Photodiodes Using Au/Ag Core/Shell Nanorods.* Journal of the American Chemical Society, 2011, 133, 16730.

234. C. Gomes Silva, R. Juárez, T. Marino, R. Molinari, and H. García, *Influence of Excitation Wavelength (UV or Visible Light) on the Photocatalytic Activity of Titania Containing Gold Nanoparticles for the Generation of Hydrogen or Oxygen from Water.* Journal of the American Chemical Society, 2010, 133, 595.

235. Z. W. Seh, S. Liu, M. Low, S.-Y. Zhang, Z. Liu, A. Mlayah, and M.-Y. Han, *Janus Au-TiO_2 Photocatalysts with Strong Localization of Plasmonic Near-Fields for Efficient Visible-Light Hydrogen Generation.* Advanced Materials, 2012, 24, 2310.

236. Y. Tian and T. Tatsuma, *Mechanisms and Applications of Plasmon-Induced Charge Separation at TiO_2 Films Loaded with Gold Nanoparticles.* Journal of the American Chemical Society, 2005, 127, 7632.

237. S. I. Dolgaev, A. V. Simakin, V. V. Voronov, G. A. Shafeev, and F. Bozon-Verduraz, *Nanoparticles produced by laser ablation of solids in liquid environment.* Applied Surface Science, 2002, 186, 546.

238. J.-P. Sylvestre, S. Poulin, A. V. Kabashin, E. Sacher, M. Meunier, and J. H. T. Luong, *Surface Chemistry of Gold Nanoparticles Produced by Laser Ablation in Aqueous Media.* The Journal of Physical Chemistry B, 2004, 108, 16864.

239. J. Zhang, G. Chen, M. Chaker, F. Rosei, and D. Ma, *Gold nanoparticle decorated ceria nanotubes with significantly high catalytic activity for the reduction of nitrophenol and mechanism study.* Applied Catalysis B: Environmental, 2013, 132–133, 107.

240. W. Haiss, N. T. K. Thanh, J. Aveyard, and D. G. Fernig, *Determination of Size and Concentration of Gold Nanoparticles from UV−Vis Spectra.* Analytical Chemistry, 2007, 79, 4215.

241. Y. Zheng, L. Zheng, Y. Zhan, X. Lin, Q. Zheng, and K. Wei, *Ag/ZnO Heterostructure Nanocrystals: Synthesis, Characterization, and Photocatalysis.* Inorganic Chemistry, 2007, 46, 6980.

242. M. A. Butler, *Photoelectrolysis and physical properties of the semiconducting electrode WO_3* Journal of Applied Physics, 1977, 48, 1914.

243. P. Li, Z. Wei, T. Wu, Q. Peng, and Y. Li, *Au−ZnO Hybrid Nanopyramids and Their Photocatalytic Properties.* Journal of the American Chemical Society, 2011, 133, 5660.

244. R. S. Sonawane and M. K. Dongare, *Sol–gel synthesis of Au/TiO_2 thin films for photocatalytic degradation of phenol in sunlight.* Journal of Molecular Catalysis A: Chemical, 2006, 243, 68.

245. A. Iwase, H. Kato, and A. Kudo, *Nanosized Au Particles as an Efficient Cocatalyst for Photocatalytic Overall Water Splitting.* Catalysis Letters, 2006, 108, 7.

246. S. K. Cushing, J. Li, F. Meng, T. R. Senty, S. Suri, M. Zhi, M. Li, A. D. Bristow, and N. Wu, *Photocatalytic Activity Enhanced by Plasmonic Resonant Energy Transfer from Metal to Semiconductor.* Journal of the American Chemical Society, 2012, 134, 15033.

247. A. Corma and H. Garcia, *Supported gold nanoparticles as catalysts for organic reactions.* Chemical Society Reviews, 2008, 37, 2096.

248. K. Prashanthi, G. Thakur, and T. Thundat, *Surface enhanced strong visible photoluminescence from one-dimensional multiferroic $BiFeO_3$ nanostructures.* Surface Science, 2012, 606, L83.

249. H.-Y. Si, C.-H. Liu, H. Xu, T.-M. Wang, and H.-L. Zhang, *Shell-Controlled Photoluminescence in CdSe/CNT Nanohybrids.* Nanoscale Research Letters, 2009, 4, 1146

250. B. A. Gonfa, M. E. A. Khakani, and D. Ma, *Quantum Dot/Carbon Nanotube Nanohybrids for Novel Nanostructured Photovoltaic Devices.* Reviews in Nanoscience and Nanotechnology, 2012, 1, 22.

251. Y. Wu, H. Liu, J. Zhang, and F. Chen, *Enhanced Photocatalytic Activity of Nitrogen-Doped Titania by Deposited with Gold.* The Journal of Physical Chemistry C, 2009, 113, 14689.

252. S.-W. Cao, Z. Yin, J. Barber, F. Y. C. Boey, S. C. J. Loo, and C. Xue, *Preparation of Au-$BiVO_4$ Heterogeneous Nanostructures as Highly Efficient Visible-Light Photocatalysts.* ACS Applied Materials & Interfaces, 2011, 4, 418.

253. K. S. Novoselov, D. Jiang, F. Schedin, T. J. Booth, V. V. Khotkevich, S. V. Morozov, and A. K. Geim, *Two-dimensional atomic crystals.* Proceedings of the National Academy of Sciences of the United States of America, 2005, 102, 10451.

254. E. Hosono, S. Fujihara, I. Honma, and H. Zhou, *The Fabrication of an Upright‐Standing Zinc Oxide Nanosheet for Use in Dye‐Sensitized Solar Cells.* Advanced Materials, 2005, 17, 2091.

255. Y. Omomo, T. Sasaki, L. Wang, and M. Watanabe, *Redoxable nanosheet crystallites of MnO_2 derived via delamination of a layered manganese oxide.* Journal of the American Chemical Society, 2003, 125, 3568.

256. C. Zhang and Y. Zhu, *Synthesis of Square Bi_2WO_6 Nanoplates as High-Activity Visible-Light-Driven Photocatalysts.* Chemistry of Materials, 2005, 17, 3537.

257. S. J. Chen, Y. C. Liu, C. L. Shao, R. Mu, Y. M. Lu, J. Y. Zhang, D. Z. Shen, and X. W. Fan, *Structural and Optical Properties of Uniform ZnO Nanosheets.* Advanced Materials, 2005, 17, 586.

258. G. Xi and J. Ye, *Synthesis of bismuth vanadate nanoplates with exposed {001} facets and enhanced visible-light photocatalytic properties.* Chemical Communications, 2010, 46, 1893.

259. J. Xie, H. Zhang, S. Li, R. Wang, X. Sun, M. Zhou, J. Zhou, X. W. Lou, and Y. Xie, *Defect-Rich MoS_2 Ultrathin Nanosheets with Additional Active Edge Sites for Enhanced Electrocatalytic Hydrogen Evolution.* Advanced Materials, 2013, 25, 5807.

260. X. Zhang and Y. Xie, *Recent advances in free-standing two-dimensional crystals with atomic thickness: design, assembly and transfer strategies.* Chemical Society Reviews, 2013, 42, 8187.

261. L. Xiaomeng, X. Jimin, S. Yuanzhi, and L. Jiamin, *Surfactant-assisted hydrothermal preparation of submicrometer-sized two-dimensional $BiFeO_3$ plates and their photocatalytic activity.* Journal of Materials Science, 2007, 42, 6824.

262. M. Valant, A.-K. Axelsson, and N. Alford, *Peculiarities of a Solid-State Synthesis of Multiferroic Polycrystalline $BiFeO_3$.* Chemistry of Materials, 2007, 19, 5431.

263. M. M. Kumar, V. R. Palkar, K. Srinivas, and S. V. Suryanarayana, *Ferroelectricity in a pure $BiFeO_3$ ceramic.* Applied Physics Letters, 2000, 76, 2764.

264. K. Byrappa and T. Adschiri, *Hydrothermal technology for nanotechnology.* Progress in Crystal Growth and Characterization of Materials, 2007, 53, 117.

265. C. M. Cho, J. H. Noh, I.-S. Cho, J.-S. An, K. S. Hong, and J. Y. Kim, *Low-Temperature Hydrothermal Synthesis of Pure $BiFeO_3$ Nanopowders Using Triethanolamine and Their Applications as Visible-Light Photocatalysts.* Journal of the American Ceramic Society, 2008, 91, 3753.

266. B. L. Newalkar, S. Komarneni, and H. Katsuki, *Microwave-hydrothermal synthesis and characterization of barium titanate powders.* Materials Research Bulletin, 2001, 36, 2347.

267. G. J. Wilson, G. D. Will, R. L. Frost, and S. A. Montgomery, *Efficient microwave hydrothermal preparation of nanocrystalline anatase TiO_2 colloids.* Journal of Materials Chemistry, 2002, 12, 1787.

268. X. Hu and J. C. Yu, *Continuous Aspect-Ratio Tuning and Fine Shape Control of Monodisperse α-Fe_2O_3 Nanocrystals by a Programmed Microwave–Hydrothermal Method.* Advanced Functional Materials, 2008, 18, 880.

269. S. Komarneni, V. C. Menon, Q. H. Li, R. Roy, and F. Ainger, *Microwave-Hydrothermal Processing of $BiFeO_3$ and $CsAl_2PO_6$.* Journal of the American Ceramic Society, 1996, 79, 1409.

270. J. Prado-Gonjal, M. E. Villafuerte-Castrejón, L. Fuentes, and E. Morán, *Microwave–hydrothermal synthesis of the multiferroic $BiFeO_3$.* Materials Research Bulletin, 2009, 44, 1734.

271. A. Maître, M. François, and J. C. Gachon, *Experimental study of the Bi_2O_3-Fe_2O_3 pseudo-binary system.* Journal of Phase Equilibria and Diffusion, 2004, 25, 59.

272. L. Xu, Y.-S. Ding, C.-H. Chen, L. Zhao, C. Rimkus, R. Joesten, and S. L. Suib, *3D Flowerlike α-Nickel Hydroxide with Enhanced Electrochemical Activity Synthesized by Microwave-Assisted Hydrothermal Method.* Chemistry of Materials, 2007, 20, 308.

273. M. Tsuji, M. Hashimoto, Y. Nishizawa, M. Kubokawa, and T. Tsuji, *Microwave-Assisted Synthesis of Metallic Nanostructures in Solution.* Chemistry–A European Journal, 2005, 11, 440.

274. Y. Chang and H. C. Zeng, *Controlled Synthesis and Self-Assembly of Single-Crystalline CuO Nanorods and Nanoribbons.* Crystal Growth & Design, 2003, 4, 397.

275. Q.-J. Ruan and W.-D. Zhang, *Tunable Morphology of $Bi_2Fe_4O_9$ Crystals for Photocatalytic Oxidation.* The Journal of Physical Chemistry C, 2009, 113, 4168.

276. W. Shi, L. Zhou, S. Song, J. Yang, and H. Zhang, *Hydrothermal Synthesis and Thermoelectric Transport Properties of Impurity-Free Antimony Telluride Hexagonal Nanoplates.* Advanced Materials, 2008, 20, 1892.

277. H.-X. Mai, L.-D. Sun, Y.-W. Zhang, R. Si, W. Feng, H.-P. Zhang, H.-C. Liu, and C.-H. Yan, *Shape-Selective Synthesis and Oxygen Storage Behavior of Ceria Nanopolyhedra, Nanorods, and Nanocubes.* The Journal of Physical Chemistry B, 2005, 109, 24380.

278. L. Wu, H. Yao, B. Hu, and S.-H. Yu, *Unique Lamellar Sodium/Potassium Iron Oxide Nanosheets: Facile Microwave-Assisted Synthesis and Magnetic and Electrochemical Properties.* Chemistry of Materials, 2011, 23, 3946.

279. E. S. Jang, J. H. Won, S. J. Hwang, and J. H. Choy, *Fine Tuning of the Face Orientation of ZnO Crystals to Optimize Their Photocatalytic Activity.* Advanced Materials, 2006, 18, 3309.

280. R. Chen, J. Bi, L. Wu, W. Wang, Z. Li, and X. Fu, *Template-Free Hydrothermal Synthesis and Photocatalytic Performances of Novel Bi_2SiO_5 Nanosheets.* Inorganic Chemistry, 2009, 48, 9072.

281. L. Zhou, W. Wang, L. Zhang, H. Xu, and W. Zhu, *Single-Crystalline $BiVO_4$ Microtubes with Square Cross-Sections: Microstructure, Growth Mechanism, and Photocatalytic Property.* The Journal of Physical Chemistry C, 2007, 111, 13659.

282. X.-H. Liao, H. Wang, J.-J. Zhu, and H.-Y. Chen, *Preparation of Bi_2S_3 nanorods by microwave irradiation.* Materials Research Bulletin, 2001, 36, 2339.

283. D. Lebeugle, D. Colson, A. Forget, M. Viret, P. Bonville, J. F. Marucco, and S. Fusil, *Room-temperature coexistence of large electric polarization and magnetic order in $BiFeO_3$ single crystals.* Physical Review B, 2007, 76, 024116.

284. A. M. Glass, D. Linde, D. H. Auston, and T. J. Negran, *Excited state polarization, bulk photovoltaic effect and the photorefractive effect in electrically polarized media.* Journal of Electronic Materials, 1975, 4, 915.

285. P. Brody and F. Crowne, *Mechanism for the high voltage photovoltaic effect in ceramic ferroelectrics.* Journal of Electronic Materials, 1975, 4, 955.

286. Y. S. Yang, S. J. Lee, S. Yi, B. G. Chae, S. H. Lee, H. J. Joo, and M. S. Jang, *Schottky barrier effects in the photocurrent of sol–gel derived lead zirconate titanate thin film capacitors.* Applied Physics Letters, 2000, 76, 774.

287. W. Ji, K. Yao, and Y. C. Liang, *Bulk photovoltaic effect at visible wavelength in epitaxial ferroelectric $BiFeO_3$ thin films.* Advanced Materials, 2010, 22, 1763.

288. M. Alexe, *Local Mapping of Generation and Recombination Lifetime in $BiFeO_3$ Single Crystals by Scanning Probe Photoinduced Transient Spectroscopy.* Nano Letters, 2012, 12, 2193.

289. A. Bhatnagar, A. R. Chaudhuri, Y. H. Kim, D. Hesse, and M. Alexe, *Role of domain walls in the abnormal photovoltaic effect in $BiFeO_3$.* Nature communications, 2013, 4, 2835.

290. A. Ohtomoa, S. Chakravertya, H. Mashikoa, T. Oshimaa, and M. Kawasakia, *Spontaneous atomic ordering and magnetism in epitaxial stabilized double perovskites*. Journal of Materials Research, 2013, 28, 689.

291. C.-W. Tai and K. Baba-Kishi, *Influence of annealing on B-site order and dielectric properties of (0.4)Pb($In_{1/2}Nb_{1/2}$)O_3:(0.6)Pb($Mg_{1/3}Nb_{2/3}$)O_3 relaxor ceramics.* Journal of Applied Physics, 2006, 100, 116103.

292. J. Andreasson, J. Holmlund, S. G. Singer, C. S. Knee, R. Rauer, B. Schulz, M. Käll, M. Rübhausen, S.-G. Eriksson, and L. Börjesson, *Electron-lattice interactions in the perovskite $LaFe_{0.5}Cr_{0.5}O_3$ characterized by optical spectroscopy and LDA+U calculations.* Physical Review B, 2009, 80, 075103.

293. E. H. Sargent, *Colloidal quantum dot solar cells.* Nature Photonics, 2012, 6, 133.

294. W. S. Choi, M. F. Chisholm, D. J. Singh, T. Choi, G. E. Jellison Jr, and H. N. Lee, *Wide bandgap tunability in complex transition metal oxides by site-specific substitution.* Nature communications, 2012, 3, 689.

295. P. Maksymovych, S. Jesse, P. Yu, R. Ramesh, A. P. Baddorf, and S. V. Kalinin, *Polarization control of electron tunneling into ferroelectric surfaces.* Science, 2009, 324, 1421.

296. D. Scaife, *Oxide semiconductors in photoelectrochemical conversion of solar energy.* Solar Energy, 1980, 25, 41.

297. M. Grätzel, *Photoelectrochemical cells.* Nature, 2001, 414, 338.

298. M. Woodhouse and B. A. Parkinson, *Combinatorial approaches for the identification and optimization of oxide semiconductors for efficient solar photoelectrolysis.* Chemical Society Reviews, 2009, 38, 197.

299. N. Serpone and A. Emeline, *Semiconductor Photocatalysis — Past, Present, and Future Outlook.* The Journal of Physical Chemistry Letters, 2012, 3, 673.

300. M. S. Wrighton, A. B. Ellis, P. T. Wolczanski, D. L. Morse, H. B. Abrahamson, and D. S. Ginley, *Strontium titanate photoelectrodes. Efficient photoassisted electrolysis of water at zero applied potential.* Journal of the American Chemical Society, 1976, 98, 2774.

301. C. Santato, M. Ulmann, and J. Augustynski, *Photoelectrochemical Properties of Nanostructured Tungsten Trioxide Films.* The Journal of Physical Chemistry B, 2001, 105, 936.

302. A. Duret and M. Grätzel, *Visible Light-Induced Water Oxidation on Mesoscopic α-Fe_2O_3 Films Made by Ultrasonic Spray Pyrolysis.* The Journal of Physical Chemistry B, 2005, 109, 17184.

303. S. P. Berglund, D. W. Flaherty, N. T. Hahn, A. J. Bard, and C. B. Mullins, *Photoelectrochemical oxidation of water using nanostructured $BiVO_4$ films.* The Journal of Physical Chemistry C, 2011, 115, 3794.

304. M. Hara, T. Kondo, M. Komoda, S. Ikeda, J. N. Kondo, K. Domen, K. Shinohara, and A. Tanaka, *Cu_2O as a photocatalyst for overall water splitting under visible light irradiation.* Chemical Communications, 1998, 3, 357.

305. A. Paracchino, V. Laporte, K. Sivula, M. Grätzel, and E. Thimsen, *Highly active oxide photocathode for photoelectrochemical water reduction.* Nature Materials, 2011, 10, 456.

306. Ingler, J. P. Baltrus, and S. U. M. Khan, *Photoresponse of p-Type Zinc-Doped Iron(III) Oxide Thin Films.* Journal of the American Chemical Society, 2004, 126, 10238.

307. S. Ida, K. Yamada, T. Matsunaga, H. Hagiwara, Y. Matsumoto, and T. Ishihara, *Preparation of p-Type $CaFe_2O_4$ Photocathodes for Producing Hydrogen from Water.* Journal of the American Chemical Society, 2010, 132, 17343.

308. K. Iwashina and A. Kudo, *Rh-Doped $SrTiO_3$ Photocatalyst Electrode Showing Cathodic Photocurrent for Water Splitting under Visible-Light Irradiation.* Journal of the American Chemical Society, 2011, 133, 13272.

309. A. Glass, D. Von der Linde, D. Auston, and T. Negran, *Excited state polarization, bulk photovoltaic effect and the photorefractive effect in electrically polarized media.* Journal of Electronic Materials, 1975, 4, 915.

310. L. Li, P. A. Salvador, and G. S. Rohrer, *Photocatalysts with internal electric fields.* Nanoscale, 2014, 6, 24.

311. D. Tiwari and S. Dunn, *Photochemistry on a polarisable semi-conductor: what do we understand today?* Journal of Materials Science, 2009, 44, 5063.

312. J. L. Giocondi and G. S. Rohrer, *Spatial Separation of Photochemical Oxidation and Reduction Reactions on the Surface of Ferroelectric $BaTiO_3$.* The Journal of Physical Chemistry B, 2001, 105, 8275.

313. Y. Cui, J. Briscoe, and S. Dunn, *Effect of Ferroelectricity on Solar-Light-Driven Photocatalytic Activity of $BaTiO_3$—Influence on the Carrier Separation and Stern Layer Formation.* Chemistry of Materials, 2013, 25, 4215.

314. Y. Inoue, K. Sato, K. Sato, and H. Miyama, *Photoassisted water decomposition by ferroelectric lead zirconate titanate ceramics with anomalous photovoltaic effects.* The Journal of Physical Chemistry, 1986, 90, 2809.

315. Y. Inoue, *Photocatalytic water splitting by RuO_2-loaded metal oxides and nitrides with d0- and d10 -related electronic configurations.* Energy & Environmental Science, 2009, 2, 364.

316. J. Chen, H. Lu, H.-J. Liu, Y.-H. Chu, S. Dunn, K. Ostrikov, A. Gruverman, and N. Valanoor, *Interface control of surface photochemical reactivity in ultrathin epitaxial ferroelectric films.* Applied Physics Letters, 2013, 102, 182904.

317. C. Wang, D. Cao, F. Zheng, W. Dong, L. Fang, X. Su, and M. Shen, *Photocathodic behavior of ferroelectric $Pb(Zr,Ti)O_3$ films decorated with silver nanoparticles.* Chemical Communications, 2013, 49, 3769.

318. R. F. Berger and J. B. Neaton, *Computational design of low-band-gap double perovskites.* Physical Review B, 2012, 86, 165211.

319. B. AlOtaibi, M. Harati, S. Fan, S. Zhao, H. P. T. Nguyen, M. G. Kibria and Z. Mi, *High efficiency photoelectrochemical water splitting and hydrogen generation using GaN nanowire photoelectrode*. Nanotechnology, 2013, 24, 175401.

320. R. Nechache, C. Harnagea, A. Ruediger, F. Rosei, and A. Pignolet, *Effect of epitaxial strain on the structural and ferroelectric properties of Bi_2FeCrO_6 thin films.* Functional Materials Letters, 2010, 3, 83.

321. L. Balcells, J. Navarro, M. Bibes, A. Roig, and J. Fontcuberta, *Cationic ordering control of magnetization in Sr_2FeMoO_6 double perovskites.* Applied Physics Letters, 2001, 78, 781.

322. R. Nechache, C. Harnagea, S. Li, L. Cardenas, W. Huang, J. Chakrabartty, and F. Rosei, *A Novel Route to Achieve Highly Efficient Multiferroic oxides photovoltaic devices*, submitted to Nature Photonics.

323. C. Malerba, F. Biccari, C. Leonor Azanza Ricardo, M. D'Incau, P. Scardi, and A. Mittiga, *Absorption coefficient of bulk and thin film Cu_2O.* Solar Energy Materials and Solar Cells, 2011, 95, 2848.

324. R. Zimmermann, P. Steiner, R. Claessen, F. Reinert, S. Hüfner, P. Blaha, and P. Dufek, *Electronic structure of 3d-transition-metal oxides: on-site Coulomb repulsion versus covalency.* Journal of Physics: Condensed Matter, 1999, 11, 1657.

325. T. Arima, Y. Tokura, and J. B. Torrance, *Variation of optical gaps in perovskite-type 3d transition-metal oxides.* Physical Review B, 1993, 48, 17006.

326. H. L. Liu, M. K. Lin, Y. R. Cai, C. K. Tung, and Y. H. Chu, *Strain modulated optical properties in $BiFeO_3$ thin films.* Applied Physics Letters, 2013, 103, 181907.

327. H. Dong, Z. Wu, S. Wang, W. Duan, and J. Li, *Improving the optical absorption of $BiFeO_3$ for photovoltaic applications via uniaxial compression or biaxial tension.* Applied Physics Letters, 2013, 102, 072905.

328. J. L. Fierro, *Metal Oxides: chemistry and* applications. 2005, CRC press.

329. A. Vailionis, H. Boschker, W. Siemons, E. Houwman, D. Blank, G. Rijnders, and G. Koster, *Misfit strain accommodation in epitaxial ABO_3 perovskites: Lattice rotations and lattice modulations.* Physical Review B, 2011, 83, 064101.

330. A. Ohtomo, S. Chakraverty, H. Mashiko, T. Oshima, and M. Kawasaki, *Spontaneous atomic ordering and magnetism in epitaxially stabilized double perovskites.* Journal of Materials Research, 2013, 28, 689.

331. K. Matsuzaki, K. Nomura, H. Yanagi, T. Kamiya, M. Hirano, and H. Hosono, *Epitaxial growth of high mobility Cu_2O thin films and application to p-channel thin film transistor.* Applied Physics Letters, 2008, 93, 202107.

332. L. Liao, B. Yan, Y. F. Hao, G. Z. Xing, J. P. Liu, B. C. Zhao, Z. X. Shen, T. Wu, L. Wang, J. T. L. Thong, C. M. Li, W. Huang, and T. Yu, *P-type electrical, photoconductive, and anomalous ferromagnetic properties of Cu_2O nanowires.* Applied Physics Letters, 2009, 94, 113106.

Appendix A

List of Acronyms

BFO	$BiFeO_3$
BCO	$BiCrO_3$
BFCO	Bi_2FeCrO_6
ITO	Tin-doped Indium Oxide
STO	$SrTiO_3$
SRO	$SrRuO_3$
NSTO	Nb-doped $SrTiO_3$
CRO	$CaRuO_3$
LAO	$LaAlO_3$
LSAT	$(LaAlO_3)_{0.3}(Sr_2AlTaO_6)_{0.7}$
NP(s)	Nanoparticle(s)
NW(s)	Nanowire(s)
NHE	Normal Hydrogen Electrode
PV	Photovoltaic
PEC	Photoelectrochemical
LSPR	Localized Surface Plasmon Resonance
BPVE	Bulk Photovoltaic Effect
PCE	Power Conversion Efficiency
PLAL	Pulsed Laser Ablation in Liquid
PLD	Pulsed Laser Deposition

M-H	Microwave Hydrothermal
UV-Vis	Ultraviolet-Visible
AFM	Atomic Force Microscopy
PFM	Piezoresponse Force Microscopy
SEM	Scanning Electron Microscopy
FESEM	Field-emission Scanning Electron Microscopy
TEM	Transmission Electron Microscopy
HRTEM	High Resolution Transmission Electron Microscopy
SAED	Selected Area Electron Diffraction
XRD	X-Ray Diffraction
RSM	Reciprocal Space Maps
XPS	X-ray Photoelectron Spectrometry
UPS	Ultraviolet Photoelectron Spectroscopy
PL	Photoluminescence
RT	Room Temperature

Appendice B

Résumé

L'introduction

Ces dernières années, le développement et la caractérisation des matériaux multiferroïques ont suscité un intérêt particulier de la part de la communauté scientifique. En effet, La coexistence des ordres ferromagnétiques et ferroélectriques au sein de la même phase de ces matériaux offre des possibilités d'application dans les domaines du stockage des données informatique, la spintronique, des capteurs, des électro-aimants, et plus récemment dans le photovoltaïque. Parmi tous les matériaux multiferroïques étudiés, $BiFeO_3$ attire une grande attention car il exhibe simultanément une ferroélectricité ($T_C \sim 1103$ K) et antiferromagnétique de G-type ($T_N \sim 643$ K) au-delà de la température ambiante. En outre, le multiferroique $BiFeO_3$ avec une énergie de bande interdite de 2.2 à 2.8 eV a été identifié comme étant un excellent candidat pour des dispositifs photovoltaïques et des photocatalyseurs dans la gamme du visible. De plus, le couplage entre les ordres ferroïques au sein du $BiFeO_3$ offre plusieurs modes permettant des degrés de liberté additionnels pour contrôler des phénomènes physiques divers tels que l'effet photovoltaïque. Ceci va promouvoir le développement de nouvelles générations de cellules solaires et de cellules photo-électrochimiques aux multiples fonctionnalités. D'un autre côté, le développement des nanostructures a base de $BiFeO_3$ a permis des progrès technologiques significatifs dans la miniaturisation des dispositifs microélectroniques et a mené à la découverte de phénomènes physiques fondamentaux à l'échelle nanométrique. Jusqu'ici, les nanomatériaux $BiFeO_3$ avec différentes tailles et formes comme les nanoparticules, les nanotubes, les nanofils et les nano-/micro cubes ont été élaborés et synthétisés au moyen de techniques chimiques et

physiques. Grâce à l'effet de taille à l'échelle nanométrique, ces nanostructures présentent de différentes propriétés physiques et chimiques comparées à celles des cristaux massifs de. La maîtrise des méthodes de synthèse de ces nanostructures et l'étude fondamentale de leurs propriétés fonctionnelles sont les paramètres critiques dans conception de nouveaux matériaux multifonctionnels combinant des propriétés magnétiques, ferroélectriques et optoélectroniques et ainsi que les mécanismes qui les régissent.

La récente découverte du multiferroïque Bi_2FeCrO_6 avec une nouvelle double pérovskite et propriétés fonctionnelles exceptionnelles à la température ambiante a ouvert la voie à des nouvelles applications pratiques dans le domaine des multiferroïques. Bi_2FeCrO_6 a une structure cristalline similaire à celle de $BiFeO_3$ et exhibe un ordre cationique Fe/Cr particulier le long de la direction pseudocubique [111] qui lui confère des propriétés optiques et magnétiques uniques. Des études récentes montrent que la phase ordonnée de Bi_2FeCrO_6 peut être obtenue dans des couches minces et les nanostructures par la technique de l'ablation laser pulsé (PLD). Les couches minces de Bi_2FeCrO_6 obtenues possèdent une polarisation ferroélectrique rémanente d'environ 55 $\mu C/cm^2$ selon la direction pseudocubique [001], et elles sont ferrimagnétiques avec un moment magnétique dépendant l'ordre cationique Fe/Cr, environ 1.8 μ_B par l'unité de formule, excède largement celui obtenu pour les couches de $BiFeO_3$. De plus, des études théoriques ont démontré que la largeur de bande interdite est d'environ de 1.4-2.0 eV pour le ferrimagnétique - ferroélectrique Bi_2FeCrO_6 correspondant à une photosensibilité dans la gamme du visible et du proche infrarouge. Par conséquent, le Bi_2FeCrO_6 constitue un candidat prometteur et sérieux pour les dispositifs photovoltaïques et des cellules photo-électrochimiques.

Les objectifs

Cette thèse comprend deux parties avec deux objectifs correspondants: La première partie est consacrée principalement à la synthèse et a l'étude des propriétés fonctionnelles (c.-à-d., ferroélectrique, magnétique et photocatalytique) de nanostructures à base de $BiFeO_3$ a une et deux dimension (1D et 2D).

A ce jour, une myriade de nanomatériaux à base de $BiFeO_3$ a été rapportée dont leurs propriétés diffèrent complètement de celle des cristaux massifs de $BiFeO_3$. Par conséquent, l'investigation sur les propriétés fonctionnelles des nanostructures multiferroïques de $BiFeO_3$ est centrée sur la compréhension des mécanismes fondamentaux régissant leurs propriétés physiques ainsi que sur la conception de nouveaux matériaux multifonctionnels combinant des propriétés magnétiques, ferroélectriques et optoélectroniques. Ces dernières années, de nombreuses recherches ont été réalisées sur la synthèse de matériaux $BiFeO_3$ à faibles dimensions mettant en évidence les défis à relever notamment au niveau du contrôle de la morphologie de ces nanostructures monocristallines.. La croissance en solutions tampons et sans additifs de nanostructures de $BiFeO_3$ ayant des facettes cristallographiques particulières reste toujours difficile à obtenir, et l'étude de leurs propriétés physiques (par exemple ferroélectriques et magnétiques) à l'échelle nanométrique n'est pas encore effectuée. Tout récemment,les matériaux multiferroïques tels que le $BiFeO_3$, ont été reconnus comme étant un candidat potentiel pour des applications dans les photocatalyseurs en raison de leur grande stabilité chimique et de leurs faibles bandes interdites relatives (2.2-2.8 eV), permettant d'exploiter la majorité du rayonnement solaire dans la lumière visible. Cependant, des études sur les nanomatériaux à base de $BiFeO_3$ pour photocatalyse de l'eau sont encore très limitées. Les nanofils de $BiFeO_3$ qui peuvent être en théorie des photocatalyseurs très actifs pour la séparation

des molécules d'eau ne sont pas encore exploités. Donc, les objectifs principaux de cette partie de l'étude sont : (1) Synthèse de nanofils de $BiFeO_3$ unidimensionnel (1D) et l'étude de leurs propriétés ferroélectriques; (2) Etude des propriétés de séparation des molécules d'eau des nanofils $BiFeO_3$ et mettre en œuvre de nouvelles stratégies afin d'améliorer leur activité photocatalytique; (3) Développement d'une nouvelle méthode simple pour la synthèse des nanostructures 2D de $BiFeO_3$ sans additifs et surfactants et la compréhension de leur comportement magnétique.

La deuxième partie de ce travail de recherche sera consacrée pour l'investigation des propriétés de la conversion de l'énergie solaire (photovoltaïque et photo-électrochimique) des couches minces à base de Bi_2FeCrO_6 déposées par l'ablation laser pulsé.

En raison de demandes croissantes de l'énergie solaire propre et renouvelable, les chercheurs sont en train d'explorer de nouveaux matériaux et d'étudier fondamentalement les mécanismes de conversion photoélectrique pour le développement de de dispositifs PVs a hauts rendements. Le mécanisme de l'effet photovoltaïque dit « massif » (bulk photovoltaic effect -BPVE- en anglais) découvert dans les matériaux ferroélectriques fournit une voie alternative pour convertir la lumière en énergie électrique. Les dispositifs PV- ferroélectriques (PVFE), dans lequel le matériau ferroélectrique homogène est utilisé comme une couche d'absorption de la lumière, ontété étudiée pendant les décennies passées en utilisant de nombreux oxydes ferroélectriques tels que le $Pb(Zr_xTi_{1-x})O_3$. Cependant, plus de 50 ans après sa découverte, l'effet BPVE reste une curiosité académique plutôt que un phénomène exploitable pour des applications réelles. Ceci est dû principalement aux très faibles efficacités de conversion d'énergie (< 1%) obtenues dans des dispositifs de PVFE résultant des très faibles densités photoélectriques (de l'ordre de ~ nA/cm^2) et aux larges bandes interdites de la plupart des matériaux ferroélectriques

(typiquement de 3 à 4 eV). Par conséquent, l'utilisation de ferroélectriques à faible bande interdite est en train de devenir une voie prometteuse vers leur application dans nouveaux dispositifs optoélectroniques et PVs. Bien que le transport électrique, la structure magnétique et électronique du Bi_2FeCrO_6 aient été étudié, les propriétés optiques n'ont pas encore été explorées. En outre, jusqu'à maintenant, des études systématiques ont été réalisées sur l'impact de l'ordre cationique B/B' sur les propriétés des films a base de double perovskites $A_2BB'O_6$, comme par exemple le Bi_2FeCrO_6. Ceci a motivé notre étude actuelle. Les objectifs de cette partie sont donc: (1) Etudier l'impact des paramètres de croissance sur l'ordre cationique Fe/Cr dans les couches minces de Bi_2FeCrO_6 et comprendre l'influence de ce dernier sur les propriétés optiques; (2) Etudier fondamentalement les propriétés PVs et l'effet de l'ordre Fe/Cr sur la performance PV des dispositifs à base de Bi_2FeCrO_6; (3) Explorer des possibilités d'utilisation de couches minces à base de Bi_2FeCrO_6 comme photoélectrode pour la séparation des molécules d'eau au moyen de la lumière solaire.

PARTIE (I): Synthèse et propriétés fonctionnelles de nanostructures à base de $BiFeO_3$

Dans la première partie, nous avons synthétisé et étudié des propriétés ferroélectrique et magnétique des nanomatériaux de $BiFeO_3$ (nanofils 1D et nanoplaques 2D). En outre, nous avons conçu et synthétisé un photocatalyseur très actif comprenant des nanofils $BiFeO_3$ et des nanoparticules d'or déposées par ablation laser.

Chapitre 3. Propriétés ferroélectriques de nanofils monocristallines de $BiFeO_3$

Nous avons étudié les propriétés ferroélectriques des nanofils de $BiFeO_3$ monocristallines unidimensionnels (1D) en utilisant la microscopie à force piézoélectrique (PFM). Les nanofils de

$BiFeO_3$, synthétisés par la méthode hydrothermale conventionnelle, ont une structure perovskite rhomboédrique avec une croissance préférentielle selon le plan cristallographique (211) rhomboédrique perpendiculaire à l'axe du nanofil, comme révélé par la diffraction des rayons X et électronique. Les mesures PFM confirme le comportement ferroélectrique des nanofils de $BiFeO_3$ ayant un diamètre inférieur à 40 nm, dont la polarisation spontanée possède des composées selon les directions axiale et radiale. De même, nous avons constaté que les signaux PFM de $BiFeO_3$ dans le plan et hors du plan a varient en fonction de la taille des nanofils et dépendent de l'orientation relative de la maille cristalline de ces derniers. Nous avons décrit ce comportement par l'estimation de la forme de surface des coefficients piézoélectriques pour la symétrie rhomboédrique au moyen de calculs théoriques.

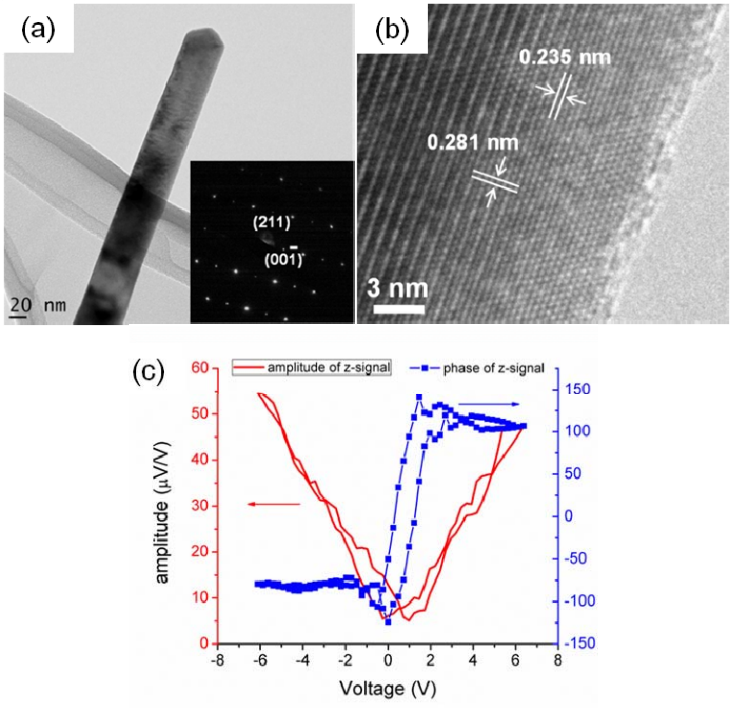

Figure R1. (a) Image MEB d'un nanofil de $BiFeO_3$. Encart: cliché de diffraction d'électrons correspondant. (b) Image en haute résolution du nanofil obtenue par microscopie électronique à. (c) Exemples de courbe d'hystérésis PFM de phase-tension et d'amplitude-tension dit "papillon" enregistrées pour un nanofil de $BiFeO_3$ selon la normale [198].

L’article traitant ces résultats décrits dans ce chapitre est le suivant

***S. Li**, R. Nechache, C. Harnagea, L. Nikolova and F. Rosei, Single-crystalline $BiFeO_3$ nanowires and their ferroelectric behavior, Appl. Phys. Lett., **101**, 102903, 2012.*

Chapitre 4. Photocatalyseurs hybrides de nanofils Au/$BiFeO_3$

Nous avons étudié les propriétés de craquage de l'eau à l’aide d’une source lumineuse des nanofils de $BiFeO_3$. Nous avons démonté que les nanofils possèdent une activité photocatalytique sous lumière visible très supérieure produisant des quantités importantes d'O_2 que celles obtenues par le $BiFeO_3$ sous d'autres formes. Ceci peut être attribué à la grande surface apparente et à la morphologie unique des nanofils Pour améliorer l'activité photocatalytique des nanofils, nous avons conçu et synthétisé un photocatalyseur nanocomposite hybride Au/$BiFeO_3$ très actif constitué de nanofils monocristallins de $BiFeO_3$ et de nanoparticules d’or déposées par ablation laser dans un milieu liquide et sans l’étape de fonctionnalisation. Nous avons constaté que les nanofils décorées par une faible quantité de nanoparticules d’or (1.0% en poids) montrent une activité photocatalytique (production d’O_2) ~30 fois plus élevé à celle des nanofils seuls, pendant les 4 premières heures de la réaction de. Leur grande activité catalytique est attribuée au rôle joué par les nanoparticules d’or tout d’abord comme centres de piégeage d'électrons et surtout a leur chimie de surface unique qui peuvent renforcer l'interaction et promouvoir le transport de charge du nanofil $BiFeO_3$ à la nanoparticule d’or. Nous avons également découvert que l'effet de plasmon de surface des nanoparticules d'or pourrait contribuer à l'amélioration de la photoactivité du système hybride.

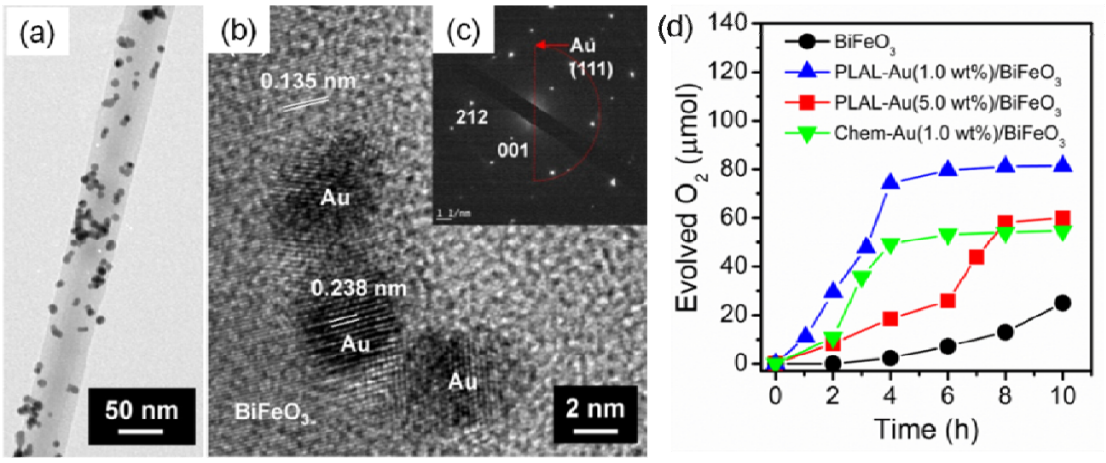

Figure R2. Images en microscopie électronique a balayage (a) et en transmission (b) de nanofils de $BiFeO_3$ décorés à PLAL-AuNPs (1.0% en masse), respectivement. (c) M Cliché de diffraction électronique correspondant (a). (d) Evolution de la quantité de d'oxygène en fonction du temps de la réaction sous une lumière visible ($\lambda > 380$ nm). La réaction est réalisée dans une solution contenant les photocatalyseurs (50 mg) et le $FeCl_3$ (4 mmol/L, 50 ml) en suspension [199].

L'article lié aux résultats décrits dans ce chapitre est le suivant:

***S. Li**, J. Zhang, M. G. Kibria, Z. Mi, M. Chaker, D. Ma, R. Nechache and F. Rosei, Remarkably enhanced photocatalytic activity of laser ablated Au nanoparticle decorated $BiFeO_3$ nanowires under visible-light, Chem. Commun., **49**, 5856, 2013.*

Chapitre 5. Synthèse hydrothermale assistée par micro-ondes et propriétés magnétiques des nanoplaques $BiFeO_3$

Nous avons développé une nouvelle méthode pour synthétiser des nanoplaques de $BiFeO_3$ (2 dimensions) avec des facettes cristallographiques orientées suivant la direction cubique (100). Les épaisseurs des nanoplaques obtenues varient entre 30 à 120 nm et leur dimensions la latérales sont de l'ordre de du micromètre, via une très simple et rapide (1~2 minutes) synthèse hydrothermale assistée par micro-ondes. Nous avons observé que le traitement par micro-ondes

permet une amélioration significative de la cristallinité des nanomatériaux de $BiFeO_3$ comparée au processus hydrothermal traditionnel et cela nécessite beaucoup moins de temps et d'énergie. En outre, nous avons constaté que la puissance de rayonnement des micro-ondes, le temps de réaction et la concentration en alcali jouent des rôles prépondérants au niveau de la cristallinité et la morphologie des nanoplaques. Un mécanisme de formation des nanoplaques de $BiFeO_3$ a été élaboré et discuté en se basant sur les résultats expérimentaux obtenus. De plus, les nanoplaques $BiFeO_3$ exhibent de faibles propriétés ferromagnétiques à température ambiante, que nous attribuons à l'effet de confinement de taille sur l'ordre magnétique.

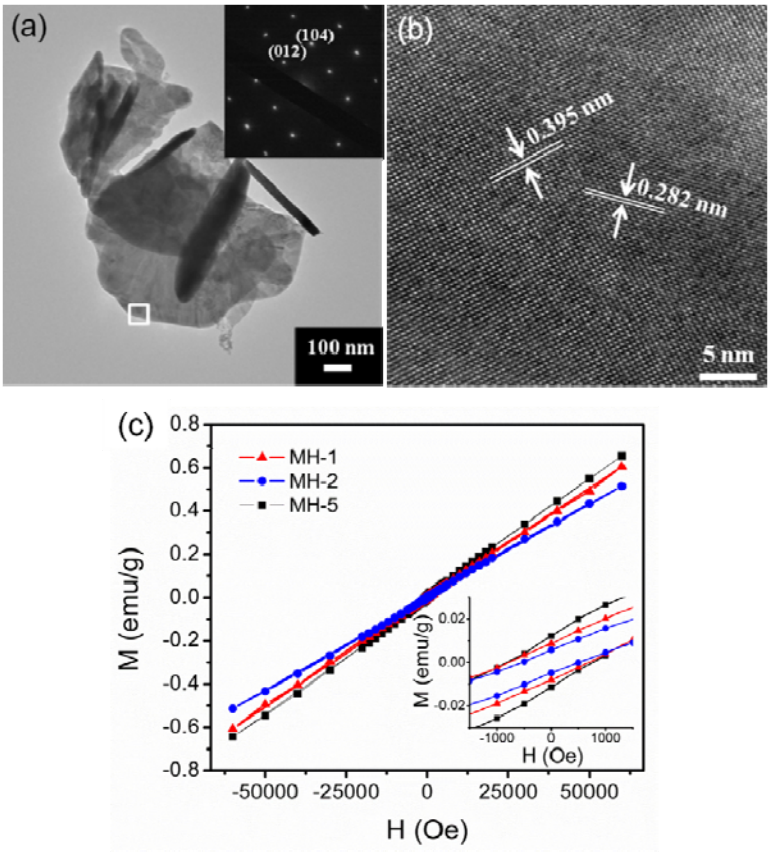

Figure R3. (a) image MEB de nanoplaques de $BiFeO_3$ (MH-5), et l'encart illustre un cliché de diffraction correspondant; (b) Image en microscopie électronique en transmission en haute résolution provenant d'une zone sélectionnée sur une nanoplaque en (a). (c) Courbes d'hystérésis magnétiques obtenues pour différentes nanoplaques de $BiFeO_3$. Encart montre des agrandissements aux alentours de zero [200].

L’article relatif aux résultats décrits dans ce chapitre:

***S. Li**, R. Nechache, I. A. V. Davalos, G. Goupil1, L. Nikolova, M. Nicklaus, J. Laverdiere, A. Ruediger1, F. Rosei, Ultrafast microwave hydrothermal synthesis of $BiFeO_3$ nanoplates, J. Am. Ceram. Soc., **96**, 3155, 2013.*

PARTIE (II) Couches minces à base de Bi_2FeCrO_6 pour l’application de conversion de l'énergie solaire

La deuxième partie s’est focalisée sur l’étude des propriétés de conversion de l'énergie solaire (photovoltaïque et photo-électrochimique) des cellules à base de couches minces de Bi_2FeCrO_6.

Chapitre 6. Effet photovoltaïque (PV) dans couches minces épitaxiales Bi_2FeCrO_6

Dans ce chapitre, Nous avons présenté et discuté les propriétés optiques et PVs de couches minces épitaxiales de Bi_2FeCrO_6 déposées sur des substrats $SrTiO_3$ orientés (100) et enrobés de couche tampon de $SrRuO_3$. Toutes les couches ont été déposées par PLD et la couche de $SrRuO_3$ assure la croissance heteroepitaxial de la structure en jouant le rôle de l’électrode de bas lors des mesures électriques. Nous avons démontré que la bande interdite des couches épitaxiales de Bi_2FeCrO_6 peut être réduite et ajustée expérimentalement sans pour autant affecter la polarisation en modifiant l'ordre cationique Fe/Cr dans ces couches. Ceci offre la possibilité de découvrir de nouveaux matériaux multiferroïques à petite bande interdite et de concevoir des cellules solaires oxydes à rendement élevé. Nous avons réalisé un ajustement de large bande interdite d'environ 1.1 eV, ce qui est important comparé aux valeurs rapportés par d'autres matériaux ferroélectriques dopés aux métaux de transition. Une combinaison équilibrée entre le de degré d’ordre cationique Fe/Cr et la taille du domaine ordonne ont été trouvée permettant d’obtenir des dispositifs PVs à base de Bi_2FeCrO_6 avec de hauts rendements de conversion. Aux conditions

expérimentales optimales, nous avons obtenu des cellules solaires avec des rendements de conversion de 3,3% sous l'illumination AM 1.5G (100 mW/cm^2).

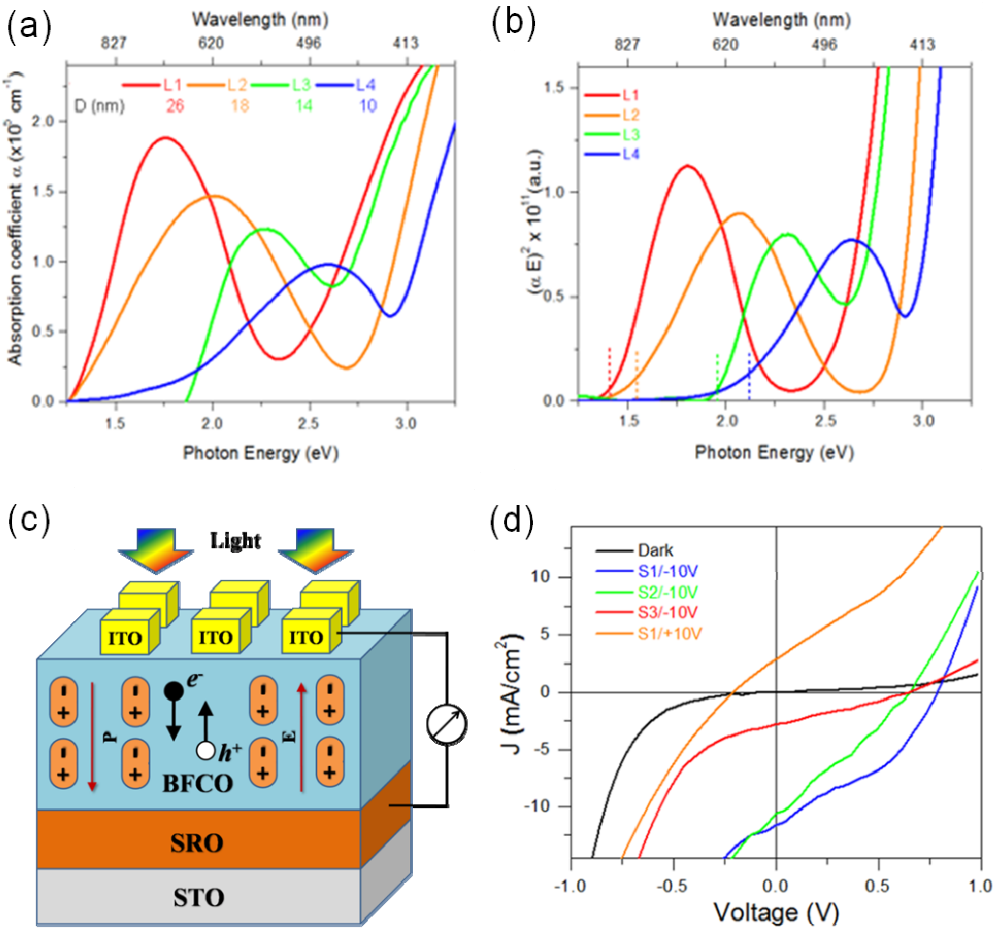

Figure R4. (a) spectres d'absorption UV-visible, et (b) l transitions optiques directes correspondant de la série L représentant des couches mince de Bi_2FeCrO_6 dépostées déposées à différentes fréquences d'ablation (f = 2, 8, 10, 14 Hz pour L1, L2, L3, L4, respectivement). (c) Représentation schématique du des cellules photovoltaïques à base de couches minces de Bi_2FeCrO_6 testées. (d) Courbes J-V caractéristiques des dispositifs à base couches minces Bi_2FeCrO_6 sous l'illumination AM1.5G générée à partir d'un simulateur solaire calibré avec une intensité d'irradiation de 100 mW/cm^2 [201].

L'article relatif aux résultats décrits dans ce chapitre est:

R. Nechache, C. Harnagea, ***S. Li****, L. Cardenas, W. Huang, J. Chakrabartty and F. Rosei, A Bandgap tuning of multiferroic oxide solar cells, Nature Photon., doi:10.1038/nphoton.2014.255.*

Chapitre 7. Propriétés photoelectrochimiques (PEC) de couches minces épitaxiales Bi_2FeCrO_6

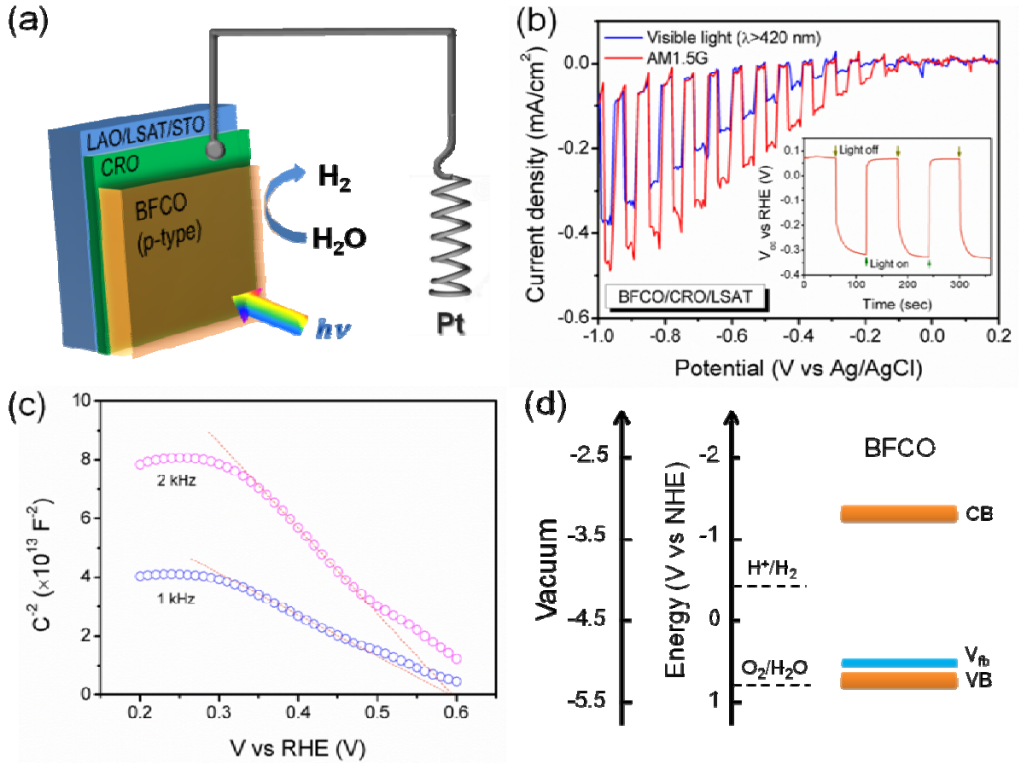

Figure R5. (a) Schéma de couche mince Bi_2FeCrO_6 de type p utilisée comme photocathode pour craquage de l'eau dans un montage PEC. (b) Variations de la densité de courant avec la tension appliquée (vs Ag/AgCl) à 1 mol L^{-1} de Na_2SO_4 à pH de 6,8 sous l'éclairage solaire simulé (AM1.5G) de couche mince Bi_2FeCrO_6 déposées sur des substrats $CaRuO_3/(LaAlO_3)_{0.3}(Sr_2AlTaO_6)_{0.7}$. L'encart illustre le changement du potentiel de l'électrode à base de Bi_2FeCrO_6 en circuit-ouvert avec et sans l'éclairage. (c) Mesures de type Mott-Schottky obtenus pour des photoélectrodes de Bi_2FeCrO_6. L'intersection de la ligne en pointillés avec l'axe des abscisses permet d'estimer V_{fb} de la couche de Bi_2FeCrO_6. (d) Schéma des niveaux de l'énergie calculés en se basant sur les résultats Mott-Schottky montrant V_{fb}, les énergies de VB et CB correspondant aux couches minces de Bi_2FeCrO_6 utilisées comme photoelectrodes [202].

Durant cette étude, nous avons démontré que grâce à sa petite bande interdite et une position de bande de conduction adéquate, le Bi_2FeCrO_6 sous forme de couche mince constituait un matériau prometteur pour la photo-réduction de l'eau en hydrogène en l'intégrant comme photocathode. Nous avons constaté que l'énergie de la bande interdite de Bi_2FeCrO_6 n'était pas

sensible aux contraintes épitaxiales, et que la quantité de lumière absorbée est faiblement liée au degré de l'ordre cationique Fe/Cr. Des mesures PEC montrent que l'utilisation de photocathode à base de couches Bi_2FeCrO_6 de type p déposée sur le substrat $CaRuO_3/SrTiO_3$ produit le fort photocourant (jusqu'à -1,0 mA/cm^{-2} à un potentiel de -1,0 V *vs* RHE). Après l'orientation de la polarisation ferroélectrique des couches dans une direction cristallographique particulière, la densité de photocourant est encore augmentée par un facteur de ~2. Ceci est dû à la modulation de la structure de bande par un contrôle adéquat du gradient de champ électrique interne. Notre étude valide ainsi l'utilisation de couches minces multiferroïques de Bi_2FeCrO_6 à faible bande interdite comme photocathode pour le craquage de l'eau. Ces résultats indiquent que la manipulation des champs internes par polarisation dans les matériaux ferroélectriques est une stratégie prometteuse pour la conception de photoélectrodes efficaces.

L'article relatif aux résultats décrits dans ce chapitre:

***S. Li**, B. AlOtaibi, Z. Mi, R. Nechache and F. Rosei, Epitaxial Bi_2FeCrO_6 Thin Film as a New Photoelectrode Material for Solar Water Splitting, submitted to Small.*

En résumé, deux types de matériaux multiferroïques $BiFeO_3$ et Bi_2FeCrO_6 ont été étudiés dans le cadre de ce travail de recherche. D'une part, des nanostructures $BiFeO_3$ a une et deux dimensions (1D et 2D) ont été synthétisées et leurs propriétés fonctionnelles (c.-à-d., ferroélectriques, magnétiques et photovoltaïques) ont été investiguées. D'autre part, des couches minces multiferroiques de Bi_2FeCrO_6 épitaxiales possédant une très bonne qualité cristalline ont été déposées par l'ablation laser pulsé (PLD) sur des substrats adéquats. Les propriétés optiques, PV et PEC des couches obtenues ont été caractérisées et étudiées en mettant l'accent sur l'influence de l'ordre cationique Fe/Cr. Nos études ont fourni des perspectives plus loin sur les

caractéristiques fondamentales physiques des nanostructures $BiFeO_3$ de faible dimension, et ont également démontré l'utilisation potentielle de $BiFeO_3$ et Bi_2FeCrO_6 sous formes de nanomatériaux à base ou des couches minces pour des applications de conversion d'énergie solaire.